Numerical Models for Tidal Turbine Farms

by

Michael Robert Shives
B.Sc., Carleton University, 2008
M.Sc., University of Victoria, 2012

A Dissertation Submitted in Partial Fulfillment of the
Requirements for the Degree of

DOCTOR OF PHILOSOPHY

in the Department of Mechanical Engineering

Numerical Models for Tidal Turbine Farms

by

Michael Robert Shives
B.Sc., Carleton University, 2008
M.Sc., University of Victoria, 2012

Supervisory Committee

Dr. C. Crawford, Supervisor
(Department of Mechanical Engineering)

Dr. N. Djilali, Departmental Member
(Department of Mechanical Engineering)

Dr. R. Karsten, Outside Member
(Department of Mathematics and Statistics, Acadia University)

Supervisory Committee

Dr. C. Crawford, Supervisor
(Department of Mechanical Engineering)

Dr. N. Djilali, Departmental Member
(Department of Mechanical Engineering)

Dr. R. Karsten, Outside Member
(Department of Mathematics and Statistics, Acadia University)

ABSTRACT

Anthropogenic climate change is approaching predicted tipping points and there is an urgent need to de-carbonize energy systems on a global scale. Generation technologies that do not emit greenhouse gas need to be rapidly deployed, and energy grids need to be updated to accommodate an intermittent fluctuating supply. Rapidly advancing battery technology, cost reduction of solar and wind power and other emerging generation technologies are making the needed changes technically and economically feasible.

Extracting energy from fast-flowing tidal currents using turbines akin to those used in wind farms, offers a reliable and predictable source of GHG free energy. The tidal power industry has established the technical feasibility of tidal turbines, and is presently up-scaling deployments from single isolated units to large tidal farms containing many turbines. However there remains significant economic uncertainty in financing such projects, partially due to uncertainty in predicting the long-term energy yield. Since energy yield is used in calculating the project revenue, it is of critical importance.

Predicting yield for a prospective farm has not received sufficient attention in the tidal power literature. this task has been the primary motivation for this thesis work, which focuses on establishing and validating simulation-based procedures to predict

flows through large tidal farms with many turbines, including the back effects of the turbines. This is a challenging problem because large tidal farms may alter tidal flows on large scales, and the slow-moving wake downstream of each rotor influences the inflow to other rotors, influencing their performance and loading. Additionally, tidal flow variation on diurnal and monthly timescales requires long-duration analysis to obtain meaningful statistics that can be used for forecasting.

This thesis presents a hybrid simulation method that uses 2D coastal flow simulations to predict tidal flows over long durations, including the influence of turbines, combined with higher-resolution 3D simulations to predict how wakes and local bathymetry influence the power of each turbine in a tidal farm. The two simulation types are coupled using a method of bins to reduce the computational cost within reasonable limits. The method can be used to compute detailed 3D flow fields, power and loading on each turbine in the farm, energy yield and the impact of the farm on tidal amplitude and phase. The method is demonstrated to be computationally tractable with modest high-performance computing resources and therefore are of immediate value for informing turbine placement, comparing turbine farm-layout cases and forecasting yield, and may be implemented in future automated layout optimization algorithms.

Contents

Supervisory Committee **ii**

Abstract **iii**

Table of Contents **v**

List of Tables **xi**

List of Figures **xiii**

Acknowledgements **xix**

Dedication **xx**

1 Introduction **1**

1.1 Problem Definition 4

1.1.1 Rotor Performance Characterization 5

1.1.2 Velocity Field Prediction 5

1.1.3 Method Requirements 7

1.2 Dissertation Outline and Research Progression 9

1.3 Research Contributions 12

2 Mesh and Load Distribution Requirements for Actuator Line CFD Simulations **15**

2.1 Introduction 16

2.1.1 Literature Review 17

2.1.2 Contributions of this Paper 21

2.2 Methodology 22

2.2.1 Software and Governing Equations 22

2.2.2 Turbulence Model 23

2.2.3 User Defined Velocity Functions 24
2.2.4 Momentum Source Terms 25
2.3 Infinite Wing 27
2.4 Constant Circulation Wing 30
2.5 Elliptically Loaded Wing 34
2.6 Conclusions 39

3 Cross Coupling Between Device-Level CFD and Oceanographic Models Applied to TISECS in Minas Passage and Petit Passage 42
3.1 Introduction 43
3.2 Overall Approach 44
3.3 Analysis Codes 45
3.3.1 Basin-Scale 46
3.3.2 Device-Scale 46
3.4 Turbine Performance Parameters and Velocity Scale 47
3.5 Turbine Forces and Power 48
3.5.1 Basin-Scale 48
3.5.2 Device-Scale 49
3.6 Simplified Channel Scenarios 50
3.6.1 Convergence with vertical resolution 52
3.6.2 Averaging volume horizontal size 52
3.6.3 Inflow velocity and vertical size 53
3.6.4 Boundary layer flows 53
3.6.5 Array tests 54
3.6.6 Summary 55
3.7 Minas Passage 56
3.7.1 Site characteristics 57
3.7.2 Device-scale Simulations 58
3.7.3 Basin-Scale Simulations 62
3.7.4 Model Results 63
3.8 Conclusions 63

4 Adapted Two-Equation Turbulence Closures for Actuator Disk RANS Simulations of Wind & Tidal Turbine Wakes 66
4.1 Introduction 67

4.2 Literature Review 68
4.3 Tuning and Validation Data 71
4.3.1 Manchester Side-by-Side Rotor Data 72
4.3.2 IFREMER Tandem Rotor Data 72
4.4 Governing Equations 75
4.4.1 RANS Equations 75
4.4.2 k-ε Turbulence Closure 76
4.4.3 k-ω Turbulence Closure 77
4.4.4 The Hybrid SST Turbulence Closure 77
4.4.5 New modification for vortex-breakdown 79
4.5 Simulation Methodology 80
4.5.1 Software 80
4.5.2 Rotor Forces 80
4.5.3 Boundary Conditions 84
4.6 Mesh Topology and Refinement 85
4.7 Verification 88
4.7.1 Method 88
4.7.2 Verification Results 89
4.8 Developing the S_k model 92
4.8.1 Error Measures and Objective Function 92
4.8.2 Tuning Results 94
4.8.3 Wake Profiles for Tuning Cases 96
4.9 Validation with Tandem Rotor Cases 101
4.10 Discussion & Conclusions 105

5 A Tuned Actuator Disk Approach for Predicting Tidal Turbine Performance with Wake Interaction 111
5.1 Introduction 112
5.2 Terminology 114
5.3 Experimental Data 116
5.4 Simulation Methodology 118
5.4.1 Governing Equations 118
5.4.2 Simulation Domain and Mesh 119
5.4.3 Boundary Conditions 121
5.4.4 Actuator Disk Model 123

5.5 Actuator Model Tuning . . . 126
5.6 Sensitivity to Mesh Density . . . 128
5.7 Validation Results and Discussion . . . 130
5.7.1 Single Rotor: Wake Profiles . . . 132
5.7.2 Single Rotor: Reference Velocity for Second Rotor . . . 135
5.7.3 Tandem Rotors: Power . . . 135
5.7.4 Twin Rotors: Rotor Efficiency . . . 137
5.7.5 Twin Rotors: Wake of Downstream Rotor . . . 138
5.8 Application to Blocked-Flow Scenarios . . . 139
5.9 Conclusions and Future Work . . . 144

6 A Tuned Actuator Cylinder Approach for Predicting Cross-Flow Turbine Performance with Wake Interaction and Channel Blockage Effects 146
6.1 Introduction . . . 147
6.2 Experimental Validation Data . . . 150
6.3 Simulation Methodology . . . 156
6.3.1 Governing Equations . . . 156
6.3.2 Mesh Generation . . . 157
6.3.3 Boundary Conditions . . . 159
6.3.4 Actuator Cylinder Model . . . 161
6.4 Actuator Model Tuning . . . 166
6.4.1 Phase 1: Tuning in the Duncan Dam Channel . . . 167
6.4.2 Phase 2: Correcting the Rotor Performance for Blockage Effect 169
6.4.3 Phase 3: Sensitizing the TACA Model to Inflow Turbulence . 171
6.5 Validation Results and Discussion . . . 173
6.5.1 Preliminary Validation for a Single Rotor . . . 173
6.5.2 Validation for the Longitudinal Arrays . . . 173
6.5.3 Validation for Lateral Arrays . . . 180
6.6 Computational Efficiency . . . 183
6.7 Conclusions . . . 185

7 Computational Methods for Tidal Turbine Farm Energy Yield, Part One: Methods and Initial Validation 197
7.1 Introduction . . . 199

7.2 Turbine Farm Scenarios and Yield Prediction Methods 202
7.2.1 Turbine Performance Characteristics 202
7.2.2 Scenario 1: Single turbine at ADP 202
7.2.3 Scenario 2: Few sparsely-packed turbines 204
7.2.4 Scenario 3: Few densely packed turbines 205
7.2.5 Scenario 4: Many turbines, densely spaced 208
7.2.6 Methodology Summary 209
7.3 Case-Study Site and Field Data 211
7.4 SWE simulations 215
7.4.1 Bottom-friction 215
7.4.2 SWE output 216
7.4.3 Time-series SLP yield 216
7.4.4 Yield-Based Scaling Factor 220
7.5 Application and Validation of SBR 222
7.5.1 Bin-Classification 222
7.5.2 RANS Simulations 224
7.6 Conclusions 234
7.6.1 Bin-averaging 236
7.6.2 Bin Sorting 238

8 Computational Methods for Tidal Farm Energy Yield Part Two: Rotor Models and Large Farms 242
8.1 Introduction 244
8.2 Yield Methodologies 245
8.3 Single-Rotor TADA Simulations to Validate SBT 246
8.3.1 TADA Turbine Model 248
8.3.2 Yield and Power using TADA 256
8.4 SWET Sub-Grid Turbine Model 260
8.4.1 Verifying SWET Force and Power 262
8.4.2 Verifying SWET wake predictions for an isolated rotor 263
8.5 Large Turbine Farms (STBT method) 266
8.5.1 Far-Field Impact 269
8.5.2 Near-Field Effects 269
8.5.3 Power and Force 272
8.5.4 Yield 277

8.5.5 Computational Expense 279
8.6 Discussion and Conclusions 280

9 Conclusions and Future Work **283**
9.1 Conclusions 283
9.1.1 3D RANS methods 283
9.1.2 2D SWE 285
9.1.3 Coupling Method 285
9.2 Yield Methodology Goals 286
9.3 Future Work 287
9.3.1 Sensitivity Analysis 287
9.3.2 Turbulence 288
9.3.3 Vertical Profiles 289
9.3.4 Turbine Motion 289
9.3.5 Sub-grid turbine force updates 289
9.3.6 Open Source 289

Bibliography **290**

List of Tables

Table 2.1 Percent over-prediction of the area integral of the Gaussian distribution for various ϵ/Δ_{grid}. 26

Table 3.1 CFD and basin-scale power (kW) at peak flood 65

Table 4.1 Inflow parameters tuned to match empty flume tank conditions. 85
Table 4.2 Verification study results and confidence limits for C_T, C_P and C_{D_S} 91
Table 4.3 Wake ERR values for the tested turbulence models. 101

Table 5.1 Inflow Parameters set to match IFREMER experimental data . 123

Table 6.1 Time required to setup, run and post process TACA simulations. 184

Table 7.1 ADP deployment locations and times 213
Table 7.2 Characteristics of the hypothetical turbine used for yield assessment. 214
Table 7.3 Summary of time periods used for evaluating yield for each ADP 214
Table 7.4 Summary of time-series yield predictions using ADP data and 2D SWE simulations. 221
Table 7.5 Table summarizing the yield scaling factor. 222
Table 7.6 Sample statistics from the binning analysis 225
Table 7.7 RMS velocity profile errors for SLP and SBR methods 231
Table 7.8 Summary of yield predictions using SLP and SBR 232
Table 7.9 Summary of yield percent errors using SLP and SBR 233

Table 8.1 Characteristics of the hypothetical turbine used for yield assessment. 250
Table 8.2 Summary of yield predictions using SLP, SBR and SBT. 257
Table 8.3 Summary of yield percent errors using SLP, SBR and SBT. . . . 258
Table 8.4 Impact on tidal amplitude and phase for farm cases A and B. . 269

Table 8.5 Yield predictions for farm cases A, B and C using SWET and TADA 278

List of Figures

Figure 1.1 Four leading tidal turbine designs 3
Figure 1.2 Typical rotor operational profiles 6

Figure 2.1 Depiction of force distributions in actuator disk and actuator line methods 18
Figure 2.2 Induced velocity produced by AL simulations compared to the analytical solution. 29
Figure 2.3 Angle of attack error calculated from 2D simulations. The error reduces with increasing ϵ and reducing Δ_{grid} 30
Figure 2.4 Induced velocity profile for various ϵ/Δ_{grid} ($\epsilon/c = 1/2$), demonstrating the degradation of the induction profile with inadequate mesh density 31
Figure 2.5 Distribution of trailed vorticity for a wing with constant circulation 32
Figure 2.6 Definition of flow angles and force components used for studies on elliptically loaded and constant chord wings 33
Figure 2.7 Resolved tip vortex induction compared to theoretical profiles using the Scully core model 35
Figure 2.8 Effect of spanwise mesh refinement on the resolved tip vortex induction 35
Figure 2.9 Downwash from simulations with constant ϵ over the entire span. (ϵ proportional to c_0) 38
Figure 2.10 Downwash predicted by simulations using ϵ proportional to c . 40
Figure 2.11 Iso-vorticity ($0.5s^{-1}$) surfaces for simulations with; $\epsilon/c_0 = \text{const}$ (left), and $\epsilon/c = \text{const}$ (right) 40

Figure 3.1 Flow Chart of Proposed Methodology 45
Figure 3.2 Example grid resolution for CFD and basin-scale simulations. . 49

Figure 3.3 Convergence trend with vertical resolution of the basin-scale simulation 53
Figure 3.4 Power error for set 1 tests 54
Figure 3.5 Variation of power error: constant vertical viscosity 55
Figure 3.6 Variation of power error: vertical viscosity determined by the k-ϵ closure 56
Figure 3.7 Power error for boundary layer tests. 57
Figure 3.8 Layout of turbines for the small array test case 58
Figure 3.9 Power error for array tests 59
Figure 3.10 Bathymetry for the Bay of Fundy region. 60
Figure 3.11 Bathymetry for the Minas Basin. 61
Figure 3.12 Bathymetry for the region around the test berths 61
Figure 3.13 Bathymetry for the CFD subdomains 62

Figure 4.1 Vertical velocity profile in the empty Manchester flume 73
Figure 4.2 Flow velocities and forces acting on the blade 81
Figure 4.3 Manchester rotor performance for a single rotor in the flume. . 83
Figure 4.4 Mesh A for the region downstream of the rotors for the Manchester cases. 86
Figure 4.5 Mesh B for the full domain for the IFREMER cases. 87
Figure 4.6 Mesh on actuator disk sub-domains, hub and tower 87
Figure 4.7 Continuum solution for $\widetilde{u^3}/u_0^3$ 91
Figure 4.8 ERR function variation with ζ_k and x_0/D 94
Figure 4.9 Curves defining the linear and $\tanh^2$ model fits 95
Figure 4.10 Wake profiles for the single rotor IFREMER I_0=3% case. . . . 97
Figure 4.11 Wake profiles for the tuned three-rotor Manchester I_0=10% case. 98
Figure 4.12 Wake profiles for the single rotor IFREMER I_0=15% case . . . 99
Figure 4.13 Wake profiles for I_0=3% IFREMER tandem rotor cases. 102
Figure 4.14 Wake profiles for I_0=15% IFREMER tandem rotor cases. . . . 103
Figure 4.15 Lateral wake profiles showing sensitivity to supporting structures. 109
Figure 4.16 Wake profiles showing sensitivity to L_x 110

Figure 5.1 Actuator disk mesh with 7-21 elements per diameter 120
Figure 5.2 Domain mesh with 7 elements-per-diameter for two rotors separated by 8D. 121

Figure 5.3 Sensitivity of velocity and turbulence intensity to the near-wall spacing. 122
Figure 5.4 Reference rotor loading profiles c_x, c_θ. 126
Figure 5.5 Tuned rotor performance curves for $C_{\mathrm{P}}^{\star}$. 127
Figure 5.6 Thrust and power error for different mesh densities. 129
Figure 5.7 Contributions of various modelling errors to the power discrepancy. 131
Figure 5.8 Velocity and turbulence intensity contours. 132
Figure 5.9 Lateral transects of the wake at several distances downstream of the rotor. $I_0 = 3\%$, $TSR = 3.67$, $u_0 = 0.8\mathrm{m/s}$ 133
Figure 5.10 Lateral transects of the wake at several distances downstream of the rotor. $I_0 = 15\%$, $TSR = 3.67$, $u_0 = 0.83\mathrm{m/s}$ 134
Figure 5.11 Disk-averaged value $100\,\langle u_{\mathrm{ref}}^3/u_0^3\rangle$ 136
Figure 5.12 Power coefficient of the downstream rotor for I_0=3%. 136
Figure 5.13 Power coefficeint of the downstream rotor for I_0=15% 137
Figure 5.14 Rotor efficiency term, $\eta_{\langle u_{\mathrm{ref}}\rangle}$. 139
Figure 5.15 Lateral transects of the second rotor wake: a/D=6, I_0=3%. . . 140
Figure 5.16 Lateral transects of the second rotor wake: a/D=6, I_0=15% . . 141
Figure 5.17 Sample domains used for studying the impact of blockage ratio. 142
Figure 5.18 Thrust and power coefficient variation with blockage ratio predicted by TADA. 143

Figure 6.1 Floating turbine assembly concept by Instream Energy Systems 150
Figure 6.2 Sample velocity and turbulence intensity profiles from stationary ADP 152
Figure 6.3 Channel depth. 153
Figure 6.4 Summary of test configurations with one, two or three turbines. 154
Figure 6.5 Measured system conversion efficiency and shaft power coefficient. 155
Figure 6.6 Actuator-cylinder (AC) mesh with employed resolution of 21 EPD 157
Figure 6.7 Domain mesh for the LAT-B B case 158
Figure 6.8 Coordinate systems used by TACA. 162
Figure 6.9 Blade forces interpreted in various coordinate systems. 163
Figure 6.10 Reference rotor loading profiles. 164
Figure 6.11 Remapped performance coefficients $C_{\{\mathrm{T,P}\}}^{\star}$ calculated from phase 1 tuning simulations in the DDM channel. 168

Figure 6.12 Lateral transects of the stream-wise velocity for different grid resolutions. 168
Figure 6.13 Rotor performance coefficients, corrected for blockage effect using TACA. 170
Figure 6.14 Sample rotor coefficients $C_{\mathrm{P}}^{\star}$ and $C_{\mathrm{T}}^{\star}$ sensitized to varying turbulence. 172
Figure 6.15 Simulation results from testing the TACA regression fits for $C_{\mathrm{T}}^{\star}$ and $C_{\mathrm{P}}^{\star}$. 173
Figure 6.16 Simulated wake contours downstream of rotor compared to ADP transect data. 175
Figure 6.17 Simulated wake transects compared to ADP transects. 176
Figure 6.18 Sensitivity of the simulated wake to $\pm 10\%$ changes to the thrust and combined generator/gearbox efficiency. 177
Figure 6.19 Power of downstream rotor for LON cases. 179
Figure 6.20 Velocity transect 8.5m upstream of the lateral array case B. . . 181
Figure 6.21 Power of central rotor for LAT cases. 182
Figure 6.22 Flow velocity through a staggered 4-row array of turbines in the Duncan Dam channel. 183
Figure 6.23 Calculated variance due to Doppler noise. 188
Figure 6.24 Contributions of Doppler noise and 5 s filter to the calculated turbulent kinetic energy. 189
Figure 6.25 Summary of the process used for developing inflow conditions. 191
Figure 6.26 Velocity transect 8.5m upstream of the lateral array case A. . . 193
Figure 6.27 Vertical velocity profile from the simulation inflow condition compared to ADP data 193
Figure 6.28 Sample mesh used for blockage ratios ranging from 1% to 40% 194
Figure 6.29 Variation of thrust and power coefficients with blockage ratio. . 195

Figure 7.1 Procedure for the SBR method. 206
Figure 7.2 Example mesh for the actuator-disk (AD) region 207
Figure 7.3 Procedure for the SBT method. 208
Figure 7.4 Procedure for the STBT method. 210
Figure 7.5 The location of the proposed tidal turbine farm. 212
Figure 7.6 Locations of the ADP deployments. 212

Figure 7.7 Performance curves for the hypothetical turbine used in the yield assessment studies. 214
Figure 7.8 Time-series comparing the signed speed from the tuned SWE model to ADP 1-5. 217
Figure 7.9 Time-series comparing the signed speed from the tuned SWE model to ADP 6-7 218
Figure 7.10 Sample time-series of rotor power for ADP 1-5 219
Figure 7.11 Variation of yield contribution with flow direction and speed. . 223
Figure 7.12 Sample bin-averaged flow fields for the highest yield bins. . . . 224
Figure 7.13 Sample SBR domain for the top yield contribution bin 226
Figure 7.14 Comparison of velocity profiles predicted by SBR and SLP to bin-averaged ADP 2-4 229
Figure 7.15 Comparison of vertical velocity profiles predicted by SBR and SLP to bin-averaged ADP 6-7 230
Figure 7.16 Sample ADCP profile data and depth-average at DG4, max ebb (left), max flood (center) and slack tide (right). 240

Figure 8.1 Procedure for the SBT method. 246
Figure 8.2 Procedure for the STBT method. 247
Figure 8.3 Sample domain used in TADA farm simulations 248
Figure 8.4 Performance curves for the hypothetical turbine. 250
Figure 8.5 Open model domain used for the TADA tuning simulations. . . 252
Figure 8.6 Re-mapped rotor performance between cut-in and rated speeds. 253
Figure 8.7 Re-mapped $C_{\mathrm{T}}^{\star ro}$ at the rated and cut-out speeds. 254
Figure 8.8 Re-mapped speeds for cut-in, rated power and cut-out. 255
Figure 8.9 Summary of yield predictions for ADP 2 and 4 from the top 30 binned flow-states. 258
Figure 8.10 Summary of yield predictions for ADP 6 and 7 from the top 30 binned flow-states. 259
Figure 8.11 Depiction of turbines in the regional-scale model 260
Figure 8.12 Elements allocated to turbines in the SWET simulations. . . . 264
Figure 8.13 SWET predictions of rotor force and power compared to TADA for ADP 2-4 264
Figure 8.14 SWET predictions of rotor force and power compared to TADA for ADP 6-7 265

Figure 8.15 Bin-averaged 2D SWET velocity (left) compared to 3D TADA (right). 266
Figure 8.16 Layout of rotors for the farm cases A, B and C. 267
Figure 8.17 Locations used for assessing far-field effects. 268
Figure 8.18 Impact of the turbines on the bin-averaged flow for the case A farm 270
Figure 8.19 Impact of the turbines on the bin-averaged flow for the case B farm 271
Figure 8.20 Bin 1 flow field predicted by SWET and TADA 273
Figure 8.21 Bin 3 flow field predicted by SWET and TADA 274
Figure 8.22 Vertical velocity profile for the case B turbine farm 275
Figure 8.23 Sample rotor power for farm A from TADA and SWET 276
Figure 8.24 Force and power predictions by TADA and SWET for the case B farm 277
Figure 8.25 Percent difference in total resistive force predicted by SWET vs. TADA 278
Figure 8.26 Yield (STBT) for turbines 1-21 for cases A and B, categorized by flood and ebb flow directions. 279

Figure 9.1 Summary of contributions and accomplishments 284

ACKNOWLEDGEMENTS

I would like to thank everyone who supported me throughout this thesis project.

First and foremost I am deeply grateful for Dr. Curran Crawford for his guidance and motivation; and for being an inspiration as a highly productive researcher, an idealist ready to take on the world's most challenging issues, a devoted husband and father, and all the while maintaining a high level of personal health and fitness. Curran you are a highly influential role model and I could never adequately express my respect. Second I thank my supervisory committee, Dr. Richard Karsten, Dr. Brian Polagye and Dr. Ned Djilali for reviewing this dissertation. Third I owe thanks to Clayton Hiles and Roy Walters from Cascadia Coast Research, to Voytek Klaptocz and Timothy Waung from Mavi Innovations Inc. and to Dave Leboe, Ronan Conron and Shane Grovue from Instream Energy Systems for their professional and enriching collaboration.

I also thank Dr. Paul Mycek, and Dr. Timothy Stallard, for providing crucial experimental validation data, and to the Offshore Energy Research Association for providing bathymetry and flow field data for Petit Passage. I owe thanks to the Pacific Institute for Climate Solutions (PICS), the Institute for Integrated Energy Systems at the University of Victoria (IESVic), the Natural Sciences and Engineering Research Council of Canada (NSERC), for financial support.

Finally I thank my family for their support and love through all the highs and lows.

No matter the risks we take, we always consider the end to be too soon, even though in life, more than anything else, quality should be more important than quantity.

Honnold

DEDICATION

To my parents, who never expected anything of me other than to be a good person, loved me unconditionally, supported me and spent incalculable amounts of time, money and effort to give me opportunities to grow and thrive.

Dad, you gave me the fortitude to tackle anything life can throw at me, it's a liberating inner strength without which I would have given-up many times.

Mom, your unstoppable kindness and light-hardheartedness will forever warm my heart. Your perseverance through tough times, while remaining kind and elegant are my definition of love.

I can only hope to maintain such outstanding qualities on my own journey through life.

Chapter 1

Introduction

There is overwhelming scientific consensus that anthropogenic greenhouse gas GHG emissions are driving a clear warming trend of the global climate, which is projected to cause detrimental impacts on natural and human systems. According to the International Panel on Climate Change [1]:

> *Continued emission of greenhouse gases will cause further warming and long-lasting changes in all components of the climate system, increasing the likelihood of severe, pervasive and irreversible impacts for people and ecosystems. Limiting climate change would require substantial and sustained reductions in greenhouse gas emissions which, together with adaptation, can limit climate change risks.*

While many governments are developing adaptation strategies, a more desirable outcome would be to limit warming altogether. However, this represents a major challenge due to the combined effects of: a) rapidly growing populations and economies, both of which are increasing demand for energy and b) a global energy infrastructure based primarily on burning fossil fuels.

The technological solution is to alter the global energy infrastructure to reduce its dependence on fossil fuels and toward alternatives which do not emit GHGs. Toward that end, there have been rapid advances in GHG-free energy generation technologies (particularly evident through reducing cost of wind and solar), energy storage (in particular rapid expansion of battery production capacity), and smart grid management technologies. These are among several key ingredients for a emissions-free energy supply which is equally reliable to present day fossil fuel based grids.

While wind turbines and solar cells are presently the leading renewable energy technologies, other forms of renewable energy will likely play a role in the future energy supply because of the intermittent and unpredictable nature of wind and solar resources. One such alternative is to extract energy from fast-flowing tidal currents, which are a reliable and predictable renewable energy source because tides are a well understood time-varying cyclical process. Tidal turbines are conceptually similar to wind turbines, but have not yet converged to a standard optimal design, which is evident observing four of the leading designs depicted in figure 1.1.

Recent isolated tidal turbine deployments have proved their technical feasibility and large-scale tidal power farms are presently in development stages in the UK and Canada, which can provide a technical and economic baseline for future developments. The MEYGEN[1] project in the Pentland Firth, Scotland plans to install 398 MW of offshore tidal stream turbines by the early 2020s, while the Cape Sharp[2] Tidal project in Minas Passage, Canada, plans to install up to 300 MW of capacity.

The economics of tidal turbine farms remain uncertain and the industry needs to establish standards for quantifying costs of manufacture, deployment, grid connection, O&M, and decommissioning. Such costs are amortized over the project lifetime considering a specific internal rate of return, and are compared to expected revenue from energy sales to determine project viability. Thus, standards must also be established for predicting revenue, which is the primary motivation for this thesis. Total revenue is the time-integral of the instantaneous farm power production multiplied by the energy price. If the price remains fixed, revenue is simply the energy yield multiplied by the price.

The International Electrotechnical Commission (IEC) standard on Tidal Energy Resource Assessment and Characterization [2] was released in 2015 and provides general guidelines for yield assessment but contains no definitive procedures. Meanwhile, research consortia [3] and consultancies [4] continue to develop their own assessment methodologies. This thesis contributes toward such efforts by proposing specific methods which have been validated and are computationally tractable for a developer to employ.

In addition to predicting energy yield, the methods presented herein can also be used for forecasting farm power output, which is essential for grid operations planning, and could be integrated into an optimization algorithm to choose the maximum-yield

[1] `http://www.meygen.com`
[2] `http://capesharptidal.com`

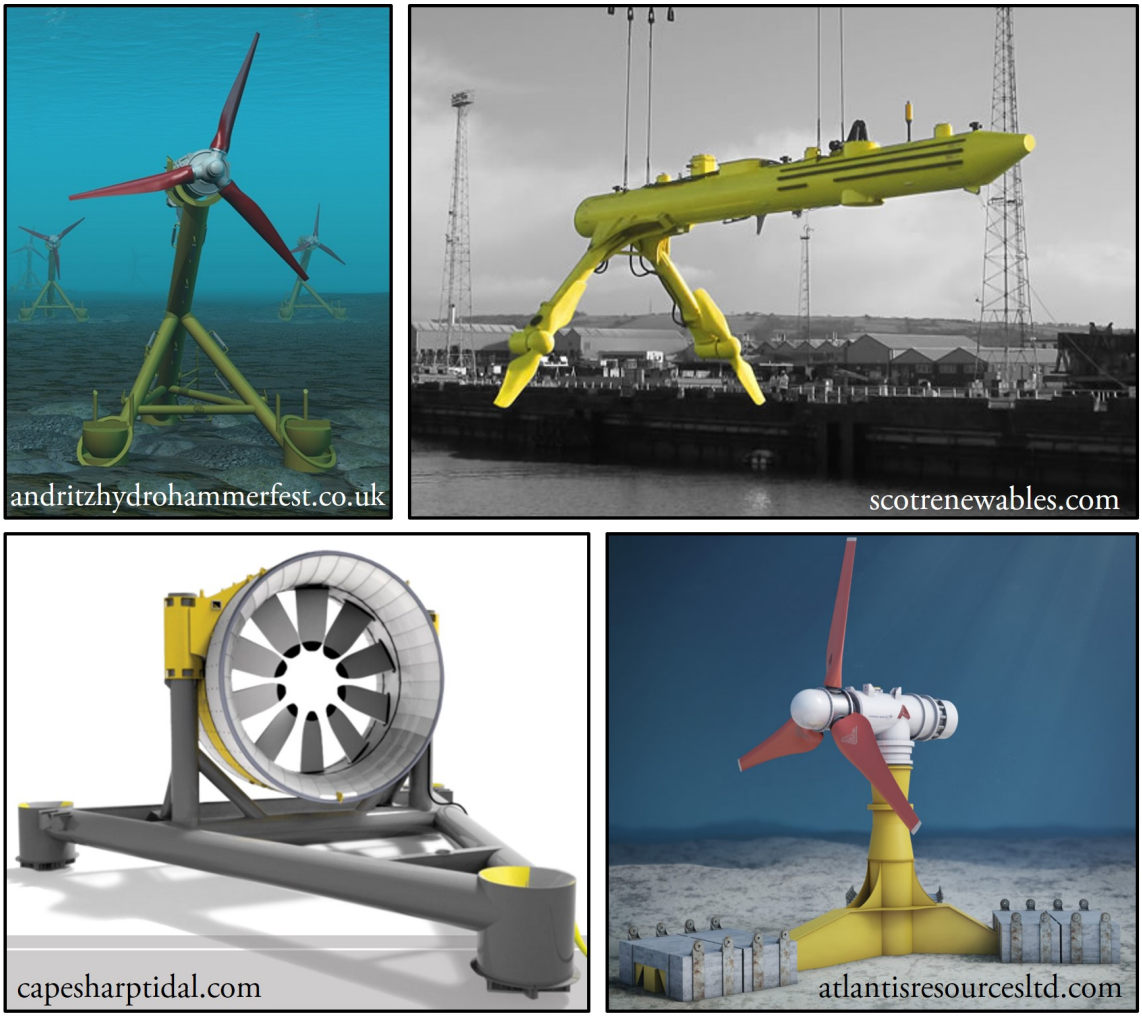

Figure 1.1: Four of the leading tidal turbine designs. The Hammerfest HS1000 (top left) and Atlantis AR1500 (bottom right) are set to be deployed in the MEYGEN tidal farm. The Open Hydro Open-Center turbine (bottom left) is operational in the Cape Sharp project. The ScotRenewables SR2000 (top right) is operational the the European Marine Energy Center. (Images reproduced with permission from source websites as shown.)

layout of turbines within a farm.

1.1 Problem Definition

Energy yield is the integral of electrical power output P over a time duration T, summed over all N_i turbines in a tidal farm.

$$Y = \int_0^T \sum_{i=1}^{N_i} P_i(t)dt \tag{1.1}$$

where the subscript i refers to the i^{th} turbine in the farm. The power of each turbine is, in general terms, a non linear function of the rotor-local inflow velocity $\langle \vec{u}_i \rangle$, turbulence intensity $\langle I_i \rangle$, and turbulent length scale $\langle L_i \rangle$:

$$P_i = P_i\left(\langle \vec{u}_i \rangle, \langle I_i \rangle, \langle L_i \rangle\right) \tag{1.2}$$

Each turbine exerts a thrust force opposing the water velocity, which can be defined by a similar functional form as the power:

$$T_i = T_i\left(\langle \vec{u}_i \rangle, \langle I_i \rangle, \langle L_i \rangle\right) \tag{1.3}$$

Finally, the rotor-local velocity, turbulence intensity and turbulent length scale are also non-linear functions of time, position, and the applied thrust of all turbines in the farm.

$$\langle \vec{u}_i \rangle = \langle \vec{u}_i \rangle \left(t, \vec{x}, T_{\{1:N_i\}}\right) \tag{1.4}$$

$$\langle I_i \rangle = \langle I_i \rangle \left(t, \vec{x}, T_{\{1:N_i\}}\right) \tag{1.5}$$

$$\langle L_i \rangle = \langle L_i \rangle \left(t, \vec{x}, T_{\{1:N_i\}}\right) \tag{1.6}$$

Thus, there are two key ingredients to predicting tidal farm yield. The first is a robust characterization to relate turbine power and thrust to the rotor-local velocity and turbulence characteristics (equations 1.2-1.3), while the second is to predict the velocity and turbulence fields which vary in time and space, and are altered by turbines (equations 1.4-1.6). Compared to wind-farms, these 'back-effects' are more pronounced in tidal channels, where the added drag from turbines may alter the flow field both locally and at macro scales.

1.1.1 Rotor Performance Characterization

Traditionally, turbine performance has been characterized as a function of inflow conditions far upstream of the turbine, known as free-stream conditions (u_0, I_0, L_0) . This is a useful definition for physical model testing in tow-tanks or flumes, where the far-upstream conditions can be measured simultaneously with turbine power output and thrust force. Often, the dependence on turbulent conditions has been neglected, so in the context of the free-stream, the traditional performance coefficients are:

$$C_T(u_0) = \frac{T(u_0)}{\frac{1}{2}\rho u_0^2 A}, \quad C_P(u_0) = \frac{P(u_0)}{\frac{1}{2}\rho u_0^3 A} \tag{1.7}$$

where T is the thrust force that the turbine applies resisting the flow, P is the shaft power of the turbine (which may be related to the electrical power output from the generator using an efficiency term), ρ is the water density, and A is the rotor cross sectional area.

The above parameters can be measured experimentally from scaled-rotor testing, or determined numerically from high-fidelity numerical simulation. Typical operational profiles are depicted in figure 1.2. Below the cut-in speed (region (i)) frictional resistance is higher than the rotor torque and no power is produced. Above the cut-in but below the rated speed (region (ii)), the coefficients remain constant and thus power scales with u_0^3 while thrust scales with u_0^2. Above the rated speed (region (iii)) the power is held constant at the rated power, by changing the rotor speed and/or the blade pitch. Finally, above the cut-out speed (region (iv)) the rotor is stopped by a mechanical brake to avoid structural overload.

As explained in chapters 5 and 6 the free-stream is an abstract concept in the context of the spatio-temporally varying flow field within a tidal turbine farm. It is therefore necessary to redefine the performance in terms of the rotor-local flow. Developing a method to do so was one of the major research contributions of this dissertation, and is described in chapter 5 for axial-flow type turbines, and in 6 for cross-flow type turbines.

1.1.2 Velocity Field Prediction

In this dissertation, the velocity field is modelled using a combination of coastal simulations using the 2D shallow-water equations (SWE) and high-resolution 3D Reynolds-Averaged Navier Stokes (RANS) simulations, both of which include turbine forcing

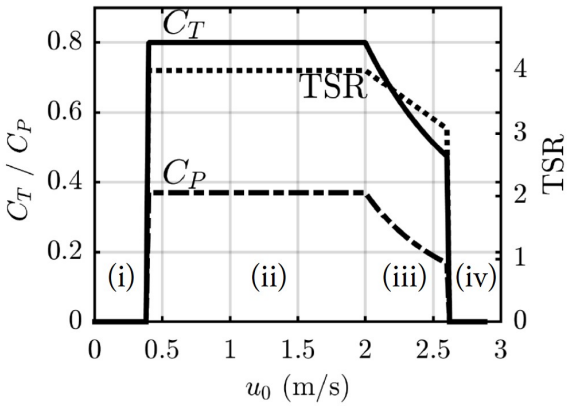

Figure 1.2: Typical turbine performance characteristic curves as a function of free-stream velocity.

terms to model their influence on the flow. Yield assessment simultaneously requires: a long temporal study period to characterize the flow's time-variation, a large model domain to predict basin-scale tidal phenomena, and a fine spatial grid to resolve turbine wakes.

Temporal flow variation can be attributed to the cyclic nature of the gravitational tidal-forcing and to large-scale eddies shed from features such as islands or ridges. Given a sufficiently long power time-series, the mean farm power ($\overline{P} = Y/T$) will converge to a constant value within a defined tolerance. The temporal flow variation must be characterized for at least that duration ($T_{\min}$) to obtain yield estimates that can be forecast to an arbitrary duration $T > T_{\min}$. The minimum duration remains an open question and is likely site dependent. One study [5] determined that $T_{\min} \approx 180$ days, for a tolerance of $\pm 1\%$.

Predicting the flow through a tidal energy site requires a large model domain, spanning many thousands of square km. This requirement arises primarily from the practise of specifying open-ocean tidal elevation as a boundary condition to SWE simulations. Simultaneously, as discussed in chapter 5, accurate predictions turbine power output requires a numerical grid with at least 9 elements spanning each rotor diameter, which is sufficient to predict the rotor wakes. Furthermore, bottom boundary layers in tidal flows require a first-layer grid spacing on the order of 0.1 m.

Thus, for yield prediction, there are simultaneous requirements to model flows for durations on the order of 3-6 months, using a domain size on the order of 1000 km^2 and with horizontal elements ranging down to 1-2 m, and vertical elements down to approx 0.1 m. These requirements make a computationally tractable methodology a significant challenge.

1.1.3 Method Requirements

From the above discussion, it is clear that the major difficulty in determining yield lies in how to deal with the temporal and spatial variability in the velocity field, which is perturbed from its natural state by the presence of turbines. It is important to understand which physical phenomena need to be accurately accounted for to obtain accurate AEP predictions. Other researchers [6] and [7] have presented descriptions of such requirements and the following discussion reflects their thinking as well as our own. At the beginning of the thesis work, we laid out the following requirements of our modelling methods:

Far-Field Effects: A large number of turbines will influence the amplitude and phase of surface elevation, potentially at large distances (many km) away from the tidal farm. For example [8] found that maximizing tidal energy production in Minas Passage in the bay of Fundy could increase the tidal amplitude by 15% along the northeast coast of the USA. For a given tidal channel, there is a balance of 1) forcing from the elevation difference of water at each end, 2) acceleration and 3) frictional terms. Far-field effects alter the phase and/or amplitude of tidal elevation, which in turn alters the velocity through the channel.

Bathymetry: Local bathymetric features influence the spatial and temporal variation of velocity by creating large-scale eddies, by altering the cross-sectional area bounding the flow, and by shaping vertical velocity profiles by e.g. creating regions of separated flow. This effects may have a profound impact on the velocity at a deployed turbine and thus need to be modelled accurately.

Changing water depth: The water depth may change significantly throughout the tidal cycle. For example, in Minas passage the tidal range is ± 6 m.This influences where turbines may or may not be placed (turbine blades too close to the surface may experience damaging cavitation), and shapes the velocity profile by changing the available cross-sectional area.

Turbine Interactions: The influence of turbines on the flow field must be well characterized by the method. These effects include wakes, flow acceleration around wakes and altering the effective cross-sectional area of the flow.

Turbulence: Small-scale turbulence influences the local flow field by increasing mixing. Turbines create turbulent fluctuations in addition to those naturally present. Turbulence affects yield indirectly by its impact on wake mixing, and directly by turbine performance sensitivity to turbulence.

Sheared Inflow: Typically, turbine performance is characterized in flows with uniform incoming velocity. However, tidal flows may vary over length scales smaller than the rotor diameter, so inflow to turbines may be significantly sheared. It is important that the turbine representation in the model can account for the influence of non-uniform inflow on power output.

Temporal Variation Obtaining accurate yield requires accurate accounting of the temporal variation of the farm power output, which arises from tidal cycle forcing, large anisotropic eddies shed from bathymetry, and smaller-scale turbulent fluctuations.

1.2 Dissertation Outline and Research Progression

This section outlines the dissertation document while simultaneously telling the story of how the research progressed. The dissertation is composed of seven papers, presented as chapters 2-8. The papers have been published in or submitted to academic journals or presented in international conferences.

Initially we considered using a promising new simulation method called the actuator-line (AL) approach. **Chapter 2** [9] presents an assessment of the grid resolution requirements for actuator line (AL) simulations of tidal turbines. The AL was an attractive option for modelling tidal turbine farms because it can be used for a priori turbine performance prediction, and can resolve detailed wake structures. Thus, it was thought to be an ideal candidate for modelling detailed wake interactions between rotors. For turbine simulations, the AL applies blade forces along rotating lines, which are specified using blade-element theory, and distributed within the computational mesh using a Gaussian smoothing function. In the paper, we compared AL simulations of infinite, constant-circulation and elliptically loaded wings to well-established analytical solutions, to identify limits to the required mesh resolution as a function of the smoothing kernel width. The paper finds that for accurate simulations, the kernel width should vary in proportion to the chord length, and the mesh should resolve the kernel width with at least 4 elements.

We realized the AL method was not practical for farms with more than a few rotors, and started to explore actuator-disk (AD) methods, which use coarser grids. We began a collaborative R&D project with Cascadia-Coast Ltd. and Mavi Innovations Inc. with two objectives: 1) to validate actuator-disk (AD) simulations and 2) to establish a hybrid method combining 2D coastal shallow-water-equation (SWE) simulations with 3D AD simulations. Toward the first goal we conducted flume tank experiments measuring wakes produced by porous disks, however those results are not included because of unresolved problems with non-axial flume-tank flow and because we obtained a more relevant experimental dataset from experiments using scaled rotors. Toward the second goal, we produced the paper in chapter 3.

Chapter 3 [10] presents an initial foray into combining AD simulations with a SWE model, done in collaboration Cascadia Coast Research Ltd. We discuss how 2D SWE simulations are well established for predicting tidal flows, but cannot resolve wake interaction effects. We establish a coupling method to use AD simulations (which resolve wake interaction effects) to generate forcing terms for SWE simula-

tions. The method required defining a reference velocity (other than the free-stream) which was consistent between the AD and SWE simulations. We used the volume-averaged velocity in a region surrounding the turbines, and found that the region had to be significantly larger than the turbine (or group of turbines) to obtain accurate results. In complex flows in the Minas Passage, the CFD and SWE simulations gave power estimates within $\pm 30\%$ of each other, which was encouraging. This study provided initial groundwork toward the final more refined hybrid SWE-RANS methods presented in chapters 7 and 8.

Following that study, we obtained high quality lab data of two interacting turbines, which allowed an extensive validation of AD methods.

Chapter 4 [11] presents a rigorous analysis of the ability of AD RANS simulations to predict turbine wakes, by comparing to flume-tank tests. The simulations defined the blade forces using tabulated airfoil coefficients and blade element theory. The paper identified mesh requirements to obtain grid-converged wakes and power. Previous literature had established that simulating turbines with AD methods predicted wakes that to mixed-out too quickly compared to wind turbine field data, and had proposed modifying the standard k-ε or k-ω models to reduce the eddy viscosity in the near wake. Our paper used high-quality lab data, and found that the SST eddy-viscosity limiter improved wake prediction significantly compared to standard models. The paper also proposed adding an empirical turbulent kinetic energy source in the wake, to account for non-resolved breakdown of tip vortices which further improved wake predictions.

The AD simulations still had onerous mesh requirements for inclusion in an overall tidal farm analysis method, and we thought it may be worthwhile establishing novel methods to obtain accurate results on coarser grids.

Chapter 5 [12] continued refining AD methods to improve computational cost. In this paper, the AD method was altered to eliminate the need to set the turbine forcing terms using blade element theory. This allowed a drastic reduction in the required number of elements needed to represent each turbine, making simulations of large arrays more tractable. Instead of using tabulated airfoil coefficients, the new method used known (from testing or high-fidelity blade-resolved CFD simulation) rotor performance coefficients $C_{\{T,P\}}$ to define thrust and power. Further, instead of the traditional free-stream velocity we used the volume-averaged velocity over the AD region as a reference, and accordingly defined new performance coefficients $C^{\star}_{\{T,P\}}$, which were established by a tuning procedure. Hence the method was named the

tuned-actuator-disk-approach (TADA). This strategy allowed the modelled rotor to react correctly to reduced inflow velocity present in a turbine wake, and to the funnelling effect of placing the rotor in a narrow channel (commonly called blockage effect). We found that TADA predicted wake recovery, the impact of wakes on downstream rotor performance, and blockage effects with reasonable accuracy.

The AD and TADA simulations presented in chapters 4 and 5 were suitable for modelling axial-flow rotors, yet many turbine developers were considering cross-flow type rotors, so we derived an adapted version of the TADA model.

In chapter 6 [13, 14], we collaborated with Vancouver-based turbine developer Instream Energy Systems (IES) to adapt TADA to cross-flow turbines. TADA had been formulated for axial-flow machines, and adapting it to cross-flow turbines was a logical progression. IES had collected performance data in a channel, which was used to tune the TACA model. They had also performed an experimental campaign to test wake interaction effects between groups of rotors in the outflow channel from a hydro dam, which was used to validate TACA's wake and power predictions in array settings. Adapting TADA to cross-flow rotors, and validating in a real-world setting, rather than a lab added confidence to both methods.

Satisfied that our TADA and TACA methods could predict turbine performance and wake interaction effects at the individual turbine and farm scales, we shifted efforts to large scale tidal flows. The next research phase was done in collaboration with Dr. Richard Karsten and his research group at Acadia University, and using field data collected by a team led by Justine McMillan and Dr. Alex Hay from Dalhouisie University. Chapters 7 and 8 present a 2-part paper that present the final hybrid method coupling 2D SWE simulations with TADA (or TACA) simulations to predict yield and far-field effects.

Chapter 7 [15] outlines physical phenomena which must be accounted for when predicting turbine farm yield; which can be broadly categorized into 1) the ambient tidal flow without the addition of turbines 2) the far-field effects and 3) near-field effects. The hybrid method uses SWE simulations to predict the ambient flow and far-field effects, and is run for a long temporal duration (on the order of 3 months). The resulting time series is categorized into discrete bins, and for each bin, boundary conditions are defined to drive a TADA simulation which predicts the near-field (i.e. wake interaction) effects on power production. The yield is then calculated statistically from the bin probability distribution and TADA-predicted power. The paper applies the hybrid method to predict vertical velocity profiles, and finds good agree-

ment with field-data. The paper also confirms that very little error is introduced into yield analysis by the bin-averaging procedure, compared to a full time-series analysis.

Chapter 8 [16] describes methods used for representing turbines in the TADA and SWE simulations. The TADA turbine models in this chapter are more refined compared to that presented in chapter 5. Generally, SWE simulations are done with grid elements larger than turbines, so turbines are modelled as sub-grid scale objects. A suitable method for calculating sub-grid-scale turbine forces is introduced in this chapter. The paper confirms the TADA rotor model for single isolated rotors, and discusses differences in how wakes are resolved in SWE vs. TADA, highlighting the importance of using adequate-resolution 3D simulations to predict wake-interaction effects. Finally, the hybrid approach is used to model hypothetical turbine farms in Digby Neck containing up to 42 rotors, demonstrating that the method is computationally tractable and able to predict wake interactions between many turbines.

Chapter 9 presents conclusions, summarizes contributions, and discusses future improvements to the methodology, and possible future research.

1.3 Research Contributions

The work presented in this thesis made the following contributions to current knowledge:

1. Established guidelines for mesh scale relative to the Gaussian spreading kernel width for actuator-line simulations (Chapter 2) applicable to tidal and wind turbines alike and followed-up by other authors e.g. [17].

2. Presented a rigorous validation of blade-element based actuator-disk RANS simulations (Chapter 4).

   (a) Established that the SST eddy viscosity limiter was adequate to alleviate the issue of standard turbulence models over-predicting initial wake recovery rate.

   (b) Introduced a novel turbulent source term in the wake to account for blade tip-vortex breakdown.

3. Established a novel tuned-actuator-disk-approach (TADA) for axial flow turbine rotors in RANS simulations (Chapter 5), which was rigorously validated using lab data to:

   (a) predict turbine performance over its operational range of tip speed ratio, and in flows of differing turbulence;

   (b) predict velocity and turbulence intensity in rotor wakes;

   (c) and to predict the influences of wake interaction and channel blockage on turbine performance and;

   (d) which was computationally less expensive than previous blade-element based actuator disk methods, allowing simulations containing many rotors to be carried out even on personal computers.

4. Adapted TADA to cross-flow type turbines (Chapter 6), establishing a novel tuned-actuator-cylinder-approach (TACA), which was validated using field data for a dam outflow channel to;

   (a) predict velocity in wakes, and to;

   (b) predict the influences of turbine wakes and channel blockage effects in turbine performance; and which;

   (c) was computationally tractable for simulations of many interacting turbines.

5. Established a comprehensive framework for predicting tidal turbine farm yield, flow fields, and alteration of the tides by the farm (Chapter 7), which used a hybrid approach combining 2D coastal SWE methods with 3D TADA or TACA simulations.

6. Assessed the ability of RANS simulations to predict vertical velocity profiles in a tidal channel, concluding that RANS simulations provide better predictions compared to neutrally stratified logarithmic profiles, because they account for the influence of changing bathymetry. (Chapter 7)

7. Established a novel cross-coupling between 2D SWE simulations and 3D RANS, which allows the RANS simulations to be run on a subset of bin-averaged flow states, rather than for a long duration time-series. (Chapters 7-8)

   (a) Defined a novel bin-averaging procedure that conserves flow power density, which is used to create bin-averaged flow states from 2D SWE simulations, to provide boundary conditions to the RANS simulations. (Chapter 7)

   (b) which was validated to introduce nearly zero error compared to performing a full time-series analysis.

(c) and which was computationally tractable with modest HPC resources.

8. Established a novel sub-grid treatment for turbine forcing terms in SWE simulations which allowed multiple rotors or portions of rotors to be contained within each grid cell, and which correctly predicts the rotor performance over its operational range including cut-in and cut-out behaviour. (Chapter 8)

9. Presented the first simulation-based full yield prediction for a large tidal farm that accounts for the temporal flow variation by a method of bins, and accounts for wake interaction effects using a validated method. (Chapter 8)

Chapter 2

Mesh and Load Distribution Requirements for Actuator Line CFD Simulations

This paper has been published as:

Shives, Michael and Crawford, Curran: *"Mesh and load distribution requirements for actuator line CFD simulations,"* Wind Energy 16 (2013) 1183-1196, DOI 10.1002/we.1546.

This paper analyzes mesh size requirements for actuator-line CFD simulations, which had been considered as a potential method for simulating tidal turbine farms. Actuator line simulations of tidal turbines allocate blade forces along rotating lines of elements, however this paper looks at canonical wing solutions and compares to lifting line theory, to establish the mesh limits. Following this study, it was realized that AL simulations would be too computationally costly for turbine farms with many rotors, so actuator disk methods were pursued instead.

The paper finds that:

1. The Gaussian load distribution kernel should scale with the blade chord;

2. The kernel width should be resolved with at least 4 mesh elements.

Abstract

Fundamental numerical testing has been done to determine mesh density and force distribution guidelines for an actuator line-based computational fluid dynamics (CFD) method for simulating kinetic turbines. The method computes forces from lifting surfaces (i.e. wings or blades) using the evolving flowfield and tabulated airfoil data. The forces are applied to the flow as momentum source terms distributed with a Gaussian smoothing function about the physical locations of the blade/wing quarter-chord line. The chosen length scale of the Gaussian distribution affects the magnitude and distribution of the resulting induction, and necessitates a minimum grid resolution for accurate results. Tests have been conducted to determine appropriate distribution length scales and mesh spacing using an infinite span wing and finite span wings with constant and elliptical spanwise circulation distributions. These test cases were chosen because they have simple analytical solutions derived from lifting line theory. The eventual goal is to simulate turbine rotors, however these fundamental test cases provide a means to evaluate the required mesh spacing and the appropriate distribution length scale without the complexity of modeling a turbine rotor wake. It was found that the source distribution length scale ϵ should be proportional to the local airfoil chord length c with a ratio ϵ/c of approximately 1/4, and that the mesh spacing at the actuator line should satisfy $\epsilon/\Delta_{grid} \geq 4$. This limit is likely somewhat code-specific and should be evaluated for all solvers used for actuator line simulations.

2.1 Introduction

The simulation of kinetic[1] turbines is often accomplished by representing the turbines as actuator disks. Such a representation assumes that the forces from each blade element are distributed uniformly in the circular annulus swept out by that element, and requires an axisymmetric assumption. This allows for relatively fast simulations, but does not inherently account for discrete blade effects such as so-called tip losses which arise due to the effects of vorticity trailed in discrete wake sheets on the induction at the blade. The trailed vorticity arises from spanwise variation in the blade's bound circulation, and is typically very strong at the blade tip. The actuator line concept was introduced to provide a method which could account for discrete blade effects

[1] "kinetic" is a broad term used here to refer to turbines used for power generation from wind, tidal flows, ocean currents or rivers.

and resolve the trailed vorticity in the wake. It achieves this by distributing the blade forces in a realistic manner at the blade location. The two concepts are depicted in figure 2.1.

The actuator line approach requires many fewer mesh elements than simulations which explicitly resolve the blade geometry, but still resolves the wake structure and can predict turbine loads and power. The approach accounts for discrete blade effects, including the trailed vorticity and in particular the tip vortices. The reduction in computational cost is made by handling the inner boundary layer resolution problem through 2D airfoil coefficients while retaining an explicit solution of the wake.

In the actuator line method, the user chooses a length scale over which the forces are distributed, and this has an impact on the magnitude and distribution of the trailed vorticity. This paper provides guidelines for making this decision and for how refined the computational mesh should be to obtain accurate solutions. These guidelines have been defined by conducting investigations of three scenarios with analytical solutions: an infinite span wing, a constant circulation wing, and an elliptically loaded wing. The results are extensible from wings to rotors, for which the actuator line approach is applicable to both axisymmetric and non-uniform inflow cases. The eventual goal of this research is to apply the actuator-line method to study discrete blade effects in ducted rotors in the context of tidal power generation. In particular, the attenuation of tip vortices by the duct is of interest.

2.1.1 Literature Review

The actuator line concept was introduced for modeling wind turbines by Sørensen and Shen [18], who implemented the technique in a finite-difference Navier-Stokes solver code formulated in velocity-vorticity variables. Sørensen and Shen applied a 3D Gaussian distribution, which took the convolution of the blade force with a regularization kernel as shown in equations 2.1 and 2.2.

$$f_{app} = f_{bld} \otimes \eta_\epsilon \tag{2.1}$$

$$\eta_\epsilon(r) = \frac{1}{\epsilon^3 \pi^{\frac{3}{2}}} e^{(-\frac{r^2}{\epsilon^2})} \tag{2.2}$$

In equation 2.2, r is the distance from the point at which the blade force f_{bld} is calculated to the point at which the applied force f_{app} is calculated. Sørensen and Shen used a computational mesh with $100 \times 99 \times 50$ nodes in the radial, axial and azimuthal

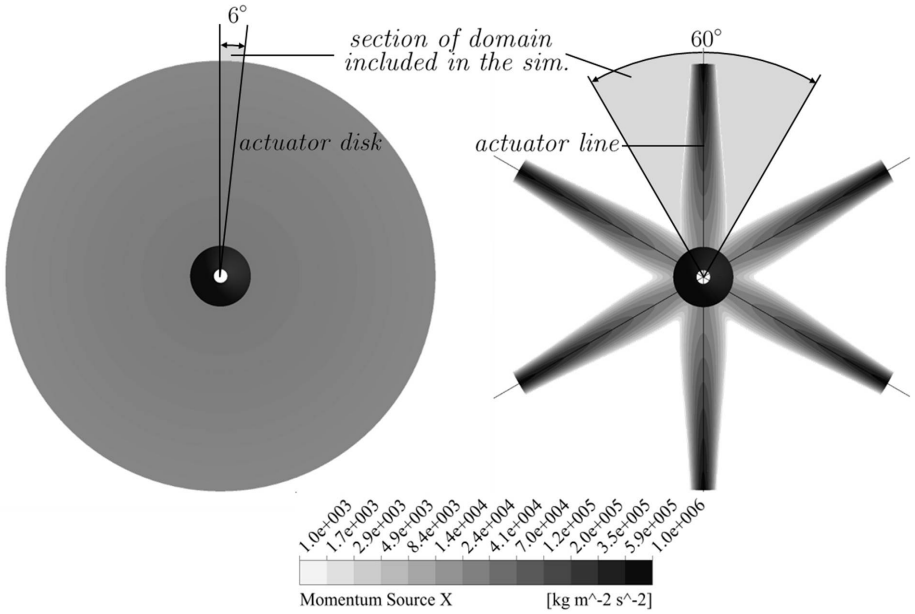

Figure 2.1: Depiction of how the forces are distributed in actuator disk and actuator line methods. Results taken from simulations of a 6-bladed, ducted rotor

directions respectively, in a domain with extents 20 rotor radii (R) up/downstream and $10R$ radially. They showed very good agreement to experimental data of the mechanical power variation with wind speed for the Nordtank 500/41 wind turbine.

In his PHD thesis, Mikkelsen [19] implemented the actuator line technique using a finite-volume solver formulated in primitive (pressure-velocity) variables in a co-located grid employing the Rhie/Chow interpolation to avoid even-odd decoupling. Mikkelsen used actuator disk and actuator line methods to simulate the 2MW Tjæreborg wind turbine. Both approaches compared well with experimental power data over a range of wind speeds and gave very similar results, bringing into question whether the increased complexity of the AL method was warranted. This is a valid question for conventional turbines where a well established empirical treatment for tip loss (i.e. the Prandtl correction) exists. However, the actuator line approach allows much richer information about the wake structure and allows the study of the interaction of the wake with solid boundaries (such as wind tunnel walls or ducts[2]), free surfaces (i.e. the water surface in the context of marine kinetic turbines) and with wakes from other turbines. Such studies are simply not possible with empirical tip-loss models.

Mikkelsen also noted that a 3D Gaussian force distribution resulted in forces being applied to grid cells beyond the physical blade tip. Thus, a 2D Gaussian force distribution, in which forces were applied in a plane perpendicular to the blade axis was employed by replacing the regularization kernel shown in equation 2.2 with that shown in equation 2.4. This 2D smoothing is also more convenient because the applied force at a particular location in the domain depends on the flow at a corresponding point at the same spanwise position along the blade (instead of depending on the flow at all points along the blade as with a 3D distribution) so the convolution defined in equation 2.1 is replaced by a multiplication.

$$f_{app} = f_{bld}\eta_\epsilon \tag{2.3}$$

$$\eta_\epsilon(r) = \frac{1}{\epsilon^2\pi}e^{(-\frac{r^2}{\epsilon^2})} \tag{2.4}$$

Mikkelsen compared the blade local induction factors to the azimuthal averages and found that there was significant sensitivity to the Gaussian distribution length scale ϵ, which was scaled as an integer multiple of the local grid spacing. He also

[2]Work is currently underway by the authors to employ the actuator line method to study the attenuation of tip vortices in ducted turbines, in the context of tidal current turbines.

found that the employed method could not reproduce the analytical solution of constant (spanwise) downwash for an elliptically loaded wing, which brought into doubt the method's accuracy in dealing with trailed vortex effects. The current paper addresses the elliptically loaded wing case and shows that much improved results can be obtained if ϵ is scaled with the local blade chord. This is discussed more in section 2.5.

In more recent work, Ivanell *et al.* [20] used the actuator line method to analyze the wake structure behind the Tjæreborg wind turbine using direct numerical simulation. This work continued to use a 2D Gaussian force distribution with ϵ being an integer multiple of the local grid spacing ($\epsilon = \{1, 2, 3\}\Delta_{grid}$). Ivanell *et al.* recommended that ϵ should be as small as possible to avoid influencing the wake structure. However, such a strategy for defining ϵ does not ensure that the applied forces are distributed over a physically meaningful length scale. This paper argues that ϵ should be chosen to distribute the applied loading over a region in space consistent with the physical airfoil being modeled. The mesh should then be defined to adequately resolve the Gaussian force distribution and resulting flowfield. For the numerical algorithms used in this study, an adequate grid resolution was found to be $\epsilon/\Delta_{grid} \geq 4$, as discussed in section 2.3.

An adaptation to the actuator line method (called the actuator surface method) where the blade forces are distributed along the blade chord using a distribution representative of the airfoil pressure distribution has recently been introduced and studied by Shen *et al.*[21]. This method provides a more realistic force distribution, but is more complex to implement than the actuator line method due to the requirement to define curve-fits to airfoil pressure distributions over the range of angle of attack. Furthermore, the method requires making some questionable assumptions when calculating the blade angle of attack (α) and relative velocity (V_{rel}). In [21], α and V_{rel} were found using the simulated velocity at a monitor point approximately one chord length upstream of the blade. This velocity was then corrected to remove the induction caused by the blade's bound circulation. This approach inherently assumed that the induction due to the wake is the same at the monitor point as it is at the blade, which is not true because shed and trailed vortices will have a much greater influence at the blade than on a location one chord length upstream of it. Sibuet Watters *et al.*[22] also studied the actuator surface method, and calculated α and V_{rel} using a sectional average along the blade chord. This inherently assumes that the induction due to the bound circulation is symmetric about the center of the chord. This may

be a good approximation considering that Sibuet Watters *et al.* used a chordwise symmetric elliptical distribution of loading, however the symmetry of induction was not demonstrated in that work.

For the actuator line approach, it would be ideal to define ϵ based on the airfoil pressure distribution, which depends on the angle of attack. This would involve re-evaluating ϵ at every iteration of the solver based on a table lookup. To avoid this additional complexity, it is likely sufficient to define ϵ as a fraction of the chord length, which is the strategy taken in this work.

2.1.2 Contributions of this Paper

In previous work, the accuracy of the actuator line approach has been evaluated by comparing the calculated power coefficient of wind turbines to experimental data. This does not provide a direct evaluation of its accuracy in resolving the influence of trailed vorticity on the flow at the blade or tease out error sources in the inner (at the blade) and outer (freestream and wake) problems. The outer problem has been examined in more detail in recent work by Troldborg *et al.* [23, 24] who have compared actuator line simulations of wake development and wake interaction to experimental data. The work presented in this paper focused on the inner problem, and a number of tests were conducted with the goal of determining how ϵ should vary along the blade, and how refined the computational mesh needs to be in order to achieve an accurate solution of the influence of trailed vorticity on the flow at the quarter-chord line.

The focus of this study was on obtaining accurate solutions of the flow at the quarter-chord line, which is critical to the actuator line method because the angle of attack and relative velocity at quarter-chord define the wing/blade loads. Analytical lifting line solutions to three well-understood cases have been used as a benchmark for the flow solution at the quarter chord. It is expected that the actuator line CFD method will prove more versatile (ability to include a hub, tower, duct, or other features) than purely vortex based methods. It is also expected that it will provide more accurate wake solutions because it inherently includes non-linear dissipative viscous effects, and should predict the interaction of vortical structures in the wake including phenomena such as vortex roll-up. A direct evaluation of the grid requirements for accurate wake solutions was not considered in this paper, and can be best addressed through comparison to experimental data.

In the actuator line method, the angle of attack α and relative velocity V_{rel} are found from the simulated velocity at the wing/blade quarter-chord line.[3] Two-dimensional airfoil coefficients are then used to determine the blade forces. When using this approach, the simulated velocity at quarter-chord line should not include any 'self induction.' In other words, the induction due to the bound circulation should be zero at the quarter-chord, otherwise the velocity used to calculate the blade forces will not correspond to the true blade relative velocity. The induction due to the wake structure on the other hand, should be present.

Section 2.2 discusses the software, governing equations and assumptions used throughout the study. In section 2.3, it is shown that for actuator line simulations of an infinitely long wing with sufficient mesh density, the resulting induction due to the applied source terms is symmetric about the quarter-chord line. Due to this symmetry, the velocity at the quarter-chord matches the freestream which, by convention, is used to define α and V_{rel} for 2D airfoils. In section 2.4 the actuator line was applied to a 3D wing with constant bound circulation to study the sensitivity of the resolved tip vortex core radius to the distribution parameter ϵ. Section 2.5 establishes that ϵ should vary in proportion to the chord c to obtain accurate trailed vorticity solutions, based on investigation of an elliptically loaded wing.

2.2 Methodology

This section describes the implementation of the actuator line method in a commercially available CFD solver. The method is therefore applicable to a wide set of practitioners utilizing both custom and standardized CFD software packages. First the solver and governing equations are described. Subsequent sections deal with the turbulence closure, user-defined velocity functions and momentum source terms.

2.2.1 Software and Governing Equations

The actuator line method was implemented in the general purpose CFD solver ANSYS CFX. A brief summary of the solver properties is given here, with further details available ([25]). CFX uses a finite volume Navier-Stokes solver formulated in primitive variables. The advection scheme chosen for all simulations was the "high resolution"

[3]Note that the actuator line method distributes momentum source terms symmetrically about a line which represents the blade/wing. Lifting line methods place sources of vorticity along an analogous line, and in both methods this line is located at the quarter-chord line of the blade/wing.

option, which is a blend between the 2^{nd} order accurate central-difference-scheme (CDS) and the 1^{st} order accurate upwind scheme, where the blend factor is determined throughout the simulation and favors the CDS scheme except in situations where the stability of the solution may be compromised. CFX uses a co-located grid and avoids even-odd decoupling with a modified Rhie/Chow interpolation. The software uses a fully implicit discretization and a coupled solver which uses an incomplete lower upper (ILU) factorization technique. This is an iterative solver which approaches the exact solution to the discretized equations over the course of many iterations. This approach allows the specification of a timestep for steady state simulations, however this term serves only to underrelax the governing equations. The solver is accelerated using an algebraic multigrid technique called additive correction.

The software has options for a variety of simulation approaches, however the Reynolds-averaged Navier Stokes (RANS) equations were used for all simulations presented here. For wind turbines, the flow is commonly considered to be incompressible, which is valid considering that tip speeds are typically limited to approximately $70m/s$ ($M \approx 0.2$) to limit noise. All simulations sought steady state solutions, which by definition neglect variations in time. For steady, incompressible flows, the RANS equations can be expressed in a compact form using Einstein notation:

$$\frac{\partial \overline{u}_i}{\partial x_i} = 0 \tag{2.5}$$

$$u_j \frac{\partial \overline{u}_i}{\partial x_j} = \frac{\partial}{\partial x_j}\left[-\frac{\overline{p}\delta_{ij}}{\rho} + \nu \frac{\partial \overline{u}_i}{\partial x_j} - \overline{u_i' u_j'}\right] + \frac{\overline{S}_i}{\rho} \tag{2.6}$$

where $\delta_{ij} = 1$ for $i = j$ and equals zero otherwise. S_i is a momentum source term, used to impose the blade forces on the flow as described in section 2.2.4.

The simulations in this paper neglected thermal effects, allowing the energy equation to be neglected. Thus, the dissipation of turbulent kinetic energy did not contribute to heat production, nor did viscous shear. The impact of heat production is negligible because as demonstrated by Corten [26], the heat produced by a turbine is insufficient to cause a noticeable temperature increase in the downstream flow.

2.2.2 Turbulence Model

The Reynolds averaging process introduces additional stress terms (Reynolds stresses) $\overline{u_i' u_j'}$ into the instantaneous Navier-Stokes equations, as documented in numerous CFD

text such as [27]. The Reynolds stresses are modeled using a turbulence model and several options exist. In all simulations presented here, the k-ω SST model by Menter [28] was used due to its well documented ([29], [30], [31], [32]) superior performance in adverse-pressure gradient flows compared to other two-equation turbulence closures. This will be important for future simulations which will apply actuator line methods to turbine rotors enclosed in diffusing shrouds which create strong adverse pressure gradients as the flow expands.

The SST model is as a combination of the standard k-ϵ and Willcox k-ω models, taking advantage of their mutual strengths. Namely, the k-ϵ model performs well for free shear flows, while the k-ω model works well in the viscous sublayer. The SST model uses a blending function to implement the k-ω model near no-slip boundaries, and a re-formulated version of the k-ϵ model outside of the boundary layer. Since the flows presented in this paper did not employ no-slip boundaries, the SST model is equivalent to the standard k-ϵ for these cases.

2.2.3 User Defined Velocity Functions

In the actuator line method, the blade forces are evaluated along the blade quarter-chord line, but applied over a region in space governed by the 2D Gaussian distribution. The forces depend on the blade angle of attack and relative velocity as described in the next section. Thus, the momentum source applied to a particular grid cell is a function of the velocity in another cell. CFX does not have a built-in capability to implement this type of dependence because it can only evaluate expressions locally within each grid cell. To overcome this limitation, an interpolation function was created to define an expression for the blade velocity which could be evaluated anywhere in the domain.[4]

To achieve this, monitor points were defined at nodes along the quarter-chord line. During simulations, CFX uses a nearest-neighbor interpolation to evaluate flow variables at monitor points. This necessitated designing the mesh such that nodes were placed exactly along the blade/wing quarter-chord line. The velocity at these monitor points (u_k) was tracked using the built-in *probe* function. Between monitor points, the velocity was defined using linear interpolation. With N_{mp} nodes, there

[4]This interpolation function was not used for the infinite wing or the constant circulation wing because their loadings were defined *a priori*. However, it is required in general for the actuator line method.

were $N_{seg} = N_{mp} - 1$ line segments along which this interpolation took place:

$$u_{seg_k} = \begin{cases} u_k + (u_{k+1} - u_k)\frac{s - s_k}{s_{k+1} - s_k} & \text{if } s_k \leq s < s_{k+1} \\ 0 & \text{otherwise} \end{cases} \tag{2.7}$$

where u_{seg_k} is the velocity along the k^{th} line segment, u_k is the velocity at the k^{th} node and s_k is the spanwise location at each node. Note that for the N_{seg}^{th} segment the logic statement was modified to $(s_k \leq s \leq s_{k+1})$ to allow the velocity to be defined *at* the N_{mp}^{th} node. A continuous function of the velocity was then defined by the summation of all u_{seg_k}:

$$u_{bld} = \sum_{k=1}^{N_{mp}-1} u_{seg_k} \tag{2.8}$$

Using this approach, the function u_{bld} can be evaluated *anywhere* that $s \leq s_{N_{mp}}$ to yield the blade relative velocity for the corresponding spanwise location.

Additionally, as pointed out by Chattot [33], in regions near the maximum c_l for an airfoil there are multiple α possible for a given c_l. It is therefore possible to have spurious spatial oscillation of the computed force along the blade. Chattot proposed applying a viscous smoothing function to the bound circulation to alleviate this issue. This is implemented in the present work as a smoothing of the blade velocity function, which is used in calculating the applied forces.

$$\begin{aligned} u_{k,sm} &= u_k + k_{sm}(u_{k-1} - 2u_k + u_{k+1}) \\ \text{for } k &= \{2 : N_{mp} - 1\} \\ \\ u_{k,sm} &= u_k \\ \text{for } k &= (1, N_{mp}) \end{aligned} \tag{2.9}$$

This was implemented using a smoothing parameter $k_{sm} = 0.25$ by replacing the u_k terms in equation 2.7 with $u_{k,sm}$. This implementation improves the overall robustness of the method by ensuring that there is no decoupling between adjacent actuator line segments.

2.2.4 Momentum Source Terms

This section provides the general methodology for determining the momentum source terms. The exact specification of these terms varies from one test case to the next,

ϵ/Δ_{grid}	0.5	1	2	4
Error	37%	1.6%	0.95%	0.53%

Table 2.1: Percent over-prediction of the area integral of the Gaussian distribution for various ϵ/Δ_{grid}.

and therefore more detail is provided for each respective case.

The blade forces were included into the domain through the momentum source term S_i in equation 2.6. In CFX, the momentum source terms are defined on a per-unit volume basis. The user defines the source terms as spatially continuous expressions which CFX evaluates at the mesh nodes. CFX uses linear shape functions [25] to define the momentum sources between nodes and to evaluate the integral of the source term expression in each computational element. This integrated quantity is then applied to the discretized momentum equations. Thus, adequate grid resolution is required to accurately represent the Gaussian distribution. The linear approximation over-predicts the integral of the Gaussian distribution by an amount which depends on the ratio ϵ/Δ_{grid} as summarized in Table 2.1.

There exists an option in CFX to include the momentum source terms in the Rhie-Chow redistribution algorithm [25], which smears the momentum source terms into adjacent elements, having a similar effect to using a slightly larger ϵ. Unless noted otherwise, the results presented here did not apply this redistribution to the momentum sources to avoid distorting the intended source distribution. In practice, it may be advantageous to use this option to improve simulation numerical stability.

In this study, the blade forces were distributed in a plane perpendicular to the blade axis using a 2D Gaussian smoothing, as done by Mikkelsen [19] and shown in equations 2.3 and 2.4. The blade forces per unit span can be found using tabulated airfoil lift and drag coefficients with the following expressions;

$$l = \frac{1}{2}\rho V_{rel}^2 c c_l \tag{2.10}$$

$$d = \frac{1}{2}\rho V_{rel}^2 c c_d \tag{2.11}$$

$$c_l = c_l(\alpha) \tag{2.12}$$

$$c_d = c_d(\alpha) \tag{2.13}$$

where V_{rel} is the magnitude of u_{bld}, neglecting the spanwise component. For example,

a blade aligned with the y axis has;

$$V_{rel} = \sqrt{(u_{x_{bld}}^2 + u_{z_{bld}}^2)} \tag{2.14}$$

Note that when the lift or drag from equations 2.10 and 2.11 is multiplied with the 2D Gaussian distribution, the result is a force per unit volume, which is specified directly to CFX. The direction of the force is specified such that the lift is perpendicular to the relative velocity, and the drag is parallel. The relative velocity V_{rel} and angle of attack α are measured at the quarter-chord line.

2.3 Infinite Wing

The actuator line methodology is similar to a lifting line approach in that the angle of attack and relative velocity are determined from the calculated velocity at the blade/wing quarter-chord line. Tests were run on a 2D domain to gain insight into the reaction of the flow to applied momentum source terms. When a momentum source is included in the simulation applying a force perpendicular to the velocity, the resulting flowfield is very similar to the superposition of a line vortex and a uniform velocity. This shows consistency between the actuator line approach and vortex methods. In both cases, the velocity gradient is very high near the center of the vortex. This provides a potential source of error in the numerical simulations, because if the numerically generated vortex is not perfectly centered on the quarter-chord line, it will induce a velocity on the point where the relative velocity and angle of attack are calculated. The steepness of the velocity gradient makes the simulation very sensitive to this "self-induction" problem when the numerical vortex is even slightly off-center from the quarter chord line.

The goal of the two-dimensional tests was to determine appropriate values to use for the Gaussian length scale ϵ and mesh spacing Δ_{grid} relative to the blade chord c. In total, 20 simulations were run for $\epsilon/c = \{1/8, 1/4, 1/2, 1, 2\}$ and $\epsilon/\Delta_{grid} = \{1/2, 1, 2, 4\}$.

In the simulations, the blade was aligned with the z axis, and the blade force was applied in the positive y direction according to:

$$S_y = \frac{1}{2}\rho u_0^2 c c_l \frac{1}{\epsilon^2 \pi} e^{\left(\frac{x^2+y^2}{\epsilon^2}\right)} \tag{2.15}$$

where $u_0 = 1\frac{m}{s}$ was the freestream velocity, $c = 0.4m$ was the chord length and

$c_l = 0.8$ was the lift coefficient. Note that in this implementation, specifying the chord length and lift coefficient serve only to set the magnitude of the applied loading. In these simulations of an infinite wing, the loading did not evolve with the flowfield, but was rather specified *a priori*. Changing u_0 modifies the applied load as well, however the induced velocity should vary linearly with u_0 such that the normalized induction (v/u_0) should be independent of u_0.

The simulation domain was a rectangle which extended $12.5c$ upstream and downstream from the origin, and $25c$ in each lateral direction. The domain was one element thick in the z (spanwise) direction. The applied load was centered on the origin. The inlet enforced uniform inflow with $u_x = u_0$ and low (1%) turbulence intensity. A pressure outlet was applied at the downstream boundary. The lateral boundaries used free-slip walls, and symmetry was used on the spanwise boundaries. This approximates an infinite length wing, preventing any blade tip effects.

The simulation was set-up to be consistent with the superposition of an infinite line vortex and uniform inflow. To avoid an infinite induced velocity at the position of the line vortex, potential flow methods use a vortex core model, which limits the maximum induced velocity and assumes a certain distribution of induction within the core radius. Irrespective of the specific core model (many exist), the induction due to any particular vortex element is always zero on that particular element. This allows the angle of attack to be determined at the vortex center. In the simulations, the velocity induced by the blade loading followed a similar profile to a theoretical vortex using the Scully ([34] p.539) core treatment and a core radius $r_c = 0.75\epsilon$ as shown in figure 2.2. The value 0.75 was determined through trial and error with the goal of producing the same maximum induction as the simulation results. As expected, using a smaller value of ϵ produced a smaller vortex core and higher local induced velocities.

To be consistent with the vortex line approach, the induced velocity should be zero at the quarter-chord line. This fact was used to define an error in terms of the computed angle of attack at the actuator line. The impact of applying the Rhie-Chow redistribution to the source terms was assessed by running a second set of simulations. The calculated errors are plotted in figure 2.3. As expected, very large errors arose when $\epsilon/\Delta_{grid} < 1$. The error showed a decreasing trend with increasing ϵ and with decreasing Δ_{grid}. Also as expected, applying the Rhie-Chow redistribution to the momentum source terms reduced the error (consistent with the fact that it smears the forces over a larger region in space, increasing the effective ϵ). Defining a limit on

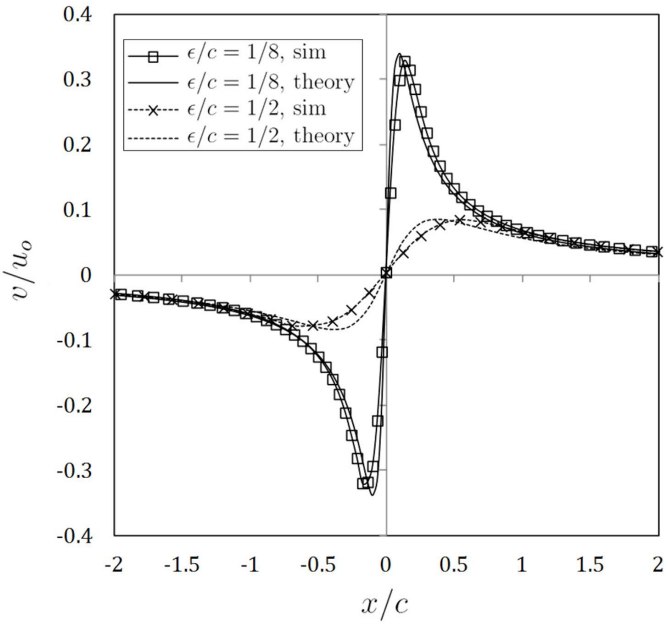

Figure 2.2: Induced velocity produced by simulations ($\epsilon/\Delta_{grid} = 4$) compared to the Scully vortex model with core radius $r_c = 0.75\epsilon$

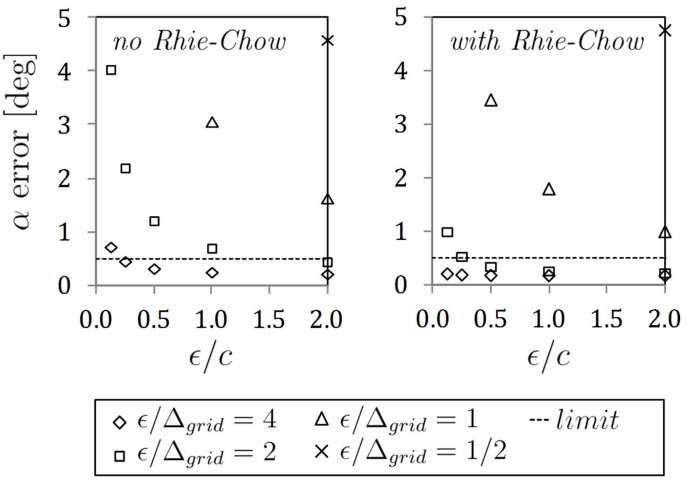

Figure 2.3: Angle of attack error calculated from 2D simulations. The error reduces with increasing ϵ and reducing Δ_{grid}

the acceptable angle of attack error of 0.5°, it is possible to define limits on ϵ and Δ_{grid}. Based on the results, it is recommended to use $\epsilon/\Delta_{grid} \geq 4$ for all simulations. This limit needs to be increased when ϵ/c is less than 1/4. If the Rhie-Chow redistribution is applied to the source terms, this limit may be relaxed somewhat, however using this option results in a slightly different distribution of source terms than intended (but with the same total integrated force). Note that the limits established in this work are likely code-dependent and ideally a similar analysis would be carried out for each code implementing the actuator line method.

The error in angle of attack arises due to insufficient grid resolution to resolve the rapidly varying velocity near the center of the loading distribution. This results in an upstream shift in the location of zero induction, and increased induction at the loading center. This behavior can be observed in figure 2.4.

2.4 Constant Circulation Wing

The case of a wing of finite length with a constant circulation of Γ is of practical interest for validating the actuator line technique because it requires that the vorticity trailed from the wing tips (and only the wing tips) be modeled correctly. Since there is an analytical solution for the induced velocity based on lifting line theory, this is a useful test case. The downwash along the quarter chord line for a constant spanwise circulation has a simple analytical solution given by the addition of the induction from

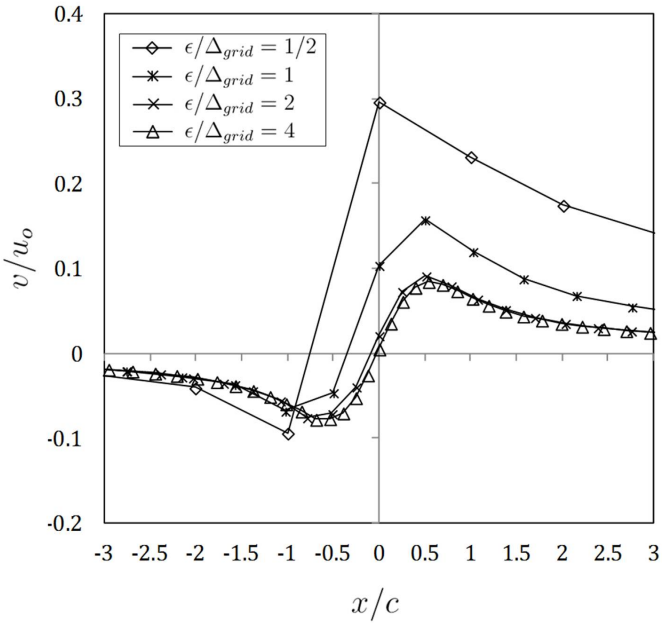

Figure 2.4: Induced velocity profile for various ϵ/Δ_{grid} ($\epsilon/c = 1/2$), demonstrating the degradation of the induction profile with inadequate mesh density

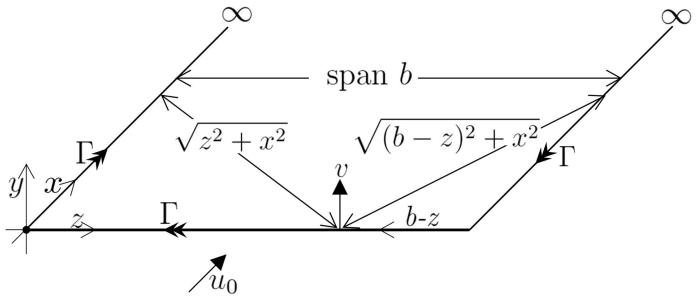

Figure 2.5: Distribution of trailed vorticity for a wing with constant circulation

two semi-infinite trailed vortices emanating from the wing tips as pictured in figure 2.5. Note that the trailed vortices are assumed to extend to infinity in a straight line aligned with the freestream direction. This straight-line vortex assumption is an approximation because in reality each trailed vortex will follow the local velocity, which includes induction effects from the wing bound vorticity, and from the trailing vortex emanating from the opposite wing tip. To obtain a simple analytical solution, the induced velocity is assumed small relative to the freestream, which implies a "lightly loaded" wing. The resulting vortex system is often referred to as a horseshoe vortex, and analytical solutions for the resulting flowfield can be found in many texts, such as [35] p.326. The induced velocity at any point along the lifting line (aligned with the z axis) is given by the integral:

$$v = -\frac{\Gamma}{4\pi}\int_0^\infty \left(\frac{z}{\sqrt{z^2+x^2}^3} + \frac{b-z}{\sqrt{(b-z)^2+x^2}^3}\right) dx \tag{2.16}$$

which evaluates to;

$$v = -\frac{\Gamma}{4\pi}\left(\frac{1}{z} + \frac{1}{b-z}\right) \tag{2.17}$$

As mentioned in the previous section, vortex methods use a core model to avoid a numerical singularity at the vortex location. Defining the vortex core radius r_c, the Scully core treatment (as shown in [34] p.539) gives the induction as:

$$v = -\frac{\Gamma}{4\pi}\left(\frac{z}{z^2+r_c^2} + \frac{(b-z)}{(b-z)^2+r_c^2}\right) \tag{2.18}$$

The downwash angle ϵ_{dw} is then defined as:

$$\epsilon_{dw} = \arctan\left(\frac{-v}{u_0}\right) \tag{2.19}$$

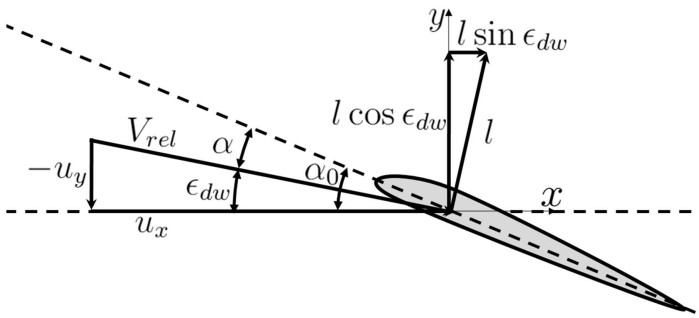

Figure 2.6: Definition of flow angles and force components used for studies on elliptically loaded and constant chord wings

The simulations specified a constant chord wing with $c = 0.1m$. The lift coefficient was set to $c_l = 1$ for the entire span. The lift force along the wing was calculated using the freestream velocity u_0 as shown in equations 2.20 and 2.21. The applied load was therefore specified *a priori* and was constant along the wing.[5] Due to the downwash, the applied force is tilted slightly to be perpendicular with the local velocity as shown in figure 2.6. The applied source terms were:

$$S_y = -\frac{1}{2}\rho u_0^2 c c_l \cos \epsilon_{dw} \eta_\epsilon \tag{2.20}$$

$$S_x = -\frac{1}{2}\rho u_0^2 c c_l \sin \epsilon_{dw} \eta_\epsilon \tag{2.21}$$

$$\eta_\epsilon = \frac{1}{\epsilon^2 \pi} e^{\left(\frac{x^2+y^2}{\epsilon^2}\right)} \tag{2.22}$$

The simulated domain consisted of a box spanning from $-2b$ to $2b$ in the streamwise (x) and normal (y) directions. In the spanwise (z) direction the domain extended from the wing root ($z = 0$) to $2b$ beyond the wing tip ($z = 2.5b$). The actuator line extended from $z = 0$ to $z = 0.5b$ and was centered on $(x, y) = (0, 0)$. This domain represented one half of the total wing span, and used a symmetry boundary condition. The inlet was located at $x = -2b$ and enforced a uniform inflow velocity $u = 1m/s$ with low turbulence intensity. The outlet was at $x = 2b$ and enforced zero relative static pressure. The boundaries at $y = 2b$ and at $z = 2.5b$ used the opening for entrainment option, which approximates an infinite domain. The fluid model employed was 'air at 25°C' with density $\rho = 1.185 \frac{kg}{m^3}$ and dynamic viscosity $\mu = 1.831 \times 10^{-5} \frac{kg}{ms}$.

[5]Note that with this configuration, the simulated circulation could vary slightly along the wingspan due to variation in the simulated relative velocity, however this varied only very slightly ($< 2\%$) in the observed results.

The mesh used $80 \times 80 \times 100$ elements in the streamwise (x), transverse (y) and spanwise (z) directions, respectively. Local refinement near the actuator line and mesh expansion were used to maintain the ratio $\epsilon/\Delta_{grid} = 4$ to avoid the accuracy problems discussed in section 2.3.

Simulations were run for $\epsilon/c = \{\frac{1}{4}, \frac{1}{2}\}$, and the resulting induction is plotted in figure 2.7. It was found that the simulated tip vortex core radius (at the blade tip) was strongly dependent on the value used for ϵ. Unsurprisingly, tighter source distributions led to smaller vortex cores and higher maximum induction. With $\epsilon/c = \frac{1}{4}$ the theoretical vortex with a core radius of 10% of the chord gave a good match to the simulated tip vortex. For $\epsilon/c = \frac{1}{2}$ the appropriate core radius was $0.2c$. These results imply an approximate relationship between the resolved tip vortex core radius and ϵ: $r_c \approx 0.4\epsilon$.

This allows selection of an appropriate value of ϵ, provided an estimate for the tip vortex core radius is available. This is a parameter which has not been widely published in the field of wind turbines, however from studies of rotorcraft tip vortices ([36] p.592), the tip vortex core (at the blade tip) is generally 5% to 10% of the chord. Given this, the range of ϵ/c should be approximately $\frac{1}{8}$ to $\frac{1}{4}$. Note that this requirement may lead to a highly refined mesh in the vicinity of the actuator line. Clearly, as ϵ becomes smaller, the mesh density must increase, and in the interest of maintaining a reasonable number of elements, it seems reasonable to use ϵ/c greater than 1/4. This should have an impact only within $0.1b$ of the wing tip; the results elsewhere should not be affected greatly.

It was thought that the resolved vortex core radius would be sensitive to both the Gaussian standard deviation ϵ and the spanwise mesh spacing Δ_z. To test the latter, Δ_z was refined by a factor of 5 compared to the original case, which had used $\epsilon/\Delta_z = 4$. The effect is displayed in figure 2.8. It can be seen that mesh refinement increases the maximum induction locally near the tip, but does not change the induction profile outboard of the original peak induction point.

2.5 Elliptically Loaded Wing

Tests were done to see how well the actuator line method could reproduce the analytical solution of an elliptically loaded wing. This was also attempted by Mikkelsen [19], who used a constant value of ϵ over the entire wing span. In this work, it is argued that to obtain correct solutions of the influence of the trailed vorticity on the

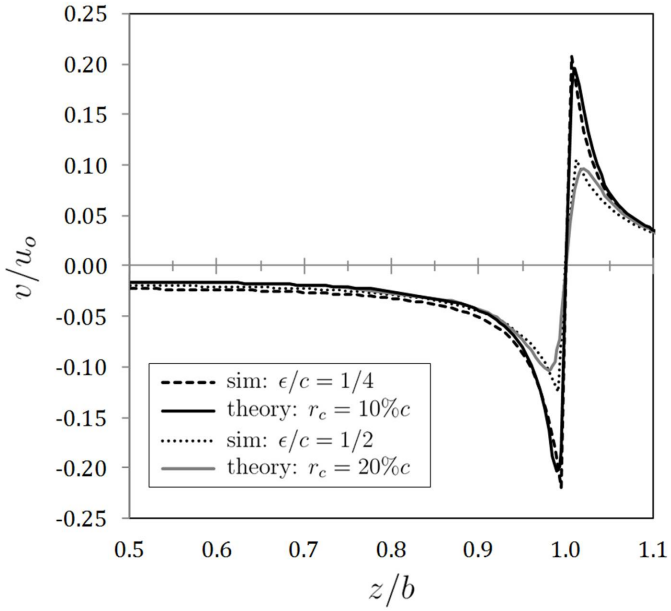

Figure 2.7: Resolved tip vortex induction compared to theoretical profiles using the Scully core model

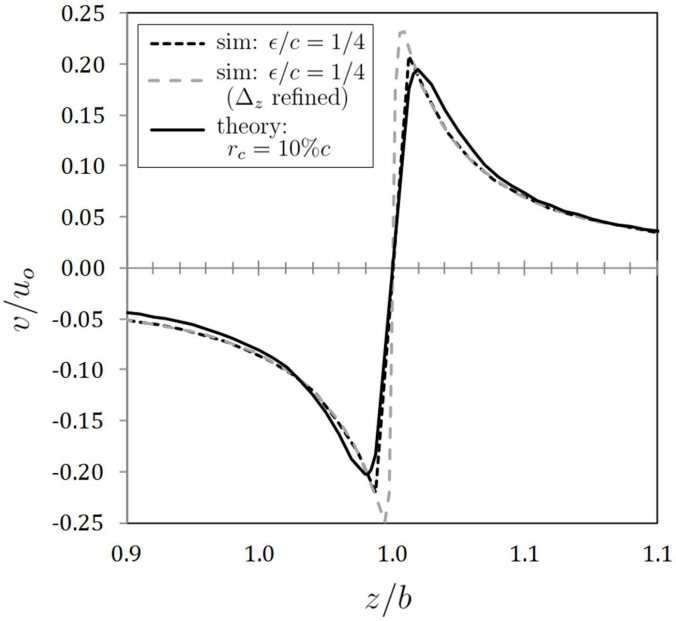

Figure 2.8: Effect of spanwise mesh refinement on the resolved tip vortex induction

flow at the quarter chord line, ϵ should be proportional to the local chord length. In fact, Mikkelsen did mention that such a proportionality would be more realistic, but did not pursue such a strategy. The analytical solution for an elliptically loaded wing is well documented ([35] p.332, for example) and gives a constant downwash along the wing defined by:

$$\epsilon_{dw} = -\frac{\Gamma_0}{2b} \tag{2.23}$$

$$\Gamma_0 = \frac{1}{2} u_0 c_0 c_l \tag{2.24}$$

where Γ_0 is the bound circulation at the blade root, c_0 is the root chord length, u_0 is the freestream velocity, and c_l is the lift coefficient.

In this paper, $c_0 = \frac{1}{8}m$ and $u_0 = 1\frac{m}{s}$ were used. The wing spanwise vector was aligned with the +z axis, and the chord was defined over the wing span by:

$$c = c_0 \sqrt{1 - \left(\frac{2z}{b}\right)^2} \tag{2.25}$$

where $b = 1m$ is the wing span.

The angle of incidence for the entire untwisted wing was then set to achieve an elliptic load distribution. This was achieved as follows. Assuming $c_l = 1$, the analytical solution for the downwash is $\epsilon_{dw} = -\frac{1}{32}$. Note that the simulation did not prescribe $c_l = 1$, but rather allowed the lift coefficient to be determined by the simulated angle of attack, according to $c_l = 2\pi\alpha$. The simulation computed the downwash angle ϵ_{dw} using;

$$\epsilon_{dw} = \arctan\left(\frac{-u_{y,bld}}{u_{x,bld}}\right) \tag{2.26}$$

The angle of attack was defined as the sum of a prescribed angle of incidence α_0 and the downwash angle, $\alpha = \alpha_0 - \epsilon_{dw}$. The analytical downwash solution was used to set the angle of incidence to $\alpha_0 = \frac{1}{2\pi} + \frac{1}{32}$. Thus, provided the simulation predicted the correct downwash angle of $-\frac{1}{32}$, the lift coefficient was $c_l = 1$ as originally assumed. This was a more stringent test for the actuator line approach than prescribing the loading *a priori*, but was designed this way to shed light on issues relating to the feedback of simulated velocity to the forcing terms, which will be required in rotor simulations.

The simulations used equation 2.10 to define the lift force. To be consistent with the theoretical solution, the airfoil drag was neglected. Note that there is still an induced drag force because the lift force is tilted slightly backwards as depicted in figure 2.6 due to the downwash angle. The forcing terms applied to the flow were defined as:

$$S_y = -l \cos \epsilon_{dw} \eta_\epsilon \tag{2.27}$$

$$S_x = -l \sin \epsilon_{dw} \eta_\epsilon \tag{2.28}$$

$$\eta_\epsilon = \frac{1}{\epsilon^2 \pi} e^{\left(\frac{x^2+y^2}{\epsilon^2}\right)} \tag{2.29}$$

The same simulation domain and meshing strategy as for the constant circulation wing were used, maintaining $\epsilon/\Delta_{grid} \geq 4$. The mesh was highly refined along the quarter-chord line to resolve the very tight Gaussian distribution at the wing tip. Two sets of simulations were run to observe the effects of using a constant value of ϵ along the wing vs. defining ϵ proportional to the chord length. The first set of simulations used constant values of ϵ defined by $\epsilon/c_0 = \{1/4, 1/2, 1, 2\}$. The second set of simulations used $\epsilon/c = \{1/4, 1/2, 1, 2\}$. Note that the chord length at the wing tip is zero, which resulted in a numerical singularity. This was avoided by truncating the simulated wing at $z = 0.499$ instead of at $z = 0.5$. The implications of this are discussed further below.

The results from the first set of simulations are shown in figure 2.9 and have decreasing induction towards the wing tip. This trend was also observed by Mikkelsen [19], who also used a constant ϵ along the blade span. Regardless of how tight of a distribution was used for the forcing terms, the induction reduces towards the wing tip because the bound vorticity is distributed over too large a region in space. There is some improvement as ϵ is reduced, however further reduction beyond what is shown here lead to numerical instability in the solution. This is thought to be due to too large a force being distributed over too small a region in space at the wing root ($\epsilon/c_0 < 1/4$ seems to lead to this instability.) In fact, a smaller timestep (i.e. relaxation) had to be applied to the solution algorithm for the $\epsilon/c_0 = 1/4$ case to avoid divergence. It is expected that further reductions to ϵ/c_0 would require excessive relaxation, and very long simulation runtimes.

The results from the second set of simulations (with ϵ proportional to the local chord) are provided in figure 2.10 and showed a much improved trend. The downwash

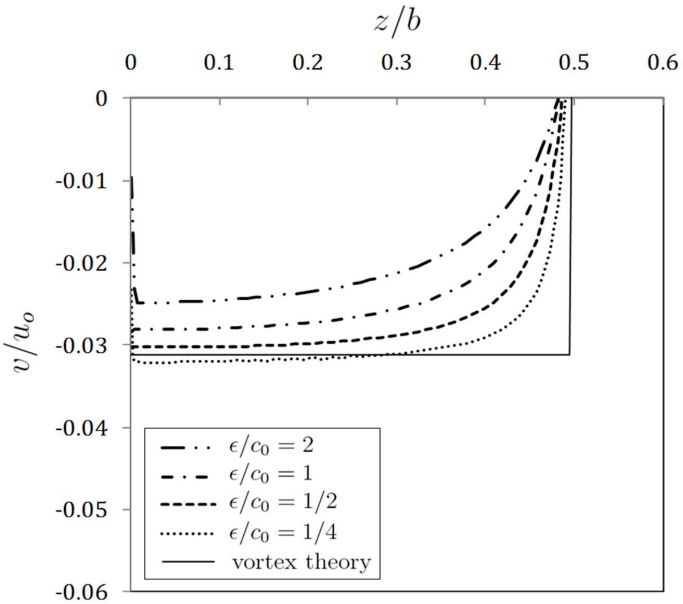

Figure 2.9: Downwash from simulations with constant ϵ over the entire span. (ϵ proportional to c_0)

was constant over most of the wing span. The behavior at the tip is though to be due to truncating the blade slightly before the actual tip. In the simulation, the bound circulation at the truncated wing tip was larger than it should be for a perfect elliptical wing (with zero circulation at the tip), which lead to the observed induction profile. This singular behavior is not a great cause for concern since real blades have some finite blade tip. Additionally, the simulated induction suggests that trailed vorticity is present at the wing root, which is inconsistent with the vortex theory solution. The behavior at the root is thought to be due to the exact treatment of the symmetry boundary condition, and preliminary work suggests that increased spanwise mesh density near the root may alleviate this error.

The simulated downwash reduced as the applied source term was spread over a larger region (i.e. for larger ϵ.) This was true for both sets of simulations, and is consistent with the trend in vortex based methods of reduced maximum induction for more distributed vortex sources. (Since the bound vorticity was more distributed, so was the trailed vorticity.) In reality, an airfoil presents a distributed source of vorticity, and the expected downwash may therefore be less than that predicted by a lifting line method, which concentrates the vorticity along a line. These results show that as ϵ/c decreases, the actuator line CFD solution approaches a lifting line vortex solution. That does not necessarily mean that ϵ/c should be as small as possible, since a distributed source could be more representative of a real airfoil.

As a final comparison of using a constant ϵ (i.e. $\epsilon/c_0 = \text{const}$) vs. having ϵ vary in proportion to the chord (i.e. $\epsilon/c = \text{const}$), an iso-surface of vorticity with a value $0.5s^{-1}$ is plotted in figure 2.11. The case with $\epsilon/c_0 = \text{const}$ produces a tip vortex which is concentrated in the spanwise (z) direction but occupies a large region in the x and y directions. This appears to be aphysical compared to the relatively symmetrical tip vortex in the case with $\epsilon/c = \text{const}$. Note that both cases display a trailed vortex along the symmetry plane, which is thought to be due to the symmetry boundary condition employed, as discussed earlier.

2.6 Conclusions

The actuator line technique introduced by Sørensen and Shen [18] has been applied to flows including an infinite wing (i.e. 2D airfoil), and 3D wings with constant and elliptical circulation distributions. From the infinite wing simulations, it has been determined that the required mesh spacing to avoid significant errors is related to the

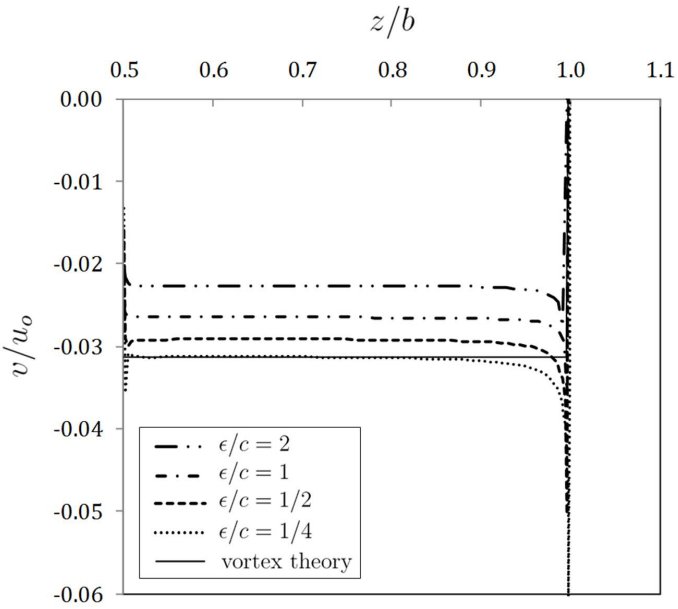

Figure 2.10: Downwash predicted by simulations using ϵ proportional to c

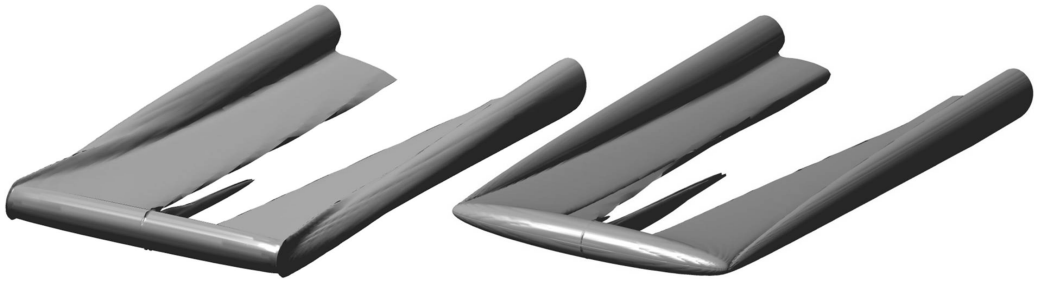

Figure 2.11: Iso-vorticity ($0.5s^{-1}$) surfaces for simulations with; $\epsilon/c_0 = \text{const}$ (left), and $\epsilon/c = \text{const}$ (right)

source distribution length scale, and that the ratio ϵ/Δ_{grid} should be at least 4. This finding is likely somewhat code-specific and should be evaluated for different solver algorithms that are to be used for actuator line simulations. The methodology outlined in this paper can serve as a guideline for such studies. From 3D wing simulations, it has been found that to obtain an accurate representation of the influence of trailed vorticity on the flow at the quarter-chord line, ϵ should vary in proportion to the local chord length. It was also found from simulations of a constant circulation wing that the tip vortex core radius varies in proportion to the source distribution length scale. Based on estimates of a realistic tip vortex core radius, the ratio ϵ/c should take on a value of approximately 1/8 to 1/4, however larger values should only impact the solution in very close proximity to the tip vortex. With these guidelines established, the actuator line method can be applied with greater confidence to more complex flows including turbine wakes and the interaction of wakes with solid boundaries, free surfaces and other wakes.

Acknowledgments

The authors thank the National Sciences and Engineering Research Council (NSERC) of Canada, the Pacific Institute for Climate Solutions (PICS) and the University of Victoria for financial support.

Chapter 3

Cross Coupling Between Device-Level CFD and Oceanographic Models Applied to TISECS in Minas Passage and Petit Passage

This paper has been published as:

Shives, Michael; Crawford, Curran; Hiles, Clayton; and Walters, Roy: *"Combining Numerical Methods for Basin and Turbine Scales for Improved Modelling of in-situ Turbine Arrays,"* Proceedings of the 10th European Wave and Tidal Energy Conference, Aalborg, Denmark, 2013.

It was unclear how to develop a hybrid method for turbine farm simulation to leverage the strengths of oceanographic SWE codes and 3D RANS codes. This paper presents initial work toward that goal, which is formalized and expanded upon in chapter 7. During this study, Roy Walters and Clayton Hiles ran the oceanographic model simulations, while I ran the 3D RANS simulations and wrote the paper. We defined the hybrid method as a team.

Abstract

This paper proposes an approach for combining device-scale and basin-scale simulation methods to provide realistic in-situ performance analysis of turbine arrays and with the eventual goal of determining basin-scale effects from large turbine arrays. The present state-of-the-art basin-scale simulation methods represent turbines as sub-grid-scale objects, typically using semi-empirical/semi-analytical turbine models. Device-scale CFD simulation methods can resolve flows around turbines and can predict turbine performance outside the idealized assumptions of analytical methods. Thus, combining the capabilities of these two types of simulations is desirable for accurate in-situ performance analysis with the correct influence of turbines on the basin flow. The approach is to parameterize turbine thrust and power using a reference velocity available to both types of model. This is a volume average over a region in space that can be resolved by the basin-scale model. The approach is accurate provided both methods predict a consistent reference velocity. This paper presents preliminary studies testing such consistency for simplified channel scenarios, finding that as long as the averaging volume has length scales twice the turbine diameter, relative error in power is typically under $\approx$5%. When applied to a complex real-world flow, the relative error was larger. It is thought that at present, the method is suitable for approximate power prediction and further improvement is required for accurate turbine performance studies.

3.1 Introduction

Tidal turbine technology is progressing from prototypes and demonstrators to commercial applications. Developers are transitioning from isolated turbines to small arrays of turbines (such as the proposed three-rotor design by Marine Current Turbines) and once the technology proves economically viable, to large arrays of many turbines. There is presently a requirement to develop methods to simulate arrays of turbines and to optimize the layout of turbines for a given site. For small arrays, a predictive capability for the mutual influence of turbines on each other will be required. Additionally, the influence of tidal flow boundaries (i.e. channel bottom, free surface, and lateral bounds) should be resolved. For larger arrays, it will also be necessary to predict the influence of the turbines on basin dynamics.

Presently, simulation methods for tide-driven basin-scale flows exist and have been

validated with good agreement to measured data in the absence of turbines. These have been used to model the effect of large arrays of turbines on basin scale flows (e.g. [8]). Such methods have used semi-analytical/semi-empirical representations of turbines which typically limited to idealized flows (such as uniform inflow, 2D flow, empirical wake models, etc.), thus such methods can only provide rough estimates for power generation. Due to the maximum resolution (10s of meters) of basin-scale models, they cannot resolve the mutual influence of turbines on each other, and their predictive capability for the influence of the flow boundaries on turbine performance remains to be assessed.

At the device scale, CFD simulation can be used to model turbines for a wide range of inflow conditions and can resolve mutual influences between turbines and influences of local bathymetry. With such simulations, is it possible to accurately simulate a wide range of array configurations but the computational expense can become very large. While there have been some applications of CFD to entire basin-scale flows, such an approach may be too computationally expensive. It is likely that since dedicated basin scale models use a reduced set of equations compared to general-purpose CFD solvers, they should run faster. They should also be more accurate for basin-dynamics since they use turbulence parameterizations specific to basin-scale flows which are different from typical CFD codes.

This paper presents work done towards combining the capabilities of basin-scale simulation methods with device-scale methods to obtain an overall approach which allows accurate in-situ performance analysis for turbines. It is thought that such a methodology could evolve to a point where it becomes possible to simulate large arrays of turbines with accurate power predictions and an accurate prediction of the back-effects on the tidal flow regime.

3.2 Overall Approach

The proposed approach is depicted in figure 3.1 and consists of the following steps. First, the basin-scale simulation is used to predict the natural tidal flow throughout the channel. Then, potential turbine sites are chosen and CFD meshes are developed for sub-domains containing single turbines, or groups of turbines. Then an iterative process begins to develop a performance model for each turbine in the array. CFD simulations are run on the sub-domains to predict the mutual influence of the turbines on each other, as well as the influences of local bathymetry. It would be computation-

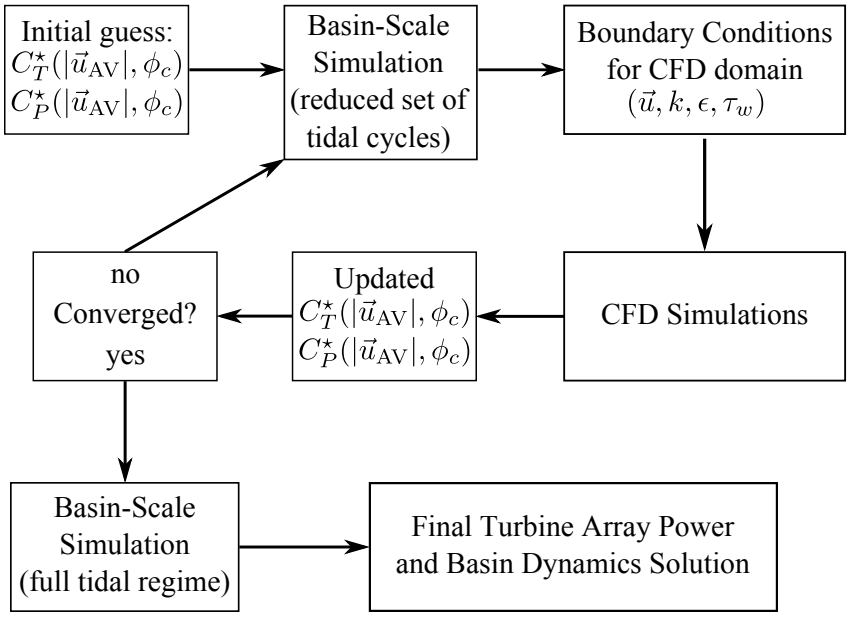

Figure 3.1: Flow Chart of Proposed Methodology

ally expensive to run a transient CFD simulation of an entire tidal cycle. However, it is likely valid to make a quasi-steady assumption and to run several steady-state CFD simulations at different phases of the tidal cycle. The CFD simulations are used to determine non-dimensional turbine performance parameters $C_T^\star$ and $C_P^\star$. Note that $C_T^\star$ and $C_P^\star$ may vary throughout the tidal cycle due to changes in flow speed ($|\vec{u}_{\mathrm{AV}}|$) or direction (ϕ), or due to the turbine control strategy, so the performance model would involve curve-fitting. Next, a new basin-scale simulation is run with the turbine forces added. This generates new boundary conditions for the CFD simulations, and the entire process is iterated until convergence of $C_T^\star$ and $C_P^\star$, resulting in the final empirical turbine model. Then, the final parameterization can be used in the basin-scale simulation for more in depth studies of longer duration[1].

3.3 Analysis Codes

This section gives a brief overview of the analysis codes employed, for further detail please refer to the supplied references (for RiCOM) or product documentation (for

[1] A 'tighter' coupling between CFD and basin-scale methods is also possible, where the two models share boundaries and simulations run over entire tidal cycles, but presently this approach has not been attempted due to the programming complexity and computational cost.

CFX). In general, basin-scale methods typically solve the shallow water equations, while CFD solvers solve the full 3D RANS equations. Both classes of model employ turbulence closures (commonly k-ϵ) but with different coefficients which have been tuned for different classes of flows and differing typical grid resolution.

3.3.1 Basin-Scale

For the basin-scale simulations, the River and Coastal Ocean Model (RiCOM) developed by Dr. Roy Walters was used. A brief general description of the model is provided here with greater detail in [37, 38, 39, 40]. RiCOM is formulated in rotating frame of reference using the Reynolds-averaged Navier-Stokes equations and the Boussinesq approximation. The equations are also spatially averaged to derive double-averaged equations that allow sub-grid spatial effects (vegetation, bottom roughness, etc.) to be included in a rigorous manner [39]. This double averaging provides a means to couple the results of small-scale CFD models with the large-scale Ocean model.

RiCOM solves the primitive hydrodynamic equations with a semi-implicit time-stepping scheme that is unconditionally stable with respect to time-step size, which allows the time-step size to be chosen to adequately resolve the temporal variation of the flow without numerical stability constraints. The model uses a semi-Lagrangian approximation for advection that is accurate, stable, and robust which yields accurate results without oscillations for high speed flows such as occur over weirs, in flow constrictions, and tidal rapids. A finite element spatial approximation is used, giving considerable flexibility in designing the computational grid [40]. Wetting and drying capabilities are inherent to the finite volume continuity equation employed and the model conserves mass both locally and globally.

3.3.2 Device-Scale

The device-scale simulations used the commercially available ANSYS CFX software. CFX solves the Reynolds-averaged-Navier-Stokes equations using finite-volume discretization. The *high resolution* advection scheme was used, which blends 2^{nd} order central differencing with 1^{st} order upwind schemes, and favours central differencing unless upwinding is required for simulation stability. CFX uses a co-located grid and avoids even-odd decoupling with a modified Rhie/Chow interpolation. The software uses a fully implicit discretization and a coupled solver which uses an incomplete

lower upper (ILU) factorization technique. The solver is accelerated using an algebraic multi-grid technique called additive correction. The standard k-ϵ turbulence closure was used for all simulations.

3.4 Turbine Performance Parameters and Velocity Scale

It was necessary to characterize the turbine performance with respect to a reference velocity available to both CFD and basin-scale simulations. This requirement was somewhat problematic for two reasons. One was that the traditional performance parameters, thrust and power coefficients, rely on the 'freestream' velocity, which is not clearly defined in basin flows. The other is that the basin-scale simulation does not have sufficient resolution to provide a mean velocity through the turbine rotor (see figure 3.2 for an example grid resolution).

The approach was to represent the turbines in basin-scale simulations using two parameters, $C_T^\star$ and $C_P^\star$. These are similar to the traditional thrust and power coefficients (C_T, C_P), except that instead of referring to the freestream velocity, a volume-averaged velocity ($\vec{u}_{\mathrm{AV}}$) for a region containing the turbine is used. This was necessary because there is no clear definition for the freestream velocity in the context of a complex basin flow. The freestream velocity is only clearly defined when the flow is unbounded and the inflow is uniform, and therefore cannot be used in general.

A second option for the reference velocity would be to use the average velocity passing through the turbine rotor. Actuator disk theory defines this as $u_d = u_\infty(1-a)$ where a is the axial induction factor. This approach could be taken for CFD simulations because they have adequate resolution, however since the basin-scale simulation represents the turbine as a sub-grid-scale object, it cannot determine u_d explicitly and would thus need to use an empirical calibration.

The basin-scale model is formulated in terms of volume-averaged velocity for each grid cell. The chosen reference velocity must therefore be a volume-average over a region at least as large as the basin-scale model grid cells. Thus, an averaging volume (denoted by the subscript $_{\mathrm{AV}}$) is introduced (see figure 3.2), and the volume-averaged velocity for this region is denoted $\vec{u}_{\mathrm{AV}}$. The averaging volume may span multiple

basin-scale grid cells.

$$\vec{u}_{\mathrm{AV}} = \frac{\int_{\mathcal{V}_{\mathrm{AV}}} \vec{u} d\mathcal{V}}{\int_{\mathcal{V}_{\mathrm{AV}}} d\mathcal{V}} \tag{3.1}$$

This integration is evaluated numerically by both the CFD and basin-scale methods to give $\vec{u}_{\mathrm{AVc}}$ and $\vec{u}_{\mathrm{AVb}}$ respectively. For the general method to work, both CFD scale and basin-scale methods must provide a consistent prediction for $(\vec{u}_{\mathrm{AV}})$.

The turbine performance parameters are defined by:

$$C_T^\star = \frac{T}{\frac{1}{2}\rho|\vec{u}_{\mathrm{AVc}}|^2 A_f} \quad , \qquad C_P^\star = \frac{P}{\frac{1}{2}\rho|\vec{u}_{\mathrm{AVc}}|^3 A_f} \tag{3.2}$$

where T is the turbine thrust (axial force), P is the power output, ρ is the fluid density, and A_f is the frontal area of the turbine rotor.

3.5 Turbine Forces and Power

3.5.1 Basin-Scale

The horizontal grid resolution of the basin-scale simulations is larger than a turbine diameter, and therefore the forces of the turbine are distributed over a horizontal region in space which is larger than the actual turbine. However, many vertical layers of cells are often used to resolve variations in depth (figure 3.2). Thus, the turbine may span several vertical layers. For any grid cell in the basin-scale model, the turbine force per-unit-volume is specified by;

$$f_{\mathrm{d,basin}} = -\frac{1}{2}\frac{A_{fc}}{\mathcal{V}_c}\rho C_T^\star |\vec{u}_{\mathrm{AVb}}|\vec{u}_{\mathrm{AVb}} \tag{3.3}$$

where A_{fc} is the portion of the turbine frontal area contained within the grid cell and $\mathcal{V}_c$ is the cell volume. For the example provided in figure 3.2, the turbine forces are distributed over cells 2 and 3, while $\vec{u}_{\mathrm{AVb}}$ is calculated using cells 1,2,3 and 4. Conceptually, $f_{\mathrm{d,basin}}$ is uniform over the rotor disk; however it's value may vary with depth due to variation in A_{fc}.

The basin-scale simulation calculates the power output using;

$$P_{\mathrm{basin}} = \frac{1}{2}\rho|\vec{u}_{\mathrm{AVb}}|^3 C_P^\star A_f \tag{3.4}$$

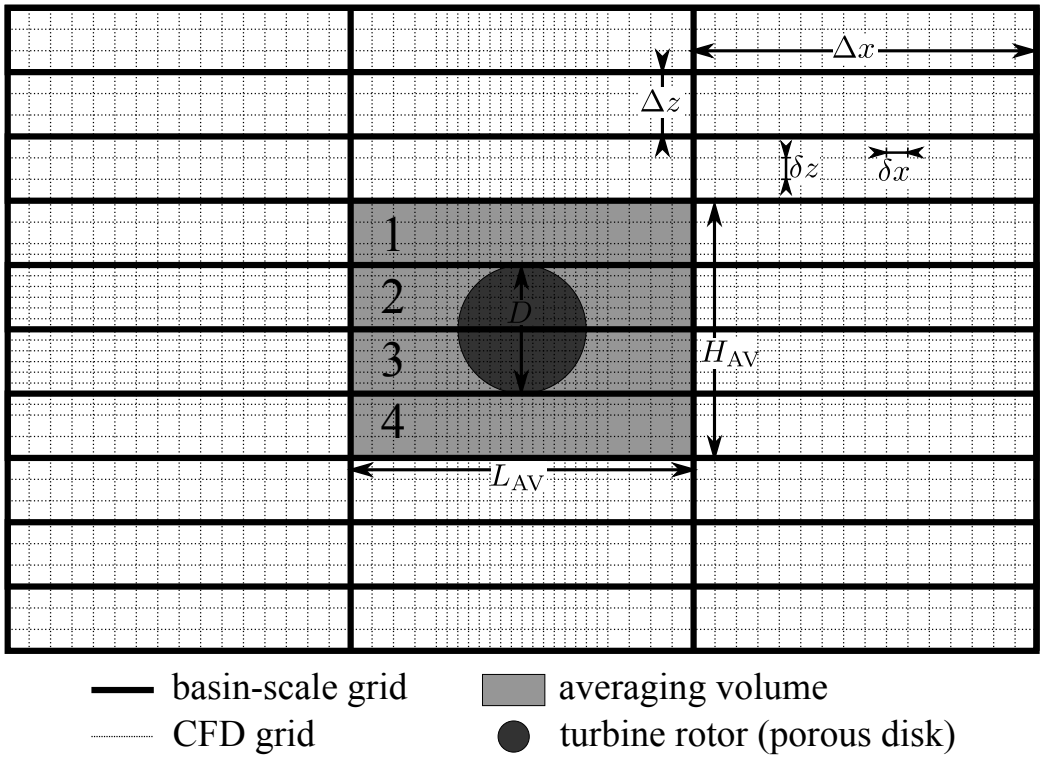

Figure 3.2: Example of grid resolution for CFD and basin-scale simulations and definition of the velocity averaging volume. L_{AV} and H_{AV} refer to the averaging volume dimensions; Δx and Δz refer to the basin-scale grid; δx and δz refer to the device scale grid.

3.5.2 Device-Scale

In the CFD scale simulations, the representation of the turbines can range in complexity from full blade-resolved simulations, to simpler porous-disk type approaches. For the initial studies reported here, the porous disk approach has been used to provide a simplified representation of turbines. The porous disk method specifies the drag-per-unit-volume using;

$$f_{\mathrm{d,cfd}} = -\frac{1}{2t_d}\rho K|u_x|u_x \tag{3.5}$$

where K is a non-dimensional resistance parameter, and t_d is the porous disk thickness in the CFD mesh. This type of specification allows the drag force to vary spatially over the disk. Such spatial variation may be present for turbines in boundary layers,

or for non-uniform inflows due to local bathymetry or other turbines. This spatial variation was included in the CFD model because it has sufficient grid density to resolve its impacts, whereas the basin-scale model used a uniform drag distribution.

Note that it is possible to specify both axial and azimuthal (swirl) forcing terms for a spinning turbine rotor based on airfoil lift and drag coefficients. (Please see [19, 41] for more details). Such an approach may provide a more realistic representation of real turbines, however the present approach has been taken due to its relative simplicity.

The turbine thrust force T was found by numerically integrating $f_{\mathrm{d,cfd}}$ over the porous disk volume region.

$$T = \int_{\mathcal{V}_{\mathrm{disk}}} f_{\mathrm{d,cfd}} \cdot d\mathcal{V} \tag{3.6}$$

Similarly, the power was found by numerical integration of the product of the local forcing term and local axial velocity.

$$P = \int_{\mathcal{V}_{\mathrm{disk}}} f_{\mathrm{d,cfd}} \cdot u_x \cdot d\mathcal{V} \tag{3.7}$$

This formulation gives an idealized power output which assumes that all of the applied force contributes directly to power production. Therefore blade drag and other losses are neglected. This was considered acceptable for these preliminary studies, but losses should be considered for more accurate power predictions. Note that the inclusion of such losses would be done at the device-scale and incorporated into the basin-scale model via reduced values for $C_P^\star$.

In general, $\vec{u}_{\mathrm{AVc}}$, T and P are first determined from CFD simulation results to find $C_T^\star$ and $C_P^\star$, which are then passed to the basin-scale code and used in equation 3.3 for the applied drag and equation 3.4 for the output power.

3.6 Simplified Channel Scenarios

The proposed methodology relies heavily on the assumption that the device-scale and basin-scale simulations will provide a consistent prediction of the volume-averaged velocity $\vec{u}_{\mathrm{AV}}$. This consistency depends on the size of the averaging volume. Larger volumes will give better consistency but reduce the ability of the basin-scale simulation to resolve the flow. Much of the work done focused on determining an appropriate size for the averaging volume using simplified tidal channel scenarios to avoid the

complexities of real basin flows.

The desired outcome was to achieve a high level of consistency between power estimates from the basin-scale and CFD simulations. Thus the target variable was the percent difference between the CFD prediction of power and the basin-scale prediction.

$$P_{\text{err}} = \frac{P_{\text{basin}} - P_{\text{cfd}}}{P_{\text{cfd}}} \tag{3.8}$$

Tests were performed with various representations of eddy viscosity, at different flow speeds, and with/without bottom friction. Additional tests were performed for a small array of turbines.

The channel was rectangular with length L=5 km, width W=1 km, and depth H=50 m. The basin-scale simulations specified the inlet mass flow rate as 50 000, 150 000 or 250 000 $^{\text{m}^3}/_{\text{s}}$ (corresponding to inflow speeds of 1, 2 or 3 $^{\text{m}}/_{\text{s}}$, respectively). The water surface height was set to η=0 at the outlet. A single turbine was placed at mid-depth 25 m on the channel centreline 2 km from the inflow boundary. For the boundary layer tests, the turbine was placed at 35m depth. The turbine had a diameter of D=10 m. In the basin-scale simulations, two parameterizations for the vertical viscosity were examined, one was a constant ν_{v}=0.1 or 0.01 $^{\text{m}}/_{\text{s}^2}$, and the other used a k-ϵ closure.

In the CFD simulations, a portion of the channel surrounding the turbine(s) was modelled. Grid refinement studies were conducted according to the GCI_{OR}[42, 43] method and estimated discretization errors were less than 1% for thrust and power. Boundary conditions were set to maintain consistency with the basin-scale flow. The inlet was located 10D upstream of the turbine and the inflow velocity was either: uniform at 1,3 or 5 $^{\text{m}}/_{\text{s}}$; or a profile provided by results of the basin-scale simulation (for boundary layer cases). The inlet turbulence was set to *high* (10% intensity) which is thought to be reasonable for tidal channels. The domain spanned the full water depth (50 m). The top boundary used a rigid-lid assumption (fixed boundary, with free-slip condition). On the bottom, a free-slip condition was used except for the boundary layer cases, where the bottom shear stress was specified. The lateral boundaries were located 6D away from the turbine and used an *opening-for-entrainment* option, which approximates an infinite domain[2]. A pressure outlet was used with the reference pressure set to 0 Pa. Symmetry planes were used when applicable to reduce

[2]Blockage effects are assumed negligible for all cases considered

computational cost. The CFD simulations used the k-ϵ turbulence closure except when otherwise noted.

3.6.1 Convergence with vertical resolution

The first set of tests observed the change in P_{err} with increasing the vertical resolution (i.e. number of layers) of the basin-scale simulation. In the following discussion, the averaging volume dimensions have been normalized with respect to the turbine diameter D.

$$\hat{L}_{\text{AV}} = \frac{L_{\text{AV}}}{D} \qquad \hat{H}_{\text{AV}} = \frac{H_{\text{AV}}}{D} \tag{3.9}$$

For these tests, the averaging volume dimensions were $\hat{L}_{\text{AV}}$=4, $\hat{H}_{\text{AV}}$=1. The power error is shown in figure 3.3, where the x-axis $D/\Delta z$ represents the number of vertical layers per-turbine-diameter. Using a constant vertical viscosity of 0.1 $^{\text{m}}/_{\text{s}^2}$ gave a convergent trend towards zero error. Using the k-ϵ closure produced a similar convergence trend, but towards -2% error. This reflects the fact that different coefficients are used in the k-ϵ closures for CFD and basin-scale models. Based on the observed trend, increasing $D/\Delta z$ from 4 to 16 (or greater) should only produce less than 2% discretization error. Therefore, $D/\Delta z$=4 (20 vertical layers for the 50 m deep channel) was typically used for the remainder of the studies.

3.6.2 Averaging volume horizontal size

The next set of tests observed the impact of changing the horizontal extent of the averaging volume. Tests were done using depth-averaged and 3D basin-scale simulations. Tests were done using $\hat{L}_{\text{AV}}$=1, 2 or 4, and are plotted in figure 3.4. Observing figure 3.4 it is apparent that the 2D depth-averaged case (H_{AV}=H) is the least sensitive to the averaging volume horizontal length-scale. For the 3D cases with 10 or 20 layers, $\hat{H}_{\text{AV}}$ was 1, and the sensitivity to $\hat{L}_{\text{AV}}$ was greater with increasing vertical resolution. Additionally, it can be seen that the sensitivity to the vertical resolution (# of layers) decreases as the averaging volume horizontal scale $\hat{L}_{\text{AV}}$ increases. In general, the consistency between CFD and basin-scale simulations improves with increasing averaging volume size. It was found that in general, $\hat{L}_{\text{AV}} = 1$ gave poor results and larger values were used for subsequent tests.

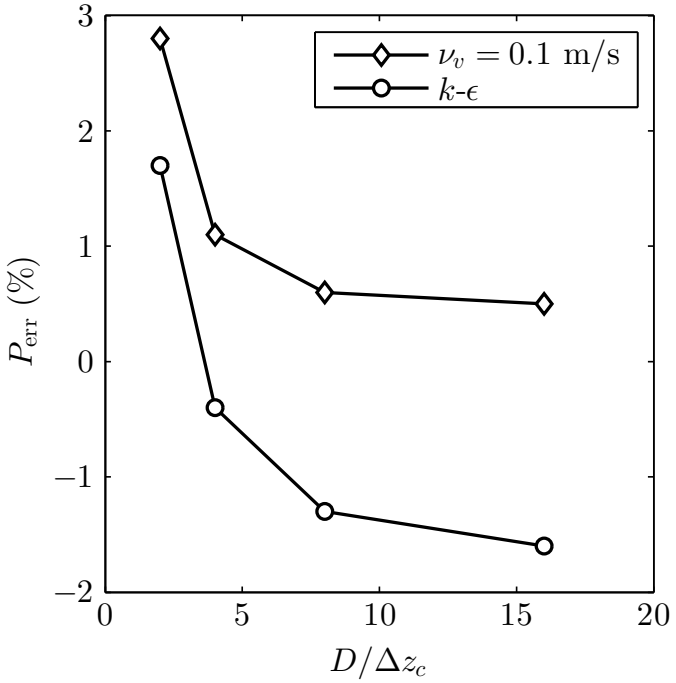

Figure 3.3: Convergence trend with increasing vertical resolution of the basin-scale simulation, $D/\Delta z$ can be interpreted as the number of vertical layers per-turbine-diameter

3.6.3 Inflow velocity and vertical size

A set of tests were conducted to validate the methodology over a range of inflow velocities covering expected values in real tidal channels (1, 3, and 5 $^{\mathrm{m}}/_{\mathrm{s}}$). Results are shown in figures 3.5 and 3.6. It was found that the basin-scale simulation tended towards under-predicting the power as the velocity increased. It is thought that this trend is partially due to differing treatments of turbulence between the two scales of simulation. Generally, the results improved with increasing the vertical and horizontal size of the averaging volume.

3.6.4 Boundary layer flows

A set of tests were conducted for simulations involving a boundary-layer. To ensure consistency between the two scales of simulation, the CFD model used a *specified shear* boundary condition for the bottom boundary instead of the typical no-slip condition. Also, to remove the impact of differing turbulence closures, some CFD simulations were run without a turbulence model but with the fluid viscosity set to be consistent

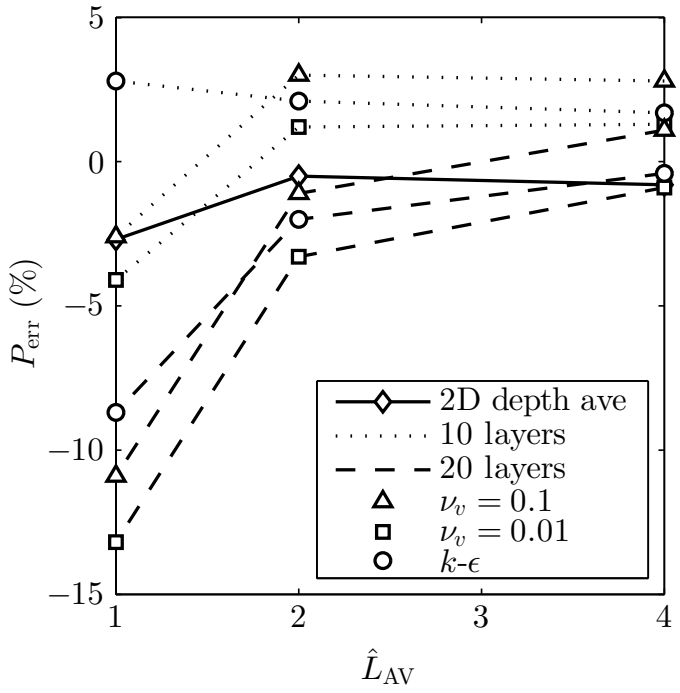

Figure 3.4: Power error for set 1 tests ($\hat{H}_{\mathrm{AV}}$=1)

with the total viscosity in the basin-scale simulations (i.e. ν_{cfd}=$\nu_{\mathrm{t,basin}}$=0.1 m^2/s). For these constant viscosity cases, the friction velocity was $u^\star$=0.1344 m/s and the bottom shear stress was τ_b=18.063 Pa. In later simulations, the k-ϵ turbulence closure of each model was used to calculate the eddy viscosity.

The power error is plotted in figure 3.7. It was found that with sufficiently large averaging volumes, the basin-scale and device-scale simulations provided adequately consistent power estimates. This was true for both the constant viscosity, and k-ϵ cases. With $\hat{L}_{AV}$=1 or $\hat{H}_{AV}$=1, the power was not consistent between the two methods, particularly for the k-ϵ cases. Note that basin-scale simulations often include source terms for turbulence that are associated with form drag, however it was found that such sources needed to be disabled to obtain consistent results.

3.6.5 Array tests

The final set of tests done using the simple channel scenario was for a simple array of turbines with uniform inflow. The CFD simulations used the k-ϵ turbulence model in all cases, while the basin-scale model was tested using both k-ϵ and constant ν_v=0.1 m^2/s. The layout of the turbines is depicted in figure 3.8. The power error is

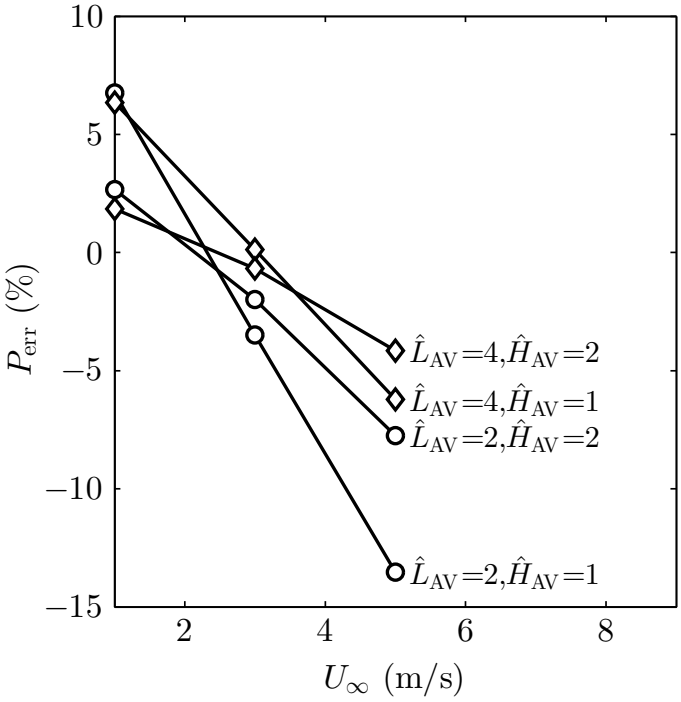

Figure 3.5: Variation of power error with changing inflow velocity and averaging volume size, for a constant vertical viscosity A_v=0.1

plotted in figure 3.9. The power discrepancy was approximately 6% with $\hat{H}_{\mathrm{AV}}$=2 and $\hat{L}_{\mathrm{AV}}$=5 or 6.

Attempts were also made to use a separate averaging volume for each individual turbine in the array but it was found that the basin-scale model could not resolve the interaction effects between the turbines adequately, so the impact of the three turbines needed to be lumped together into a single basin-scale element.

3.6.6 Summary

All of the tests indicated that the averaging volume size should be least twice the dimension of the turbine (or array of turbines) in order to maintain consistency with the device-scale simulations. Physically, the volume should average-out the differences between the hydrostatic basin-scale model and non-hydrostatic CFD model. Typical errors range up to 7%. The general degree of accuracy holds across the velocity range typical for operation of turbines with higher errors at high velocity.

Reducing the size of the averaging volume leads to substantial errors due to differences in the flow around the turbine caused by formulation differences between the

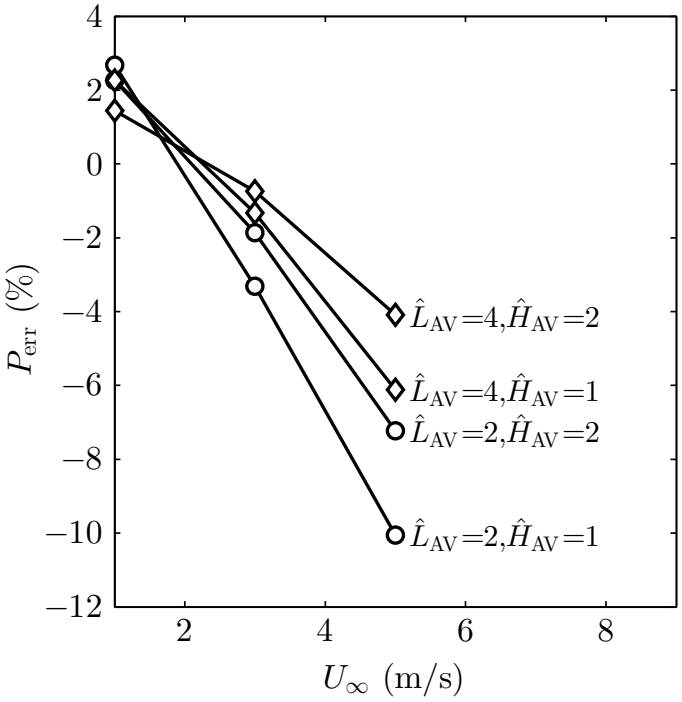

Figure 3.6: Variation of power error with changing inflow velocity and averaging volume size, with vertical viscosity determined by the k-ϵ closure

Ocean and CFD model.

The k-ϵ turbulence closure model yields a more realistic and accurate calculation of vertical viscosity and its important horizontal and vertical variations. It also produces more realistic turbine wake recovery. However, it was found that typical turbulence sources associated with form drag had to be disabled to obtain power results consistent with the CFD simulations.

3.7 Minas Passage

The simplified channel scenarios gave some insight into the behaviour of the method, however a more realistic scenario was also pursued to determine the feasibility for real-world scenarios. The chosen site was the FORCE test site in Minas Passage in the Bay of Fundy. At this preliminary stage, it has been assumed that the turbine performance parameters $C_T^\star$ and $C_P^\star$ remain constant over the tidal cycle. In reality, they would vary somewhat with the inflow velocity and direction and due to limitations in real turbine operation such as cut-in speed.

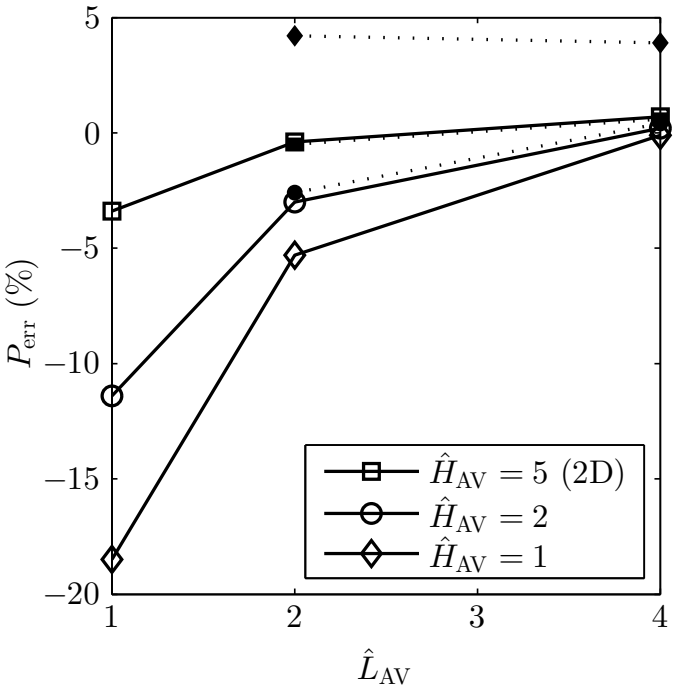

Figure 3.7: Power error for boundary layer tests, unfilled symbols are for cases with constant vertical viscosity, filled symbols are for the k-ϵ turbulence model

3.7.1 Site characteristics

The Bay of Fundy is located on the east coast of North America between approximately 44° and 46° N latitude (figure 3.10). The resonant period of this system is slightly longer than the period of the dominant M2 tidal constituent and this area is well known for the large tide range in the upper bay. The node point for the oscillation is near the shelf break east of Georges Bank; however, this is complicated by other resonances parallel to the shelf that extend down to Boston and Cape Cod.

For several reasons, the entire bay down to Cape Cod and extending offshore has been modelled in this study. For one, modifying the form drag in the upper bay can alter the resonance so that it becomes difficult to specify boundary conditions in a more limited area model. Moreover, previous studies have shown that introducing features such as barrages can modify the resonance and have significant effects on tides as far as Boston [44]. The particular areas of interest were Minas Basin where the largest tide range occurs, and Minas Passage that connects Minas Basin with the upper Bay of Fundy (figure 3.11). The region contains extensive tidal flats, and sensitivity tests indicated that treating wetting and drying of these flats accurately

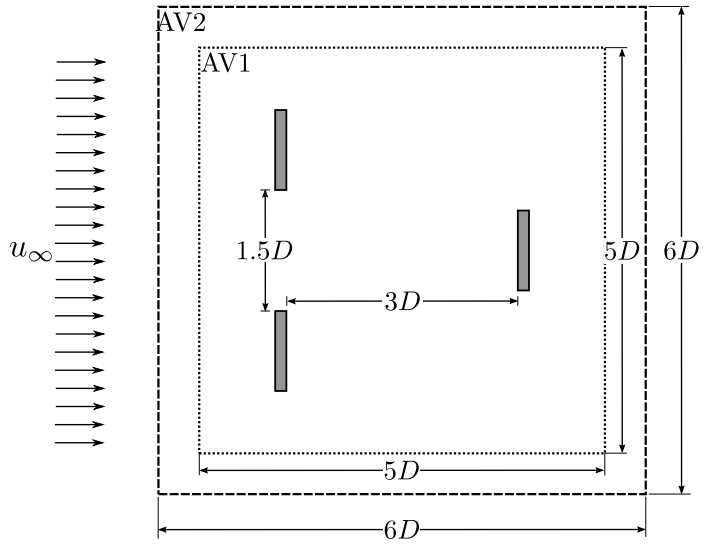

Figure 3.8: Layout of turbines for the small array test case

is important for attaining accurate model results for velocity amplitude and phase.

The dominant tidal constituent is the M2 and the amplitude varies from 0.5 m at the open boundary to over 6 m in Minas Basin. In an earlier study, 8 constituents were used in the open boundary conditions (M2, S2, N2, K2, K1, O1, P1, Q1). Most of these constituents are small compared to the M2 (particularly the diurnal constituents) but were retained in order to assess the accuracy of the model against tide and current observations. The nonlinear interactions between the semi-diurnal constituents are important in many situations. The earlier results indicated that this representation of the system was reasonably accurate with constituent amplitude errors of a few cm and phase errors of a few degrees in general.

3.7.2 Device-scale Simulations

There are plans for four berths at the FORCE test site for demonstration turbines. The present study used simplified turbines located at these sites. For each berth, a CFD sub-domain was created aligned with the expected flow at the maximum flood condition from basin-scale simulations with no turbine forcing present (see figure 3.12). The sub-domains were 200×200 m, and the bottom boundary was generated using 5 m resolution bathymetry data [45] (figure 3.13). The upper boundary location was set using the initial basin-scale simulation results for depth at the centre of the sub-domain for the max-flood condition. The sub-domains were discretized

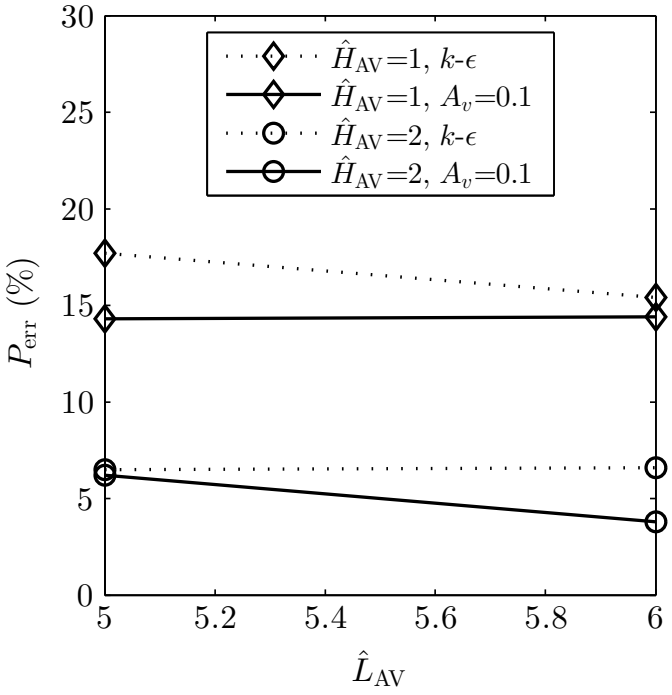

Figure 3.9: Power error for array tests

using the same meshing strategy as for the simple channel cases, except that the elements conformed to the irregular bottom geometry. For all cases, a generic turbine with D=16 m was used for each berth. The porous disk resistance coefficient was set to a value of K=1.8. The turbines were placed at mid-depth in the centre of each sub-domain. The boundary conditions for the CFD simulations were set using output data from the basin-scale model.

1. *Inflow:* At the upstream boundary (inlet) the velocity was specified using a 2D cubic interpolation of the nodal values from the basin-scale grid. This interpolation was done with respect to the lateral position (y) along the boundary, and the height (h) above the bottom[3]. The inlet turbulent kinetic energy k and dissipation rate ϵ were set using a 2D linear interpolation (with respect to y and h) of the face-centred values output from basin-scale simulations.

2. *Sides:* At the lateral boundaries, an *opening* condition was specified. For cases with inflow through the boundary (i.e. when the flow was yawed relative to the

[3]Using the depth below mean-sea-level for the interpolation instead of h resulted in non-physical velocity profiles at the bottom boundary due to better resolution of the irregular bottom by the CFD grid compared to the basin-scale grid

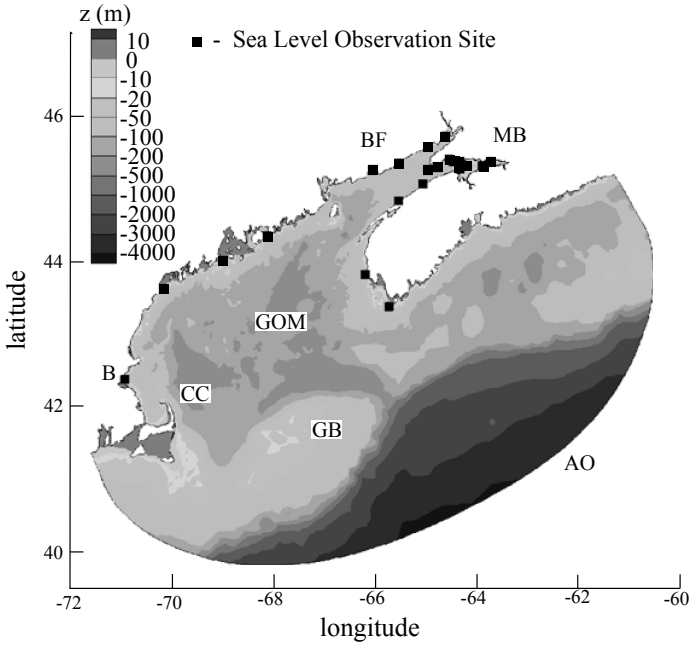

Figure 3.10: Bathymetry for the Bay of Fundy region. AO - Atlantic ocean; GOM - Gulf of Maine; BF - Bay of Fundy; MB - Minas Basin; GB - Georges Bank; B - Boston; CC - Cape Cod

grid), the velocity and turbulence quantities were set using the same interpolation methods as for the inlet. For cases where there was no inflow through the boundary (all outflow) the *opening for entrainment* option was used with zero relative pressure and zero-gradient conditions for k and ϵ.

3. *Bottom:* Along the bottom boundary, the shear stress was specified using a linear interpolation of face-centred values from the basin-scale simulation. The shear stress was specified in this manner to ensure consistency between the two models.

4. *Top:* The top boundary used a *rigid lid* approximation, with a constant-height, free-slip wall. The height of the boundary was set based on the basin-scale model prediction at the domain centre. Note that since the water surface height is different at different phases of the tidal cycle, the present methodology requires a different mesh for each phase being simulated. Additionally, a new mesh is also required for each iteration of the overall tuning loop (see figure 3.1) since the surface height may change with each iteration.

5. *Outlet:* A pressure outlet with zero relative pressure was used.

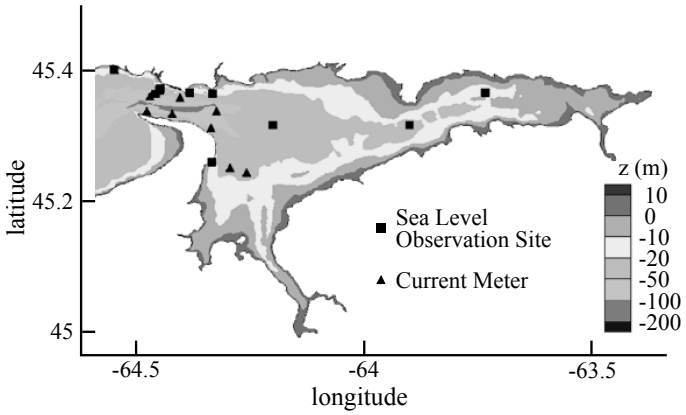

Figure 3.11: Bathymetry for the Minas Basin

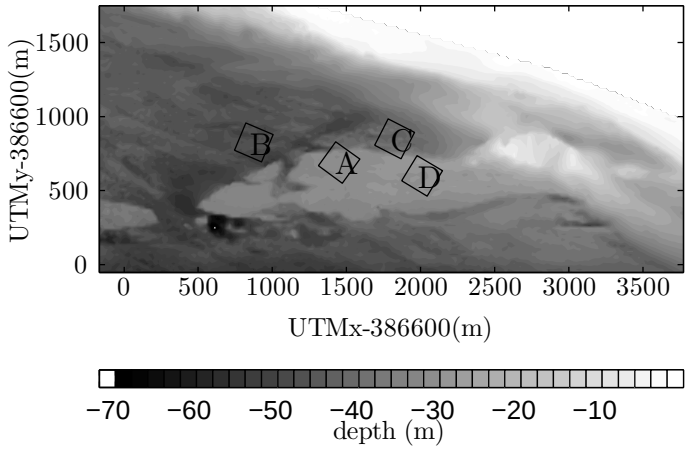

Figure 3.12: Bathymetry for the region around the test berths

It is of interest to note that due to the spatial interpolations employed, the inflow conditions specified at the domain boundaries were not guaranteed to be perfectly compatible with the RANS equations. It was found that the iterative convergence of residual values was affected by this near the inflow boundaries. Thus, iterative convergence was assessed by observing trends in velocity at several points within the domain (concentrated in the wake of the turbine). In post-processing, the rms and max residuals were verified within a region offset by 20m from the inflow conditions. It was verified that the rms residuals converged by 6 orders within this region. The values of $C_T^\star$ and $C_P^\star$ were then calculated from the converged flowfield.

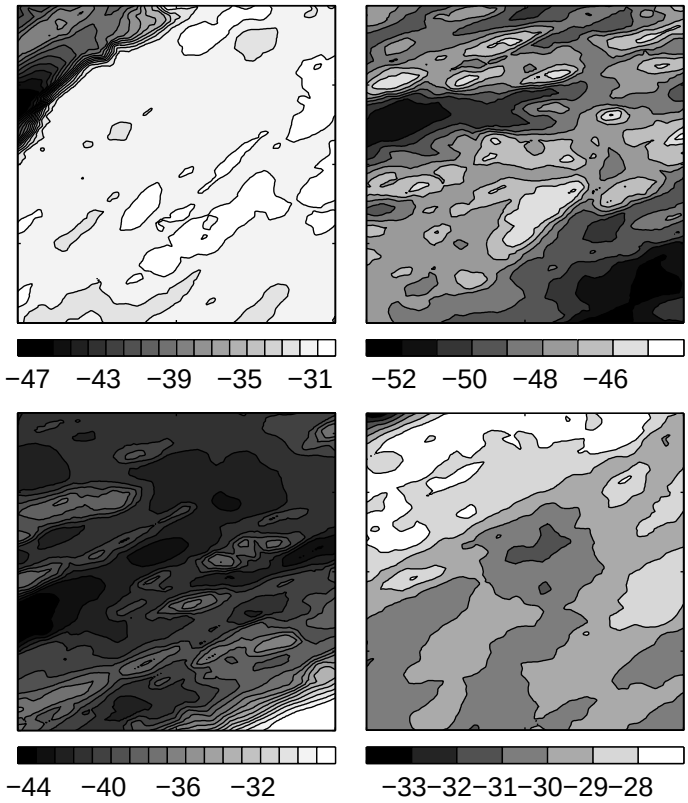

Figure 3.13: Bathymetry for the 200×200 m CFD subdomains (x aligned with flow direction at peak flood). Berth A (top left), B (top right); C (bottom left); D (bottom right). Depths are in meters relative to chart datum (approx 6m below MSL)

3.7.3 Basin-Scale Simulations

The grid was constructed from unstructured triangles that varied in edge length from 12 km on the open boundary to 40 m at the berth sites. In total, there were 69 583 vertices and 135 101 triangular elements in the horizontal. Two types of simulations were run; depth-averaged (2D); and 3D flow resolved using 24 terrain-following layers. The layer spacing was refined near the bottom to resolve the boundary layer. On a desktop computer, the model ran 60 times faster (2D) and 15 times faster (3D) than simulated time. The domain extended down to Cape Cod and far offshore. The flow was driven by the M2 tidal forcing.

Initially the basin model was run with approximate turbine parameter values to provide boundary conditions to the CFD model. The CFD model was then used to recalculate the turbine parameters. The basin model was then re-run with the updated turbine parameters. The CFD simulation was then re-run and the output

$C_T^\star$ and $C_P^\star$ were checked against the previous run to determine if further iteration was necessary. For all berths, a single iteration was sufficient to achieve converged results for $C_T^\star$ and $C_P^\star$.

3.7.4 Model Results

As with the simple channel tests, the consistency between the CFD and basin-scale power estimates was of key concern. It was found that with the increased complexity of the flows, there was a greater discrepancy in $\vec{u}_{\mathrm{AV}}$. Table 3.1 summarizes the turbine performance parameters and power output from CFD and basin-scale simulations.

The FORCE test site scenario tested here is a significantly more complex problem, however the power predictions remain consistent within 16% for 2D simulations and within 26% for the 3D simulations for each considered berth location. Note that since the power is proportional to the cube of the velocity, even small discrepancies in the averaged velocity lead to large discrepancies in power. The CFD models are driven with boundary conditions derived from the basin model, but even within the small sub-domain the models are resolving the flow differently. This is most pronounced for the 3D simulation of Berth A, where most of the sub-domain sits on a ledge of about 32 m depth. But in the north portion of the domain the bottom falls down to about 50 m depth. Current speed is highly variable within the sub-domain; even when simulated without the presence of a turbine there is an estimated 10 $^{\mathrm{cm}}/_{\mathrm{s}}$ difference in flow speed across the face of the averaging volume. The different resolutions and physics between the models result in different estimates of the flow field and therefore different estimates of velocity and power at the turbine.

Testing with a range of inlet conditions has shown the turbine parameters $C_T^\star$ and $C_P^\star$ to be quite stable. This suggests that any discrepancy in the flow field between the CFD and basin model will have little impact on the values of $C_T^\star$ and $C_P^\star$. The turbine power is much more sensitive to the current speed. The difference in power estimates comes down to the consistency of the velocity estimates of each model.

3.8 Conclusions

This paper has presented a methodology for representing turbines in basin-scale simulations based on performance metrics obtained from CFD simulation results. A major challenge for such modelling is choosing how to parameterize the turbine per-

formance. The standard thrust and power coefficients are of little value since it is not possible to define a freestream velocity for such flows. This paper proposes using a volume-averaged velocity $\vec{u}_{\mathrm{AV}}$ taken from a region large enough that CFD and basin-scale simulations give a consistent value of $\vec{u}_{\mathrm{AV}}$. The thrust and power are then normalized using this average velocity.

Simple channel scenarios showed fairly good agreement for power (within 7% or less) when the averaging volume is a cube with side-lengths roughly twice the turbine diameter. Using larger volumes resulted in better consistency for the simple cases.

The complex Minas Passage cases were more challenging and good consistency was not achieved in general. Two dimensional basin-scale simulations produced peak-flood power consistent within about 16% to CFD simulations.

An advantage of the volume-averaging method is that it allows the CFD model to do what it does best in modelling the small-scale flow accurately, and allows the ocean model to do what it does best in efficiently modelling the large-scale flows. For given power conditions, the coefficients $C_T^\star$ and $C_P^\star$ are relatively constant over a range of current speeds so that the method is robust.

To achieve agreement in power estimates between the basin-scale and CFD models in complex scenarios such as this, further work is required. Possible improvements may be achieved by making the formulation for bottom friction consistent between the models, modifying the turbulence closures to be more consistent or to include free surface effects in the CFD model. As it stands, the methodology is adequate for rough power predictions, but greater confidence would be gained with better consistency to CFD results for power.

The results presented here highlight the difficulty in modelling tidal turbines in-situ. It is relatively easy to perform simulations of idealized flows, but real tidal flows are vastly more complex. It may be that a tighter coupling between basin-scale models and CFD scale models is required, where the two models are solved simultaneously with shared boundaries. This approach is currently being considered at the University of Victoria.

Acknowledgment

The authors thank the Offshore Energy Research Association of Nova Scotia (OERA) for financial support.

Berth	$\hat{L}_{\mathbf{AV}}$	$\hat{H}_{\mathbf{AV}}$	$C_T^\star$	$C_P^\star$	$P_{\mathbf{cfd}}$	$P_{\mathbf{basin}}$	% diff
A	2.5	>2	1.031	0.767	990	1117	13%
B	4.7	>2	0.988	0.727	1501	1266	-16%
C	4.7	>2	1.002	0.739	1424	1284	-10%
D	2.5	>2	1.020	0.761	1350	1397	3%
A	2.5	2	1.080	0.822	990	1249	26%
B	4.7	2	0.995	0.734	1501	1220	-19%
C	4.7	2	0.981	0.716	1424	1249	-12%
D	2.5	2	1.072	0.821	1350	1456	8%

Table 3.1: CFD and basin-scale power (kW) at peak flood

Chapter 4

Adapted Two-Equation Turbulence Closures for Actuator Disk RANS Simulations of Wind & Tidal Turbine Wakes

This paper has been published as:

Shives, Michael; and Crawford, Curran: *"Adapted two-equation turbulence closures for actuator disk RANS simulations of wind & tidal turbine wakes,"* Renewable Energy 92 (2016) 273-292 DOI: 10.1016/j.renene.2016.02.026.

This paper validates actuator-disk simulations using blade-element theory for their ability to predict wake velocity and turbulence profiles. Such simulations require modifications to standard turbulence treatments, and herein it is found that the SST eddy viscosity limiter is sufficient. The paper also presents a novel model to introduce turbulent energy in the wake to account for tip-vortex breakdown.

Abstract

Reliable methods for modelling wake recovery within a farm of wind or tidal turbines are critical for obtaining accurate estimates of annual energy production, and for detailed farm layout optimization. These are important objectives for maximizing energy yield while minimizing costs. Computational fluid dynamics (CFD) simulation

is rapidly being adopted as a tool for flow modelling in wind and tidal farms, gaining favour over more traditional and simpler empirically-determined wake models. The most practical methodology for CFD simulations of turbine farms uses an actuator disk (AD) representation for each rotor, which imposes the rotor forces by adding source terms to the governing equations rather than explicitly resolving the flow over the turbine blades. It is well understood that when using the AD approach, standard turbulence models tend to predict faster wake recovery than is observed in real flows. Thus, the standard CFD turbulence models must be adapted for use with the AD methodology. Additionally, because of the manner in which the AD approach distributes the rotor forces, it cannot resolve the system of discrete vortices trailed from the blade tips.

This article presents two contributions to improving AD simulations of wind/tidal turbine wakes. The first is identifying that the well-established k-ω SST turbulence model is appropriate for AD simulations because it mitigates the problem of over-predicting the initial wake recovery rate. The second contribution is a method to include the typically un-modelled production of turbulent kinetic energy due to the breakdown of trailed vortices. This method was tuned to minimize the wake error for three experimental test cases with different rotors and different ambient turbulence intensities $\{3,10,15\}\%$. The new model was validated and compared to existing turbulence methods for the wake of a second rotor in a tandem array configuration with different separation distances and ambient turbulence intensities. The different models were assessed using an error metric designed to estimate the error in predicting the power production of a turbine array. The reduction of this error by the new model varied from case to case, but was on the order of 3.5-10%, compared to the standard k-ε model.

4.1 Introduction

This article explores turbulence modelling options for Reynolds-averaged Navier Stokes (RANS) simulations of wind or tidal turbine farms. For simulating an entire turbine farm, it is not computationally feasible to explicitly model each rotor geometry, so the influence of the rotor on the flow is often represented by adding momentum source terms to the governing equations. As summarized by [46, 47], there are several approaches to how the source terms are distributed within the flow domain. The actuator-line (AL) approach concentrates the blade forces near the turbine blades

and requires time-resolved simulations. The actuator-disk (AD) approach applies time-averaged forces over the swept area, allowing for steady-state simulations and reducing computational expense.

For turbine farm simulations the AD approach strikes a reasonable balance between accuracy and computation cost. This method is well established and predicts turbine performance with high accuracy for isolated rotors (e.g. [48]) and for rotors in flume tanks with high blockage [49]. However, a problem with the AD approach is that when using standard turbulence models, the wake recovers too quickly and hence interactions with downstream rotors are not well predicted. The primary problem is that the eddy viscosity is over estimated in the high-shear flow near the actuator disk region, resulting in overly fast mixing of the wake. Despite this, the AD approach remains a popular option due to its low cost and relative ease of implementation.

Several studies, reviewed in §4.2, have presented turbulence model modifications to improve wake recovery predictions by limiting the eddy viscosity. In this article, the eddy viscosity limiter of the two-equation SST turbulence model [32] is shown to provide good initial wake recovery predictions.

A secondary shortcoming of the AD approach is that it does not resolve the helical vortex system in the wake. A real wake is composed of a discrete system of vortices trailed from the blades, with the strongest vortices coming from the blade tips. The vortices are coherent immediately downstream of the rotor, but quickly become unstable and decay into small-scale turbulence. The timescale for this decay process is fastest when the ambient flow is highly turbulent. Since the vortices are not resolved in the AD method, it cannot resolve the production of turbulence resulting from the breakdown process. Therefore, this production must be modelled to obtain good predictions of wake turbulence. This article presents a model to account for this production which improved the match to experimental profiles of velocity and turbulence intensity.

4.2 Literature Review

Many studies dating back to 1985 [50, 51, 52, 53, 54, 55, 56, 57, 58, 59] have noted that the AD approach, combined with either the k-ε [60] or the k-ω [61] turbulence closure, overestimates the initial recovery rate by a wide margin. With both of these two-equation closures the primary interaction between the momentum equations and turbulence model is through the eddy viscosity μ_t. Thus the primary goal of the

turbulence model is to accurately predict μ_t.

There have been many studies presenting modified turbulence closures to improve wake recovery predictions. Most have employed a limited set of field experiments at small wind-farms for validation. Field experiments of the following turbines/farms have been employed: the NASA/DOE Mod-0A 100 kW turbine [62]; the Nibe A and B turbines [63, 64]; four Danwin 180 kW turbines [65]; eighteen 310 kW turbines at the Sexbierum farm [66]; five 2.5 MW turbines at the ECN test farm [67]; and three turbines at the Risø campus of DTU [59].

Based on such field data, researchers have proposed model modifications for neutrally- and stably-stratified atmospheric boundary layers (ABL). Crespo [50] initially proposed changing the constants of the k-ε model for consistency with a neutrally-stratified ABL. Building on Crespo's suggestion, El Kasmi and Masson [51] further introduced a source term in the ε equation, applied in a region near the turbine rotor, to represent the enhanced transfer of turbulent energy from large scales to small scales caused by the presence of the rotor. The source acts to reduce μ_t near the rotor, slowing the initial wake recovery, and greatly improved results for the Mod-0A and Nibe field studies compared to Crespo's formulation. For convenience, the model introduced by El Kasmi and Masson [51] is herein referred to as the k-ε+S_ε model.

Rados *et al.* [53] adapted El Kasmi's correction for use in Wilcox's k-ω model [61] and compared to results for stably-stratified conditions using ECN field-data, with reasonable wake profiles at 2.5D and 3.5D downstream of the rotors. Cabezon *et al.* [52] tested both the k-ϵ+S_ϵ model and a seven-equation Reynolds-stress model, comparing to data from the Sexbeirum experiment for neutral stratification. Both models overestimated the velocity in the near wake, but the far wake was reasonably predicted. The turbulence intensity was grossly under predicted in the near wake, however.

In very detailed studies, Réthoré *et al.* [54] and Réthoré [55] compared several modified two-equation turbulence closures to the Nibe and Sexbierum experiments, and to high fidelity LES simulations. The modified closures included: the k-ε+S_ε model; an eddy-viscosity limiter accounting for adverse pressure gradients; an eddy-viscosity limiter based on *realizability* constraints; and a model adapted from forest canopy modelling. Réthoré remained unsatisfied with all of these modifications. He noted that the k-ε+S_ε model produced an unphysical increase in ε near the rotor, which persisted downstream. He found that the realizability-based eddy viscosity limiter was the most theoretically sound, but did not produce sufficient change from

the original k-ε model to give a good match to experiments.

Continuing from the work of Rados *et al.* [53], Prospathopoulos *et al.* [56] tested several modifications to Wilcox's k-ω model including (among others) El Kasmi's modification (adapted for k-ω) and a μ_t limiter based on Durbin's [68] realizability constraint for stagnation-point aerodynamics. El Kasmi's model required very different tunings for the Sexbierum and Nibe experiments, bringing into question its general applicability. The μ_t limiter approach was tuning-free and improved the results compared to the baseline (Wilcox) k-ω model, but did not achieve the same fidelity as El Kasmi's approach. Because of its better generality, Prospathopoulos *et al.* [56] recommended the μ_t limiter method for future studies.

Very recently, van der Laan *et al.* [69] tested a number of non-linear eddy viscosity models, which improved model predictions but unfortunately degraded the stability of the numerical solvers employed. Van der Laan *et al.* [59] presented a reduced-order version of a non-linear eddy viscosity model called the k-ε-f_P model; which accounts for non-equilibrium turbulence (*i.e.* local production and dissipation rates not in balance) by limiting μ_t in regions of high strain rate. This reduces the initial wake recovery rate similar to the k-ε+S_ε model, but without artificially increasing the dissipation rate. The k-ε-f_P model compared very well to detailed large-eddy-simulation (LES) results, and gave reasonable agreement to velocity profiles from the ECN, Nibe, and DTU experiments.

In summary, many modifications have been proposed to improve simulation fidelity of two-equation turbulence models. The most widely tested is the k-ε+S_ε model of El Kasmi and Masson [51], which has shown reasonable fidelity for a wide variety of cases. However as noted by [56] and [55], El Kasmi's approach requires different tuning coefficients for different experimental cases. Its addition of ε near the rotor has been shown to be non-physical [55, 58]. It achieves a good match to the near-wake velocity by artificially increasing ε, which causes the wake turbulence to decay too quickly, thus resulting in too slow recovery further downstream. Despite these deficiencies it has achieved the best fidelity in matching field data so far. Most of the more recently proposed modifications involve limiting the eddy viscosity in regions of high mean strain. Proposed forms of this general strategy are based on: Durbin's limiter [56]; realizability constraints [55]; and non-equilibrium turbulence [59].

Higher-fidelity turbulence models such as LES and detached-eddy-simulation (DES) are now emerging as options for turbine-farm simulations. Recently, Troldborg *et*

al. [70] used DES with actuator-disk, actuator-line and blade-resolved rotor representations. They showed good agreement between the three rotor representations, concluding that the actuator-disk is sufficiently accurate for wind-farm simulations. While this is a promising result, the high cost of DES simulations means that RANS simulations remain attractive for farm layout configuration and energy assessment studies. It is likely that such higher-fidelity turbulence models could be used to inform the development of future modifications to two-equation turbulence closures for RANS simulations.

4.3 Tuning and Validation Data

This study used experimental data from two experimental campaigns. One involved three rotors in a side-by-side configuration and was carried out at Manchester University. The other involved two rotors in tandem (one directly downstream of the other) and was carred out at the French Research Institute for Exploitation of the Sea (IFREMER). This section summarizes the experimental data from both.

The velocity field was characterized using Reynolds decomposition. The total velocity u_i is the sum of a mean $\overline{u}_i$ and fluctuating u_i' component. The subscript $i = \{1, 2, 3\}$ refers to the three velocity component directions, with $i = 1$ corresponding to the streamwise direction (x), $i = 2$ to the transverse (y), and $i = 3$ to the vertical (z). Turbulence was characterized by the turbulent kinetic energy:

$$k = \frac{1}{2} \sum_{i=1}^{3} \overline{u_i' u_i'} \tag{4.1}$$

A characteristic velocity u_0 was defined as the mean streamwise component ($\overline{u}_1$) measured at hub-height at the rotor location, but without the rotor or support structure in the flume. This is commonly called the *freestream* velocity. As a convention for the present paper, velocity and k measured in the wake were both normalized by u_0. For velocity, this is presented as the ratio ($\overline{u}_i/u_0$). Turbulent energy k was normalized to provide intensity I:

$$I = \frac{\sqrt{\frac{2}{3}k}}{u_0} \tag{4.2}$$

4.3.1 Manchester Side-by-Side Rotor Data

The Manchester University data [71, 72, 73][1] were measured in a flume test section 5 m wide by 12 m long, filled to a depth of 0.45 m. Experiments were done with several arrays of identical rotors of diameter D=0.27 m (1/70 of full scale). The rotor blades were designed to produce similar loading (thrust and torque) as a full-scale turbine, despite operating at much lower Reynolds numbers (Re) [71]. This was done using an airfoil suited to low Re (Goettingen 804) rather than geometric downscaling.

Experiments were done with a single rotor, as well as three identical rotors placed side-by-side with a centre-to-centre spacing of 1.5D. The rotors were located 6 m downstream of the test section inlet. Each rotor was coupled to a dynamometer for measuring torque. The nacelle (35 mm diameter) was supported by a 15 mm diameter tower which was strain gauged above the water surface for measuring thrust.

All three velocity comonents u_i were measured at 200 Hz using NORTEK Vectrino+ probes, allowing the calculation of Reynolds-averaged velocities $\overline{u}_i$ and turbulence statistics $\overline{u_i' u_j'}$.

The flow in the empty flume was first measured. There was some variation of $\overline{u}_1$ with transverse position (y), seen as scatter in figure 4.1, attributed to regions of transverse circulation ($u_2 \approx 0.05 u_0$), but not expected to affect wake recovery [73]. The reference velocity u_0 was 0.47 m/s. The depth-averaged turbulence intensity I in the empty flume was $I \approx 10\%$ at the rotor location, decaying to $\approx 8\%$ 3 m further downstream.

With rotors present, the wake(s) were traversed in both vertical and transverse directions, at streamwise positions x/D={2,4,6,8,10,12} downstream of the rotor.

The Re based on rotor diameter was $\mathrm{Re_D} \approx 1.2 \times 10^5$. In experiments with similar turbulence intensity, Chamorro *et al.* [75] identified that wake velocities became Re-independent above $\mathrm{Re_D} \approx 4.8 \times 10^4$, and higher-order turbulent statistics above $\mathrm{Re_d} \approx 9.3 \times 10^4$. Thus the experimental wake results should be applicable to full-scale rotors.

4.3.2 IFREMER Tandem Rotor Data

The IFREMER data [76, 77] were collected in flume with a test section 18 m long, 2 m wide, filled to 1 m depth. Experiments were carried out with a single rotor, and

[1] A more recent article [74] detailing the wake of a single rotor was also published after the present article was submitted for review.

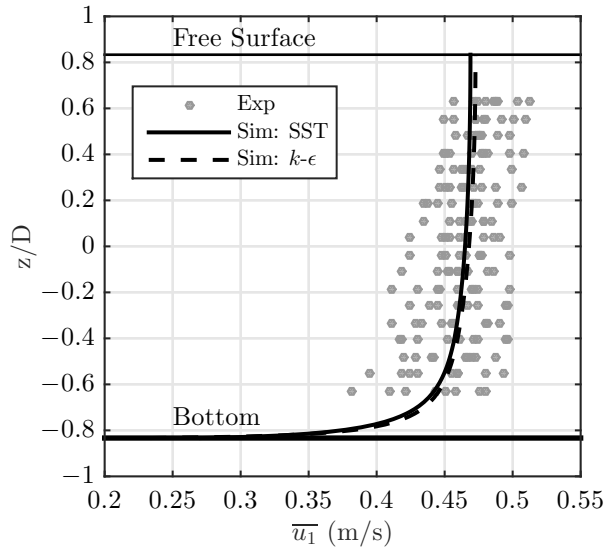

Figure 4.1: Vertical profile of the streamwise velocity $\overline{u_1}$ in the empty Manchester flume, at the rotor location. Experimental data are shown for lateral positions spanning ±5D (±1.35 m) from the flume centreline.

with two rotors in tandem separated by distances x/D=$\{$2,3,4,6,8,10,12$\}$. The rotors were placed at mid-depth. Experiments were done with I_0=$\{$3%,15%$\}$, and with u_0 ranging from 0.4 to 1.0 m/s. The high turbulence was generated by removing the flow conditioning honeycombs from the flume.

The rotor diameter was D=0.7 m. The diameters of the supporting tower and hub were $\{0.08, 0.092\}$m. The blades were geometrically downscaled from a full rotor using a NACA 63-418 airfoil. At 3/4 of the blade span, the chord-based Reynolds number Re_c ranged from 9.3×10^4 to 4.5×10^5 depending on tip-speed ratio and freestream velocity. This is a range where airfoil performance is typically Re dependent. Indeed, the rotor performance depended strongly on u_0 and I_0 (see figs 6 and 7 of [76]).

The rotor was driven by a speed-controlled motor, and the mechanical torque was measured by a sensor located between the rotor and motor. A six component load cell located above the water surface measured the total axial load acting on the rotor and its supporting structures.

Wake data were collected for two different flow conditions: (u_0=0.8, I_0=3%) and (u_0=0.83, I_0=15%). Velocities u_i (i=$\{$1,2$\}$) were measured using a traversing Laser Doppler Velocimeter (LDV), ensuring stable statistics for mean velocities ($\overline{u}_1$,$\overline{u}_2$) and Reynolds stresses ($\overline{u_1'u_1'}$, $\overline{u_1'u_2'}$, $\overline{u_2'u_2'}$) had converged [76, 77].

Since the vertical velocity (u_3) was not measured, $\overline{u_3'u_3'}$ had to be assumed when calculating k and I, for comparing to simulations. From the Manchester data set, it was possible to observe the ratios;

$$\gamma_{31} = \frac{\overline{(u_3'u_3')}}{\overline{(u_1'u_1')}}, \quad \gamma_{32} = \frac{\overline{(u_3'u_3')}}{\overline{(u_2'u_2')}} \tag{4.3}$$

from both vertical and transverse wake transects. This provided γ_{31}=1.08 $\pm$ 0.10 (standard deviation) and γ_{21}=0.85$\pm$0.09. Thus, for the IFREMER data, an estimate of $\overline{(u_3'u_3')}$ was made using;

$$\overline{(u_3'u_3')} = \frac{1}{2}\left(\gamma_{31}\overline{(u_1'u_1')} + \gamma_{32}\overline{(u_2'u_2')}\right) \tag{4.4}$$

4.4 Governing Equations

4.4.1 RANS Equations

The steady, incompressible Reynolds-averaged Navier Stokes (RANS) equations were used for all simulations, shown below using tensor notation:

$$\frac{\partial \overline{u}_i}{\partial x_i} = 0 \tag{4.5}$$

$$\overline{u}_j \frac{\partial \overline{u}_i}{\partial x_j} = \frac{\partial}{\partial x_j}\left[-\frac{\overline{p}\delta_{ij}}{\rho} + 2\nu S_{ij} - \overline{u_i' u_j'}\right] + \frac{\overline{S_{Mi}}}{\rho} \tag{4.6}$$

where p is the pressure, x_i is the spatial co-ordinate, ν is the fluid kinematic viscosity and ρ is the density. The Dirac function, δ_{ij}=1 for i=j and equals zero otherwise. $\overline{S_{Mi}}$ is a Reynolds-averaged momentum-source term, used to impose the rotor forces on the flow. The term S_{ij} is the mean rate-of-strain tensor:

$$S_{ij} = \frac{1}{2}\left(\frac{\partial \overline{u}_i}{\partial x_j} + \frac{\partial \overline{u}_j}{\partial x_i}\right) \tag{4.7}$$

The Reynolds averaging process introduces Reynolds stresses $\overline{u_i' u_j'}$ into the Navier-Stokes equations [27], which are modelled using a turbulence closure model. The most widely used turbulence closures relate the Reynolds stresses to the mean velocity gradients using the Boussinesq hypothesis:[2]

$$-\overline{u_i' u_j'} = 2\frac{\mu_t}{\rho} S_{ij} - \frac{2}{3}\left(k + \frac{\mu_t}{\rho}\frac{\partial \overline{u}_k}{\partial x_k}\right)\delta_{ij} \tag{4.8}$$

where μ_t is the eddy viscosity and k is the turbulent kinetic energy. The primary interaction between the turbulence model and the momemtum equations is through the eddy viscosity μ_t. The Boussinesq hypothesis assumes that μ_t is an isotropic scalar, which is not strictly true but allows solving only two turbulence-related transport equations, one for k and another for either ε or ω.

[2]To avoid using the Boussinesq hypothesis requires solving additional transport equations for each Reynolds stress (known as *Reynolds-stress* or *second moment closure* models), or solving for each Reynolds stress algebraically. Both options increase computational cost and degrade solution stability, and it is thought that errors associated with the Boussinesq hypothesis are acceptable, to maintain robust and fast simulations.

4.4.2 k-ε Turbulence Closure

The most widely used turbulence model is the standard k-ε model by Launder and Spalding [60]. Assuming steady incompressible flow without buoyancy, the model solves the following transport equations for k and ε:

$$\frac{\partial \rho k \overline{u}_j}{\partial x_j} = \frac{\partial}{\partial x_j}\left[\left(\mu + \frac{\mu_t}{\sigma_k}\right)\frac{\partial k}{\partial x_j}\right] + P_k - \rho\varepsilon + S_k \tag{4.9}$$

$$\frac{\partial \rho \varepsilon \overline{u}_j}{\partial x_j} = \frac{\partial}{\partial x_j}\left[\left(\mu + \frac{\mu_t}{\sigma_\varepsilon}\right)\frac{\partial \varepsilon}{\partial x_j}\right] + C_{1\varepsilon}\frac{\varepsilon P_k}{k} - C_{2\varepsilon}\rho\frac{\varepsilon^2}{k} + S_\varepsilon \tag{4.10}$$

where σ_k=1.0, σ_ε=1.3, $C_{1,\varepsilon}$=1.44 and $C_{2\varepsilon}$=1.92 are the standard model constants. S_k and S_ε are additional source terms set to zero in the standard model. The eddy viscosity μ_t and production term P_k (production of k from mean velocity gradients) are calculated using:[3]

$$\mu_t = C_\mu \rho \frac{k^2}{\varepsilon} \tag{4.11}$$

$$P_k = \mu_t 2 S_{ij} S_{ij} \tag{4.12}$$

with the standard constant being $C_\mu = 0.09$.

The k-ε+S_ε model, introduced by El Kasmi and Masson [51], adds a source term to the ε equation in a region surrounding the rotor, which is of equal diameter to the rotor and extends ±0.25D (arbitrarily set by [51]) up/downstream. Physically, this source "represents the energy transfer rate from large-scale turbulence to small-scale turbulence controlled by the production range scale and the dissipation rate time scale"[51].

$$S_\varepsilon = C_{4\varepsilon}\frac{P_k^2}{\rho k} \tag{4.13}$$

with the coefficient $C_{4\varepsilon}$ tuned to a value of 0.37 by [51].

The more recent k-ε-f_P model by van der Laan *et al.* [59] is also noteworthy and has shown very promising results. Initially, the present study intended to test the k-ε-f_P model, however while attempting to model the empty water-tunnel, it was found to significantly increase the decay-rate of turbulent kinetic energy compared to the current experimental results.[4] Since the model did not match the ambient flume-tank

[3]The tensor product $2S_{ij}S_{ij}$ evaluates to $2\frac{\partial \overline{u}}{\partial x}^2 + 2\frac{\partial \overline{v}}{\partial y}^2 + 2\frac{\partial \overline{w}}{\partial z}^2 + \left(\frac{\partial \overline{u}}{\partial y} + \frac{\partial \overline{v}}{\partial x}\right)^2 + \left(\frac{\partial \overline{v}}{\partial z} + \frac{\partial \overline{w}}{\partial y}\right)^2 + \left(\frac{\partial \overline{w}}{\partial x} + \frac{\partial \overline{u}}{\partial z}\right)^2$

[4]This discrepancy may be due to using standard model coefficients in this study compared to coefficients tuned for a neutral ABL as done in [59].

flow, it was not tested further. It may be possible to modify $C_{1\varepsilon}$ to alter the decay rate, however it was felt that the present dataset was not sufficient to validate such a change.

4.4.3 k-ω Turbulence Closure

Instead of solving a transport equation for the dissipation rate ε, it is possible to solve one for the specific dissipation rate, defined as $\omega = \beta'\varepsilon/k$.[5] The standard k-ω model is given by Wilcox [61]:

$$\frac{\partial \rho k \overline{u}_j}{\partial x_j} = \frac{\partial}{\partial x_j}\left[\left(\mu + \frac{\mu_t}{\sigma_k}\right)\frac{\partial k}{\partial x_j}\right] + P_k - \beta'\rho k\omega + S_k \tag{4.14}$$

$$\frac{\partial \rho \omega \overline{u}_j}{\partial x_j} = \frac{\partial}{\partial x_j}\left[\left(\mu + \frac{\mu_t}{\sigma_\omega}\right)\frac{\partial \omega}{\partial x_j}\right] + \alpha\frac{\omega P_k}{k} - \beta\rho\omega^2 + S_\omega \tag{4.15}$$

with the standard coefficients: β'=0.09, σ_k=2, σ_ω=2, α=5/9, β=0.075. This formulation is preferable for modelling the sublayer in boundary layers, avoids the requirement for complex damping functions used by the ε model for near-wall flows, and is superior for flows with streamwise pressure gradients [78]. The Boussinesq hypothesis (eq. 6.7) is used to find the Reynolds stresses, with μ_t defined by:

$$\mu_t = \rho\frac{k}{\omega} \tag{4.16}$$

Attempting to improve turbine wake predictions, Prospathopoulos *et al.* [56] tested several modifications to the k-ω model, and recommended Durbin's eddy-viscosity limiter for future work because it is tuning-free and improved the model predictions. Durbin's limiter was derived for stagnation point aerodynamics, and following [56] can be written as:

$$\mu_t = \frac{\rho k}{\max\left(\omega, \sqrt{3}\sqrt{2S_{ij}S_{ij}}\right)} \tag{4.17}$$

4.4.4 The Hybrid SST Turbulence Closure

Menter [79] noted that the eddy viscosity formulation in the k-ω model leads to an unacceptable sensitivity to the prescribed value of ω for turbulence-free freestream

[5] As described in [61] ω has several different interpretations including "frequency characteristic of the turbulence decay", or "RMS fluctuating vorticity".

boundaries.[6] Taking a pragmatic empirical approach, Menter [28] developed a hybrid model which uses the k-ω formulation for the near-wall and logarithmic regions, with a smooth transition to a k-ε formulation for the outer-region of the boundary-layer and for freestream flows. The transition uses a blending function F_1, with three terms to decide which model to use (see [28] for details). For the flows considered herein, the most important term is the ratio of the turbulent length scale ($\frac{\sqrt{k}}{\beta'\omega}$) to the distance to the nearest wall boundary (y), which is large near walls and approaches zero moving away from the wall, at a rate depending on the length scales in the flow.

The flume tank flows studied herein are similar to full scale wind/tidal turbine farms, in that the rotors were located within the log-layer of the surface/bottom boundary layer. When applied to the empty flume-tank flows studied herein, the length scales in the CFD simulations were large enough such that the k-ω formulation was used throughout the entire test section (in other words, the log-layer extended up to the water free-surface [7]). With rotors present, the k-ε formulation became active only in the wake region behind the turbines because of the reduced length scales associated with increased dissipation rates.

As with all two-equation closures, Menter's hybrid model does not explicitly solve the transport of turbulent shear stresses ($\overline{u_i' u_j'}$, $i \neq j$), which is known to be important for adverse-pressure-gradient and separating flows. As discussed by [28], two equation turbulence models tend to over predict the eddy viscosity in adverse-pressure-gradient flows where the production of k can be significantly larger than the dissipation rate. To overcome this deficiency, Menter [32] presented an alternative eddy viscosity formulation:[8]

$$\mu_t = \frac{a_1 \rho k}{\max\left(a_1 \omega, F_2 \sqrt{2 S_{ij} S_{ij}}\right)} \tag{4.18}$$

which limits the eddy viscosity in regions with high turbulence production. The term F_2 is a second blending function which also depends primarily on ($\frac{\sqrt{k}}{\beta'\omega y}$) as discussed above. F_2 restricts the limiter to the logarithmic or viscous sublayer regions of boundary layers (including the bottom boundary layer, and those developing on turbine structural components). Outside of this, equation 4.16 is recovered. There is

[6] This sensitivity may not be an issue for practical turbine-farm simulations, which will always be turbulent.

[7] This is evident for the Manchester Flume (Figure 4.1, but could not be verified for the IFREMER flume since vertical profiles were not collected for those experiments.

[8] Menter originally proposed using the 'absolute value of the vorticity' [28] in place of the term $\sqrt{2 S_{ij} S_{ij}}$. The formulation shown herein was adapted in [32] and is currently implemented in CFX [80].

an obvious similarity to Durbin's limiter, but Menter's formulation is tailored to flows with streamwise pressure gradients (applicable to flows approaching and immediately downstream of a turbine rotor) and separating flows, rather than for stagnation points. The motivation for using the SST model is that it has been extensively validated for a wide range of flows (e.g. [28, 32, 30]) and is particularly applicable to separating flows, which may be important for turbine farms in complex terrain.

4.4.5 New modification for vortex-breakdown

The present study (and others e.g. [54]) found that although the k-ε+S_ε model improved predictions of $\overline{u}_1$ in the near wake,[9] it also under predicted k. The SST model showed the same trend. This article asserts that the AD approach inherently neglects the production of k associated with the breakdown of trailed vortices, which are not represented in the simulations, but nonetheless do contribute to the production of k for real rotors. Thus, it is physically arguable to augment the production term P_k to capture this physical effect.

$$P_{k,\text{total}} = P_k(1 + \zeta_k) \tag{4.19}$$

where P_k is the shear production associated with the resolved AD flow field, and ζ_k represents the percentage augmentation of P_k arising from the unresolved vortices. This is implemented using a source term in the k equation.

$$S_k = \zeta_k P_k \tag{4.20}$$

A challenge is to allocate the magnitude and spatial limits for the augmentation term ζ_k. Since S_k is proportional to the shear production term (P_k), it is naturally strongest in the center of the shear layer (tip vortex location), and naturally decays moving radially inward or outward. Thus, it is reasonable to apply the term in a cylindrical region which extends radially beyond the actual simulated wake, and to allow the natural distribution of shear production determine exactly where S_k should be strongest. An appropriate radial limit has thus been chosen as $0<r<\sqrt{2}R$ where the $\sqrt{2}$ corresponds to the analytical solution of the wake expanding to twice the area of the rotor at the optimal performance condition [82].

Appropriate streamwise limits for applying S_k should correspond with the loca-

[9] The near wake is best defined as being upstream of the point where the shear layer from the rotor edge reaches the centerline, typically 2-5D downstream of the rotor [81].

tion of vortex breakdown, which is expected to depend primarily on the streamwise velocity, an appropriate length scale (rotor diameter D), and the influence of turbulent fluctuations in the ambient flow.[10] The streamwise limits can be defined as $\{x_0 \leq x \leq (x_0 + L_x)\}$. Thus, the augmentation model has three parameters (ζ_k,x_0,L_x), which need to be defined. These terms are expected to vary between test cases because vortex breakdown will occur faster in more turbulent flows, and some rotors will have stronger tip vortices than others. In this article (§4.8) we have developed curve fits to define these parameters over a range of inflow conditions.

4.5 Simulation Methodology

4.5.1 Software

The general purpose CFD solver ANSYS CFX 15.0 was used for all simulations. CFX uses a finite volume Navier-Stokes solver formulated in primitive variables. The advection scheme chosen for all simulations was the *high resolution* option, which is a blend between the 2^{nd} order accurate central-difference-scheme (CDS) and the 1^{st} order accurate upwind scheme, where the blend factor is determined automatically and favours the CDS scheme unless the upwind scheme is required to maintain stability. The turbulence transport equations were solved using first-order numerics which was confirmed to show negligible difference from a second-order scheme. Further details on the solver are available in the product documentation [80].

4.5.2 Rotor Forces

The blade lift and drag forces were imposed using the momentum source term $\overline{S_{\mathrm{M}i}}$ in equation 6.5. The source terms are defined on a per-unit volume basis, as spatially continuous expressions. CFX evaluates these expressions at the mesh nodes and uses linear shape functions to integrate the source over each computational element. The integrated source is then applied to each finite volume. The linear integration approach requires sufficient mesh density at the blade tips where the applied force diminishes rapidly as $r \rightarrow R$. A more sophisticated integration approach is described in [48] which allows coarser grid resolution while maintaining accurate force specification.

[10] Recent studies have begun to analyse tip-vortex breakdown using PIV[83] and LES[84]. [83] found breakdown to occurr at approximately x≈{2 to 3}D in a lab flow with I≈2%. [84] found breakdown at x≈1D with I_0=8%.

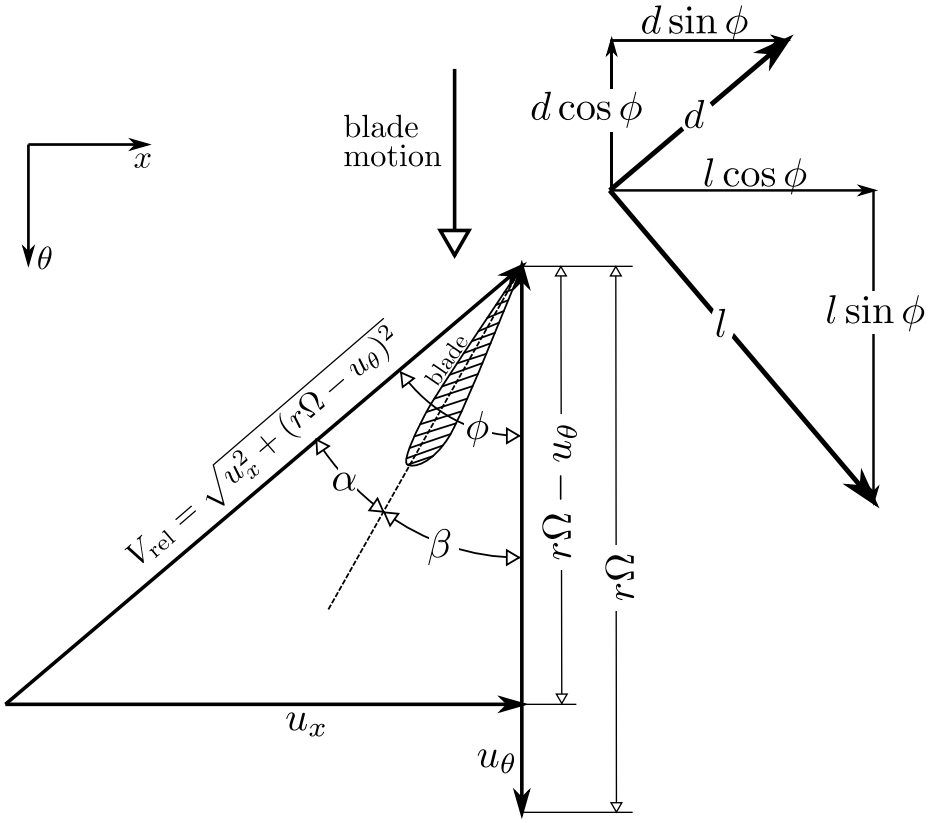

Figure 4.2: Flow velocities and forces acting on the blade. Definitions: (u_x, u_θ)-axial and tangential velocity components (azimuthally averaged), r-radial position along the blade, Ω-rotor angular speed, β-blade twist angle, α-angle-of-attack, ϕ-inflow angle, (l, d)- lift and drag (per-unit-span)

The momentum sources for each rotor were specified by using blade-element (BE) equations based-on the local flow field, a specified tip-speed-ratio (λ) and tabulated lift and drag coefficients as depicted in figure 4.2. The lift and drag coefficients for the present airfoil were taken from [85] and extended to cover the range of α from $-180°$ to $180°$ using the method described by Viterna and Corrigan [86]. The lift force acts perpendicular to the relative velocity, while the drag acts perpendicular:

$$l = \frac{1}{2}\rho V_{\text{rel}}^2 c \text{F}_{\text{tip}} c_l, \quad d = \frac{1}{2}\rho V_{\text{rel}}^2 c c_d \tag{4.21}$$

$$\text{F}_{\text{tip}} = \frac{2}{\pi}\arccos\left(\exp\left(\frac{B(R-r)}{2r\sin|\phi|}\right)\right) \tag{4.22}$$

where the term F_{tip} is the Prandtl tip-loss factor[11] (published in [82] for example).

[11]Prandtl's tip loss correction was derived considering a single turbine in an unbounded flow, and

Such correction is necessary because the AD approach does not resolve the individual blades and associated tip-vortices and thus tends to over-predict the lift near the blade tips.

The lift and drag are rotated into the rotor's cylindrical coordinate system to obtain axial and tangential force components.

$$f_x = l\cos\phi + d\sin\phi, \quad f_\theta = l\sin\phi - d\cos\phi \tag{4.23}$$

Time-averaging the blade force over a full revolution is done by assuming a constant rotational speed Ω, in a manner similar to [87]. Consider an element with finite axial thickness Δ_x spanning the actuator disk and infinitesimal dimensions $(\delta_r, \delta_\theta)$. The fraction of time that a blade spends in this element is $\delta_\theta/2\pi$. The instantaneous axial blade force in the element is $f_x\delta_r$. The time-averaged axial blade-force is $f_x\delta_r\delta_\theta/2\pi$. Then dividing by the element volume $\Delta_x\delta_r r\delta_\theta$[12] and multiplying by the number of blades B gives the source terms:

$$\overline{S_{\mathrm{M}x}} = \frac{Bf_x}{2\pi r\Delta_x}, \quad \overline{S_{\mathrm{M}\theta}} = \frac{Bf_\theta}{2\pi r\Delta_x} \tag{4.24}$$

This method determines the blade forces based on local flow conditions within each finite volume (similar to that of [48] and [70]) and therefore is applicable to non-uniform incoming flow. The total thrust T and power P can be found by numerical integration of the sources over the AD region:

$$T = \int_{\mathcal{V}} \overline{S_{\mathrm{M}x}} d\mathcal{V}, \quad P = \int_{\mathcal{V}} \overline{S_{\mathrm{M}\theta}} r d\mathcal{V} \tag{4.25}$$

Model Tuning for Low Re

The AD+BE formulation (equations 4.22 to 4.24) was able to predict the rotor performance fairly well for the Manchester rotor, as shown in figure 4.3, which also shows predictions using a blade-element-momentum (BEM) code (for unblocked conditions [74] with airfoil data [88]), and experimental data collected in the Manchester flume [74]. The performance was not well-predicted for the IFREMER rotor. The difference is that the Manchester rotor used an airfoil (Goettingen 804) suited to low Re, and

loses validity when the flow surrounding the rotor is constrained by the presence of tunnel walls, or other rotors. Presently, there is no robust analytical tip-loss correction available which is valid for such constrained flows.

[12] Note that Δ_x is the thickness of the actuator disk region, not of the mesh elements within it.

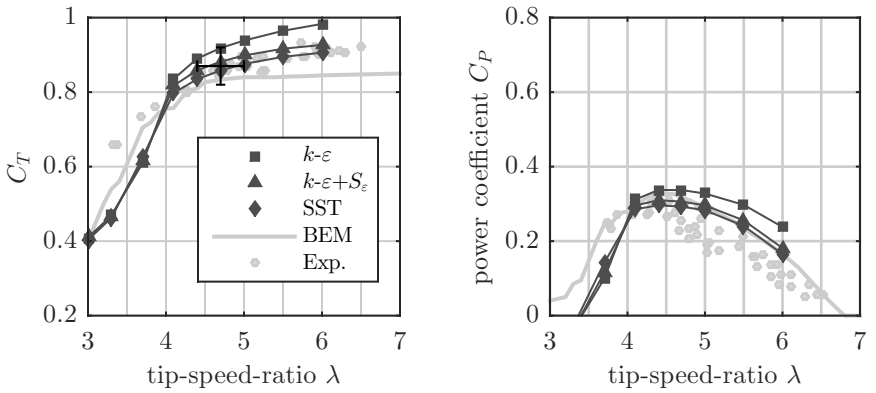

Figure 4.3: Manchester rotor performance for a single rotor in the flume. BEM prediction neglects blockage effects. For a single rotor at λ=4.7, C_T=0.87, C_P=0.30. For the three-rotor case (not shown) λ={4.75,4.80,4.75}, C_T={0.92,0.93,0.92} and C_P={0.33,0.33,0.33}.

.

for which tabulated airfoil coefficients were available [85, 88] for the range of Re used by the experiments. The IFREMER rotor used the NACA 63-418 airfoil, for which coefficients have been published only for $\mathrm{Re}_c = \{3, 6, 9\}\times10^6$ [89] (compared to 1×10^5 in the IFREMER tests) and even at these higher Re, showed significant Re dependence. Since no appropriate tabulated airfoil data are available for the IFREMER rotor, it was necessary to adapt the BE methodology to replicate the rotor thrust and torque obtained from experiments. This was done by incorporating coefficients Ax and A_θ into equations 4.24, which are automatically tuned such that T and P found using equation 6.18 match the experiments.

$$\overline{S_{\mathrm{M}x}} = \frac{A_x B f_x}{2\pi r \Delta_x}, \quad \overline{S_{\mathrm{M}\theta}} = \frac{A_\theta B f_\theta}{2\pi r \Delta_x} \tag{4.26}$$

where f_x and f_θ were found using the $\mathrm{Re}_c = 3\times10^6$ performance data of [89].

The primary goal of the present study is to evaluate turbulence modelling for wake recovery, rather than to evaluate the ability of the AD+BE method to predict turbine performance per se. Therefore tuning the rotor momentum source terms in this manner does not detract from the wake modelling assessment. The AD BE method is expected to predict rotor performance well for full-scale rotors because appropriate airfoil coefficients are more widely available.

4.5.3 Boundary Conditions

The inflow conditions were tuned to match the ambient turbulence intensity and velocity from experiments. The tuning phase used simulations of the entire flume test section with no turbines present. The bottom boundary, flume sides, and supporting structures used a smooth wall no slip condition and employed wall functions for the near wall flow. This allowed boundary layers to develop naturally along the tunnel test section. The water free surface used a rigid-lid, free-slip condition. The outlet employed a typical pressure condition (p=0).[13] Constant values for u, k and ε were set at the inlet, which were tuned to match the reported velocity profile at the location where the rotor would later be placed. The tuned velocity profile (at the rotor location) for the Manchester experiment is shown in figure 4.1. The inflow k and ε were set to match I at different downstream locations.

[13]This is suitable for modelling the flow with the rigid-lid assumption. Modelling free surface deformation would require including gravity terms, a free surface tracking method (e.g. volume-of-fluid), and specifying a hydrostatic pressure gradient at the outlet.

test case			turbulence	inlet conditions		
institution	I_0	U_0	model type	u (m/s)	k (m^2/s^2)	ε (m^2/s^3)
Manchester	3%	0.80	k-ε	0.790	7.3×10^{-4}	3.0×10^{-6}
Manchester	3%	0.80	SST	0.790	7.3×10^{-4}	3.0×10^{-6}
IFREMER	10%	0.47	k-ε	0.458	1.0×10^{-2}	3.5×10^{-4}
IFREMER	10%	0.47	SST	0.458	1.0×10^{-2}	4.5×10^{-4}
Manchester	15%	0.83	k-ε	0.822	2.8×10^{-2}	1.0×10^{-3}
Manchester	15%	0.83	SST	0.822	2.9×10^{-2}	1.1×10^{-3}

Table 4.1: Inflow parameters tuned to match empty flume tank conditions.

For the Manchester experiments, I was 10% at 6 m downstream of the inlet, and (8%) at 9 m. For the IFREMER experiments with no rotors present, $\overline{u}_1$ and I were reported at the nominal rotor location only. Tuning the inlet k and ε parameters required I at a minimum of two streamwise locations to match the dissipation rate. For a second streamwise location, I was taken from single-rotor experiments outside of the wake at 10D downstream of the rotor. It was not possible to tune the inflow conditions to perfectly match the environmental turbulence intensity for the $I_0 =$ 15% case. The intensity decayed too quickly compared to the experiments, and I was 2% too low at 12D downstream of the rotor. The tuned inflow conditions are summarized in table 4.1.

4.6 Mesh Topology and Refinement

The mesh topology was designed and tested using the Manchester rotor and data. This section pertains to the Manchester rotor, however simulations of the IFREMER rotor used the same meshing strategy.

Structured meshes were generated using ICEM CFD software. To allow estimation of discretization error, three meshes of successively higher refinement were created and are referred to by letters A (coarsest) to C (finest). The mesh topology consisted of a number 'O-grid' blocks surrounding the actuator disk sub-domains, hubs and towers. This strategy allowed for a smooth transition of the mesh geometry from the circular disk regions to the rectangular tunnel cross-section. It also maintained cell orientations orthogonal to the actuator-disks and the resulting shear layers. The mesh was designed to have refined radial grid spacing δ_r in the shear layer at the outer edge of the AD.

The supporting tower and nacelle were explicitly resolved by the mesh. For the

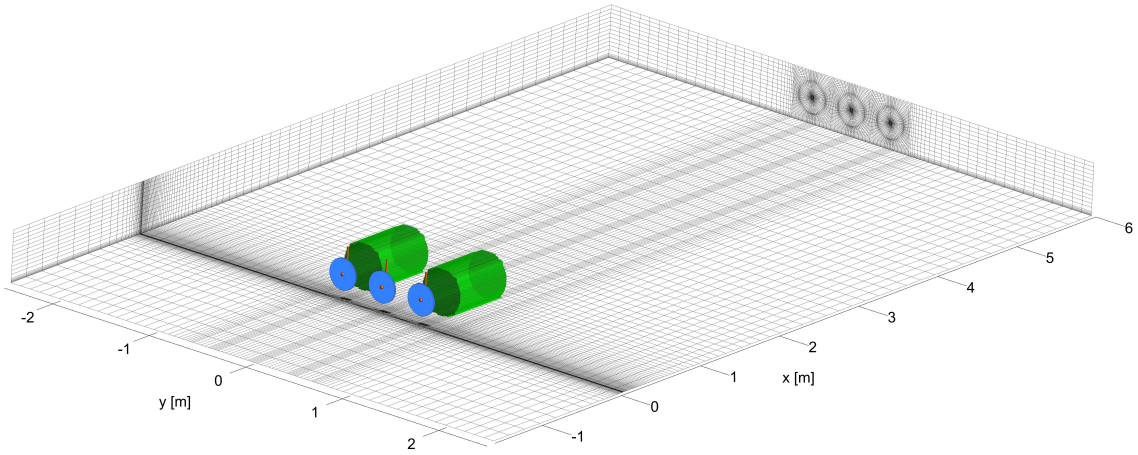

Figure 4.4: Mesh A for the region downstream of the rotors for the Manchester cases. Transparent green is used to depict regions where turbulence production was augmented (not shown behind central rotor for clarity). Note that the grid verification study only had one rotor present.

Manchester rotor, $y^+ < 150$ (mesh A), and $y^+ < 50$ (mesh C) on the support structures. For the IFREMER rotor, only mesh B was used, giving $y^+ < 200$. These y+ values are somewhat high compared to the ideal of ≈ 50 but are still considered to be within the range where wall functions are valid.

The mesh used for the Manchester cases (spacings A) is depicted in figures 4.4 and 4.6. The mesh for the IFREMER cases (spacings B) is shown in figures 4.5 and 4.6. The mesh around each AD can best be described in terms of radial, azimuthal, and streamwise directions (r, θ, x), normalized by rotor diameter D. For mesh A, the radial spacing δ_r/D was 0.009 at the hub and tower surfaces, and expanded to a maximum of 0.046 near the mid-span. At the outer edge of the AD δ_r/D=0.016. δ_r/D was 0.333 at the lateral domain boundaries. The radial spacings used a bi-geometric expansion law with a ratio of 1.2. Radially, there were 21 elements from the hub to the outer radius. The azimuthal spacing (δ_θ) was uniform, and used 52 elements over the full geometry; each element spanned $\approx$7°. The axial spacing used 3 elements spanning the AD, which had an axial thickness of Δ_x/D=0.05. Moving upstream from the disks, the axial spacing expanded geometrically (ratio=1.3) to a maximum of δ_x/D=0.726 at the inlet boundary. Moving downstream, the spacing expanded (ratio=1.1) to a maximum of Δ_x/D=0.544. The bottom boundary layer was resolved using a first layer spacing giving y^+ values of approximately 60, and expanding with a ratio of 1.2.

The strategy described by [90] was used to refine the mesh. The index i refers

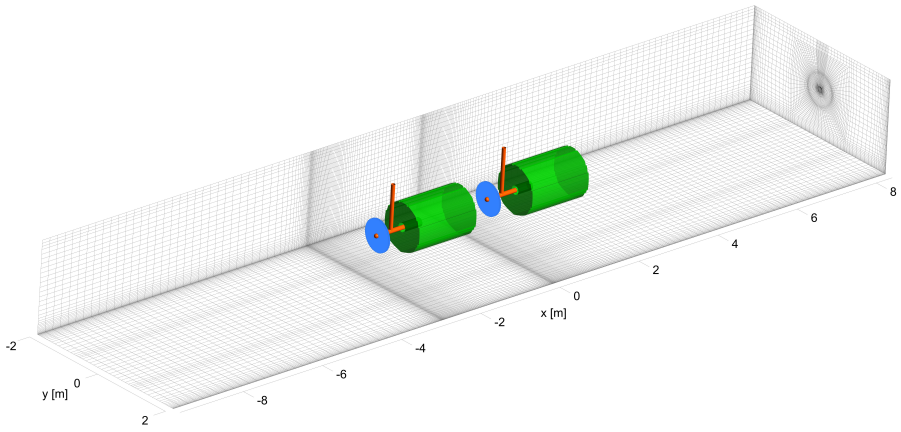

Figure 4.5: Mesh B for the full domain for the IFREMER cases, (this mesh for tandem rotors separated by 4D). Transparent green is used to depict regions where turbulence production was augmented.

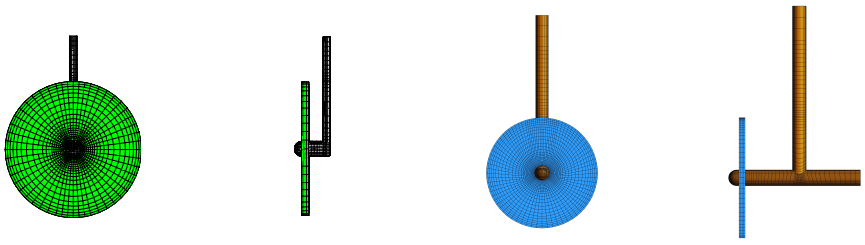

Figure 4.6: Mesh on actuator disk sub-domains, hub and tower. Manchester rotor (D=0.27 m) on left, IFREMER rotor (D=0.7 m) on right.

to the i^{th} mesh, i.e. $i = \{A, B, C\}$. For a grid refinement ratio γ, the number of elements (N) spanning each edge were increased, the spacings δ were reduced, and the expansion ratios ER were refined according to:

$$N_{i+1} = \gamma N_i; \quad \delta_{i+1} = \frac{\delta_i}{\gamma}; \quad \mathrm{ER}_{i+1} = \mathrm{ER}_i^{\frac{1}{\gamma}} \tag{4.27}$$

The meshes A, B and C contained 0.25M, 0.68M and 1.76M elements, respectively.

4.7 Verification

Verification is the process of estimating the error introduced by finite grid resolution. This error is primarily due to numerical diffusion, which artificially enhances diffusive processes, effectively increasing the fluid viscosity. Since two-equation turbulence models increase the effective viscosity, the relative importance of numerical diffusion is decreased in highly turbulent flows. Thus, coarser meshes may be employed in highly turbulent flows. The verification study found that the coarsest tested mesh (A) was sufficiently refined for further work with the Manchester experiments.

A separate grid refinement study was not conducted for the IFREMER rotor. Those simulations used the mesh B spacings relative to the rotor diameter. Scaling the mesh with rotor diameter is expected to give similar discretization error for turbine performance and wakes.

4.7.1 Method

Discretization error was estimated using the well-established $\mathrm{GCS}_{\mathrm{OR}}$ grid convergence method described by [42] and [43], which uses results from three meshes of successively greater resolution to estimate the continuum solution (i.e. that which would be obtained on a grid of infinitesimal elements) through Richardson Extrapolation. This method was used for detailed studies applying actuator-disk modelling to tidal turbines by Harrison [90].

For a given calculated parameter φ, the continuum solution is denoted φ_∞, and the calculated value from each mesh is φ_a,φ_b and φ_c. The continuum solution is

estimated using Richardson extrapolation:

$$\varphi_\infty = \varphi_c - \delta_c; \quad \delta_c = \frac{\varphi_b - \varphi_c}{\gamma^p - 1}; \quad p = \begin{cases} 0.5 & p_{\text{re}} \leq 0.5 \\ p_{\text{re}} & 0.5 < p_{\text{re}} \;\&\; \frac{p_{\text{re}}}{p_{\text{th}}} < 0.9 \\ p_{\text{th}} & \text{otherwise} \end{cases} \tag{4.28}$$

where p_{re} is the observed order-accuracy determined from the three solutions, p_{th} the theoretical order-accuracy for the numerical scheme and γ is the grid refinement ratio. The above logic is used to determine whether to use p_{re} or p_{th} for the extrapolation (see [43] for more detail). The expected discretization errors for the coarse and medium meshes are then:

$$\delta_b = \varphi_b - \varphi_\infty; \quad \delta_a = \varphi_a - \varphi_\infty \tag{4.29}$$

An uncertainty U_i is defined for the i^{th} mesh such that the exact solution φ_{exact} is bounded within the interval $\varphi_i \pm U_i$ with 95% confidence[14]. The GCI_{OR} method defines the value of U_i by applying a safety factor SF to the expected discretization error δ_i as follows.

$$U_i = \text{SF}|\delta_i|; \quad \text{SF} = \begin{cases} 1.25 & 0.9 \leq \frac{p_{\text{re}}}{p_{\text{th}}} \leq 1.1 \\ 3.0 & \text{otherwise} \end{cases} \tag{4.30}$$

When the convergence of φ is monotonic, the appropriate 95% confidence interval should be $[0, \text{SF}|\delta_i|]$ for increasing ϕ, and $[-\text{SF}|\delta_i|, 0]$ for decreasing ϕ. This logic halves the confidence interval without reducing the confidence level since for monotonically convergent cases it is extremely unlikely that the trend in ϕ with grid refinement would lead away from the exact solution.

4.7.2 Verification Results

The grid convergence studies were done using simulations of a single rotor in the Manchester flume. The boundary conditions for the convergence study were somewhat different than for the finalized simulations. Namely, a uniform inflow at $0.47\,^{\text{m}}/_{\text{s}}$ and a free-slip bottom boundary condition were employed. Thus, the convergence studies did not include a developing bottom boundary layer. The inflow turbulence

[14]Note that there is some debate (see [43]) over the exact confidence (90% to 95%) levels for the defined limits.

was tuned to give the proper intensity at the rotor plane (10%) and 3 m downstream thereof (8%). Neglecting the bottom boundary layer should have negligible effect on the outcome of the grid refinement study, because the highest velocity gradients (and therefore numerical diffusion) are present in the near-wake region just downstream of the rotors. Furthermore, the bottom boundary layer is a very common flow situation, for which guidelines on mesh resolution are well established.

Thrust and Power Coefficients

Thrust T and power P were found using equation 6.18, and the drag acting on the structural components (D_S) was also determined. These quantities were normalized according to:

$$C_T = \frac{T}{\frac{1}{2}\rho u_0^2 A}, \quad C_{D_S} = \frac{D_S}{\frac{1}{2}\rho u_0^2 A}, \quad C_P = \frac{P}{\frac{1}{2}\rho u_0^3 A} \tag{4.31}$$

The observed order of accuracy was 1.76 for C_T and 2.08 for C_P. These values are within the range of expected order-accuracy of 1 to 2 for the hybrid advection scheme employed by CFX. The observed order was 2.49 for C_{D_S}, indicating poor convergence. The solutions for C_T, C_P and C_{D_S} and the determined confidence intervals are summarized in table 4.2, which also shows the expected continuum solution.[15] Even the coarsest mesh resolved the turbine performance well, with confidence intervals less than 2% for C_T and C_P. The mesh was not sufficient to resolve the drag on the supporting structures with good accuracy, however this was not problematic for the present study because the structure drag is small ($< 8\%$) compared to the rotor thrust. A simulation with zero rotor forcing terms found C_{D_S}=0.0507 (mesh A), only 2% higher than with the rotor operating. The wake due to the supporting structure alone is characterized more fully in Appendix A.

Wake Recovery

The wake recovery was assessed by evaluating the area-average of the cubed axial velocity $\widetilde{u^3}$ over a disk of equal radius to the rotor, for a range of locations downstream of the rotor. The power produced by a turbine in the wake of an upstream turbine should scale approximately with $\widetilde{u^3}$, which motivated this choice for a convergence parameter. The estimated confidence interval size U_i is summarized in figure 4.7. The error for $\widetilde{u^3}$ was below 3.5% for all meshes and downstream locations. The error

[15] The higher C_T and C_P compared to figure 4.3 are due to not resolving the bottom boundary layer in the verification studies.

mesh	C_T	C_P	C_{D_S}
A	0.9239+1.5%	0.3304+1.4%	0.0346+93.2%
B	0.9296+0.9%	0.3324+0.8%	0.0400+67.0%
C	0.9325+0.6%	0.3333+0.5%	0.0496+35.0%
continuum	0.9378	0.3350	0.0669

Table 4.2: Verification study results and confidence limits for C_T, C_P and C_{D_S}, for the Manchester rotor (λ=4.7). The confidence intervals are one-sided due to the monotonic convergence, as discussed in §4.7.1

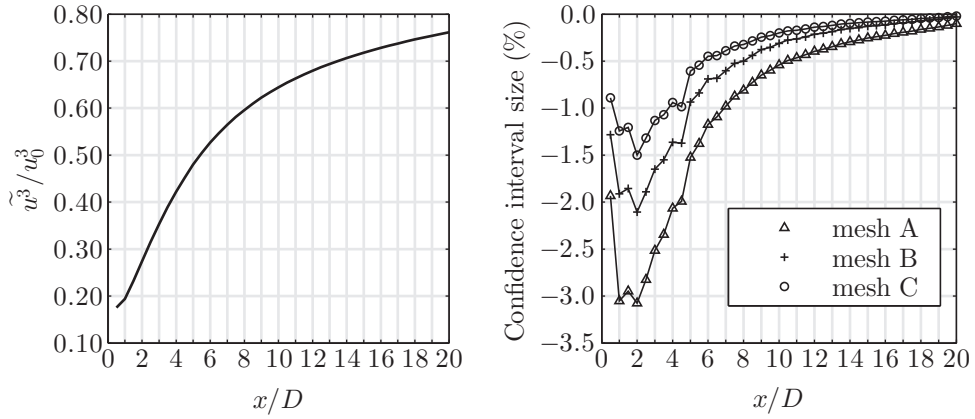

Figure 4.7: left: Estimated continuum solution for $\widetilde{u^3}/u_0^3$. right: Variation of U_i (%) with x/D

for $\widetilde{u^3}$ was maximal at 2D downstream of the rotor and decayed to less than 2% by 5D and 1% by 7D. The discretization error for a second turbine placed within the wake of the first would be acceptably low, even using the coarsest mesh tested in this study. Even though the drag on structural components is not well converged, the wake is dominated by the rotor thrust, with the drag acting on the structures contributing slightly to the shape of the wake. The tower wake does have an impact on the turbulence intensity however, and it may be that finer grids would have altered the wake turbulence somewhat. Appendix A observes the impact of the supporting structures on the wake in more detail.

4.8 Developing the S_k model

The S_k model was tuned for each of three experimental cases. These were, 1) the three rotor case from the Manchester data, 2) the single rotor case from IFREMER with (u_0=0.8, I_0=3%) and 3) the single rotor IFREMER case with ($u_0 = 0.83$, I_0=15%).

4.8.1 Error Measures and Objective Function

Transects of $\overline{u}_1$ and I provide useful qualitative comparison between experiments and simulations. Quantitative measures were the rms error in $\overline{u}_1^3$ and I, evaluated for each wake transect.

$$\mathrm{rms}\left(u^3_{\mathrm{err}}\right) = \sqrt{\mathrm{mean}\left[\left(\frac{\overline{u}^3_{1,\mathrm{sim}} - \overline{u}^3_{1,\mathrm{exp}}}{u_0^3}\right)^2\right]}, \qquad \mathrm{rms}\left(I_{\mathrm{err}}\right) = \sqrt{\mathrm{mean}\left[\left(I_{\mathrm{sim}} - I_{\mathrm{exp}}\right)^2\right]} \tag{4.32}$$

The term $\overline{u}_1^3/u_0^3$ was used because it is a good proxy for the power of a downstream rotor in the wake, relative to that of the upstream rotor. These rms errors were evaluated for each wake transect, at $x/D = \{1.2,2,3,4,5,6,7,8,9,10\}$ for the IFREMER tests, and at x/D=$\{2,4,6,8,10,12\}$ for the Manchester test. An objective function was required for tuning the model parameters. First an error function ERR was defined. This was formulated to provide an estimate of the error in predicting the power of a turbine array arising from errors in both $\overline{u}_1^3$ and I in the wake. Combining these two

sources of error required a scaling parameter to relate I to $\overline{u}_1^3$.

$$\mathrm{ERR} = \mathrm{mean}\left(\mathrm{rms}\left(u_{\mathrm{err}}^3\right) + \frac{\partial\left(\frac{\overline{u}_1^3}{u_0^3}\right)}{\partial I_0}\mathrm{rms}\left(I_{\mathrm{err}}\right)\right) \tag{4.33}$$

The required scaling parameter is the partial derivative term. This is the sensitivity of $\overline{u}_1^3/u_0$ in a rotor wake, to the turbulence intensity of the flow approaching that rotor. This was estimated to be 0.028 by comparing $\overline{u}_1^3/u_0^3$ from experiments with I_0=$\{$3 and 15$\}$% (see [77] Fig. 7b). The mean is taken over all available wake transects, with equal weighting. Thus, this formulation for ERR gives a proxy for the error in predicting the power output of a turbine array, due to errors in $\overline{u}$ and I in the modelled wakes. When testing different model curve fits, the optimization objective function was:

$$\mathrm{OBJ} = \mathrm{mean}\left(\mathrm{ERR}_i\right) \tag{4.34}$$

where i is the index of the tuning case. Thus, the goal was to minimize the average ERR from the three model development cases.

Adjusted Experimental data for I_0=15%

The 15% turbulence cases were difficult to model because the wake skewed somewhat laterally and because the simulations predicted a faster decay of turbulence intensity. For each experimental wake transect, the wake center was determined using the following weighted average:

$$y_c = \frac{\sum\left(1 - \overline{u}_1/u_0\right)y}{\sum\left(1 - \overline{u}_1/u_0\right)} \tag{4.35}$$

The experimental wake was then shifted laterally to align y_c with y=0. The shift varied linearly from 0 at x=0, to 0.4D at x=6D, then stayed constant at 0.4D to the end of the measurement range (x=12D). To compensate for the turbulence decay rate discrepancy, the experimental I was decreased by an amount varying linearly from 0% at x=4D to 2% at x=12D. This was done to avoid tuning the S_k model to compensate for the inability of the simulations to maintain the high level of ambient I, which is a separate issue from modelling the turbine wake.

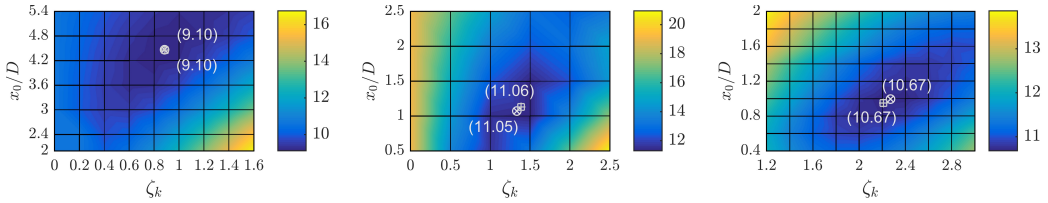

Figure 4.8: ERR function (eq. 4.33) variation with ζ_k and x_0/D for the IFREMER cases with I_0=3% (left), I_0=15% (right) and the Manchester case with I_0=10% (center). Symbols show the optimal points (circles) and points determined using the $\tanh^2$ model fits (squares).

4.8.2 Tuning Results

The S_k model has three free parameters: the production augmentation factor ζ_k, offset distance x_0 and length L_x over which production augmentation is applied. For this study, a constant length $L_x = 2D$ was assumed to make the tuning procedure more tractable. Of course, the method is somewhat sensitive to L_x, and Appendix B shows this sensitivity for the Manchester case. The first step in the tuning strategy was to run simulations of the three development cases, over a grid of (ζ_k, x_0) values to define the ERR maps shown in figure 4.8. The minimum ERR values were 9.10, 11.05 and 10.67, shown as circles in 4.8, giving a minimum possible value for OBJ of 10.2771. Note that the optimal ζ_k and x_0 are case-dependent, as expected.

The next step was to select an appropriate predictor variable for defining curve fits for ζ_k and x_0. Potential variables were taken as volumetric averages over the AD region between 40% and 80% span. This range was selected to avoid sensitivities to the boundary layer region near the nacelle and to the strong shear region near the AD edge. The goal was to use predictor variables representative of the ambient flow, taken at the disk region. It was desirable to use a non-dimensional predictor variable, which was linked to the vortex breakdown process in a physical manner. Two non-dimensional groups were considered. One was the local intensity $I = \sqrt{(2/3)k}/\overline{u}_1$ and the other was a group we call the turbulent Reynolds number $\mathrm{Re}_t = uD/\nu_t = uD\omega/k$. Of these, Re_t produced more reasonable model fits. Re_t represents the ratio of inertia to turbulent viscosity, which is physically meaningful for vortex breakdown dynamics.

A variety of function forms were tested, where the model coefficients were optimized to minimize OBJ using Matlab's *fminsearch* function. It was found that ζ_k varied with Re_t^{-1} and x_0/D varied with Re_t. Initially, the following linear fits were

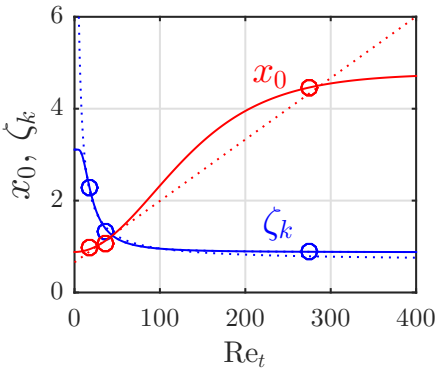

Figure 4.9: Curves defining the linear (dotted lines) and $\tanh^2$ (solid lines) model fits. Circles show the optimal points from figure 4.8.

found;

$$x_0/D = 0.656 + 0.0134\mathrm{Re}_t \tag{4.36}$$

$$\zeta_k = 0.691 + 26.8\mathrm{Re}_t^{-1} \tag{4.37}$$

with OBJ = 10.2888. The trend $\zeta_k \to \infty$ as $\mathrm{Re}_t \to 0$ was concerning, as was the linearly increasing x_0. These trends could easily lead to unstable convergence in simulations. Thus, to obtain stable asymptopic model behavior, fits were tuned using a $\tanh^2$ variation:

$$x_0/D = 3.88\tanh^2(0.0071\mathrm{Re}_t) + 0.882 \tag{4.38}$$

$$\zeta_k = 2.23\tanh^2\left(19\mathrm{Re}_t^{-1}\right) + 0.876 \tag{4.39}$$

with OBJ = 10.2786, a slight improvement over the linear fits. The motivation for the tanh fits were to improve simulation robustness rather than improving OBJ.

The same procedure was used to tune the coefficient for the k-ε model modification by El Kasmi *et. al* for the three experiments. This gave $C_{4\varepsilon}$=0.01 (OBJ = 15.81), compared to to optimal tuning found by [51] of 0.37 (OBJ=17.93).

4.8.3 Wake Profiles for Tuning Cases

Figures 4.10, 4.11 and 4.12 show profiles of u/u_0 and I for the tuning cases. It is evident in all cases that the standard k-ε model over-predicts the wake recovery rate.

Figure 4.10 shows results for I_0=3%. k-ε misrepresents the shape of the wake velocity and intensity profiles, producing large errors in both u and I. Both the k-ε+S_ε and SST models predict the shape and magnitude of the u and I profiles well, but under-predict I beyond x=4D. The SST model slightly over predicts the velocity beyond x=7D. The tuned SST+S_k model produces the lowest wake errors, producing very good agreement throughout the wake.

Figure 4.11 shows results for I_0=10%, with three rotors. k-ε over predicts the velocity recovery, and under predicts I from x = 4 to 8D. k-ε also does not predict the double-peak I profile evident at x=2D. The added S_ε term improves u but degrades I throughout the wake. The added dissipation reduces k, worsening the under prediction of I. The SST model gives the best predictions of u at x=2D, but predicts faster jets in between the rotors, and slower flow in the center of the wakes at 4-8D. The SST model also under predicts I throughout the entire wake, leading to a a larger ERR compared to the k-ε models. However the SST model does do a better job predicting

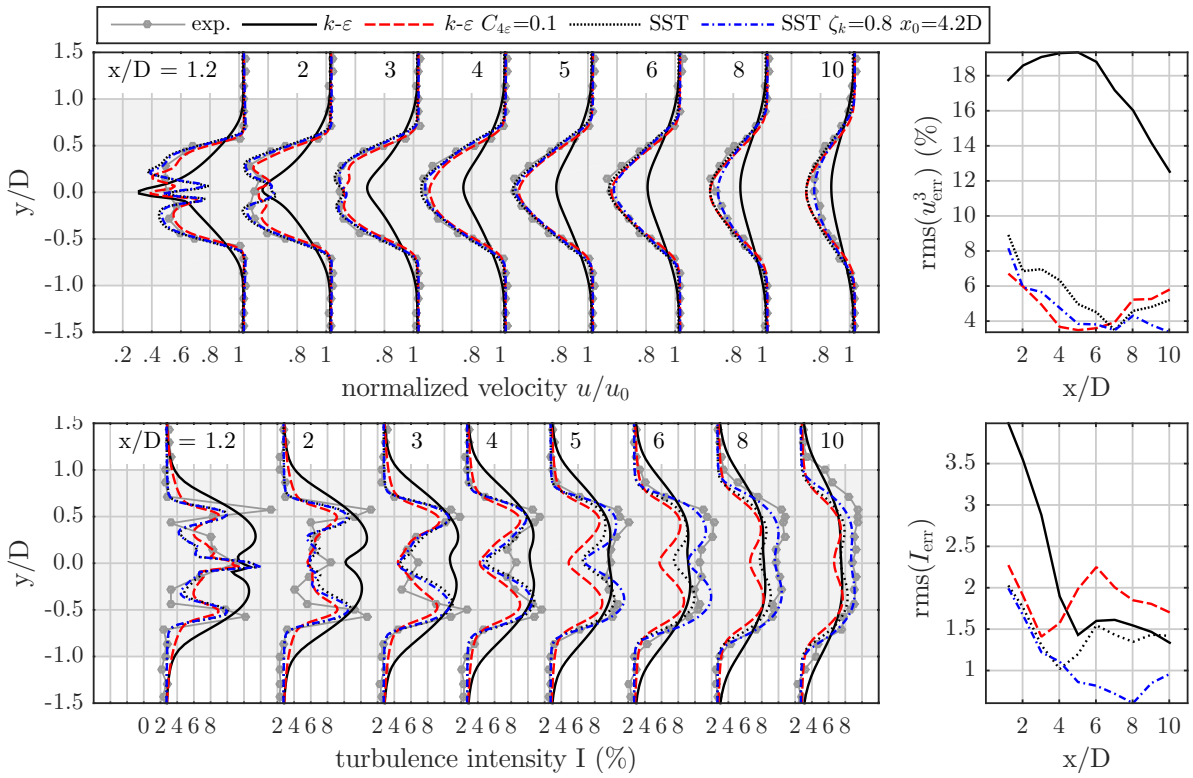

Figure 4.10: Wake profiles for the tuned single rotor IFREMER I_0=3% case. The shaded region depicts the y/D range where the rms errors were evaluated.

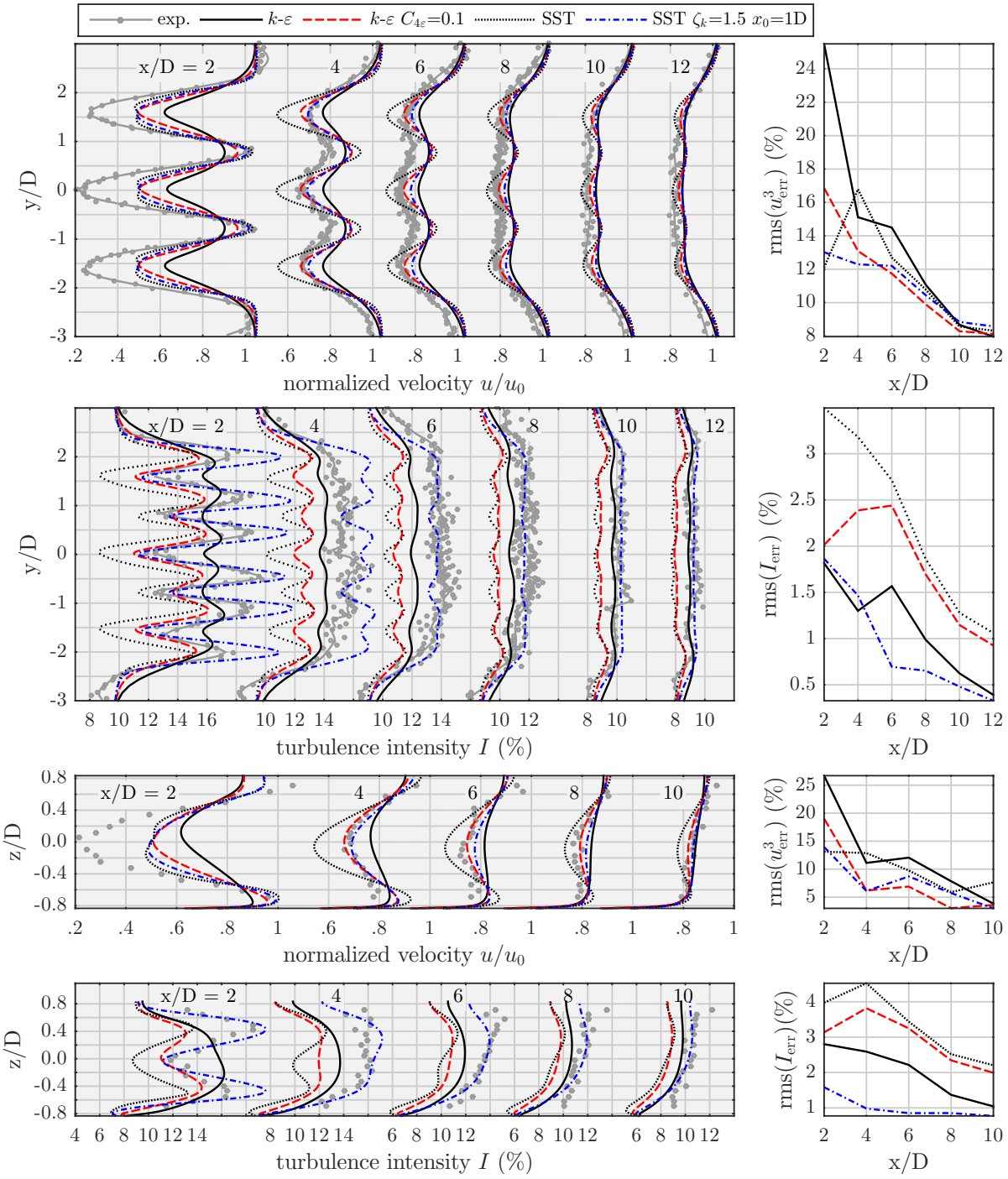

Figure 4.11: Wake profiles for the tuned three-rotor Manchester I_0=10% case.

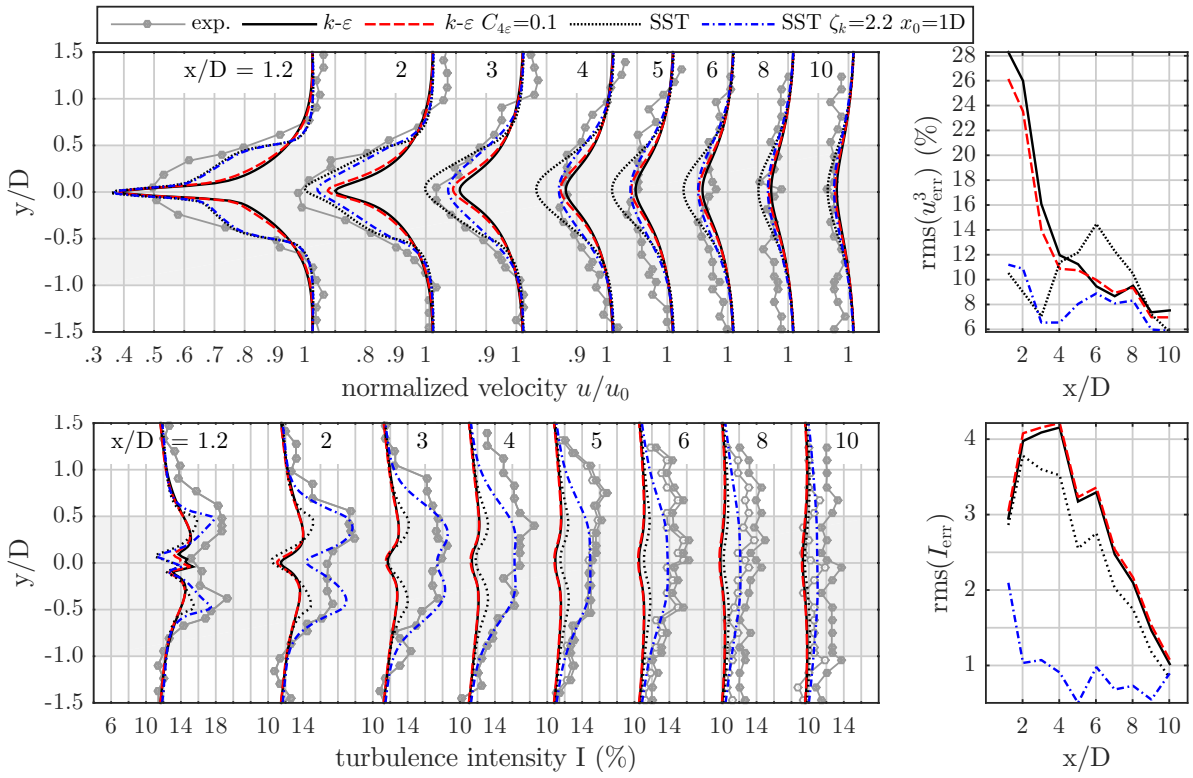

Figure 4.12: Wake profiles for the tuned single rotor IFREMER I_0=15% case. The shaded region depicts the y/D range where the rms errors were evaluated. The open circles depict the compensated I values.

the shape of the I profiles. The tuned SST+S_k model improves the prediction of the I profiles, and gives a marginal improvement to the u profiles, most evident from x=2 to 6D. All three models give similar rms(u^3_{err}) from x=8 to 12D. Compared to the k-ε model, the main improvements made by the tuned SST+S_k model are improving the velocity prediction from x=4 to 6D and improving the prediction of I in the depthwise profiles throughout the wake. The process of wake merging is evident in both the simulations and experiments. The three wakes are very distinct immediately downstream of the rotors, by 8D the wakes are almost indistinguishable and by 10D they have merged fully. The simulations represent this merging process fairly well but the experiments indicate a somewhat faster merging. The vertical profiles show the wake interacting with the bottom boundary layer. All simulations under predicted I near the bottom at x>6D, possibly indicating a rougher bottom than assumed. At the top free surface I was under predicted, potentially due to turbulence induced by waves, which were not modelled in simulations.

Figure 4.12 shows results for I_0=15%. k-ε predicts a very narrow wake, with much faster velocity recovery than the experiments from x=1.2 to 3D. Beyond this, it predicts the velocity profiles well. The intensity is under predicted by k-ε, and SST in the near wake, but the prediction becomes better progressing downstream of the rotor. The added S_ε term has very little impact on the wake for this case, and increasing its value only further decreases I in the near wake, degrading the overall match. SST predicts the velocity most accurately from x=1.2 to 3D. The tuned SST+S_k model improves the prediction of I throughout the wake. It also gives the best overall prediction of the velocity throughout the entire wake.

In general, the approach of adding S_ε improves the near wake velocity. This is achieved by reducing the eddy viscosity by increasing the dissipation term, slowing down wake mixing. This is problematic however as the increased dissipation reduces k leading to under predicted intensity. Thus with the S_ε approach, a compromise must be made between correctly modelling the velocity, or the turbulence intensity. Alternatively, with the SST model the mechanism for reducing the eddy viscosity is the limiter function. In the tested cases, the SST model under-predicted the turbulence intensity as the same time as under predicting the wake recovery rate. Thus, with the SST model, the addition of the S_k term improves both the wake velocity and intensity profiles.

The values of ERR for the four tested turbulence models are summarized in table 4.3. ERR was designed to give an approximate estimate of the error in array power

Test Conditions			ERR				S_k Parameters		
Exp. Facility	I_0	a	k-ε	k-ε+S_ε	SST	SST+S_k	Re_t	ζ_k	x_0/D
IFREMER	3%	n/a	23.23	10.11	9.72	7.73	274	0.80	4.20
Manchester	10%	n/a	18.06	16.17	19.20	11.31	36.5	1.50	1.00
IFREMER	15%	n/a	21.64	20.98	17.00	10.68	18.5	2.20	1.00
IFREMER	3%	4D	14.95	11.46	10.10	8.46	113	0.94	2.59
IFREMER	3%	6D	12.39	12.08	12.36	8.72	54.8	1.12	1.42
IFREMER	3%	8D	10.44	12.45	13.34	9.73	58.0	1.10	1.47
IFREMER	15%	4D	19.40	19.65	21.82	11.91	25.8	1.75	1.01
IFREMER	15%	6D	19.80	20.43	25.14	12.05	28.5	1.63	1.04

Table 4.3: Wake ERR values for the tested turbulence models. The first block is for the S_K model development cases (§4.8), while the second block is for the tandem rotor validation cases(§4.9). The column 'a' refers to the separation distance between tandem rotors. For k-ε+S_ε, $C4_\varepsilon$=0.1

production. For the three model development cases, the k-ε model consistently gave ERR≈21%. Adding the S_ε term improved ERR to 10% with I_0=3%, and to 16% for I_0=10% but did not improve ERR for I_0=15%. The SST model gave slightly better improvements to ERR compared to the k-ε model but overall similar performance. On average, the SST+S_k approach reduced ERR to 10%, a significant improvement compared to the other tested models. Since S_k was specifically tuned for these cases, this may represent the best improvement possible using the S_k approach.

4.9 Validation with Tandem Rotor Cases

This section describes simulation performance for the IFREMER tandem rotor cases [77]. These cases were not used in developing the S_k model, so they serve as independent validation tests. They are also challenging test cases, as they involve comparing to results of mixed turbine wakes. Simulations replicated experiments with I_0=3% with rotors separated by {4,6,8}D, and I_0=15% with rotors separated by {4,6}D.

Wake profiles for I_0 =3% are shown in figure 4.13. The 8D separation distance case is not shown but had very similar results to the 6D case. As with the I_0=3% single rotor case, k-ε over predicts the initial velocity recovery rate, but gives improving estimates of the velocity progressing further downstream. k-ε predicts an intensity profile which is broader than experiments and under-predicts I at the two distinct peaks at (x/D<4, y/D=±0.5D). By x=10D, k-ε predicts u and I as well as any of the other models. Both k-ε+S_ε and SST predict the shape of the u and I profiles quite

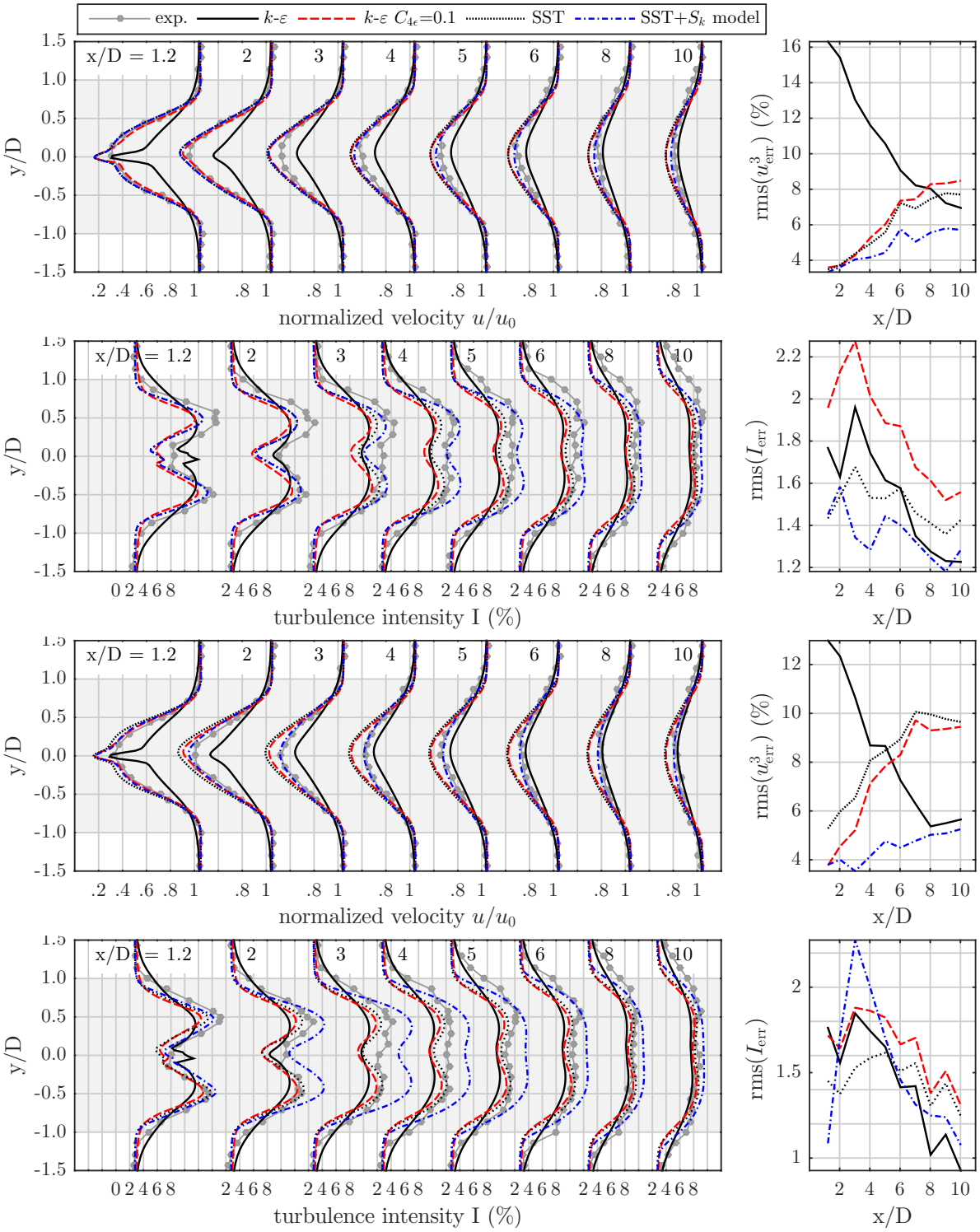

Figure 4.13: Wake profiles for I_0=3% IFREMER tandem rotor cases with separation distances of 4D (top two plots), 6D (bottom two plots). Profiles for the wake of two rotors at 8D separation (not shown) were similar to the 6D case. (x/D is downstream of the second rotor)

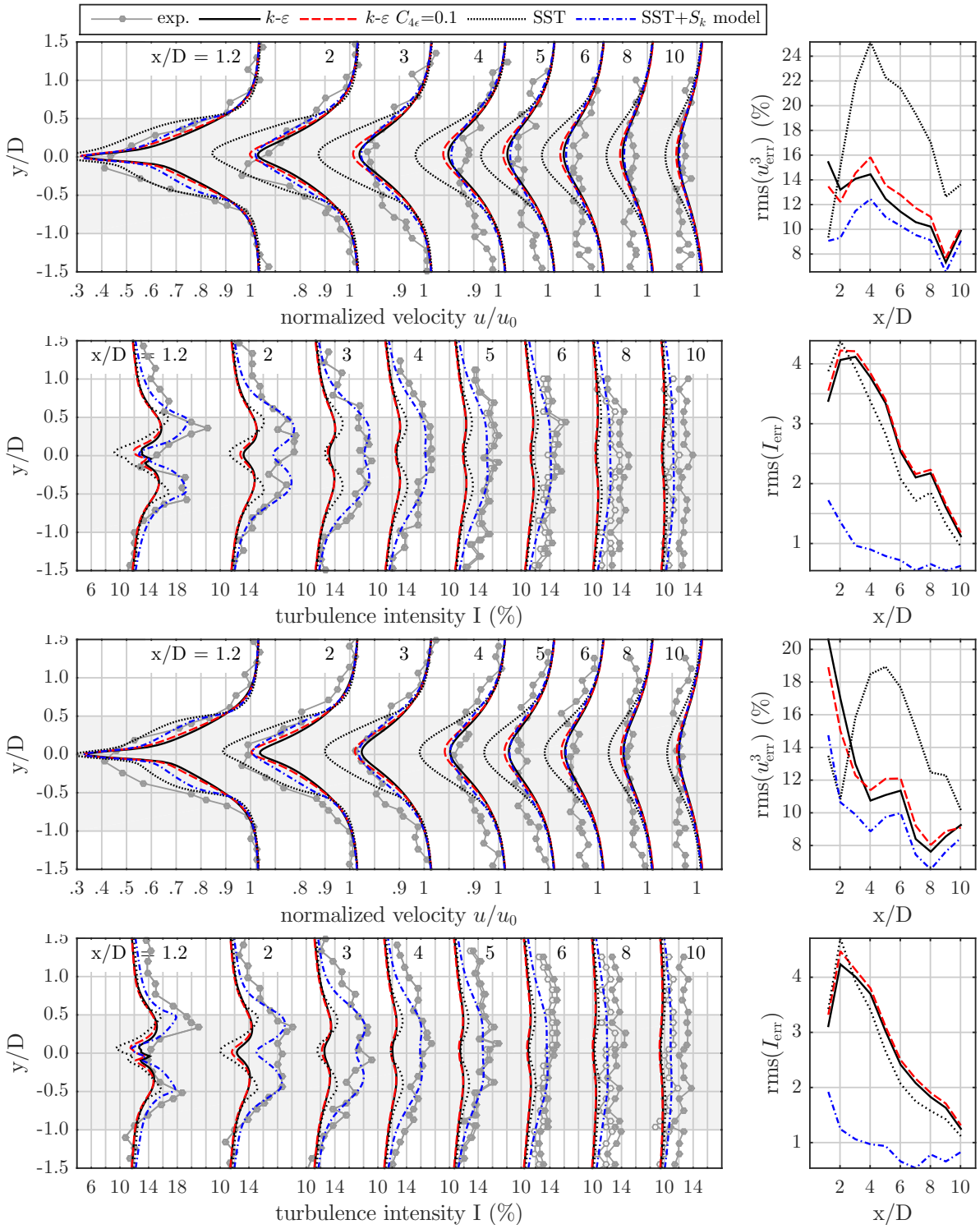

Figure 4.14: Wake profiles for I_0=15% IFREMER tandem rotor cases with separation distances of 4D (top two plots), 6D (bottom two plots). (x/D is downstream of the second rotor)

well. They give excellent u predictions of the velocity for x<2D, but under predict the velocity recovery rate, giving the increasing trend in rms(u^3_{err}). Both k-ε+S_ε and SST slightly under predict I (rms(I_{err})$\approx$ 1.8 for SST, $\approx$1.5 for k-ε+S_ε), which is consistent with under predicting the u recovery rate (higher I is expected to increase the mixing rate). The SST+S_k model gives the best predictions of u (rms(u^3_{err})<6 throughout the entire wake) for all 3 cases (separation distances of {4,6,8}D). It predicts I very well for the 4D separation case, but augments the production too much for the 6D and 8D separation cases, predicting too high I, most evident within 2D<x<6D. Interestingly, this over-compensation provides a good mixing rate resulting in excellent u profiles. The main advantage of the SST+S_k model for the I_0=3% cases is improving the prediction of the u profiles.

Profiles for I_0=15% are shown in figure 4.14. As with the I_0=15% single rotor case, k-ε predicts too narrow a wake at x=1.2D, but less so than in the single rotor case. It predicts the u profiles with similar accuracy as the other models especially for x>6D. k-ε under predicts I, particularly at the twin peaks at (x=1.2D,y=$\pm$0.5D), but with an improving trend proceeding downstream. The added S_ε term has little impact on the results for these cases, and a stronger source would only further decrease I. The SST model gives the best u prediction at x=1.2D but under predicts the recovery rate, consistent with its under prediction of I. With SST the velocity remains too low in the wake, which does not mix fast enough. The S_k model increases I to provide a very good match to the exp data (rms(I_{err}) <2% for all x). This augmentation corrects the predicted mixing rate appropriately, giving the best u profiles of all the models. Compared to the k-ε model, rms(u^3_{err}) is reduced approximately 4% at x=2D and 0.5% at x=4D. The main advantage of the SST+S_k model for the I_0 =15% cases, however is the improvement in predicting I.

The wake ERR values are summarized in table 4.3. The results for the validation cases are presented in the second block of the table. First, trends regarding the I_0=3% cases are discussed. Interestingly, k-ε performs much better in the I_0=3% tandem cases than for a single rotor, with an improving trend as rotors are spaced further apart (ERR=15 for 4D separation and ERR=10 for 8D). Both k-ε+S_ε and SST models improved ERR for the 4D separation case, but degraded it equally for the 8D case, showing no clear advantage over the basic k-ε. The SST+S_k model improved ERR for all separation distances, with 6.5% improvement compared to k-ε for 4D separation, but only 0.7% for 8D separation. The I_0=15% cases showed some different trends. The k-ε model gave slightly lower ERR for the tandem cases

compared to the single rotor, but this was not as pronounced as for the I_0=3% cases. Both k-ε+S_ε and SST models actually degraded ERR somewhat compared to k-ε. The SST+S_k model gave the lowest ERR, reducing it by 7.6% compared to k-ε.

4.10 Discussion & Conclusions

This paper contributes to the growing body of literature aiming to develop and validate 2-equation turbulence models for wake recovery for AD simulations of wind/tidal turbines. Efficient methods for modelling turbine wakes are vital for simulations of entire turbine farms, where wake interactions can alter turbine performance significantly, yet fully blade-resolved simulations remain overly expensive.

Using standard k-ε or k-ω turbulence models, the wake recovery is too fast because the eddy viscosity is over predicted. The most widely tested modification [51] to correct this problem introduces a source of ε in a region surrounding the rotor. This correction requires tuning $C_{4\varepsilon}$. In this study, an optimal value of 0.1 was found, compared to 0.37 in previous work [51]. Several other tuning-free correction methods have been proposed by various researchers [54, 55, 56, 59] to limit the eddy viscosity in regions of high strain-rate, with varying degrees of success.

In this paper, the possibility of using the SST eddy viscosity limiter [32] to improve wake recovery predictions has been explored. The SST limiter is similar in form to that of Durbin [68] but was formulated for adverse pressure gradients, rather than stagnation points. It was found that close to the rotor (x<2D) both the SST and k-ε+S_ε models predict wake velocity profiles quite well. Both of these models tended to under predict the turbulence intensity however.

This article identifies that the AD approach inherently neglects the production of turbulent kinetic energy by tip-vortices, and proposes a correction which enhances turbulence porduction in the wake shear layer. Physically, this production is associated with the breakdown of the tip-vortices into smaller-scale turbulent eddies. The proposed correction augments the existing turbulence production by a factor ζ_k. The magnitude of ζ_k and the region over-which it is applied was tuned to achieve a good match to experimental data for three model development cases. An alteranate approach to this tuning procedure would be to use high-fidelity simulations (likely LES) such as [84], or detailed experiments such as [83] to resolve the vortex breakdown process, providing a numerical baseline for the magnitude of turbulence production by vortices, and the appropriate spatial region over which breakdown occurs.

Additionally, as mentioned in Appendix A, RANS simulations inherently neglect turbulence produced by vortices shed from turbine supporting structures. A cylindrical support tower would be expected to produce a typical von Karman vortex street, which is an unsteady phenomenon. Although the present model was formulated under the premise of adding turbulence generation due to tip vortices, the added source term may also be compensating for unresolved eddies from support structures. Furthermore, support structures may alter the rate of tip-vortex breakdown, so it is difficult to isolate effects of tip-vortices vs. supporting structures.

This article shows that using the SST turbulence model with an additional source term S_k in the k equation, can provide good predictions of wake velocity and turbulence intensity. The added source term is applied in a region which spans the wake ($0<r<\sqrt{2}R$), starting at an offset distance x_0 downstream of the rotor and ending at a distance x_0+L_x. Thus, the model is defined using three parameters (ζ_k,x_0,L_x). It was found that appropriate values for ζ_k,x_0 and L_x varied between the tested cases. Physically, vortex breakdown is expected to occur faster in more highly turbulent flows. Thus, we propose that vortex breakdown depends primarily on the so called turbulent Reynolds number Re_t, which defines the ratio of inertial terms to mixing by turbulent eddies (analogous to Re, which is the ratio of inertia to viscous forces). Curve fits were developed to define the variation of ζ_k and x_0 with Re_t (L_x was held constant at 2D). These fits were optimized to give the best match to experimental data for three experiments with varying ambient turbulence I_0=$\{3,10,15\}$%.

After this fitting procedure, the proposed SST+S_k model was validated for the wake of the downstream rotor in a tandem array, with I_0=$\{3,15\}$%. The standard k-ε, k-ε+S_ε, and SST models were also tested for comparison. The validation used an error metric ERR formulated as an estimate of the error in predicting the power output of a turbine array. The SST+S_k model gave the lowest ERR values of the tested models. The standard k-ε model gave good predictions at x>8D but poor predictions for x<4D. The SST and k-ε+S_ε models showed the opposite trend. Without the added S_k term, all of the tested models under predicted I at its peak values at the wake edge (y/D=$\pm$0.5D). This can be explained by the lack of turbulence production by tip vortices. The new SST+S_k model gave the best overall predictions because it has similar performance as SST close to the rotor, but augments the production of turbulence in the wake shear layers, which improved both the I and u profiles.

For turbine arrays with rotors separated by 1D to 10D the SST+S_k model is expected to reduce the array power error by between $\approx$3.5% (I_0=3%) and $\approx$7.5%

(I_0=15%), compared to k-ε. This range of I_0 is thought to cover ambient turbulence intensity for operating conditions of tidal/wind turbines. With rotors separated by >10D, the improvements are smaller and the additional effort in implementing the model may not be warranted, since k-ε performs quite well for the wake by 10D, except in the lowest turbulence cases studied.

Acknowledgments

The first author is funded by a Post Graduate Scholarship from the National Sciences and Engineering Research Council (NSERC) of Canada, and a NRCan CHTTC project.

Appendix A: Impact of Support Structures

The support structures were explicitly modelled in this study. Simulations were run with no rotor forcing terms and a free-slip condition on the bottom to isolate the impact of the support structures on the wake. On the structures, a no-slip condition was used with a hydraulically smooth wall. A wall function approach was used, which defines ω in the first grid cell adjacent to the wall using a blend between known analytical expressions for ω in the viscous sublayer and logarithmic region. The k flux is set to zero in a direction tangent to the wall. The wall shear stress is calculated using typical log law relationships, blending automaticaly into a low Re formulation for small y^+. The wall shear is added to the momentum equations in the first cell adjacent to the wall. See [80] for further detail.

The wake is shown in figure 4.15, which also shows the wake with a single active rotor. The wake of the IFREMER support structure has u/u_0=0.8 at x=2D, compared to u/u_0>0.9 for the MANCHESTER rotor. The IFREMER measurements at 1.2D are immediately downstream of the nacelle trailing edge, explaining the relatively large velocity deficit. Relative to the wake of the rotor, however, the velocity deficit of the support structures is quite small.

The nacelle and tower produced both k via. shear production, and ω (or ε), via. the wall function boundary condition. The impact on I depended on the ambient turbulence intensity. For I_0=3% the shear production had a dominant effect, producing a peak in the I profiles downstream of the nacelle. This feature of the wake is also evident in the experimental data for x≤4D. For I_0={10,15}% the structures

caused a peak in I for x<2D but further downstream caused a reduction in I. This suppression of turbulence intensity is somewhat counter-intuitive, but may be sensible for a flow with high ambient turbulence, where the presence of a body acts to suppress large turbulent eddies. Further study of wakes downstream of bluff bodies in highly turbulent flows may shed light on this issue, but was beyond the scope of the present work.

It is possible that the suppression of I by the supporting structures is non physical. Indeed it would seem logical that a RANS model would not resolve the turbulence produces by eddy shedding off of the supporting tower. Therefore, even though the added S_k term introduced in this paper was developed under the premise of compensating for the lack of tip-vortices with the AD approach, it may also be compensating for the lack of shed vortices from supporting structures. Further study is certainly warranted to assess this possibility. This would not detract from the utility of the model though as it has demonstrated a clear improvement to reproducing wakes.

Appendix B: Sensitivity to L_x

The S_k model curve fits were optimized over the (ζ_k, x_0) design space, and figure 4.8 shows the sensitivity of ERR to (ζ_k,x_0). This appendix is included to show the sensitivity to the third model parameter, L_x. This was assessed using the Manchester I_0=10% case, with constant values of ζ_k=1.5, x_0=1.5D. Simulations were run with L_x = {1,2,3}D, giving ERR = {12.41, 11.33, 11.75}. L_x=2 was selected for developing the model because it produced the lowest ERR. Wake profiles are shown in figure 4.16, with results also shown for k-ε for reference. The highest sensitivity is noted at x=4D, where I is under predicted with L_x=1, but over predicted with L_x={2,3}. The velocity profiles are relatively insensitive to L_x for this particular scenario. It is expected that the sensitivity would increase with increasing ζ_k and reducing x_0.

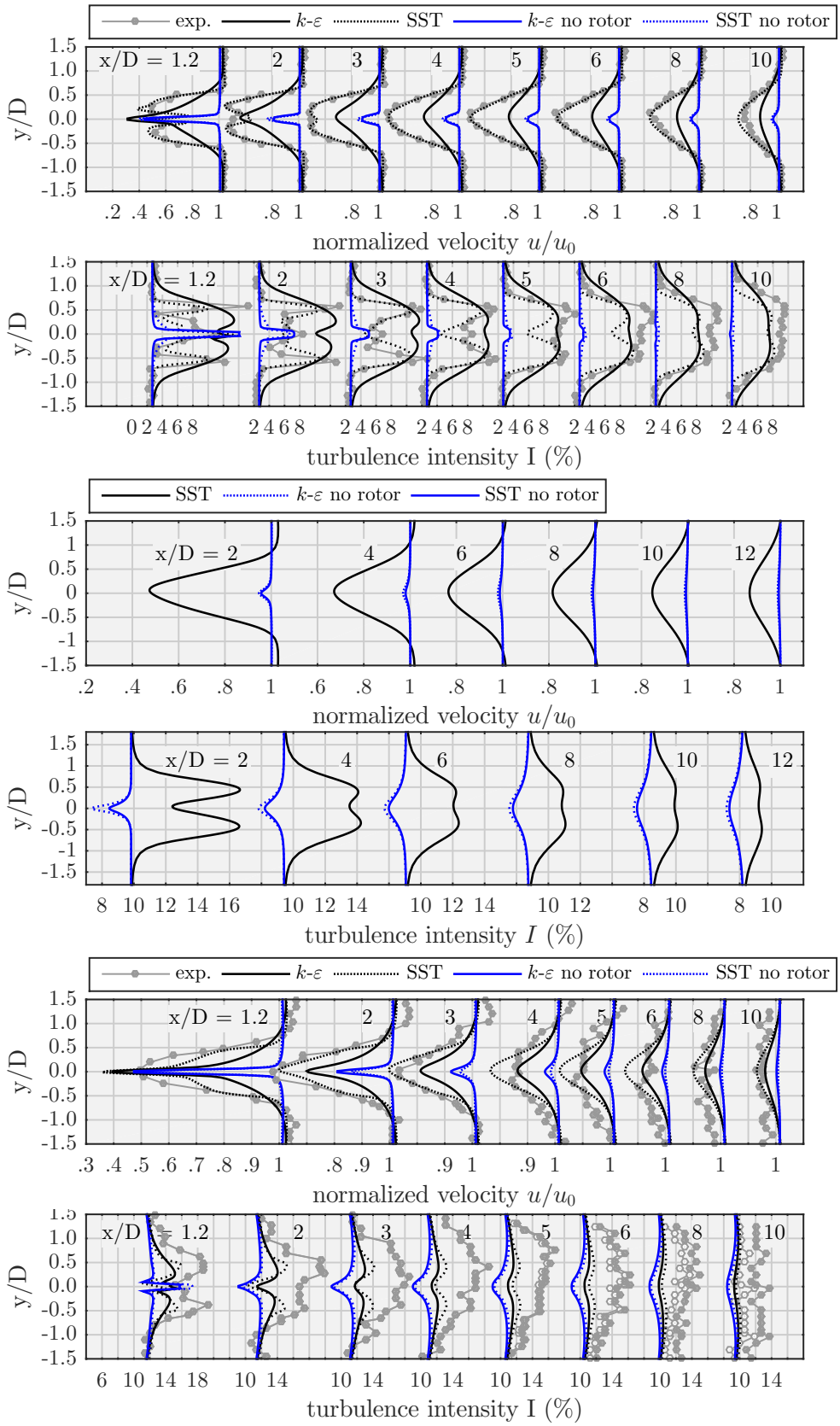

Figure 4.15: Lateral wake profiles for the IFREMER I_0=3% case (top two plots), Manchester single-rotor case with I_0=10% case (middle two plots) and IFREMER I_0=15% case (bottom two plots), showing results with only the supporting structures present.

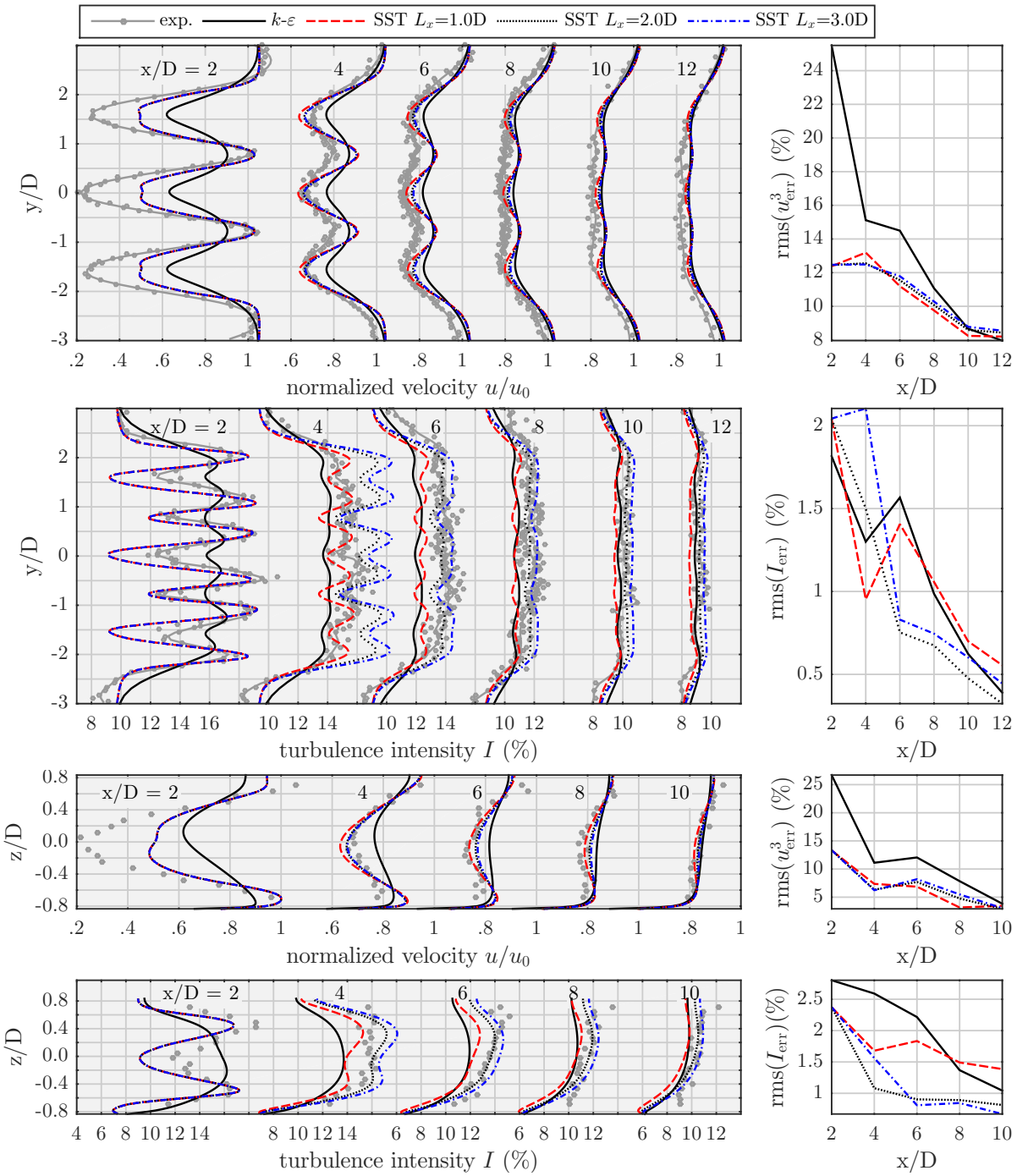

Figure 4.16: Wake profiles for the Manchester I_0=10% case, showing sensitivity to L_x (ζ_k=1.5, x_0=1.5D).

Chapter 5

A Tuned Actuator Disk Approach for Predicting Tidal Turbine Performance with Wake Interaction

This paper has been published as:

Shives, Michael; and Crawford, Curran: *"A Tuned Actuator Disk Approach for Predicting Tidal Turbine Performance with Wake Interaction,"* International Journal of Marine Energy 17 (2017) 1-20, DOI: 10.1016/j.ijome.2016.11.001.

Actuator disk simulations based on blade-element formulations require fairly refined grids to obtain accurate solutions and require empirical corrections to account for tip-loss. This paper provides an alternate approach suitable for coarser grids, which uses tested performance curves to populate a table lookup of rotor performance based on the AD-local velocity, which can then be applied to predicting turbine performance in blocked-flow conditions, and with interacting wakes. This method is used by the final yield-assessment methodologies presented in chapters 7 and 8.

Abstract

This article presents a practical method for predicting the power output of tidal farms with device wake interactions. The method uses Reynolds-averaged Navier-Stokes

(RANS) simulations to predict turbine wakes and bathymetry effects. The power of each turbine depends on the local velocity, which is influenced by other turbine wakes. Therefore, the accuracy of power predictions depends heavily on proper wake modelling. This is a critical issue for the tidal power industry because best practise for predicting tidal farm energy yield has yet to be established, and wake interaction effects may drastically alter energy yield in a dense turbine farm.

This article introduces a methodology which accurately predicts power output while minimizing computational expense, named the *tuned actuator disk approach* (TADA). Rotors are resolved using 9–15 elements across their diameter, allowing for very fast simulations of multiple turbines. The model is tuned to match known thrust and power operational profiles for a set of calibration cases based either on experiments or a limited set of high-resolution simulations. In this study, TADA was used to model a tandem configuration of two scaled rotors in a flume tank, and gave accurate predictions of the rotor thrust, power and wake velocities. Predictions of thrust and power became independent of grid density with more than 15 elements spanning the rotor diameter, however errors associated with using 9 elements were limited to 3% for thrust and 6% for power. Once calibrated for a specific turbine and computational mesh, TADA can be used in full farm-scale simulations at reasonable computational expense, which is an important capability for predicting tidal farm energy yield.

5.1 Introduction

A critical metric for determining the feasibility of any energy project is the annual energy production (AEP). Without an accurate AEP prediction for developing farms of tidal turbines, the uncertainty in revenue makes it hard to obtain financing to proceed with the larger scale projects required to drive the industry forward. The tidal energy industry is still maturing, and current standards [2] for predicting AEP for a tidal farm provide rough guidelines rather than an exact methodology. Research groups [3] and consultancies [4] are gradually converging toward methods for AEP prediction in tidal farms. In general terms, accurate AEP prediction requires: 1) spatial fields of velocity arising from bathymetry and turbine wakes, 2) robust characterization of rotor performance in changing inflow velocity and turbulence, and 3) accounting for temporal variability of velocity over a long time frame (months to years).

This article focuses on spatial flow variability due to turbine wakes, and proper

turbine performance characterization. Our group is also testing an approach to account for temporal variability, which uses 2D regional-scale oceanographic simulation (e.g. [91]) to predict an annual time series of velocity and depth. The time series is characterized statistically[1] by binning the full time series into a subset of representative flow-states, based on the flow speed, direction and water elevation.For each flow-state, a 3D steady Reynolds Averaged Navier Stokes (RANS) simulation, similar to those described in this paper, predicts the spatial velocity field (including wakes) and the farm power output.[2] AEP is then found using the binned probability distributions and flow-state power predictions.

Presently, available methods for representing turbines in RANS simulations range from very high-resolution (blade-resolved), to very low resolution (momentum methods with turbines as sub-grid-scale terms). The computational expense of high-resolution methods makes them inappropriate for farm layout optimization or for predicting annual energy yield, which requires either: a) long duration (at least one spring-neap cycle) simulations, or b) simulations of a set of discrete flow states as described above. With very low resolution methods it is feasible to run long-duration simulations, however their accuracy in predicting wake effects is poor and representing turbines with sub-grid models offers no hope for predicting mutual wake interactions.

This paper presents a 3D RANS simulation method which provides accurate predictions of turbine performance with wake interaction, which our group plans to use in the AEP strategy described above. The method uses an actuator-disk (AD) approach to represent turbines, which has become very prevalent in tidal and wind farm simulations. The AD approach allows using a coarse mesh compared to higher-fidelity CFD approaches (e.g. physically resolving the blades, or actuator line methods e.g.[92]). The specific approach presented herein was developed independently by the authors [93], but is similar to that of [94]. It is encouraging that multiple groups are converging to a similar methodology.

A critical component of this method is a tuning procedure to populate lookup tables for turbine performance. Thus, the method is analogous to the well-established practice of using tabulated airfoil coefficients for aerodynamic wing simulation, however, instead of looking up lift and drag coefficients for a lifting surface, it looks up

[1] It is also possible to perform harmonic analysis to characterize flow conditions at a point in space, and to predict AEP for an isolated rotor. However methods for accounting for turbine wake interaction using harmonic analysis have yet to be developed.

[2] As the 2D regional model only provides rough turbulence predictions, future enhancements could incorporate field-data of turbulence into the boundary conditions for the RANS simulations.

thrust and power coefficients for an entire rotor. This is made somewhat complicated because the turbine slows the flow significantly local to the rotor; the tuning must therefore account for this induction effect. The lookup tables for thrust and power are generated using a set of calibration simulations. Because of the requisite tuning procedure, the method has been named the *tuned actuator disk approach* (TADA).

Other AD-based approaches suitable for turbine layout studies e.g. [11] [95] have been developed using blade-element (BE) theory, which relies on tabulated airfoil data. Compared to TADA, such methods avoid the tuning procedure, provided that accurate airfoil lift and drag curves are available. BE-based AD methods require finer meshes compared to TADA, resulting in longer runtimes. Therefore, TADA has a higher computational cost upfront (for tuning) but once the model is established it allows for much more rapid simulations.

In this paper, TADA was validated using published experimental data [76, 77] of two turbines in a tandem configuration. The primary validation metric was the power of the downstream rotor, which was quite accurate over ranges of inflow turbulence and separation distance between rotors. TADA's ability to predict turbine wakes was also validated for single-rotor and twin-rotor configurations with very encouraging results. Tests of sensitivity to grid resolution showed grid independence with 15 elements spanning the rotor diameter.

The paper is organized as follows. Section 5.2 identifies key terminology. Section 6.2 summarizes the experiments used for validation. Sections 6.3 and 6.4 describe TADA in detail, including the turbulence model, boundary conditions, mesh, and rotor parameterization. Section 5.6 provides an an assessment of the impact of grid resolution on accuracy. Comparisons between the model and experiments are given in section 6.5, and conclusions are presented in section 6.7.

5.2 Terminology

The instantaneous velocity u_i is characterized in terms of Reynolds decomposition into averaged and fluctuating components:

$$u_i = \overline{u}_i + u_i' \tag{5.1}$$

The subscript $_i$ indicates components aligned with the coordinate system axes (i=$\{1,2,3\}$ corresponding to $\{x,y,z\}$). x is aligned with the flume longitudinal axis, positive in

the flow direction, y is oriented laterally and z is oriented vertically. The overline indicates the Reynolds average, while the prime indicates the fluctuating component. For convenience, the convention $\{u,v,w\}=\{\overline{u}_1,\overline{u}_2,\overline{u}_3\}$ is used for the averaged components.

Throughout this article the term *freestream* refers to measurements of the flow present at the location in the flume where the rotor would be placed, but without any rotors (or associated structures) present, and is denoted using the subscript $_0$. The freestream velocity u_0 is defined as the Reynolds-averaged axial velocity (u) measured in freestream conditions. The freestream turbulence intensity I_0 is defined later in this section.

In the context of a turbine array, it is also useful to define a *reference* condition, which is unique to each turbine in the array. The reference condition for turbine A corresponds to the flow at location A, with all turbines present in the flow except for turbine A. Standard thrust and power curves can be used to predict turbine performance if the reference conditions are known. However, such an approach is difficult to implement in practical simulations since it requires sequentially adding/removing turbines one at a time from the array. The subscript $_{\text{ref}}$ is used for this reference condition.

TADA instead uses a *disk averaged* condition to relate the turbine thrust and power to the local flow conditions (see §5.4.4 for details). This disk averaged condition is denoted with braces, e.g. $\langle u \rangle$ is the disk averaged, Reynold averaged velocity component in the x direction.

The turbulent kinetic energy k is defined as:

$$k = \frac{1}{2}\overline{u_i' u_i'} \tag{5.2}$$

where the tensor notation convention of summation over repeated indices is used. The turbulence intensity in freestream conditions is defined as:

$$I_0 = \frac{\sqrt{\left(\frac{2}{3}k_0\right)}}{u_0} \tag{5.3}$$

The main parameters used for validating the methodology were the power of the downstream rotor P^{down} as well as lateral transects of axial velocity $u(y)$ and turbulent kinetic energy $k(y)$ in the rotor wake. The downstream rotor power was non-dimensionalized using the freestream kinetic power density, according to the tra-

ditional definition of power coefficient:

$$C_{\mathrm{P,u_0}}^{\mathrm{down}} = \frac{P^{\mathrm{down}}}{\frac{1}{2}\rho u_0^3 \pi R^2} \tag{5.4}$$

where R is the rotor radius. In simulations the rotor speed Ω was set using the tip-speed ratio TSR=$R\Omega/u_0$.

The turbulent kinetic energy in the wake was quantified using:

$$I_{\mathrm{u_0}} = \frac{\sqrt{\left(\frac{2}{3}k\right)}}{u_0} \tag{5.5}$$

This differs from the standard definition of turbulence intensity (I), which would use the local velocity magnitude in the denominator, instead of u_0. $I_{\mathrm{u_0}}$ is a more suitable metric for the present validation because it depends only on the local k in the wake, whereas I depends on both the local velocity and k.

5.3 Experimental Data

The experimental data-set was collected by Mycek *et al.* [76, 77] at the IFREMER (French Research Institute for Exploitation of the Sea) wave and current flume tank. Both single and tandem rotor configurations were tested, using both the normal flume configuration (I_0=3%) and with the flow conditioning honeycombs removed (I_0=15%). Experiments were done over a range of u_0=$\{0.4, 0.6, 0.8, 1.0\}$ m/s. The flume test section was 18 m long, 4 m wide and the water depth was 2 m. For the tandem rotor configurations, the rotors were separated axially by distances of a = 2D–12D, where D=0.7 m is the rotor diameter.

The model turbines were suspended in the water, with their rotors centred at mid-depth (z=0). The rotor was driven by a speed-controlled motor, with a torque cell. A load cell located above the water surface measured the total axial load acting on the rotor and its supporting structures.

Velocities u_i (i=$\{1,2\}$) were measured using a traversing Laser Doppler Velocimeter (LDV), ensuring stable statistics for mean velocities ($\overline{u}_1$,$\overline{u}_2$) and Reynolds stresses ($\overline{u_1'u_1'}$, $\overline{u_1'u_2'}$, $\overline{u_2'u_2'}$) had converged [76, 77].

Since the vertical velocity (u_3) was not measured, $\overline{u_3'u_3'}$ had to be estimated when calculating k and I for comparison to simulations. To make this estimate, a different

data-set of turbine wakes in a flume, collected at the University of Manchester [73, 74] was used. That data allowed calculation of the ratios:

$$\gamma_{31} = \frac{\overline{(u_3' u_3')}}{\overline{(u_1' u_1')}}, \quad \gamma_{32} = \frac{\overline{(u_3' u_3')}}{\overline{(u_2' u_2')}} \tag{5.6}$$

from both vertical and transverse wake transects. This provided γ_{31}=1.08 $\pm$ 0.10 (standard deviation) and γ_{21}=0.85 $\pm$ 0.09. Thus, for the IFREMER data, an estimate of $\overline{(u_3' u_3')}$ was made using:

$$\overline{(u_3' u_3')} = \frac{1}{2}\left(\gamma_{31}\overline{(u_1' u_1')} + \gamma_{32}\overline{(u_2' u_2')}\right) \tag{5.7}$$

This allowed calculating k with eq. 5.2 and I_{u_0} using eq. 5.5, which was used to validate the simulations.

The wake dynamics are expected to be representative of full-scale turbines. The rotor diameter was D=0.7 m, and the freestream velocity ranged from 0.4 m/s to 1.0 m/s, giving a minimum Reynolds number (based on D) of Re=2.8×10^5, which is above the threshold of 9.3×10^4 for Re-independent wake behavior [75], for wind turbine wakes.[3]

The turbine performance itself was however *not* Reynolds-independent. Mycek *et al.* [76] showed that the power coefficient varied significantly with u_0. This sensitivity was likely due to the chord-based Reynolds number being within the Re-sensitive regime for the selected airfoil. This sensitivity presented challenges to parameterizing the rotor for simulations, as discussed in section 6.4.

The I_0=15% turbulence cases were difficult to model because the wake skewed somewhat laterally. The inflow along the centreline had a transverse component in these cases, suggesting a transverse circulation pattern, which was not adequately measured to allow including it in simulations. The simulations assumed a purely axial flow, and thus to compare apples-to-apples, each experimental wake transect was shifted laterally to align the wake centre to y=0. The experimental wake centre was found using the following weighted average:

$$y_c = \frac{\sum (1 - \overline{u}_1/u_0) y}{\sum (1 - \overline{u}_1/u_0)} \tag{5.8}$$

[3] In theory, Re-dependence of tidal turbine wakes should be similar to wind turbines. The authors are not aware of an analogous study targeting tidal turbine wakes.

The required shift varied linearly from 0 at x=0, to 0.4D at x=6D, then stayed constant at 0.4D to the end of the measurement range (x=12D).

5.4 Simulation Methodology

TADA relies on Reynolds-averaged Navier-Stokes (RANS) simulations to predict wake effects.[4] While not specifically validated herein, RANS methods are suitable for predicting the influence of the bottom boundary topology on velocity, which has been shown for atmospheric wind in complex terrain (e.g. [96], [97], [98]). Such capability is important for future application of TADA to modelling real-world tidal farms.

In the simulations, the turbine was represented using an actuator disk e.g.[19], which was implemented in the commercial software ANSYS CFX.

5.4.1 Governing Equations

The steady, incompressible Reynolds-averaged Navier Stokes (RANS) equations were used for all simulations, shown below using tensor notation:

$$\frac{\partial \overline{u}_i}{\partial x_i} = 0 \tag{5.9}$$

$$\overline{u}_j \frac{\partial \overline{u}_i}{\partial x_j} = \frac{\partial}{\partial x_j}\left[-\frac{\overline{p}\delta_{ij}}{\rho} + 2\nu S_{ij} - \overline{u'_i u'_j}\right] + \frac{\overline{S_{\mathrm{M}i}}}{\rho} \tag{5.10}$$

where p is the pressure, x_i is the spatial co-ordinate, ν is the fluid kinematic viscosity and ρ the density. The Dirac delta function, δ_{ij}=1 for $i = j$ and equals zero otherwise. $\overline{S_{\mathrm{M}i}}$ is a Reynolds-averaged momentum-source term, used to impose the rotor forces on the flow. The term S_{ij} is the mean rate-of-strain tensor defined by:

$$S_{ij} = \frac{1}{2}\left(\frac{\partial \overline{u}_i}{\partial x_j} + \frac{\partial \overline{u}_j}{\partial x_i}\right) \tag{5.11}$$

[4]It may also be possible to implement a similar methodology in the context of simpler empirical wake models, or more complex time-resolved CFD methods. RANS was specifically selected for this study as a reasonable compromise between accuracy, robustness, and computational expense.

The turbulent Reynolds stresses were modelled using the Boussinesq turbulent viscosity hypothesis, which for incompressible flows is;

$$-\overline{u_i' u_j'} = 2\frac{\mu_t}{\rho} S_{ij} \tag{5.12}$$

where μ_t is the eddy viscosity and k is the turbulent kinetic energy. The eddy viscosity enhances momentum exchange across shear layers, and is critically important for predicting the mixing of turbine wakes with the surrounding flow. This mixing influences the flow velocity in the wake, and therefore the power available to the downstream rotor. Thus, μ_t is a critical parameter for predicting the impact of wake shadow.

Numerous methods have been formulated for defining μ_t, the most widely applied being the standard k-ε [60] and k-ω [61] models. However, when using either of these formulations for AD simulations, rotor wakes tend to mix-out too quickly. Many researchers (e.g. [50, 51, 55, 57, 59]) have proposed modifications that limit the eddy viscosity in rotor wakes to mitigate this issue.

Shives and Crawford [99, 11] found that the shear-stress-transport SST model of Menter [32] (which is a hybrid k-ε/k-ω model) provided the best wake predictions out of several options, and it is used throughout this article. The SST model has been extensively validated and is known to perform well in flows with adverse pressure gradients and mild regions of separated flow ([29], [32]). For these reasons, the SST model is expected to perform well for tidal-channel flows, which may have complex bathymetric features.

5.4.2 Simulation Domain and Mesh

The simulation domain was the entire test section of the IFREMER flume tank. Computational meshes were generated using an automated in-house mesh generation tool. The mesh spacing was characterized by the quantity EPD (elements per-diameter). Meshes with EPD=$\{7, 9, 11, 15, 21\}$ (see figure 5.1) were used to study sensitivity to grid resolution. These meshes were quite coarse compared to the grid-independent meshes found in [11], which used a different style of AD employing blade-element methods to characterize the rotor forces. The present TADA methodology compensates for a coarse mesh by tuning the rotor parameterization specifically for the employed mesh (see section 6.4).

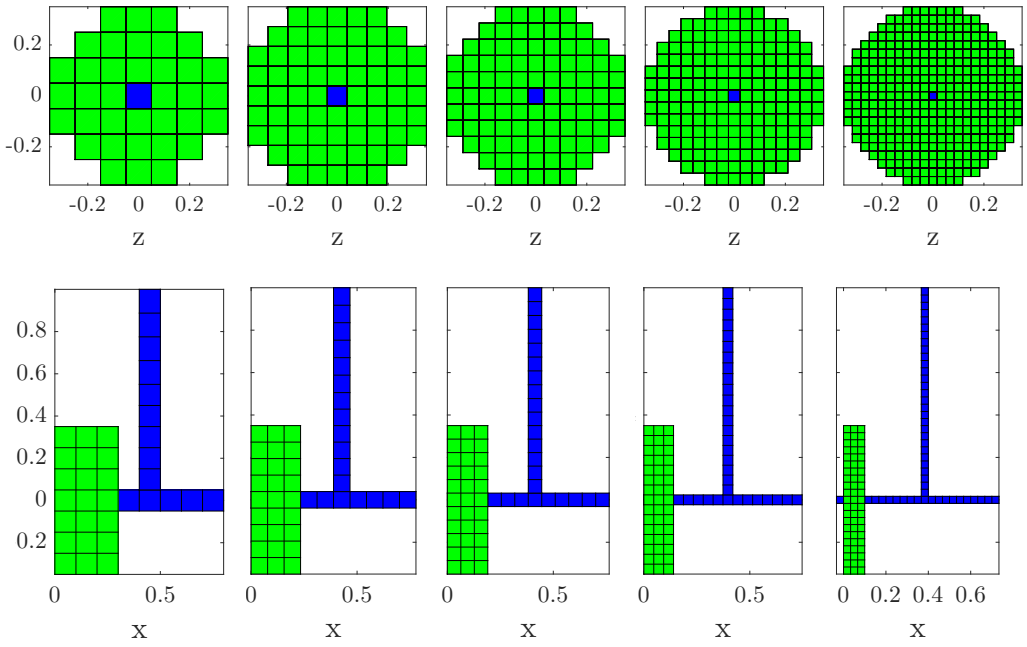

Figure 5.1: Actuator disk mesh with {7,9,11,15,21} EPD from left to right.

The hexahedral elements had dimensions Dx (streamwise), Dy (depthwise) and Dz (transverse), which are normalized using the rotor diameter D or water depth H. Near the rotors, Dx was constant at Dx=D/EPD within a region from D/2 upstream of each rotor to 2D downstream of each rotor. Upstream of that region, Dx increased using a geometric growth law with a ratio of 1.2 to a maximum of 0.1H. Downstream of the constant Dx region, Dx increased with a ratio of 1.07 to a maximum of 0.07H. The depthwise spacing Dy was 0.0025H at the flume bottom, expanding to Dy=D/EPD (ratio=1.2) at the bottom of the rotor, remaining constant to the water free surface. The transverse spacing was 0.0025H at the flume sides, increasing with an expansion ratio of 1.2, then decreasing with a ratio 1.2 to Dz=D/EPD at the edge of the rotor. The near-wall spacing of Dy_1=0.0025H gave y^+ ranging from 90 (u_0=0.4 m/s, I_0=3%) to 230 (u_0=1.03, I_0=15%). The flow parameters of interest (u and I_{u_0}) were found to be insensitive to the near-wall spacing, as depicted in figure 5.3.

The AD region included elements whose centroids were within the rotor radius, and spanned 3 elements in the axial (x) direction. Using less than 3 elements was found to degrade the simulation convergence behaviour, while using more elements was undesirable since it expanded the AD region over a much larger volume than the real rotor. Sample meshes are depicted in figure 5.2, with the AD regions shown in

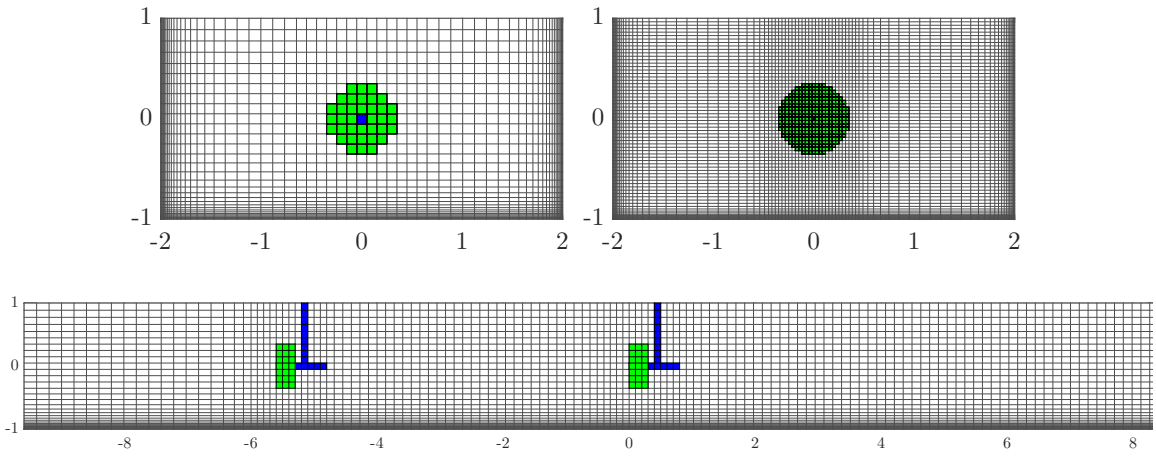

Figure 5.2: Front (top) view of the mesh with 7EPD (left), 21EPD(right). Side View (bottom) for the 7EPD mesh with two rotors separated by 8D.

green and the hub/tower in blue.

The hub and supporting tower were represented by removing mesh elements from the fluid domain. Thus, the meshed diameter of the hub and tower corresponds to the element size rather than their true physical size. This mis-represents somewhat the drag associated with the structural components of the turbine. A detailed analysis of the error in predicting the drag on the structural elements was not possible because the validation experiments measured the total axial force on the turbine rather than the rotor thrust and tower drag individually. In [11] the tower was explicitly resolved by the computational mesh, and it's drag was predicted to be approximately 10% of the rotor thrust with I_0=3%, and 20% of the thrust with I_0=15%. For comparison, with I_0=3%, TADA predicted the tower drag to be ≈{30%,23%,19%,14%,10%} of the rotor thrust on grids with {7,9,11,15,21} EPD. With I_0=15% the tower drag was ≈{34%,26%,22%,16%,12%} of the rotor thrust for the respective grid resolutions. It is not clear whether the tower drag was well predicted in any of the above cases, since RANS simulations inherently do not resolve the characteristic unsteady Von-Karman vortex shedding from cylinders in cross-flow. While this is an issue requiring further study, as demonstrated in section 6.5 TADA predicts the turbine wakes well, even with the support structures under-resolved.

With 9 EPD the twin-rotor meshes contained ≈320,000 elements, and the simulations converged in under 10 minutes using 3 cores on a Intel®i7 CPU (2.67GHz). The scalability of runtime with number of turbines and mesh size has not yet been established.

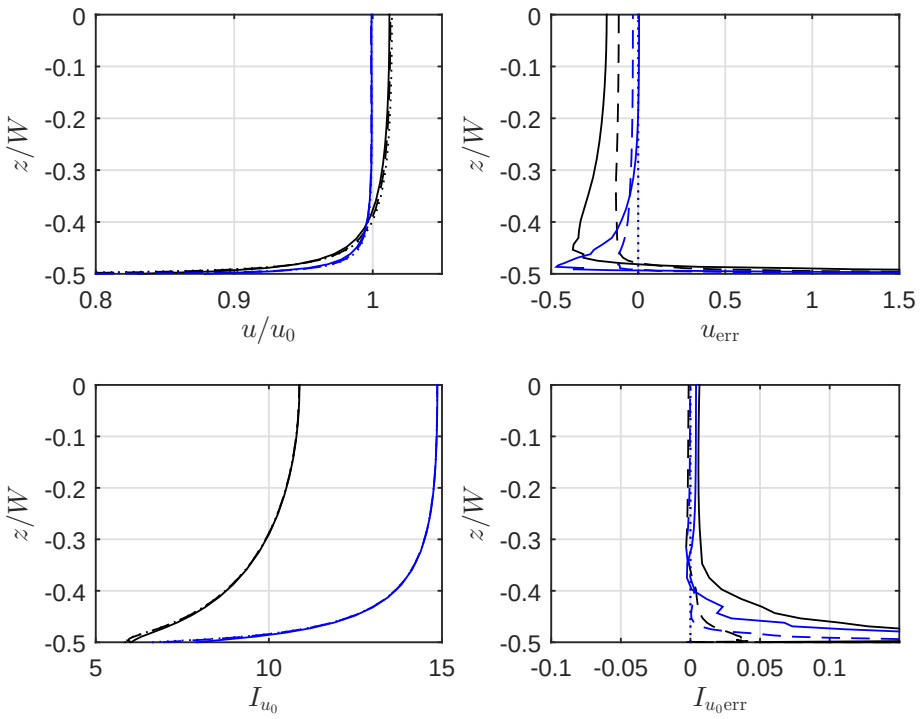

Figure 5.3: Sensitivity of velocity and turbulence intensity to the near-wall spacing. Blue (black) lines are for results 8D upstream (downstream) of the rotor nominal location. Results shown for $\mathrm{Dy}_1 = \{1, 5, 20\}$ mm {dotted, dashed, solid} lines. u_{err} is defined as $(u - u_{\mathrm{Dy=1mm}})/u_0$

5.4.3 Boundary Conditions

The inflow was specified using a plug flow condition, specifying u_{IN}, k_{IN} and ω_{IN}. These parameters were tuned to obtain the best possible match to the freestream (i.e. no rotors present) velocity and turbulence intensity as measured by [76]. The tuned inflow conditions are summarized in table 5.1, which also shows the eddy lengthscale defined as $L_{\mathrm{IN}} \equiv \sqrt{k_{\mathrm{IN}}}/(\beta' \omega_{\mathrm{IN}})$, corresponding loosely to the largest-scale eddies in the flow.[5] Note the larger length-scales for the high turbulence cases, for which the flow conditioning screens had been removed.

In the absence of the turbines, the turbulence intensity decayed exponentially along x from the inlet to the outlet. For the case with (I_0=2.7, u_0=0.8), $I_{\mathrm{u_0}}$ was {3.1, 2.6, 2.3}% at x/D={-10, 0, 10} respectively. For the case with (I_0=14.7, u_0=0.83), $I_{\mathrm{u_0}}$

[5]This lengthscale corresponds to ideal isotropic turbulence and does not necessarily represent the true size of eddies in the flow. Note that $\beta' = 0.09$ is a turbulence model coefficient.

freestream		inlet conditions			
I_0	u_0(m/s)	u_{IN} (m/s)	k_{IN} (m^2/s^2)	ω_{IN} (m^2/s^3)	L_{IN} (m)
2.7%	0.40	0.394	2.90×10^{-4}	0.368	0.51
2.6%	0.60	0.592	5.70×10^{-4}	0.480	0.55
2.7%	0.80	0.790	1.08×10^{-3}	0.607	0.60
2.7%	1.00	0.988	1.68×10^{-3}	0.763	0.60
15.3%	0.41	0.404	8.80×10^{-3}	0.152	6.88
14.7%	0.62	0.611	2.00×10^{-2}	0.333	4.71
14.7%	0.83	0.819	3.20×10^{-2}	0.347	5.72
14.7%	1.03	1.017	4.90×10^{-2}	0.408	6.03

Table 5.1: Inflow Parameters set to match IFREMER experimental data

was {16.5, 13.5, 11.1}% at x/D={-10, 0, 10}. Based on the wake transect data, the turbulence did not decay as quickly in the I=15% experiments, for which k remained relatively constant along the channel. A possible explanation for the faster decay rate in the simulations is that they did not model any transverse circulation, which may have been present in the experiment. The spatial velocity gradients created by a transverse circulation would contribute to shear production of k preventing its decay along the channel. There was not sufficient measured data to include such transverse circulation in the simulations, so as a compromise, the turbulence was set too high at the inlet, and dissipated to the measured values at the rotor, while becoming too low by the outlet.

The flume bottom and side walls used a no-slip condition assuming smooth walls. The *automatic* wall function treatment of CFX [100] was used, which assumes a universal log profile to set the wall shear stress based on the first grid cell velocity and height. The same condition was enforced for the hub and tower. The boundary layers on the flume walls evolved according to the numerical method downstream of the inlet. The water free-surface used a rigid-lid assumption (no surface deformation, and a free-slip wall condition).[6] The outlet used a typical static pressure condition.

[6]Previous work [41] found that modelling a dynamic free-surface (volume-of-fluid) was an order of magnitude more computationally expensive, and only gave significantly different results for very high blockage ratios, justifying the use of a rigid lid.

5.4.4 Actuator Disk Model

The forces created by the turbine rotor were imposed on the flow domain via the momentum source term $\overline{S_{\mathrm{M}i}}$ in equation 6.5. These sources were applied only within the AD region (displayed in green in figure 5.2). The rotor forces are best specified in terms of axial ($\overline{S_{\mathrm{M}x}}$) and tangential ($\overline{S_{\mathrm{M}\theta}}$) components, in a cylindrical coordinate system aligned with the rotor. Various AD implementations differ in the manner in which they specify these source terms. The simplest approach is to assume a uniform distribution within the AD:

$$\overline{S_{\mathrm{M}x}} = -\frac{1}{2V}\rho C_{\mathrm{T}} u_{\mathrm{ref}}^2 \pi R^2, \quad \overline{S_{\mathrm{M}\theta}} = -\frac{1}{2r\Omega V}\rho C_{\mathrm{P}} u_{\mathrm{ref}}^3 \pi R^2 \tag{5.13}$$

where Ω is the the rotor speed, V is the volume of the AD region, R is the rotor radius and u_{ref} is a reference velocity, which for a single rotor corresponds to the freestream. For turbine farms, and in complex bathymetry, it is challenging to define the appropriate reference velocity u_{ref} for each rotor.

Politis *et al.* [98] discuss this issue at some length, and identified several methods for defining u_{ref}. One method, applicable for a turbine farm consisting of rows of turbines oriented perpendicular to the flow direction, was to run simulations sequentially. The first simulation would have no rotors present, and the hub-height velocity at the location of each rotor in the first row would be used as u_{ref}. For the next simulation, the first row of rotors would be added to the simulation, with their thrust and power specified using the pre-determined values of u_{ref}. Each sequential simulation would add a new row of turbines. According to this methodology, u_{ref} can be defined as the flow velocity at the rotor location, when the rotor is not present. Politis *et al.* [98] note that such a methodology is quite impractical, particularly for arrays not perpendicular to the flow.

Politis *et al.* [98] also tested setting u_{ref} as the velocity at hub-height 1D upstream of the turbine. This consistently under-predicted the rotor trust and power, due to the rotor slowing the upstream flow. They concluded that a correction to account for this slowing was necessary. It would be difficult to design a robust correction applicable to a wide variety of situations, because alterations of the flow due to terrain and wakes cannot be effectively combined by linear superposition [98]. Setting u_{ref} from an upstream location presents additional problems because complex bathymetry and/or turbine wakes can cause significant variations in flow speed and direction over distances on the order of 1-3 turbine diameters.

Various alternative methods for specifying the reference velocity were tested by [94], who concluded that the best approach is to define alternative thrust and power coefficients, which use the volume-averaged velocity in the AD as a reference velocity. This approach was also suggested by the current authors [10], and avoids the need to run sequential simulations, and also avoids problems associated with setting u_{ref} from a point upstream of the rotor. The volume averaging process is defined for a general variable ϕ as:

$$\langle \phi \rangle = \frac{\int_{\mathcal{V}} \phi d\mathcal{V}}{\int_{\mathcal{V}} d\mathcal{V}} \tag{5.14}$$

The above integrals are evaluated numerically over all mesh elements within the AD region. CFX [80] has a built-in capability for such volume integrals. Using the volume-averaged velocity $\langle u \rangle$ as the reference velocity requires defining alternative rotor performance parameters:

$$C_{\text{T}}^{\star} = \frac{T}{\frac{1}{2}\rho \left\langle u^2 \right\rangle \pi R^2}, \quad C_{\text{P}}^{\star} = \frac{P}{\frac{1}{2}\rho \left\langle u^3 \right\rangle \pi R^2} \tag{5.15}$$

Using $C_{\text{T}}^{\star}$ and $C_{\text{P}}^{\star}$ to specify the rotor performance allows for one-shot simulations of turbine farms in complex terrain, however it requires tuning, as discussed in section 6.4. Using this approach, the momentum source terms can be specified as:

$$\overline{S_{\text{M}x}} = -\frac{1}{2V}\rho C_{\text{T}}^{\star} \left\langle u^2 \right\rangle \pi R^2, \quad \overline{S_{\text{M}\theta}} = -\frac{1}{2r\Omega V}\rho C_{\text{P}}^{\star} \left\langle u^3 \right\rangle \pi R^2 \tag{5.16}$$

The above equations distribute the momentum sources uniformly over the AD, which is a fairly crude assumption. In reality, the rotor forces vary radially and with the local inflow velocity. The distribution of loads along each blade could be found using blade-element-momentum theory (e.g. [101]), or higher-fidelity modelling approaches (e.g. blade-resolved CFD simulations, or AD simulations which use blade element theory predict the blade loads [11] [102]). However, such higher-fidelity models require finer meshes than the present AD approach, and their computational expense makes them less appropriate for simulating large arrays of turbines.

An alternate approach is to define 'reference' profiles ($c_x(r)$, $c_\theta(r)$) to distribute the rotor loads in a realistic manner. This approach was taken by [59], who created reference profiles for the NREL 5-MW reference wind turbine, which they later applied to several different wind turbines, with good success. For the present study, reference profiles were created for the rotor used by Mycek *et al.*, using high-resolution blade-

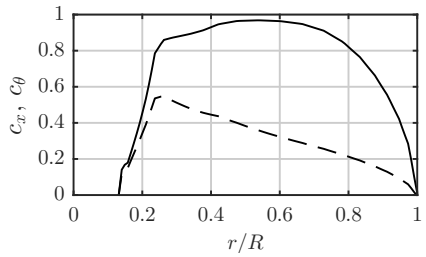

Figure 5.4: Reference rotor loading profiles c_x (solid), c_θ (dashed)

element AD simulations [11]. The reference profiles are shown in figure 5.4, and correspond to the rotor operating at its design tip-speed-ratio.[7]

Thus, with known $C_{\mathrm{T}}^{\star}$, $C_{\mathrm{P}}^{\star}$, $c_x(r)$ and $c_\theta(r)$, the appropriate momentum source terms are defined as:

$$\overline{S_{\mathrm{M}x}} = -\frac{1}{2}\rho \left\langle u^2 \right\rangle C_{\mathrm{T}}^{\star} \pi R^2 \left[\frac{u^2 c_x}{\int_{\mathcal{V}} u^2 c_x d\mathcal{V}} \right] \tag{5.17}$$

$$\overline{S_{\mathrm{M}\theta}} = -\frac{1}{2}\rho \frac{1}{r\Omega} \left\langle u^3 \right\rangle C_{\mathrm{P}}^{\star} \pi R^2 \left[\frac{u^2 c_\theta r}{\int_{\mathcal{V}} u^2 c_\theta r d\mathcal{V}} \right] \tag{5.18}$$

where the terms in square braces distribute the rotor loading according to c_x, c_θ, and the square of the local velocity. The dependence on local velocity is included to enhance the model performance in sheared or yawed flows, which will have a significant impact on how the loads are distributed across the disk. In the present work, equations 5.17 and 5.18 were used to specify the AD momentum sources.

5.5 Actuator Model Tuning

TADA relies on tabulated values of $C_{\mathrm{T}}^{\star}$ and $C_{\mathrm{P}}^{\star}$ to define the rotor performance over a wide range of inflow conditions. Populating these tables is done by running simulations which use known performance data (thrust and power) to specify the momentum sources, and then calculating $C_{\mathrm{T}}^{\star}$ and $C_{\mathrm{P}}^{\star}$ as a post-processing step. The present study used experimental data [76] for a single rotor in the flume to generate the tables. A total of 56 tuning simulations were run, spanning two inflow turbulence intensities (I_0), four inflow velocities (u_0), and seven different tip-speed-ratios (TSR).

[7] For simplicity, the same shape profiles were used for all simulations, neglecting the dependence on TSR. The variation in the total loading with TSR is modelled correctly however, via the $C_{\mathrm{T}}^{\star}$, $C_{\mathrm{P}}^{\star}$ terms.

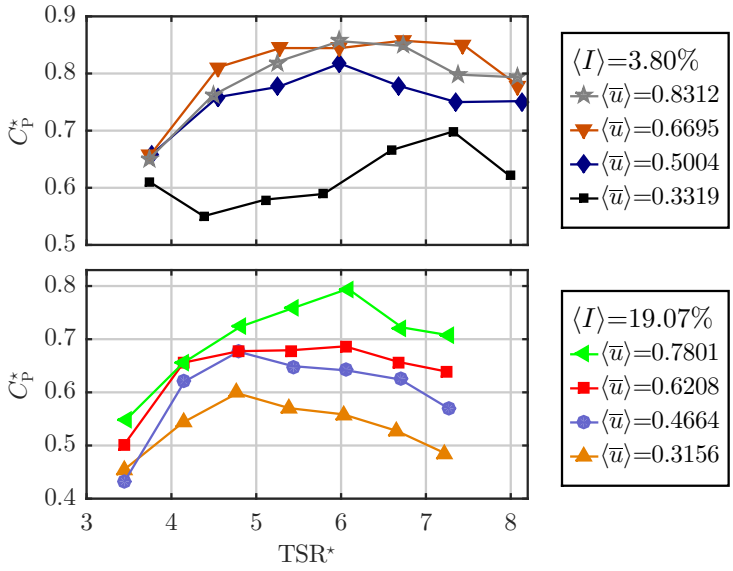

Figure 5.5: Calibrated rotor performance curves for $C_P^\star$. ($\langle u \rangle$ has unit m/s)

For each tuning simulation, the momentum source terms were set using the experimental results for thrust and power (T_{ex}, P_{ex}) according to:

$$\overline{S_{Mx}} = -T_{ex}\left[\frac{u^2 c_x}{\int_{\mathcal{V}} u^2 c_x d\mathcal{V}}\right] \tag{5.19}$$

$$\overline{S_{M\theta}} = -\frac{1}{r\Omega} P_{ex}\left[\frac{u^2 c_\theta r}{\int_{\mathcal{V}} u^2 c_\theta r d\mathcal{V}}\right] \tag{5.20}$$

Then, $C_T^\star$ and $C_P^\star$ were found from the final converged values of $\langle u^2 \rangle$ and $\langle u^3 \rangle$ according to equation 6.27.

The ensuing performance model was sensitive to the disk-averaged axial velocity $\langle u \rangle$, disk-averaged turbulence intensity $\langle I \rangle = \left\langle \sqrt{(2/3)k}/u \right\rangle$, and the re-normalized tip-speed-ratio $\text{TSR}^\star = R\Omega / \langle u \rangle$.

The resulting lookup table for $C_P^\star$ is depicted in figure 5.5. A similar lookup table (not shown) was created to define $C_T^\star$. The different curves in figure 5.5 correspond to different freestream speeds and turbulence intensities. These plots highlight the rotor's sensitivity to inflow speed, which is the result of the airfoil's sensitivity to the chord-based Reynolds number.[8]

TADA was configured to do linear interpolation between the tabulated $C_T^\star$ and $C_P^\star$, based on the current values of $\text{TSR}^\star$, $\langle I \rangle$ and $\langle u \rangle$, which need to be evaluated at each

[8] At 3/4 span Re_c varied from 5×10^4 (u_0=0.4 m/s, TSR=3) to 2×10^5 (u_0=1 m/s, TSR=6)

iteration of the solver algorithm. The interpolation was done in a three-step process, first finding $(C_{\mathrm{T}}^{\star}, C_{\mathrm{P}}^{\star})$ at the current $\mathrm{TSR}^{\star}$ for each of the 8 performance curves, then interpolating with respect to $\langle u \rangle$ and finally interpolating with respect to $\langle I \rangle$.[9] This approach differs from [94], who re-tuned their $C_{\mathrm{P}}^{\star}$, $C_{\mathrm{T}}^{\star}$ curves specifically for different inflow turbulence intensities. The interpolation used herein allows applying TADA for turbulence intensities in between calibration cases, assuming a linear variation.

Thus, the rotor parameterization was sensitized to changes in the rotor speed, flow velocity, and turbulence intensity. This was necessary because the rotor performance varied with all three of these parameters. Full-scale rotors will operate at much higher Reynolds numbers, and therefore the sensitivity to $\langle u \rangle$ (which arises from the airfoil's Re-dependence) may not be important for full-scale turbines. It is presently unclear whether full-scale rotor performance will be very sensitive to turbulence intensity or not.

5.6 Sensitivity to Mesh Density

The actuator model is somewhat sensitive to the mesh density. The goal with TADA is to tune the actuator model for the specific mesh density to be used in turbine farm simulations. However, for realistic tidal channels with variable depth, it may be difficult to ensure that all rotors are resolved with the same mesh density, and some rotors may have more or less elements spanning their diameter. Thus it is prudent to determine the sensitivity of thrust and power to using lookup tables calibrated for a certain grid density, on finer or coarser grids.

The tuning procedure (§6.4) was done for the 56 tuning cases, using a mesh with EPD=9, to populate the $(C_{\mathrm{T}}^{\star}, C_{\mathrm{P}}^{\star})$ lookup-tables. TADA was then run, using the lookup-tables to define the rotor performance, for the same 56 cases. These simulations were done with grids using EPD=$\{7, 9, 11, 15, 21\}$ to assess the sensitivity to using a mesh with a different density than that used for tuning. The thrust (T) and power (P) error were then found from:

$$T_{\mathrm{err}} = \frac{T_{\mathrm{sim}} - T_{\mathrm{ex}}}{T_{\mathrm{sim}}}, \quad P_{\mathrm{err}} = \frac{P_{\mathrm{sim}} - P_{\mathrm{ex}}}{P_{\mathrm{sim}}} \tag{5.21}$$

and are shown for all tests in figure 5.6. As expected, the errors were very low

[9] An alternative to this interpolation may be to use multi-variable regression to fit an equation to the lookup tables.

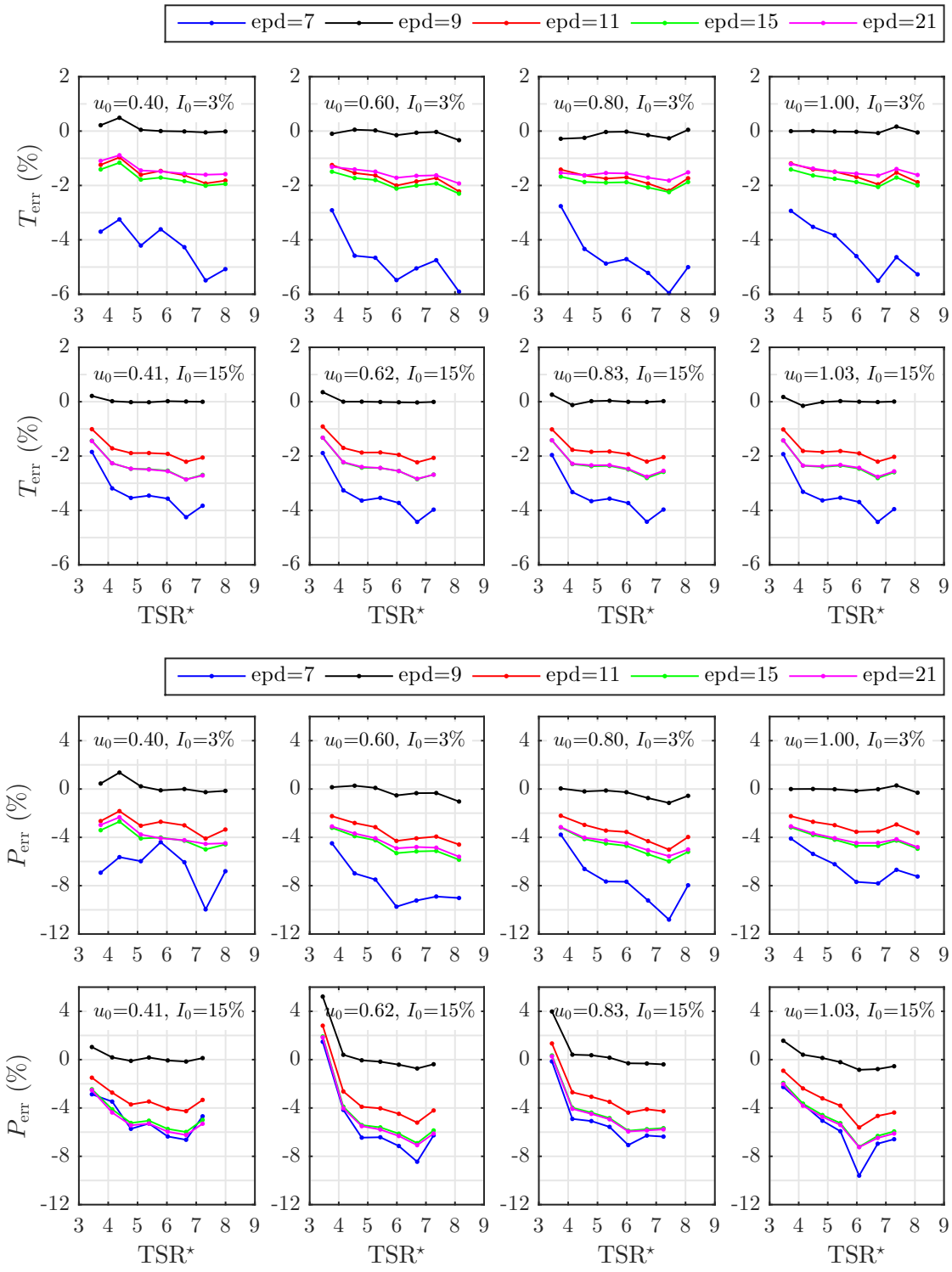

Figure 5.6: Thrust and power error for different mesh densities. Results are shown for all 56 tuning cases, which were for a single rotor in the flume.

on the 9EPD grid since that was the resolution used for the calibration procedure. Interestingly, the coarser and finer grids both under predicted thrust T and power P. The worst errors were on the EPD=7 grid, with T under-predicted by about 4%-5%, and P under predicted by about 6%-11%. The finer grids gave lower errors. There was a convergent trend with increasing density; the 15 and 21 EPD grids gave almost identical errors. Therefore, it is reasonable to assume that further refinement above 21 EPD would produce similar errors as the 21EPD grid. The error associated with using the 9EPD calibrated model on finer grids therefore hits a maximum of about 3% for T, and 6% for P.

The power predicted by the simulations depends on the tuned $C_{\mathrm{P}}^{\star}$ lookup, and the modelled $\langle u^3 \rangle$:

$$P = \frac{1}{2}\rho \left\langle u^3 \right\rangle C_{\mathrm{P}}^{\star} \left(\langle u \rangle, \langle I \rangle, \mathrm{TSR}^{\star} \right) \pi R^2 \tag{5.22}$$

The difference in power (ΔP) between the 9 EPD grid and the other grids arises from differences in $\Delta C_{\mathrm{P}}^{\star}$ and $\Delta \langle u^3 \rangle$.

$$\Delta P = \frac{1}{2}\rho\pi R^2 \left[C_{\mathrm{P}}^{\star} \Delta \left\langle u^3 \right\rangle + \left\langle u^3 \right\rangle \Delta C_{\mathrm{P}}^{\star} \right] \tag{5.23}$$

$$\Delta C_{\mathrm{P}}^{\star} = \left(\frac{\partial C_{\mathrm{P}}^{\star}}{\partial \langle u \rangle} \Delta \langle u \rangle + \frac{\partial C_{\mathrm{P}}^{\star}}{\partial \langle I \rangle} \Delta \langle I \rangle + \frac{\partial C_{\mathrm{P}}^{\star}}{\partial \mathrm{TSR}^{\star}} \Delta \mathrm{TSR}^{\star} \right) \tag{5.24}$$

When the simulations were run on different grids, the predicted values for $\langle u \rangle$, $\langle I \rangle$, $\mathrm{TSR}^{\star}$ and $\langle u^3 \rangle$ are somewhat different for each grid. The above equations allow determination of the contribution of each of these difference terms to ΔP. Figure 5.7 shows the contribution from these various terms for the 21EPD simulations. It is clear that the discrepancy between 9EPD and 21EPD models is primarily due to the discrepancy in the modeled $\langle u^3 \rangle$, with a smaller contribution from the $\mathrm{TSR}^{\star}$ term[10].

In summary, the impact of using a finer mesh density than used in the tuning procedure (9 EPD) is limited to about a 3% error in T, and a 7% error in P. The primary cause of this discrepancy is a change to the modelled $\langle u^2 \rangle$ (for T) or $\langle u^3 \rangle$ (for P).

[10] which actually reflects changes to $\langle u \rangle$ since Ω was defined as an input for each of these cases

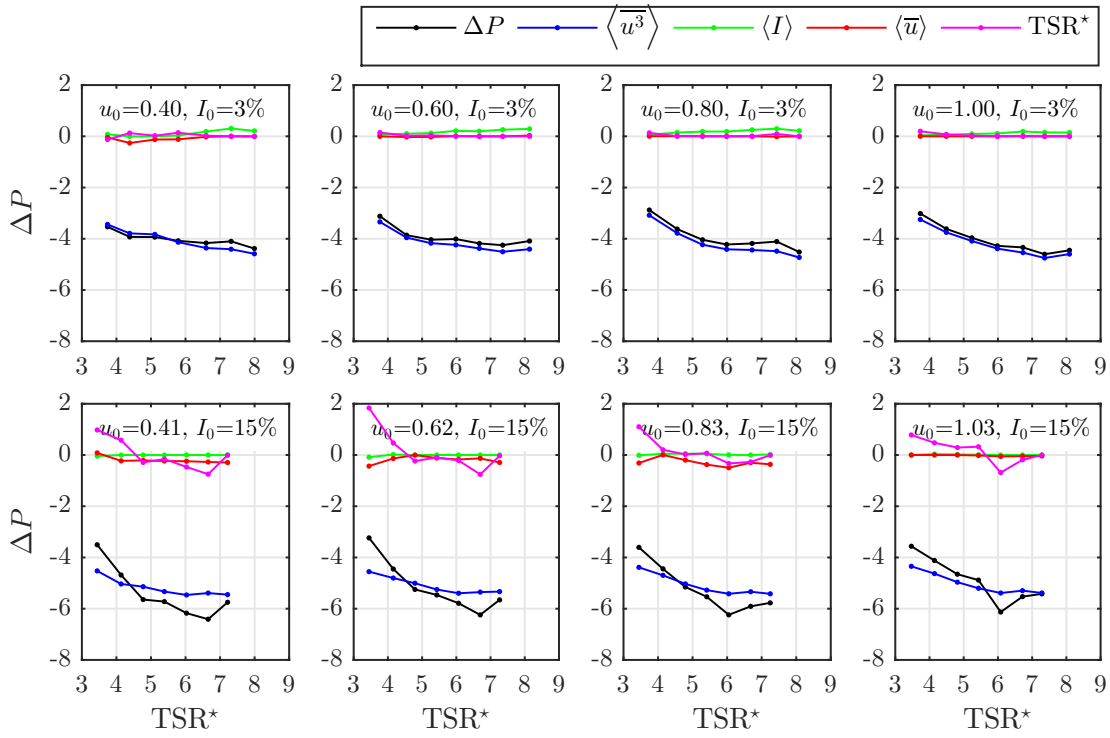

Figure 5.7: Contributions of various modelling errors to the ΔP discrepancy between 9EPD and 21EPD grids.

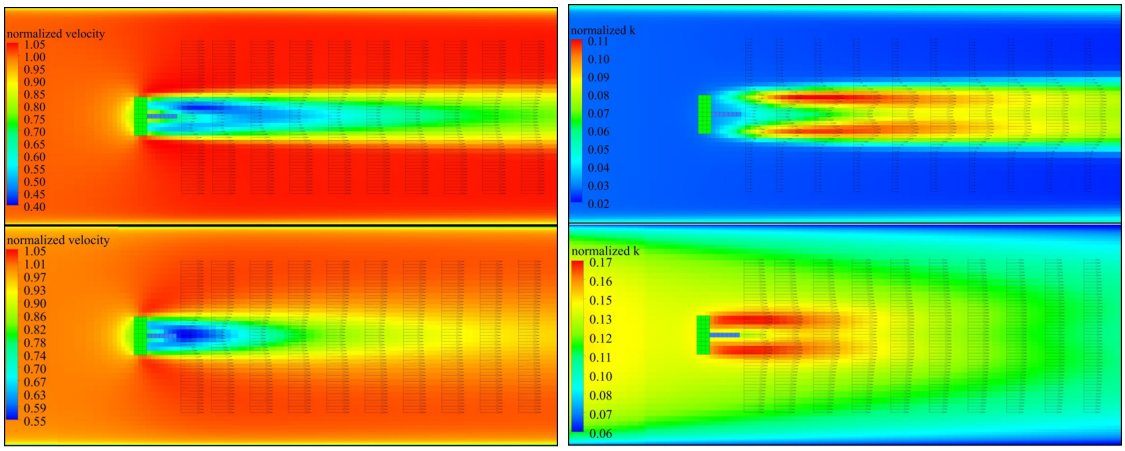

Figure 5.8: Qualitative images showing the velocity (u/u_0) and turbulence intensity (I_{u_0}) for the $I_0 = 3\%$, $u_0 = 0.80$m/s (upper) and $I_0 = 15\%$, $u_0 = 0.83$m/s (lower) cases (both with TSR=3.67).

5.7 Validation Results and Discussion

TADA was validated for its ability to model wakes (single and tandem rotor configurations) and to predict turbine power (tandem rotor configuration). The validation simulations set the rotor speed Ω to match the experiments. Then the lookup tables for $C_T^\star$ and $C_P^\star$ defined the rotor loads and performance. Simulations were run on all grid resolutions (EPD=$\{7, 9, 11, 15, 21\}$) but always using $C_T^\star$, $C_P^\star$ tuned for the 9EPD grid.

Validating the rotor wakes was done qualitatively by plotting profiles of velocity and turbulence intensity. Quantitative measures [11] were also used, including the rms error in u^3 and I, evaluated for each wake transect.

$$\text{rms}\left(u^3_{\text{err}}\right) = \sqrt{\text{mean}\left[\left(\frac{u^3_{\text{sim}} - u^3_{\text{ex}}}{u^3_0}\right)^2\right]} \tag{5.25}$$

$$\text{rms}\left(I_{\text{err}}\right) = \sqrt{\text{mean}\left[\left(I_{\text{sim}} - I_{\text{ex}}\right)^2\right]} \tag{5.26}$$

The term u^3/u_0^3 was used because it is a good proxy for the power of a downstream rotor in the wake, relative to that of the upstream rotor. These rms errors were evaluated for each wake transect, at $x/D = \{1.2, 2, 3, 4, 5, 6, 7, 8, 9, 10\}$.

TADA's prediction of the wake behind a single turbine is validated in sections 5.7.1 and 5.7.2. Its ability to predict the power of the downstream rotor is validated

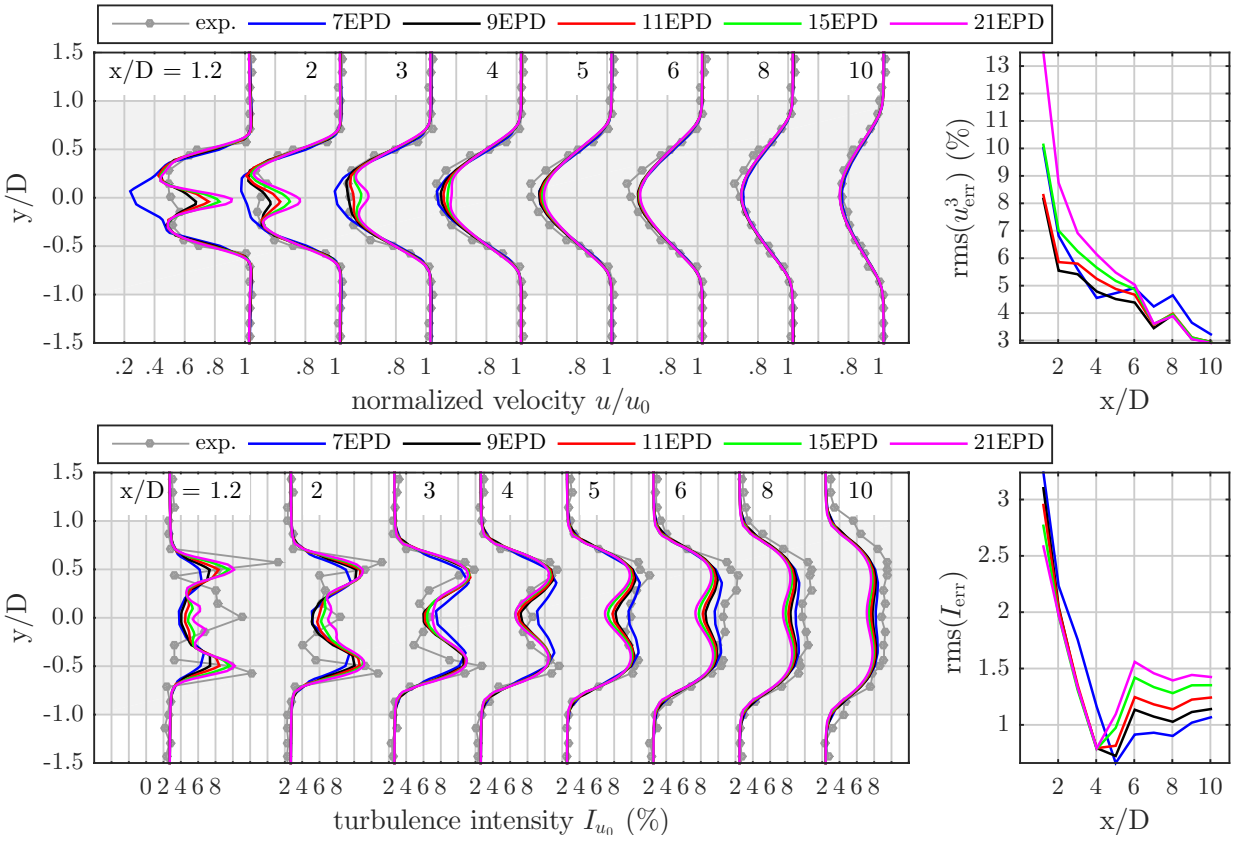

Figure 5.9: Lateral transects of the wake at several distances downstream of the rotor. $I_0 = 3\%$, $TSR = 3.67$, $u_0 = 0.8$m/s

in section 5.7.3. The rotor efficiency is discussed in section 5.7.4. Finally, the wake downstream of the second rotor is compared to experiments in section 5.7.5.

5.7.1 Single Rotor: Wake Profiles

The wake of a single rotor is depicted qualitatively in figure 5.8. It is evident that the velocity in the wake recovers more quickly in the higher turbulence scenario. Also evident is the distinct double-peak in the turbulence intensity profile in the shear layer of the wake.[11] Figure 5.8 also shows vector plots at the wake transects used for comparing to experimental results, shown in figures 5.9 (I_0=3%) and 5.10 (I_0=15%).

For the low turbulence case (figure 5.9), the wakes are predicted well compared to the experimental data. The axial velocity matches the experiments very well, with

[11] A point of interest is that the side-wall boundary layer is a source of k in the I_0=3% case, while it is a sink in the I_0=15%. This contributed to difficulty in maintaining a high level of turbulence in the simulations of the empty flume.

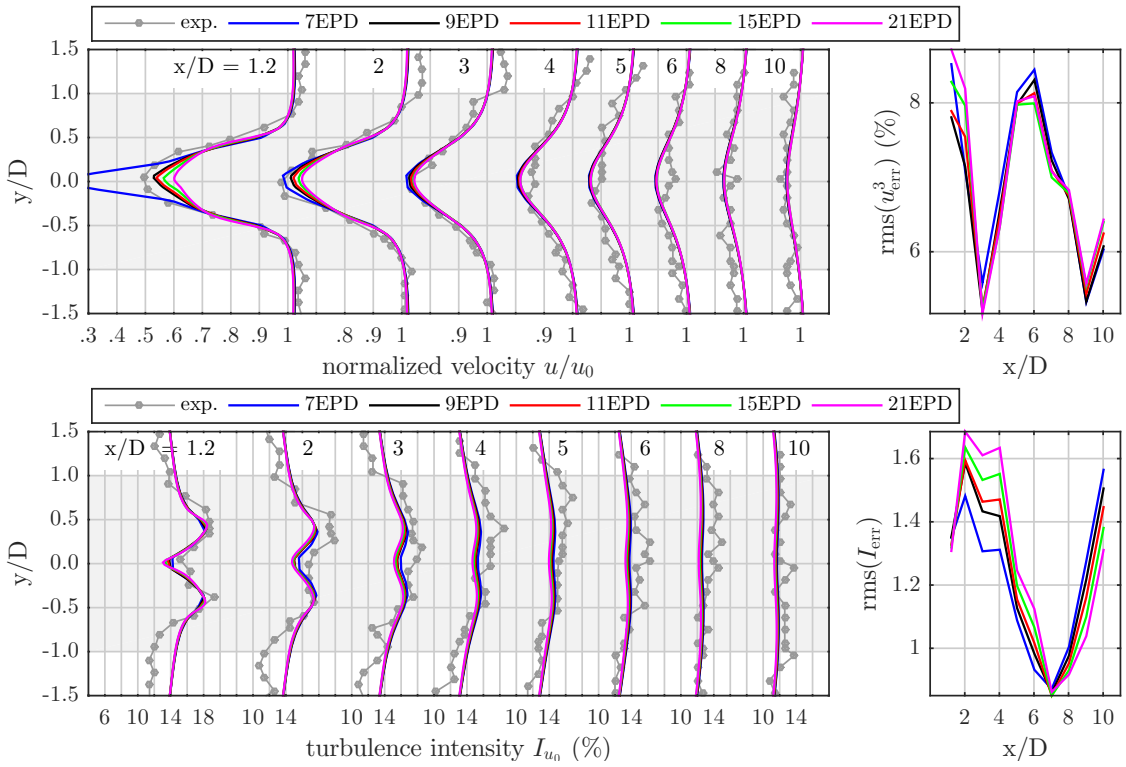

Figure 5.10: Lateral transects of the wake at several distances downstream of the rotor. $I_0 = 15\%$, $TSR = 3.67$, $u_0 = 0.83$m/s

only a slight over-prediction of the centreline velocity from 4D to 8D. The accelerated velocity along the wake edges ($u/u_0 > 1$) is correctly modelled. The turbulence intensity is reasonably predicted as well; the distinct double-peak profile is captured, but is somewhat under resolved (smeared-out) at 1.2D and 2D. Further downstream, I_{u_0} is a close match to the experiments, but it seems the turbulence decays slightly faster in the simulations.

The influence of grid resolution on the wake is evident in figure 5.9. The 7EPD grid gives poor results at x=1.2D, with the wake of the supporting tower producing a large velocity deficit. Interestingly, increasing the grid resolution decreases the velocity deficit in a region downstream of the supporting tower, which degrades the simulation result compared to the experimental data. This arises due to the centre grid element being physically smaller than the actual hub/tower. Therefore there is a gap between the edge of the hub element and the location where the rotor loading profile (figure 5.4) becomes non-zero. The flow accelerates through this path of least resistance. The accelerated flow mixes with the surrounding fluid and by x=5D the influence of grid resolution is negligible.

The high turbulence case is presented in figure 5.10. To achieve a high turbulence level, the experimenters removed the flow conditioning screens from the flume. A side-effect of doing this was that the flow through the test section was no longer directly axial along the test section length; Mycek *et al.*[76] reported a transverse velocity of approximately -0.05 m/s near the rotor location. For this reason, the experimental data have been manipulated to re-centre the wake, as described in §6.2.

The high turbulence simulations predict the velocity profiles very well compared to the experimental data. The wake mixes much faster than the 3% turbulence case, and TADA correctly predicts the influence of turbulence on wake mixing. The impact of grid resolution is similar as in the 3% turbulence case. The turbulence intensity profiles are reasonably predicted throughout the wake, with almost no sensitivity to grid resolution.

5.7.2 Single Rotor: Reference Velocity for Second Rotor

As mentioned in section 5.4.4, using the traditional C_T and C_P for specifying the rotor power would require defining an appropriate reference velocity u_ref for the downstream rotor. One way to find u_ref is the sequential simulation approach where u_ref is the axial velocity in the wake of the upstream rotor. Mycek et al. [76] published results showing disk-averaged values of the ratio u_ref^3/u_0^3 in the wake of a single turbine, at a range of distances downstream of the rotor. Note that the 'disk-average' in this case was taken over a region in the wake, not an actuator-disk. The same quantity was extracted from the CFD simulations of a single rotor, and is compared to the experiments in figure 5.11.

This parameter shows the kinetic power available to the downstream rotor, as a percentage of the power available to the upstream rotor. The simulations compare well to the experiments for I_0=3%, but under-predict the kinetic power by about 5-10% for I_0=15%, from 3D to 7D. This under-prediction is likely due to the experimental wake being slightly off-centre, and thus the integral areas not being directly comparable.

Figure 5.11 shows results for the 9EPD and 21EPD grids, both using the calibrated model for 9EPD. The impact of grid resolution is found to be minimal.

Note that if the turbine performance were not sensitive to turbulence intensity or inflow velocity, then the power of the downstream rotor would scale directly with $100\,\langle u_\mathrm{ref}^3/u_0^3\rangle$.

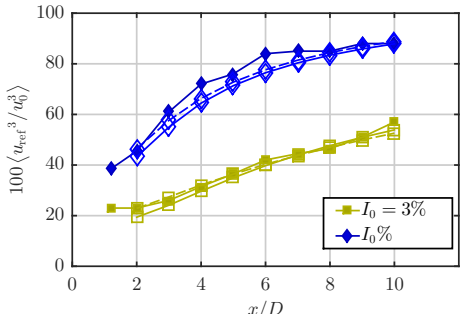

Figure 5.11: Disk-averaged value, $100\,\langle u_{\mathrm{ref}}^3/u_0^3\rangle$. Filled symbols correspond to the experiment data while open symbols are from the CFD simulations. Solid lines are for 9EPD and dashed lines are for 21EPD.

5.7.3 Tandem Rotors: Power

The power of the downstream rotor is compared directly to the experimental data in figures 5.12 and 5.13.

For the low turbulence cases (figure 5.12), the power predictions are very reasonable. Note that the downstream rotor performance is drastically reduced in the wake. Even with 10D separation between rotors, the downstream rotor power is about half that of the single rotor. The simulations over-predict the downstream rotor power for separation distances from 2D to 6D. However, the single-rotor wake was well-predicted in this region, in terms of the velocity/turbulence transects (section 5.7.1) and in terms of the kinetic power (section 5.7.2). Thus the discrepancy in the predicted power must be the result of some deficiency of the rotor performance model (i.e. the lookup procedure for $C_{\mathrm{T}}^{\star}$, $C_{\mathrm{P}}^{\star}$). There may be a performance degradation which occurs when the downstream rotor is affected by the tip vortices of the upstream rotor, which could not be captured by TADA.

The right hand plot shows results using the 21EPD grid with the AD model calibrated for 9EPD. The impact of this is a small reduction in the predicted C_{P} of approximately 4% compared to the optimal C_{P} of the single rotor. This is consistent with the impact found for the single rotor cases in §5.6.

Similar trends are seen for the high turbulence cases shown in figure 5.13. However, the simulations under-predict the power significantly for 4D rotor separation. This under prediction is consistent with the under prediction of the kinetic power density in the single rotor wake shown in figure 5.11, and may again be attributed to the experiment wake being somewhat off-centre, whereas the simulated wake remains centred. For separations of 8-10D the simulations compare well to the experiments.

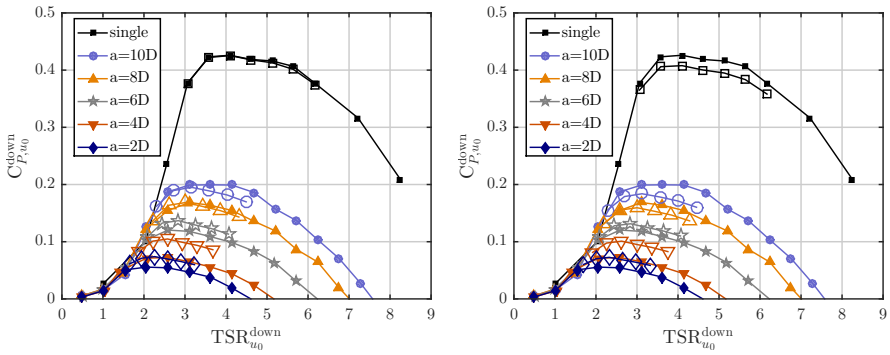

Figure 5.12: Power coefficient of the downstream rotor for I_0=3%. Left plot for 9EPD grid, right for 21EPD grid (AD calibrated for 9EPD). Filled symbols: experiment data, open symbols: simulations.

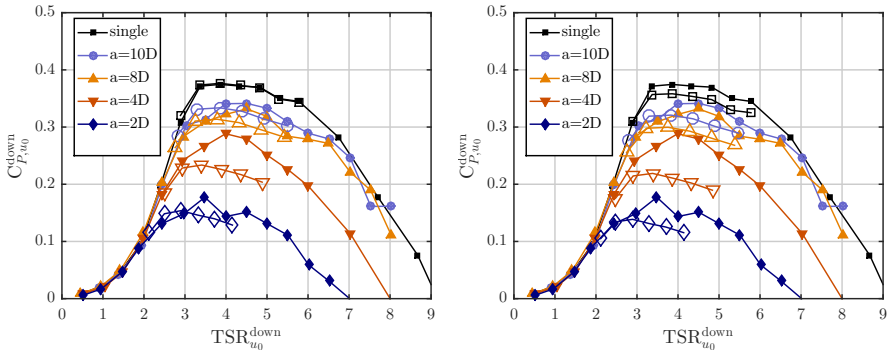

Figure 5.13: Power coefficeint of the downstream rotor for I_0=15%. Left plot for 9EPD grid, right for 21EPD grid (AD calibrated for 9EPD). Filled symbols: experiment data, open symbols: simulations.

At these larger separation distances, the wake was almost fully mixed and being off-center had little impact. The right hand plot shows results on the 21EPD grid. Using the finer resolution with the AD model calibrated for 9EPD reduced the predicted C_P by about 6% compared to the single rotor.

5.7.4 Twin Rotors: Rotor Efficiency

In the previous section, the downstream rotor power was non-dimensionalized using the freestream velocity. This approach is useful for studies looking at the farm performance as a whole. A different option for defining the downstream rotor power coefficient uses the 'reference' velocity (described in section 5.7.2, and shown in figure

5.11):

$$C_{\mathrm{P}\langle u_{\mathrm{ref}}\rangle}^{\mathrm{down}} = \frac{P^{\mathrm{down}}}{\frac{1}{2}\rho\,\langle u_{\mathrm{ref}}^3\rangle\,\pi R^2} \tag{5.27}$$

This power coefficient represents the ratio of power generated by the downstream rotor, to the kinetic power available to it, taking into account the wake deficit from the upstream rotor. If the rotor performance varied only with TSR, then the maximum $C_{P,\langle u_{\mathrm{ref}}\rangle}^{\mathrm{down}}$ would reach the same value for the downstream turbine as for a single turbine. However the rotor performance also depends on factors other than TSR. Based on the single-rotor experiments, it was known that both turbulence intensity, and incoming velocity (blade Re) have an impact on rotor performance. To observe the impact of such sensitivities, it is useful to observe the ratio of the maximum $C_{\mathrm{P}\langle u_{\mathrm{ref}}\rangle}$ achieved by the downstream rotor, to that of a single rotor. This ratio defines the rotor efficiency term:

$$\eta_{\langle u_{\mathrm{ref}}\rangle} = 100\frac{\max\left(C_{\mathrm{P},u_{\mathrm{ref}}}^{\mathrm{down}}\right)}{\max\left(C_{\mathrm{P},u_0}^{\mathrm{single}}\right)} = 100\frac{\max\left(P^{\mathrm{down}}\right)}{\max\left(P^{\mathrm{single}}\right)}\frac{u_0^3}{\langle u_{\mathrm{ref}}^3\rangle} \tag{5.28}$$

where the maximum is taken over the set of tested TSR (from the curves shown in figures 5.12 and 5.13). The efficiency is plotted in figure 5.14.

Several useful observations can be made by examining this plot. First, the experiments show that in high turbulence, the downstream rotor has enhanced efficiency compared to a single rotor, for separation distances from 2D to 6D, with $\eta_{\langle u_{\mathrm{ref}}\rangle}\approx$107%. This is unexpected, because the single rotor performance was degraded with increasing turbulence intensity and decreasing $\langle u\rangle$. Thus, there may be some other factor affecting the rotor performance at close separation distances, for which the simulation model was not tuned. However, since u_{ref} and P^{down} were taken from different experimental runs, the observed boost in efficiency may be due more to experimental repeatability issues rather than a real physical phenomenon. This argument is particularly relevant for the high turbulence cases, for which the flow was not as well-conditioned.

In low turbulence, the experiments show a drastic degradation in the rotor efficiency from 2D to 6D. Some degradation was expected based on the trends in performance observed from the single rotor cases. Notably, the increased turbulence in the wake was expected to reduce the rotor efficiency, as was the sensitivity to $\langle u\rangle$. The simulation model predicted $\eta_{\langle u_{\mathrm{ref}}\rangle}\approx$85% for all separation distances, whereas the experimental value of $\eta_{\langle u_{\mathrm{ref}}\rangle}$ was as low as 60% for a/D=4. This may indicate that the rotor performance varies non-linearly with respect to the incoming turbulence

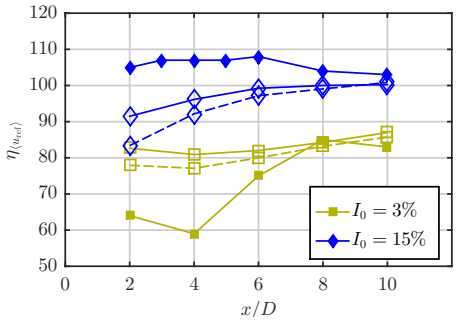

Figure 5.14: Rotor efficiency term, $\eta_{\langle u_{\text{ref}} \rangle}$. Filled symbols correspond to the experiment data while open symbols are from the CFD simulations. Solid lines are for 9EPD and dashed are for 21EPD.

intensity, rather than the linear trend assumed by the performance model. Another possibility is that the rotor performance is degraded when exposed to tip-vortices. Note that because the flow was better conditioned in the low turbulence cases, the trend in rotor efficiency observed with I_0=3% is likely more reliable than with I_0=15%.

5.7.5 Twin Rotors: Wake of Downstream Rotor

Profiles of the wake downstream of the second rotor in the array (separated by 6D) are shown in figures 5.15 and 5.16. These profiles give some indication of how well the simulation method will perform for turbine arrays with multiple rows of turbines. The wake is well-predicted for I_0=3%. With I_0=15%, the simulations under-predict the turbulence intensity, and the velocity recovers too slowly, particularly between 3D–5D. The simulation results can be brought closer to the experiments by incorporating a source term for k in the rotor wake, as described in [11], which was formulated to account for the generation of turbulence by tip-vortices, which are inherently neglected by the AD approach. That source term was not included in the current study because it had been developed for high-resolution AD simulations, and would need to be re-tuned for the present coarse-resolution model. Additionally, the wakes were found to be well-represented in the present simulations without requiring additional sources of turbulence. This discrepancy between the present coarse gird simulations and the previous high-resolution sims ([11]) is thought to be due to numerical diffusion, and also due to much smaller dissipation terms calculated by the wall functions in the grid cells adjacent to the tower and hub.

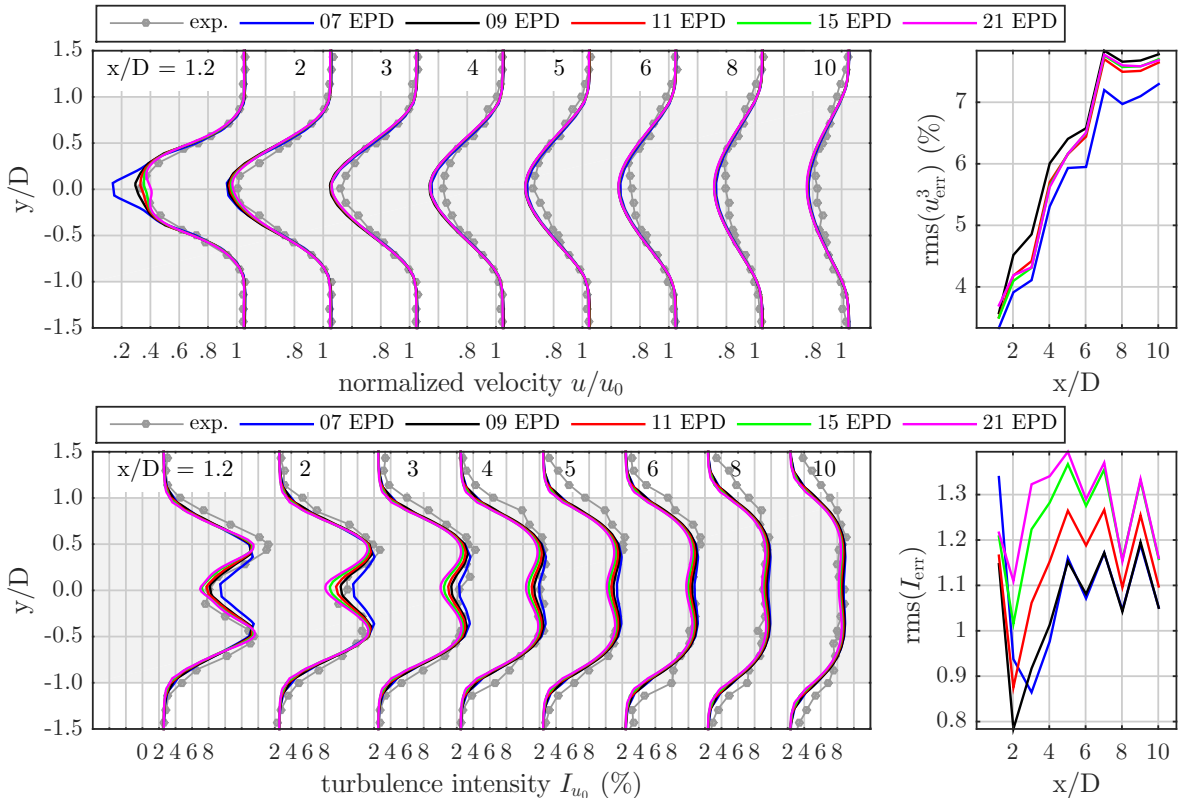

Figure 5.15: Lateral transects of the second rotor wake: a/D=6, I_0=3%, TSR_{u_0}=3.67 (both rotors), u_0=0.80m/s

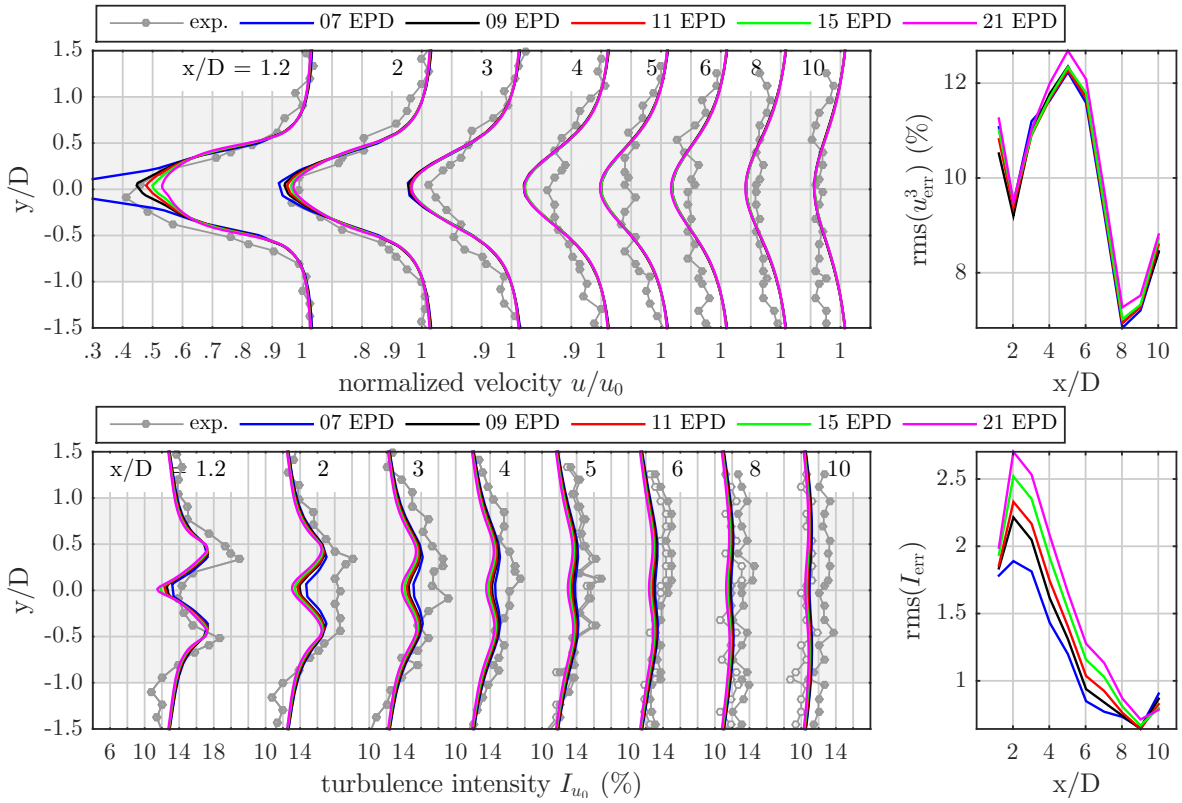

Figure 5.16: Lateral transects of the second rotor wake: a/D=6, I_0=15%, TSR_{u_0}=3.67 (both rotors), u_0=0.83m/s

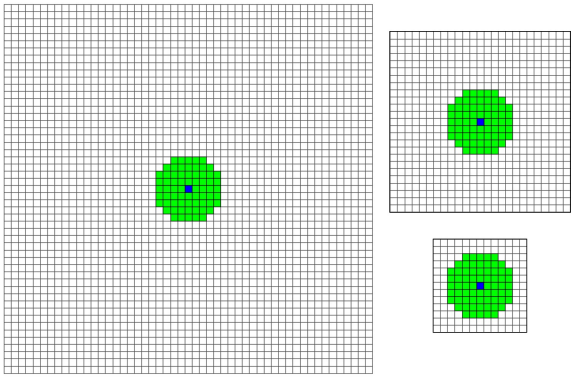

Figure 5.17: Simulation domains used for studying the impact of blockage ratio, with side lengths of {2,1,0.5}m, corresponding to BR={2.4,9.6,38.5}%.

5.8 Application to Blocked-Flow Scenarios

The optimal layout of turbines is not to locate them directly in each other's wakes. In idealized scenarios of rectangular channels, the optimal layout would place turbines side-by-side in a fence spanning the entire channel. This is obvious considering conservation of mass-flow, simply because more water is forced through each turbine. The physics of a turbine fence have been studied analytically in detail by Garrett and Cummins [103, 104] and later by Vennell [105, 106]. The main factor affecting the performance of a turbine fence is the blockage ratio BR, which is the total swept area of turbines in a given transect, compared to the transect cross sectional area.

It is important for TADA to be able to predict the influence of BR on the performance of turbines. This capability was assessed by running TADA in artificial flumes of decreasing cross sectional area. As the flume became narrower, the blockage ratio increased, and TADA predicted higher thrust and power. To assess the accuracy of TADA's predictions, an analytical correction for blockage effects [107][12] was used to correct the TADA-predicted thrust and power to unblocked conditions. Those corrected results were then compared to TADA's prediction of thrust and power in an unblocked simulation domain.

To isolate blockage effect from variations in rotor performance, the TADA simulations used constant values $C_{\mathrm{T}}^{\star}$=1.28 and $C_{\mathrm{P}}^{\star}$=0.86, corresponding to the optimal $\mathrm{TSR}^{\star}$ of 6.7, rather than using table-lookups. A plug flow of 0.8 m/s was specified at the inlet, and a static pressure condition at the outlet. The analytical correction was derived assuming laminar flow, so for consistency the simulations did not use a

[12] which is mathematically equivalent and was published earlier to the more often cited [103]

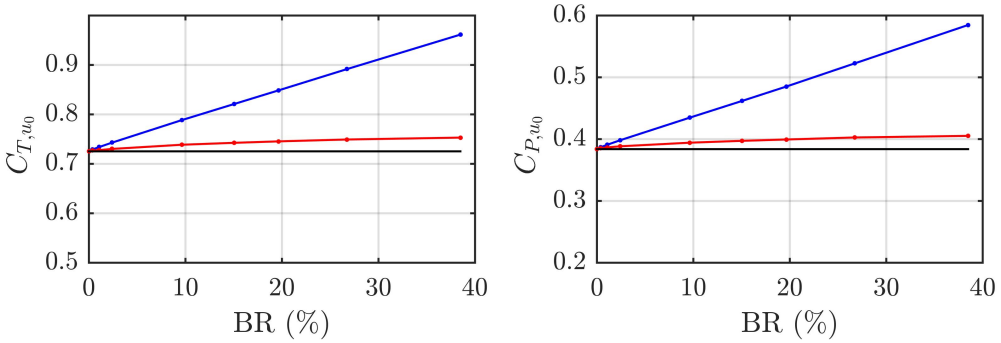

Figure 5.18: Thrust and power coefficient variation with blockage ratio, as predicted using TADA (blue). The red line shows the TADA result, corrected for unblocked conditions using [107]. The black line shows TADA's prediction in unblocked conditions.

turbulence model. The simulations used a free-slip wall condition on the flume sides, top and bottom, also for consistency with the analytical correction. To model the rotor in an unblocked environment (BR=0), one simulation used an 'opening' boundary condition on the top bottom and sides, using the largest domain (5m side length).

The domain used a square cross section, with side lengths of {5,3,2,1,0.8,0.7,0.6, 0.5} m, giving BR ranging from 0.4% to 38.5%. Sample meshes are shown in figure 5.17.

The results are summarized in figure 5.18. The blue lines show the thrust and power coefficient variation with blockage ratio predicted by TADA. The red line shows the result from TADA corrected to unblocked conditions using [107]. The black line shows TADA's prediction for the unblocked model domain. The discrepancy between the black and red lines ranges from 0 at BR=0, to 3.8% (for $C_{\mathrm{T,u_0}}$) or 5.6% (for $C_{\mathrm{P,u_0}}$) at BR=38.5%. These discrepancies are not very large compared to the influence of blockage effect, which is expected to increase $C_{\mathrm{P,u_0}}$ by 52% at BR=38.5%. Thus, within a reasonable margin, TADA predicts blockage effects consistently with a well established analytical model.

Note that the analytical method is somewhat imperfect, as it makes a number of simplifying assumptions including 1D laminar flow. With future validation, TADA may prove to be a more versatile blockage correction because it can use exact flume/channel geometries, and can account for the impact of turbulence on wake mixing.

Maintaining a constant value of TSR* in the blockage simulations is theoretically equivalent to tracking the maximum power point by altering the rotor speed. As the

disk-averaged velocity increases with blockage ratio, the rotor speed increases as well. This should track the maximum power point by keeping the flow angle of attack constant on the rotor blades. Thus, theoretically the optimal TSR* operating condition should be insensitive to changing BR, as should the associated $C_{\mathrm{T}}^\star$ and $C_{\mathrm{P}}^\star$, which are also set relative to the disk-averaged velocity. Therefore, table lookups tuned using experimental data at a certain blockage ratio should be valid for application at other blockage ratios. This claim is supported partially by the results presented in this section, but does requires further validation against experimental data, which will be the focus of future studies as data become available.

5.9 Conclusions and Future Work

This paper has introduced and validated the tuned actuator disk approach (TADA) for simulating rotors in tidal-turbine farms. Key components of TADA are: 1) to normalize rotor thrust and power with respect to the disk-averaged velocity, rather than the freestream, which is not available in realistic farm simulations, 2) to generate table lookups for rotor thrust and power coefficients, analogous to airfoil table lookups, 3) to use the SST turbulence model, or another eddy-viscosity limiter to improve simulation predictions of near wakes.

TADA gave reasonable predictions of the rotor's wake, and its impact on the power produced by a second rotor located in the wake, at a range of separation distances. This validation was done for flows with 3% and 15% turbulence intensity, a range which likely covers most tidal energy sites. The largest discrepancies between TADA and experiments were in the high-turbulence cases, when the downstream rotor was between 3D to 6D downstream of the first rotor. It is difficult to be certain whether these discrepancies were due to secondary flows in the flume experiments which could not be simulated, or due to a true deficiency in the methodology.[13] Further validation of TADA is certainly recommended as more experimental data become available.

The sensitivity of TADA to grid resolution was assessed by calibrating the thrust and power lookup tables ($C_{\mathrm{T}}^\star$, $C_{\mathrm{P}}^\star$) using 9 EPD, and then applying them using resolutions of EPD=$\{7, 9, 11, 15, 21\}$. It was found that the error in predicting thrust and

[13]Since rotor power scales with the cube of velocity, it is important that experiments measure the flow-field with high accuracy and with adequate spatial coverage. The experiments used herein were of very high quality, however the validation could have been more conclusive if the empty-flume flow had been characterized with greater spatial coverage.

power became constant (at 3% for thrust, and 6% for power) above 15 EPD, which suggest that TADA becomes grid independent at 15 EPD. Using less than 9 EPD produced the worst errors and is not recommended.

TADA will be implemented in future studies for predicting AEP in a tidal farm, which must account for the temporal variability of the flow. This will be done by categorizing an annual time-series (obtained from a 2D regional-scale model) of the flow into representative flow states, and running a steady TADA simulation for each flow state. AEP will then be found based on the predicted farm power for each state, and its probability of occurrence. It is also important to predict the influence of channel blockage ratio on power and thrust predictions. Based on results presented in section 5.8 TADA gives reasonable estimates of blockage effect. This paper gives evidence that TADA will provide sufficient spatial accuracy for modelling wakes and blockage effects in turbine farms, without being restrictively expensive in terms of computational cost.

Chapter 6

A Tuned Actuator Cylinder Approach for Predicting Cross-Flow Turbine Performance with Wake Interaction and Channel Blockage Effects

This paper has been published as:

Shives, Michael; Crawford, Curran; and Grovue, Shane: *"A Tuned Actuator Cylinder Approach for Predicting Cross-Flow Turbine Performance with Wake Interaction and Channel Blockage Effects,"* International Journal of Marine Energy (2017) DOI: 10.1016/j.ijome.2017.03.007.

This paper adapts the TADA method presented in the previous chapter to cross-flow type turbines, with validation against real-world data collected in a dam outflow channel. The modelling work was all done by myself, and Shane Grovue provided consultation on the experimental data used for tuning and validating the model.

Abstract

This article presents a practical method for predicting the power output of cross-flow tidal/river turbines with wake interaction and channel blockage effects. In a

turbine farm, the power generated by each rotor depends on the cube of the local velocity, which is influenced by the bottom topology, by other turbines' wakes and also by finite channel cross sectional areas restricting wake expansion. Therefore, the accuracy of power predictions depends strongly on proper modelling of rotor wakes and the influence of the channel/river boundaries. This is a critical issue for the tidal and river kinetic turbine power industries because best practise for predicting energy yield has yet to be established, while project revenue streams are primarily a function of yield.

This article introduces a simulation-based method to predict individual turbine and total farm power output with modest computational expense, named the *tuned actuator cylinder approach* (TACA). Rotors are represented in the simulations as momentum sink terms, using approximately 21 elements across their diameter, allowing for very fast simulations of multiple rotors. The model is tuned to match known (from experiments or high-fidelity blade-resolved simulation) thrust and power operational profiles for a particular turbine, with known inflow conditions. Once tuned, the TACA model can be applied to a wide range of turbine array configurations, and arbitrary flow environments. Thus, TACA is an appropriate tool for case-studies and/or optimization of turbine array layout at real-world tidal/river energy sites.

6.1 Introduction

Commercial-scale tidal/river power extraction remains elusive for a number of key reasons, including immature technology and high uncertainly in energy yield impacting future revenue streams and hence investor confidence. Existing standards [2] for predicting energy yield for tidal/river turbine farms provide rough guidelines rather than an exact methodology. Research groups [3] and consultancies [4] are also gradually developing guidelines, but standard practise is not yet established in industry, and proposed analysis methods have yet to be validated. Meanwhile, investors are faced with high upfront costs with much uncertainty on project revenue. Thus, establishing robust and computationally efficient methods for predicting energy yield is an important impediment for the tidal/river power industries to overcome.

Energy yield is the integral of the farm power output over time, through all possible tidal ranges or river flows. The power generated by each turbine essentially depends on its water-to-wire efficiency, and the kinetic power density of the flow in which it is placed. Kinetic power density is proportional to the cube of the flow velocity.

Therefore, yield prediction requires:

- prediction of the spatial variation of velocity within the farm, which depends on bottom topology, channel cross-sectional area, and turbine wakes
- robust characterization of rotor performance in changing inflow velocity and turbulence
- prediction/characterization of the temporal variability of the flow field over the project lifetime.

This article proposes using an actuator-cylinder-based approach for predicting spatial flow variability and its impact on turbine performance. The actuator cylinder (AC) is analogous to the more prevalent actuator-disk (AD) method used for representing horizontal-axis turbines (e.g. [108, 90, 94, 12]). Such *actuator* methods allow a coarse mesh compared to higher-fidelity blade-resolved CFD, drastically reducing computational effort to the point that turbine-array studies are feasible on personal computers. Accuracy is maintained with a coarse mesh by replacing physical blades by momentum sources, to emulate their effect on the flow, which alleviates the need to resolve the blade boundary layers.

AC methods simultaneously solve two sets of equations, one to determine the flow field, and another to determine the blade loads. The earliest AC implementation [109], solved for an inviscid flow, where the blade loads were specified a priori as a trigonometric function of azimuth angle. Soon thereafter, [110] added blade-element theory to calculate rotor loads and solved time-averaged, viscous, Navier-Stokes equations to simulate a Darrieus rotor. Coupling the blade force calculation to the flowfield was necessary for a predictive method. More recently, research efforts have tested different AC based methods for various purposes. For example, [111] has focused on computational speed, and derived a fast linear flow solution with the blade lift coefficient defined by a 2π slope, for use in aero-elastic simulations. Other research [112] has focused more on turbine wakes, and implemented transient large-eddy simulations using both an AC approach (with the blade forces averaged temporally) and an actuator line (AL) approach (with blade forces moving throughout the simulation). Both methods produced reasonable wakes compared to time-averaged experiment data, while the AL predicted transient effects and more accurate turbulent mixing.

Other research [113] focused on creating a robust AC model for a ducted-dual rotor system. Their innovative work used blade-resolved simulations to determine the

rotor performance for a wide variety of inflow conditions. They then post-processed those results to parametrize a so called hybrid *local/global* AC model. The *local* component used airfoil coefficients to predict blade loads based on the local velocity in an individual element as previously done by e.g. [110]. The innovative *global* component used novel loading coefficients to define the blade loads based on the flowrate velocity through the rotor. This *global* approach was analogous to previous/concurrent AD simulation methods for axial flow turbines [94, 12] in that the blade forces were calculated based on the flowrate through the entire rotor, rather than the local velocity in each element.

This paper presents a purely *global* AC strategy, which employs a regression model to predict turbine performance over a wide range of operational speed and inflow conditions. The transition to a purely *global* strategy has important implications. For one, it allows for a significantly coarser mesh since forces are no longer sensitive to the element-local flow. On the other hand, it requires assumptions regarding the distribution of load (i.e. its variation with angular position) within the AC region.

The purely global approach presented herein is analogous to using tabulated airfoil coefficients except instead of using blade-local lift and drag coefficients, it uses rotor-local thrust and power coefficients. Since turbines significantly slow the rotor-local flow, the tuning must account for this induction effect and cannot simply be based on some upstream velocity [94]. A regression model is fitted to a set of calibration points obtained from single-unit manufacturer performance data and/or experimental data, while the specified spatial load variation is obtained from blade-resolved CFD or experimental measurements. Because of this requisite tuning procedure, the method has been named the *tuned actuator cylinder approach* (TACA), and is a direct adaptation of a similar methodology developed by the authors for horizontal-axis turbines [12]. Compared to previous AC methods, TACA is less computationally intensive, without a penalty in accuracy owing to its unique tuning strategy. Also, compared to [113], TACA has been developed to cover the rotor's entire operational range of TSR, and for a range of turbulence conditions. Once the TACA rotor model is tuned using single-unit tests, it can subsequently be used in its intended application, which is to predict performance of multiple rotors in turbine arrays in a wide variety of flow environments.

This paper introduces the theoretical basis for TACA, and validates the model using experimental data from small arrays of turbines located in a hydro dam discharge channel. Such validation is critical for assessing the application of AC models

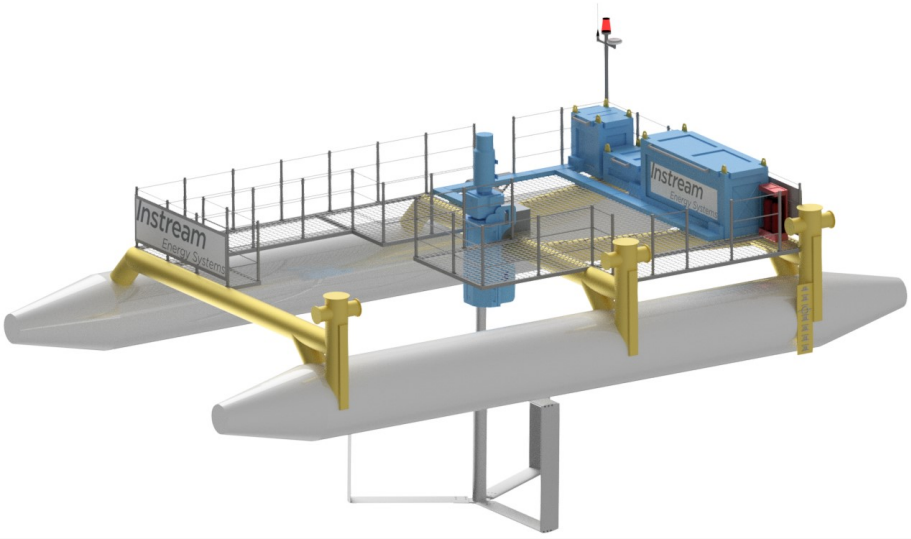

Figure 6.1: Floating turbine assembly concept by Instream Energy Systems

to real-world scenarios, and is conspicuously lacking in the present literature. The paper is organized as follows. Section 6.2 summarizes the experiments used for tuning and validation. Sections 6.3 and 6.4 describe TACA in detail, including the turbulence model, boundary conditions, mesh, and rotor parameterization. Comparisons between the model and experiments are presented in section 6.5. The computational cost is discussed in section 6.6 and conclusions are presented in section 6.7.

6.2 Experimental Validation Data

Experiments were performed by PowerTech Labs Inc. during Jan-Feb 2010, in the Duncan Dam discharge channel, located approximately 200 km east of Kelowna B.C. The channel was approximately 50 m wide, and lined with rip-rap ranging in diameter between 0.3 m to 1 m. The controlled outflow from the dam provided relatively constant flow suitable for testing performance. Tests were run with arrays of up to three four-bladed, vertical axis turbines mounted on pontoons, similar to that shown in figure 6.1.

The rotor diameter D was 4 m and its vertical height H was 1.7 m, for a total swept area A of 5.7 m^2. The rotor was submerged with the top tips of the blades 0.33 m below the water surface. The generator electrical output power P_{ex} was measured using a Hioki 3169 clamp-on meter, taking approximately 150 samples per rotor revolution. The variable AC output from the generator(s) was converted to DC using a Siemens

variable-frequency motor drive (VFD), and dissipated using a 100kW resistor bank. The VFD was operated in speed control mode which varied the resistive load to maintain a close match between rotor rotational speed and a specified set point.

The channel flow velocity at hub-height ranged between approximately 1.5 to $2.0\,\mathrm{ms}^{-1}$. Vertical profiles of velocity (u, v, w) were measured using a SonTek 1.5 MHz mini River Surveyor Acoustic Doppler Profiler (ADP), with a vertical resolution of 0.25 m and ping rate of 9 Hz. Single ping profiles were temporally-averaged at a sample rate of 0.2 Hz (45 pings per sample) to reduce contamination by Doppler noise. Taglines and a rope and pulley system were positioned crossing the channel, and the ADP was mounted on a floating platform, so it could be positioned stationary in front of a turbine, or slowly dragged across the channel channel. The ADP post-processing algorithms removed ADP motion from the measurements.

Stationary ADP measurements were made concurrently with power, to develop the turbine power curve shown in figure 6.5. The stationary measurements were taken over approximately 10-20 minutes to obtain converged temporal averages, in a column of water centred upstream of the rotor. The transect measurements, on the other hand, provided a temporal snapshot of the flow across the channel width.

The velocity component signals from stationary deployments were separated into mean and fluctuating components using Reynolds decomposition to calculate turbulent kinetic energy from the signal variance. Single-ping ADP velocity signals are typically contaminated by high levels of Doppler noise, which can be reduced by temporal averaging or by subtracting the variance due to noise (e.g. [114]). Temporal averaging reduces variance by eliminating true fluctuations above the re-sampling rate in addition to reducing variance due to noise and thus can cause under-prediction of turbulent kinetic energy (e.g. [115] showed significant under-prediction using 8 Hz pings averaged to 0.4 Hz). Therefore, to obtain reasonable estimates of the turbulent kinetic energy, it was necessary to estimate the competing influences of Doppler noise and temporal averaging on the measured signal variance. An analysis presented in Appendix A found that the two competing influences are expected to approximately cancel for the present dataset, which allowed turbulent kinetic energy and intensity to be found using:

$$I = \frac{\sqrt{\frac{2}{3}k}}{U}, \quad k = \frac{1}{2}\left(\overline{u'u'} + \overline{v'v'} + \overline{w'w'}\right) \tag{6.1}$$

where U is the time-average velocity magnitude, k is the turbulent kinetic energy, and $\{\overline{u'u'}, \overline{v'v'}, \overline{w'w'}\}$ are the measured Reynolds normal stresses. The intensity was

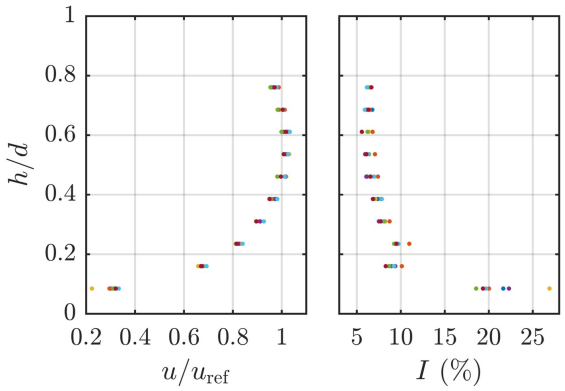

Figure 6.2: Sample velocity and turbulence intensity profiles from stationary ADP measurements taken during the LAT tests. On the vertical axis, h is the height above bottom and d is the water depth. Each dot colour is from a unique 10-20 minute measurement.

calculated from the LAT tests (see figure 6.4) with the ADP located upstream of the central rotor. Figure 6.2 shows sample velocity and intensity profiles.

The channel depth was measured by BC Hydro, and by the ADP units during transects. These two sources provided a point cloud used to create a bottom topology model[1] depicted in figure 6.3. Care was taken to perform the testing in a region of mostly consistent depth, since the channel was not perfectly rectangular and had significant depth variations. Experiments were done with rotors in a variety of layouts depicted in figures 6.3 and 6.4. Note that for the LON tests, the rotor position was recorded relative to the ADP wake transects, and was slightly off-centre compared to the shown figures.

The velocity and power data from single-unit (SU) tests were used to calculate the turbine's power conversion efficiency:

$$\eta^{\text{sys}}_{u_{\text{ref}}} = \frac{\text{P}_{\text{gen}}}{\frac{1}{2}\rho u^3_{\text{ref}} A} \tag{6.2}$$

where P_{gen} was the time-averaged generator electrical output power and A was the turbine swept-area. The quantity u^3_{ref} was taken as a spatio-temporal mean of the cube of the horizontal velocity (u_h=$(u^2 + v^2)^{1/2}$) taken by ADP approximately 8 m upstream of the rotor. For stationary ADP data, the averaging was done for the same time period as the measured power[2] and over the range of depths occupied by the

[1] using the *gridfit.m* Matlab script (available through Matlab Central).

[2] For some data points simultaneous power and flow data were not available, and u_{ref} was inferred

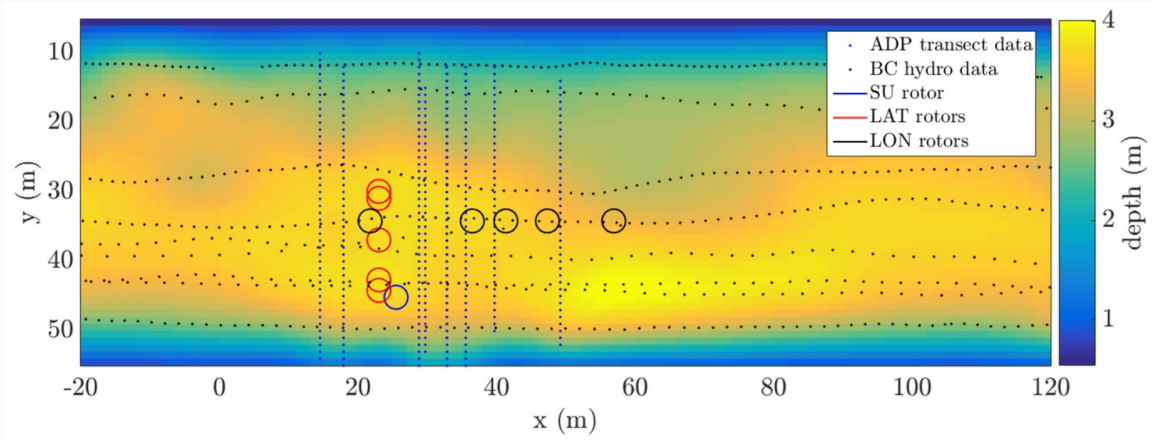

Figure 6.3: Channel depth with approx $2\,\mathrm{ms}^{-1}$ surface flow velocity (the flow was along the x-axis, from left to right). The depth was approximately 0.3m less with $1.7\,\mathrm{ms}^{-1}$ flow. Rotor positions from the various tests are also shown.

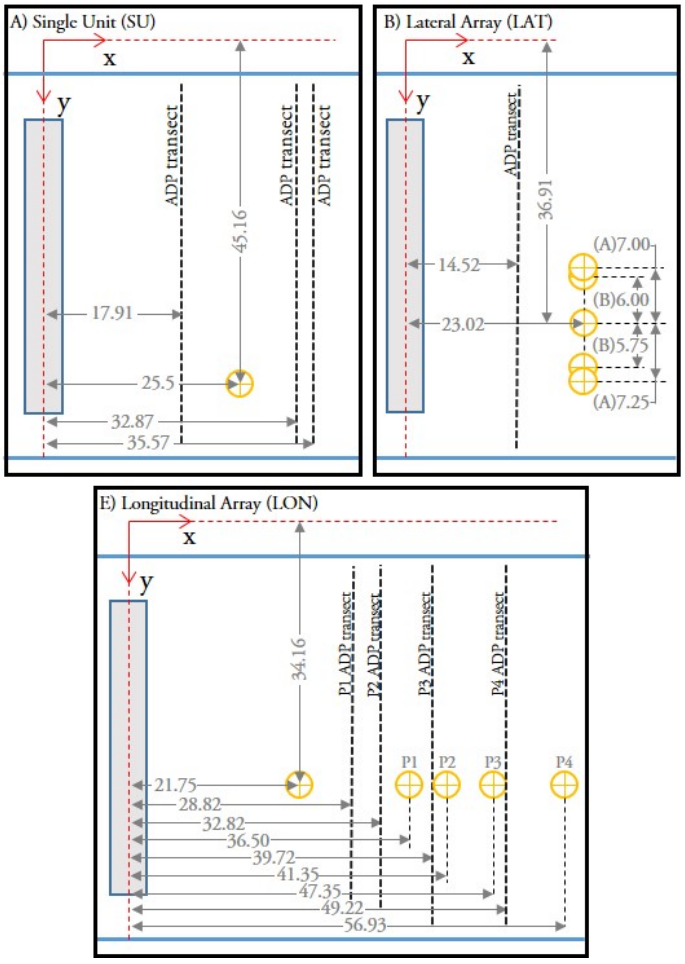

Figure 6.4: Summary of test configurations with one, two or three turbines. The flow is from left to right. The large rectangular area is a barge used for anchoring the turbines, which are represented by yellow cross-circles. The single rotor cases (SU) were used to develop the rotor performance characteristic. The LAT and LON cases were used for validating TACA. (units in meters)

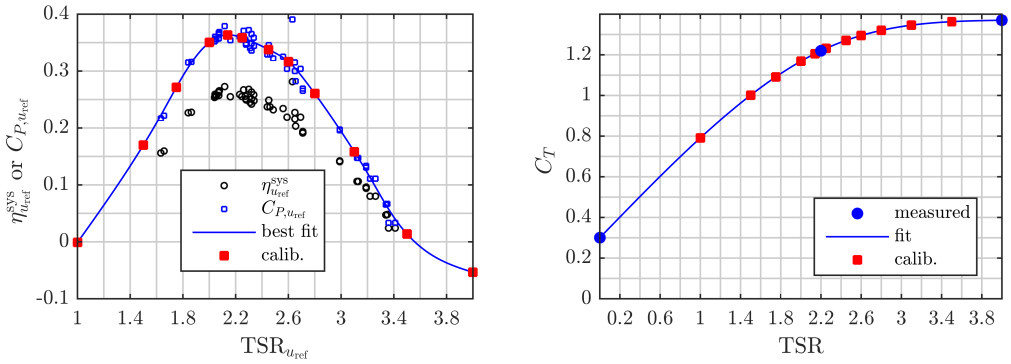

Figure 6.5: System conversion efficiency and shaft power coefficient, normalized using the reference velocity measured by ADP (left). Rotor thrust coefficient as determined from towing tests (right).

rotor. For transect ADP data u_{ref} was a spatial mean taken over a region upstream of the rotor swept area.

The tip-speed ratio was calculated as $\text{TSR}_{\text{u}_{\text{ref}}} = \Omega R/u_{\text{ref}}$, where Ω is the rotor speed and R is its radius. The shaft power coefficient was calculated using:

$$C_{\text{Pu}_{\text{ref}}} = \frac{\eta^{\text{sys}}_{u_{\text{ref}}}}{\eta_{\text{gen}}\eta_{\text{gb}}} \tag{6.3}$$

with the generator and gearbox efficiencies estimated as η_{gen}=0.8 and η_{gb}=0.9.[3] The rotor power characteristic is shown in figure 6.5.

The thrust coefficient was estimated by towing the turbine platform and measuring the line tension.[4] The pontoon drag was estimated based on empirical coefficients, and the remaining drag was attributed to the rotor. The tow tests were done with the rotor locked, operating at $\text{TSR}_{\text{u}_{\text{ref}}}$=2.2, and at a freewheeling condition (interpreted as $\text{TSR}_{\text{u}_{\text{ref}}}$=3.5, which is the zero-crossing of the $C_{\text{Pu}_{\text{ref}}}$ curve.) The thrust characteristic is plotted in figure 6.5.

The channel cross sectional area was approximately 150 m^2, and the blockage ratio BR with a single rotor present was approximately 4%. Typically this BR would increase rotor power by approximately 3.5% (see Appendix C for more discussion on blockage effect). The experimental results may have been more strongly affected by

from the closest available time period.

[3]The efficiencies likely varied over the range of TSR, however efficiency curves were not available. The sensitivity of TACA to changing efficiencies is studied in § 6.5.2.

[4]The exact procedure and equipment to test thrust used were not well documented so the accuracy is not characterized. TACA's sensitivity to changing thrust is studied in § 6.5.2.

blockage because, as indicated by ADP transect data, the fast-flowing core (≈80% of the total volume flow rate) was limited to a smaller cross section (100 m^2), and because the turbine occupied approximately half of the channel depth. TACA was used to assess the impact of blockage on performance, as described in §6.4.2.

6.3 Simulation Methodology

TACA uses Reynolds-averaged Navier-Stokes (RANS) simulations[5] to predict the influence of turbine wakes, bottom topology and channel cross-sectional area. This section describes the employed governing equations, and the TACA rotor model in detail.

6.3.1 Governing Equations

The steady, incompressible RANS equations were used for all simulations, shown below using tensor notation:

$$\frac{\partial \overline{u}_i}{\partial x_i} = 0 \tag{6.4}$$

$$\overline{u}_j \frac{\partial \overline{u}_i}{\partial x_j} = \frac{\partial}{\partial x_j}\left[-\frac{\overline{p}\delta_{ij}}{\rho} + 2\nu S_{ij} - \overline{u_i' u_j'}\right] + \frac{\overline{S_{\mathrm{M}i}}}{\rho} \tag{6.5}$$

where p is the pressure, x_i is the spatial co-ordinate, ν is the fluid kinematic viscosity and ρ the density. The Dirac delta function, δ_{ij}=1 for $i = j$ and equals zero otherwise. $\overline{S_{\mathrm{M}i}}$ is a Reynolds-averaged momentum-source term, used to impose the rotor forces on the flow. The term S_{ij} is the mean rate-of-strain tensor defined by:

$$S_{ij} = \frac{1}{2}\left(\frac{\partial \overline{u}_i}{\partial x_j} + \frac{\partial \overline{u}_j}{\partial x_i}\right) \tag{6.6}$$

The turbulent Reynolds stresses were modelled using the Boussinesq turbulent viscosity hypothesis:

$$-\overline{u_i' u_j'} = 2\frac{\mu_t}{\rho} S_{ij} - \frac{2}{3}\left(k + \frac{\mu_t}{\rho}\frac{\partial \overline{u}_k}{\partial x_k}\right)\delta_{ij} \tag{6.7}$$

where μ_t is the eddy viscosity and k is the turbulent kinetic energy. The eddy viscosity enhances momentum exchange across shear layers, and is critically important for predicting the mixing of turbine wakes with the surrounding flow.

[5] implemented in ANSYS CFX 15.0

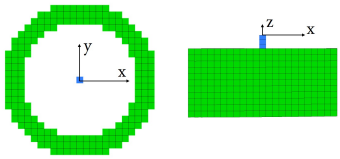

Figure 6.6: Actuator-cylinder (AC) mesh with employed resolution of 21 EPD

The most common methods for specifying μ_t, are the k-ε [60] and k-ω [61] turbulence models. However, when using either of these formulations for AD simulations, rotor wakes tend to mix-out too quickly. Many researchers (e.g. [50, 51, 55, 57, 59]) have proposed various treatments, including adding source terms for turbulent dissipation and/or production or using eddy viscosity limiter functions to mitigate this issue. Shives and Crawford [99, 11] found that the shear-stress-transport SST model of Menter [32] (which is a hybrid k-ε / k-ω model) provided reasonable predictions of wakes from horizontal-axis turbines using AD simulation. Because of the clear analogy between AD and AC methods, the SST model has also been used in the present study.

The SST model has become very prevalent in industrial CFD applications, and is known to perform well in flows with adverse pressure gradients and mild regions of separated flow ([29, 32]). Thus the SST model may be suitable for river and tidal-channel flows with complex bottom topologies.

6.3.2 Mesh Generation

The meshes was generated by an in-house automated code. Two types of domain were used. The first was a *channel domain* with geometry matching the Duncan dam outflow. The second was an *open domain*, which was used to model the rotor far from any solid boundaries, i.e. without any influence of channel blockage effect or boundary-layers. For both types, the mesh tool used well defined rules to set the element sizes. The simulation coordinate system aligned x with the flow direction, with the origin at the central (or upstream) rotor.

The element size was characterized by the quantity epd (elements per-diameter). For this study, epd was typically set to 21, but the small sensitivity to increasing this to 31 or 41 is explored briefly in section 6.4. The tuning procedure (§ 6.4) corresponds to a specific resolution, so simulations done with a different resolution will introduce some error into the results.

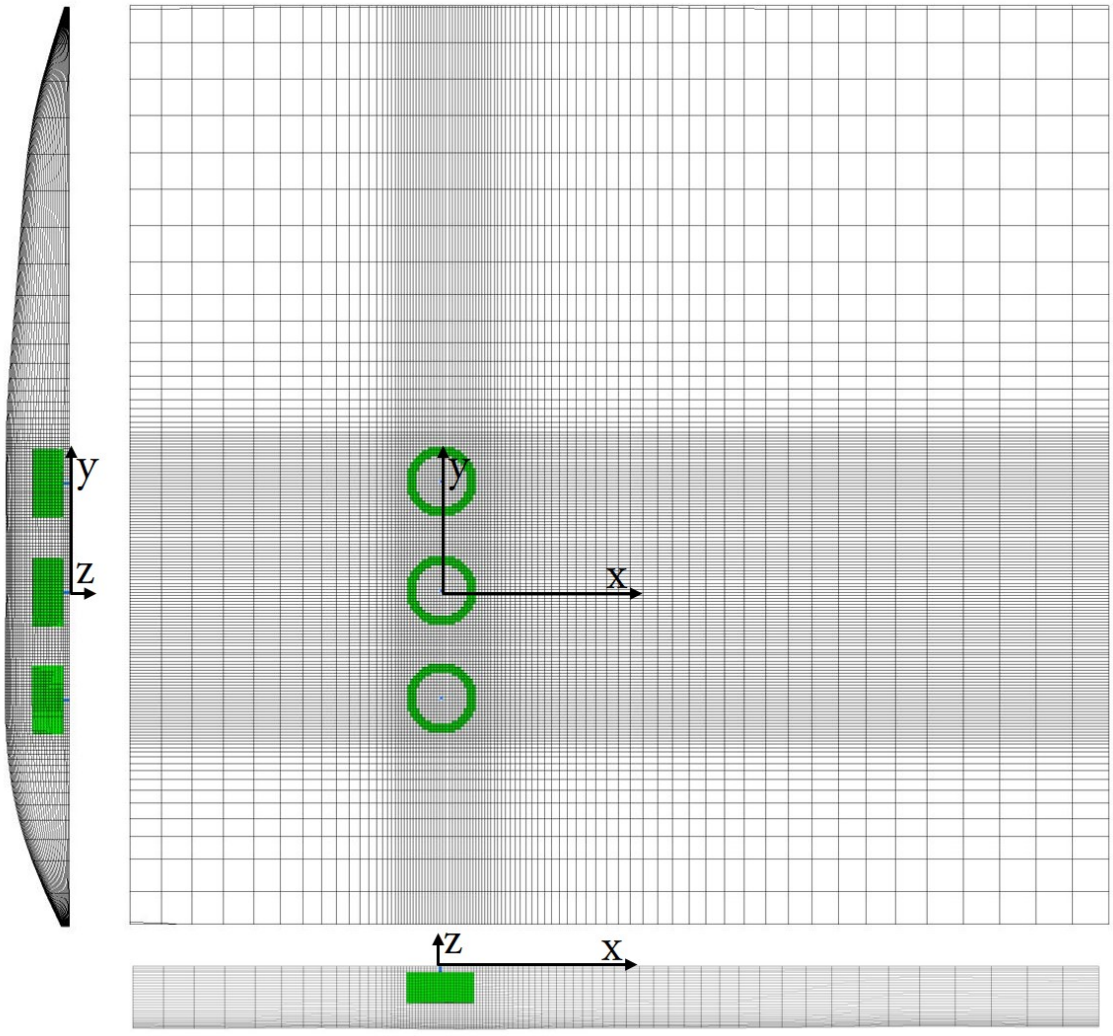

Figure 6.7: Domain mesh for the LAT-B B case. The cylindrical AC regions are hi-lighted in green and have a diameter of 3.4m.

The mesh used hexahedral elements, with dimensions Dx (streamwise), Dy (transverse) and Dz (depthwise).

Dx was constant at Dx=D/epd within x=±0.7D of each turbine shaft. Up/downstream of that region, Dx increased using a geometric growth law with a ratio of 1.2/1.07 to a maximum of 0.6D.

For channel domains, Dz was 0.05 m (0.015D) at the bottom[6] expanding to Dz=D/epd (ratio=1.2) at the bottom of the rotor, remaining constant to the water free surface. In open domains Dz was D/epd within the actuator region and expanded (ratio=1.2)

[6]In Appendix B, figure 6.27, it is confirmed that decreasing the first layer spacing to 0.01 m did not alter the resolved boundary layer.

to a maximum of 0.6D at the domain top and bottom.

For both domain types, Dy was D/epd within y=±0.7D of each rotor, expanding outwards (ratio of 1.2) to a maximum of 0.6D. Therefore, boundary layers on the channel side walls were not well resolved, however this had little impact on the rotor power because the sides have a much smaller surface area compared to the bottom, and the rotors were not within the side-wall boundary layer.[7]

The AC region included elements whose centroids were within the rotor radius, and spanned a minimum of 3 elements in the radial direction, based on previous experience with TADA [12], where 3 elements was found to give good convergence behaviour without increasing the blade-swept region excessively. A sample mesh of the AC region is depicted in figure 6.6. A sample mesh of an entire domain (case LON-B) is depicted in figure 6.7.

The central shaft was represented by removing mesh elements from the fluid domain. Thus, the meshed diameter of the shaft corresponded to the element size rather than its true physical size. This mis-represented somewhat the drag associated with the central shaft, however as demonstrated in section 6.5.2, TACA predicted the turbine wakes fairly well, even with the support structures under-resolved.

6.3.3 Boundary Conditions

The boundary conditions were different for open and channel type domains.

Open Domains

For open domains, the top, bottom and sides were located 5D away from the rotor, and used an 'opening for entrainment' option, which sets a zero relative pressure condition and zero gradient for velocities and turbulence quantities, which is appropriate for simulating flows without lateral bounds on a grid of finite dimensions.

The inlet was located 10D upstream of the rotor and set a plug-flow condition setting u=u_{ref}, v=0, w=0. The turbulence quantities k and ω were set in terms of a length-scale L_0 and intensity I_0 as:

$$k_{\text{in}} = \frac{3}{2} u_0^2 I_0^2, \quad \omega_{\text{in}} = \frac{\sqrt{k_{\text{in}}}}{C_\mu L_0} \tag{6.8}$$

[7] As a test, case LAT-B was run with the side-wall boundary layers resolved using the same first-layer spacing (0.05 m) and expansion ratio (1.2) as the bottom, which altered the rotor power by less than 0.04%.

The outlet was 20D downstream of the rotor, and used a static pressure condition. Sensitivity studies confirmed that the local flow at the rotor was not influenced by proximity to the boundaries.

The open domain was used for tuning simulations (§6.4) done over ranges of L_0 and I_0, to sensitize TACA to varying turbulence. Since there were no boundary-layers in the open domain (with no rotor present) there were no spatial gradients to the velocity, so without any shear production, the turbulence decayed naturally from the inlet to the turbine location. This decay was undesirable for tuning purposes, and was prevented by adding source terms to the k and ω equations:

$$S_k = C_\mu \rho k_{\text{in}} \omega_{\text{in}}, \quad S_\omega = \beta \rho \omega_{\text{in}}^2 \tag{6.9}$$

which were applied to all grid cells in the open domain.[8] Effectively, these terms modified the natural turbulence level in the simulation to k=k_{in}, ω=ω_{in} rather than to k=0, ω=0. Thus, higher turbulence (produced in e.g. turbine wakes) decayed to the same values as at the inlet, but not below.

Channel Domains

For channel domains, the top boundary used a rigid-lid approximation, which is a free-slip condition on a stationary boundary.[9] The bottom boundary used a rough wall function based on equivalent sand-grain roughness height h_s. The wall-function [80] sets a source term in the momentum equation in the wall-adjacent grid cell using:

$$\overline{S_{\text{M}i}} = \rho u_{\tau_i} u_i^* \tag{6.10}$$

with

$$u_{\tau_i} = \frac{\overline{u}_i}{u^+}, \quad u_i^* = \sqrt{a_1 k} \tag{6.11}$$

$$u^+ = \frac{1}{\kappa} \ln\left(y^+\right) + 5.2 - \frac{1}{\kappa} \ln\left(1 + 0.3 h_s^+\right) \tag{6.12}$$

$$h_s^+ = \frac{\rho h_s u_{\tau_i}}{\mu} \tag{6.13}$$

[8] To the knowledge of the authors, this is a novel methodology for maintaining turbulence levels in RANS simulations, which may be overly dissipative when simulated flows are simplified (e.g. neglecting buoyancy, free-surface effects, or secondary flow structures etc.)

[9] The impact of free-surface deformation was therefore neglected in the present study, although a sensitivity study is warranted considering the shallow depth.

$$y^+ = \max\left(\rho \Delta y u_i^* / \mu, h_s^+ / 2\right) \tag{6.14}$$

where $\overline{u}_i$, and k are the velocity and turbulent kinetic energy in the wall-adjacent grid cell, Δy is the first-layer grid spacing normal to the wall, and a_1 is a tuned coefficient. The wall function sets ω in the wall-adjacent grid cell using:

$$\omega = \frac{u^*}{a_1 \kappa \Delta y} \tag{6.15}$$

From a practical perspective, the impact of roughness h_s is to increase the wall shear-stress, which in turn increases the shear production of k, resulting in higher turbulence, and therefore faster mixing of wakes, and greater momentum transfer between the bulk flow and boundary layer.

In this study, the value h_s=0.15 m was specified to match turbulence intensity at hub-height as measured by stationary ADP (see Appendix B). Note that in channel domains, the ambient turbulence was maintained through shear production in the resolved boundary layer and the turbulence source terms (equation 8.4) were not applied.

The inflow boundary specified spatial profiles $u(y,z)$, $k(y,z)$, ω(y,z), which were created as a compromise between matching measured ADP velocity profiles, and being consistent with the governing equations of the simulations. The profiles were generated using precursor simulations which provided fully-developed boundary layer profiles for the channel geometry, as described in Appendix B.

For channel domains, the outlet was 10D downstream of the nearest rotor and used a static pressure condition. A longer domain would have allowed the wake velocity to recover more fully before the outlet, however since the pressure recovers quickly in the wake, the outlet proximity had little impact on the results.[10]

6.3.4 Actuator Cylinder Model

TACA was formulated using the various coordinate systems (CS) depicted in figure 6.8. The CS used by the RANS solver was termed the global Cartesian system (subscript $_G$). Each rotor had its own local CS (subscript i for the i^{th} rotor) with the origin at the rotor shaft, and the z-axis pointing upward. The flow may approach the

[10]The sensitivity of power to moving the outlet to 15D was less than 0.2% for a single rotor at TSR=2.14, and for case LAT-B. Moving the outlet to 20D changed the downstream rotor power by 0.4% for case LON-A. The small sensitivity justified using a shorter domain.

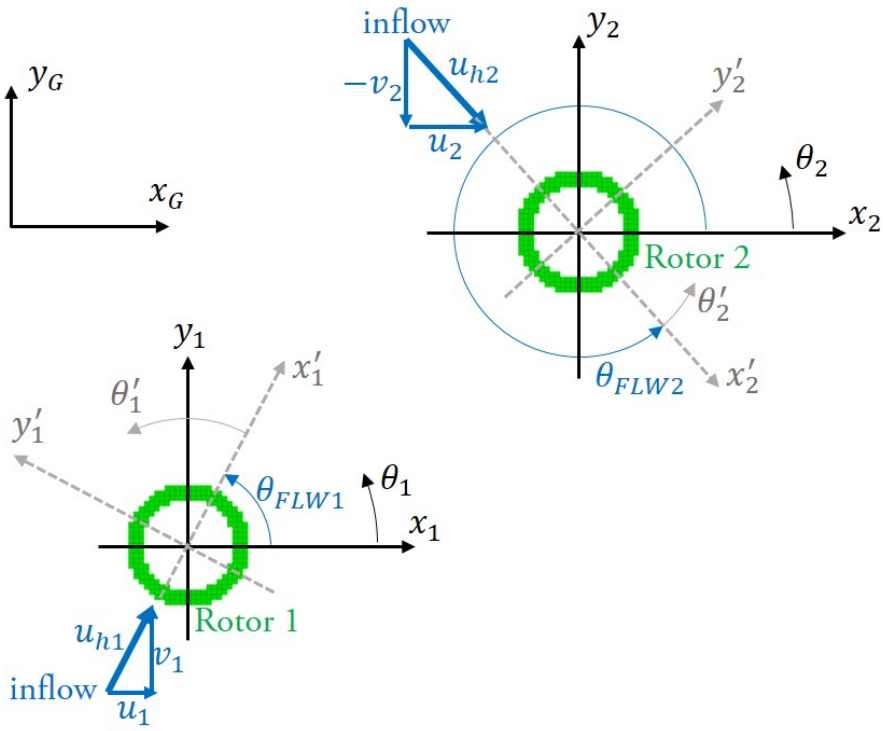

Figure 6.8: Coordinate systems used by TACA. The subscript G refers to the global CS employed by the RANS solver; the subscript $_i$ refers to the local CS associated with the i^{th} rotor and the superscript $'$ refers to the flow-aligned CS.

rotor at any given angle θ_{FLW}, and a local flow-aligned coordinate system (superscript $'$) was defined with its x-axis aligned with the local flow direction. The angle θ' describes position relative to the flow-aligned CS. Rotor rotation is defined as positive counter-clockwise (as viewed from above), at a speed Ω. To allow for both clockwise and counter-clockwise rotation, it was convenient to also define an angle $\theta''=\theta'\Omega/|\Omega|$.

Physically, the blade force (per unit span) can be interpreted as lift L and drag D components in a CS aligned with the relative velocity V_{rel} between the flow and the blade. V_{rel} is the result of local water flow and rigid body motion of the rotor. The blade force can also be interpreted in a cylindrical CS as radial (f_r') and tangential (f_t') components, or in a Cartesian CS as streamwise (f_x') and transverse (f_y') components. These interpretations and transforms[11] relating them to each other, are depicted in figure 6.9.

TACA imposes blade forces via the momentum source term $\overline{S_{\text{M}i}}$ (force per unit volume) in equation 6.5, within each AC region. This is specified in the flow-aligned

[11] which are formally defined in ref. [110]

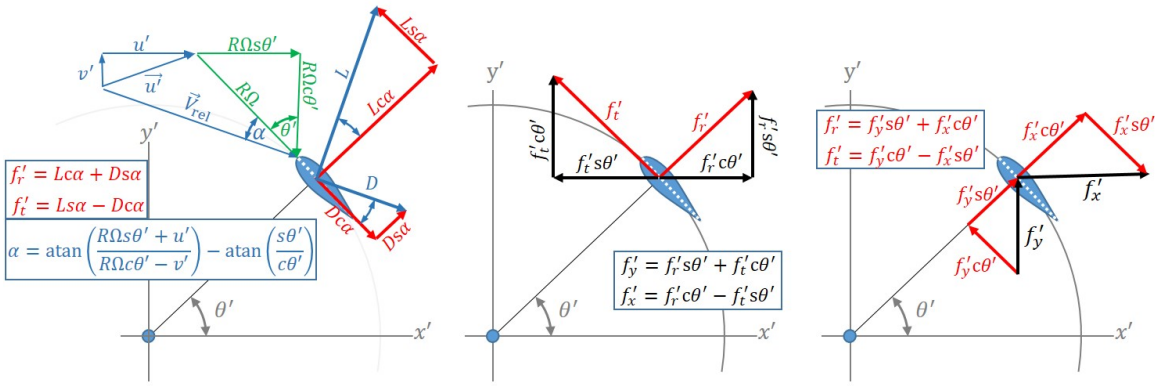

Figure 6.9: Blade force, interpreted as lift and drag (left), as tangential and radial components (middle) and as stream-wise and transverse components (right). Note the shorthand $c\phi$=cos(ϕ), $s\phi$=sin(ϕ).

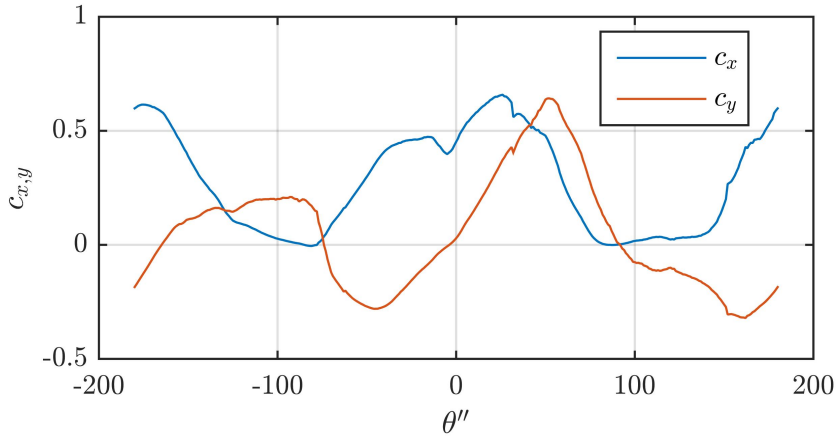

Figure 6.10: Reference rotor loading profiles.

coordinate system (i.e. $\overline{S_{\mathrm{M}x'}}, \overline{S_{\mathrm{M}y'}}$) which is related to tangential and normal components by:

$$\overline{S_{\mathrm{M}t'}} = \overline{S_{\mathrm{M}y'}} \cos\theta' - \overline{S_{\mathrm{M}x'}} \sin\theta' \tag{6.16}$$

$$\overline{S_{\mathrm{M}r'}} = \overline{S_{\mathrm{M}y'}} \sin\theta' + \overline{S_{\mathrm{M}x'}} \cos\theta' \tag{6.17}$$

The applied sources are related to total rotor thrust T and shaft power P by:

$$T = \int_{\mathcal{V}} -\overline{S_{\mathrm{M}x'}} d\mathcal{V} \tag{6.18}$$

$$P = \Omega R \int_{\mathcal{V}} -\overline{S_{\mathrm{M}t'}} d\mathcal{V} \tag{6.19}$$

Thus, the power can be decomposed into components arising from $\overline{S_{\mathrm{M}x'}}$ and $\overline{S_{\mathrm{M}y'}}$:

$$P_{x'} = \Omega R \int_{\mathcal{V}} \overline{S_{\mathrm{M}x'}} \sin\theta' d\mathcal{V} \tag{6.20}$$

$$P_{y'} = \Omega R \int_{\mathcal{V}} -\overline{S_{\mathrm{M}y'}} \sin\theta' d\mathcal{V} \tag{6.21}$$

$$P = P_{x'} + P_{y'} \tag{6.22}$$

In a physical rotor, as the blades rotate their relative velocity, angle of attack and applied force vary in time. In a steady inflow this temporal variation can be re-interpreted as a spatial variation of force with azimuth angle (i.e. $\vec{F}(t) \equiv \vec{F}(\theta'')$). TACA accounts for this spatial variation using reference profiles $c_x(\theta'')$, and $c_y(\theta'')$ to

define the variation of blade force with angular position[12] in the same manner as the *global* model of [113]. For the present study, those profiles were created using results from high-fidelity blade-resolved transient CFD simulations of the rotor (proprietary report[13]), operating near its optimal TSR, and are shown in figure 6.10. TACA scales the reference profiles to ensure that specified thrust and power (T_{spec}, P_{spec}) are achieved. Thus, the stream-wise momentum source is:

$$\overline{S_{Mx'}} = -T_{\text{spec}} \frac{c_x(\theta'')}{\left| \int_V c_x(\theta'') d\mathcal{V} \right|} \tag{6.23}$$

which guarantees that equation 6.18 evaluates to $T{=}T_{\text{spec}}$, and also sets the value of $P_{x'}$ as defined by equation 6.20. The transverse momentum source is:

$$\overline{S_{My'}} = -\frac{1}{R\Omega} \left[P_{\text{spec}} - P_{x'} \right] \frac{c_y(\theta'')}{\left| \int_V c_y(\theta'') \cos\theta'' d\mathcal{V} \right|} \tag{6.24}$$

which guarantees that equation 6.22 gives $P{=}P_{\text{spec}}$. The momentum sources in the local CS for each rotor are then:

$$\overline{S_{Mx}} = \overline{S_{Mx'}} \cos\theta_{\text{flw}} - \overline{S_{My'}} \sin\theta_{\text{flw}} \tag{6.25}$$

$$\overline{S_{My}} = \overline{S_{My'}} \sin\theta_{\text{flw}} + \overline{S_{My'}} \cos\theta_{\text{flw}} \tag{6.26}$$

For simplicity, the same reference profiles ($c_x(\theta'')$, and $c_y(\theta'')$) were used for all TSR. This misrepresented the load distribution at off-design TSR, particularly due to dynamic stall at low TSR. The variation of total thrust and power with TSR are modelled correctly, however, via the $\{T, P\}_{\text{spec}}$ terms. Flow-field errors associated with neglecting the TSR variation in $c_{x,y}(\theta'')$ should be limited to the near-wake because mixing will produce a return to a typical Gaussian shaped wake, with a velocity deficit depending on the total applied thrust more so than the local distribution of thrust. Because the total thrust and power are set independently from the loading profiles, TACA is not expected to be highly sensitive to the loading profiles, which serve mainly to provide a more accurate distribution of force compared to, e.g. a uniform distribution. For example, in the context of axial-flow machines, [59] created reference profiles for the NREL 5-MW reference wind turbine, which they later applied successfully to several different turbines.

[12] This approach was pioneered in the context of horizontal axis wind turbines by [94]

[13] produced by BAE for Instream Energy Systems

The manner in which $\{T, P\}_{\text{spec}}$ are set is critical for TACA's versatility for a variety of flow environments. Similar to [113] using the rotor flowrate velocity, TACA calculates rotor performance based on the volume-averaged horizontal velocity (u_h=$(u^2 + v^2)^{1/2}$) within the AC region, rather than a velocity upstream from the rotor. The rationale for this approach is that an appropriate upstream reference velocity is difficult to define in the context of arbitrary layouts of rotors, and with complex bottom topology, which is discussed more thoroughly [12] in the context of AD methods.

Using the volume-averaged horizontal velocity $\langle u_h \rangle$[14] to define performance required defining alternative rotor performance parameters:[15]

$$C_{\text{T}}^{\star} = \frac{T}{\frac{1}{2}\rho \left\langle u_h^2 \right\rangle A}, \quad C_{\text{P}}^{\star} = \frac{P}{\frac{1}{2}\rho \left\langle u_h^3 \right\rangle A}, \quad \text{TSR}^{\star} = \frac{\Omega R}{\langle u_h \rangle} \tag{6.27}$$

Thus, with known $C_{\text{T}}^{\star}$ and $C_{\text{P}}^{\star}$ the rotor thrust and power can be set in simulations using.

$$T_{\text{spec}} = \frac{1}{2}\rho C_{\text{T}}^{\star} \left\langle u_h^2 \right\rangle A, \quad P_{\text{spec}} = \frac{1}{2}\rho C_{\text{P}}^{\star} \left\langle u_h^3 \right\rangle A \tag{6.28}$$

To summarize, TACA's rotor motor model requires as primary inputs: rotor speed Ω, reference loading profiles $c_{\{x,y\}}(\theta'')$, and target values for thrust and power $\{T, P\}_{\text{spec}}$. The key is to obtain regression models for $C_{\text{T}}^{\star}$ and $C_{\text{P}}^{\star}$ by calibrating with experimental performance and flow data.[16] To emulate rotors, simulations specify momentum sources (equations 6.23 to 6.24) to produce specified thrust (T_{spec}) and power (P_{spec}), which are set using single-unit experimental data during tuning stages (§6.4), and thereafter using equation 6.28 once the regression models for $C_{\text{T}}^{\star}$ and $C_{\text{P}}^{\star}$ have been calibrated, allowing TACA to be used for its intended application which is to predict array performance.

6.4 Actuator Model Tuning

TACA relies on robust models for $C_{\text{T}}^{\star}$ and $C_{\text{P}}^{\star}$ to define the rotor performance over a wide range of inflow and operational conditions. Developing those models can be thought of as re-mapping the standard $C_{\{\text{T,P}\}}(\text{TSR})$ performance characteristics to

[14] Braces $\langle\rangle$ are used throughout this article to refer to quantities which are volume-averaged over the AC region. CFX has built-in functionality for evaluating such volume averages.

[15] As suggested by [116] the velocity is squared/cubed before spatial averaging.

[16] High fidelity simulations could be used in lieu of experiment data.

new set of $C^{\star}_{\{\mathrm{T,P}\}}(\mathrm{TSR}^{\star})$ characteristics.

In this paper, the tuning process involved three distinct phases. The first was to tune the model with single-unit experimental field data. The second phase used TACA to correct the measured performance for channel blockage effect to obtain performance characteristic curves $C_{\{\mathrm{T,P}\}}(\mathrm{TSR})$ appropriate for unblocked (i.e. *freestream*) conditions. The final phase was to develop regression models for $C^{\star}_{\{\mathrm{T,P}\}}$ valid over ranges of $\mathrm{TSR}^{\star}$ and differing turbulence conditions.

6.4.1 Phase 1: Tuning in the Duncan Dam Channel

This phase used a *channel* domain, with the rotor located as depicted in figure 6.4 for the SU tests. The inflow was developed as described in Appendix B, giving a reference velocity u_{ref}=1.87 m/s. The turbulence intensity and length-scale incident on the rotor were I_0=6.8% and L_0=4.4 m, respectively.

TACA was run with the rotor running at the operational points marked as 'calib.' in figure 6.5, with $\{\mathrm{T,P}\}_{\mathrm{spec}}$ set using:

$$T_{\mathrm{spec}} = \frac{1}{2}\rho u_{\mathrm{ref}}^2 C_{\mathrm{T,u_{ref}}} A, \quad P_{\mathrm{spec}} = \frac{1}{2}\rho u_{\mathrm{ref}}^3 C_{\mathrm{P,u_{ref}}} A \tag{6.29}$$

The converged values of $\langle u_h^2 \rangle$ and $\langle u_h^3 \rangle$ were used to calculate $C^{\star}_{\mathrm{T}}$ and $C^{\star}_{\mathrm{P}}$ (shown in figure 6.11) using equation 6.27. The tuned coefficients were relatively insensitive to the grid resolution, as shown in figure 6.11. Increasing the resolution to 41 epd from 21, changed the peak $C^{\star}_P$, by 1.5%, which would imply a 1.5% error in power if a 41 epd grid were used with coefficients tuned for 21 epd, or vice versa. Increasing the grid resolution had very little impact on the velocity field as shown in figure 6.12, which demonstrates that 21 epd was sufficient to adequately capture wake mixing.

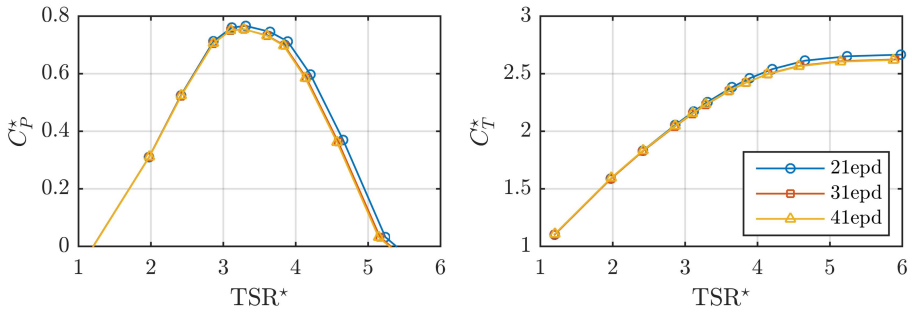

Figure 6.11: Rotor performance coefficients $C^\star_{\{\mathrm{T,P}\}}$ calculated from phase 1 tuning simulations in the DDM channel (§ 6.4.1). Each circle represents a tuning/experimental case. There is a small sensitivity to the grid resolution as shown.

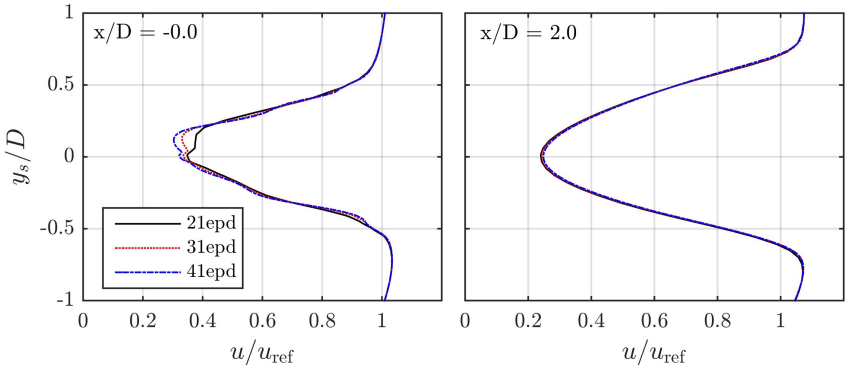

Figure 6.12: Lateral transects of the stream-wise velocity for different grid resolutions. The left plot passes through the rotor centre, while the right plot is 2D further downstream.

6.4.2 Phase 2: Correcting the Rotor Performance for Blockage Effect

The second phase was to correct the rotor performance curves for channel blockage effect. Current best-practise would use an analytical correction (e.g. [103]). However, in this article TACA is presented as a more versatile alternative. Both AD (e.g. [41, 117, 12]) and AC (e.g. [110, 113]) methods have previously been used to compute blockage/terrain effects.

Analytical blockage corrections do not account for real bottom topology, assume laminar flow and assume uniform velocity over the entire channel area. TACA is not limited by such assumptions and is therefore applicable to more realistic scenarios. The trade-off is that it is far more difficult to implement and computationally intensive than analytical corrections. In Appendix C, TACA is shown to be consistent with a standard analytical correction [103] within its limiting assumptions.[17]

TACA simulations were run in an *open* domain with u_0, I_0 and L_0 set to match the phase 1 tuning stage (§6.4.1). T_{spec} and P_{spec} were set using equation 6.28, with $C_{\text{P}}^{\star}$ and $C_{\text{T}}^{\star}$ defined as functions of $\text{TSR}^{\star}$, as shown in figure 6.11.

Compared to the previous simulations in the channel, the rotor-local velocity was reduced because the wake was allowed to expand freely without the influence of any solid/free-surface boundaries. Consequently, the thrust and power were reduced for the same reference velocity.

The corrected performance curves are shown in figure 6.13, where the subscript $_{\text{u}_0}$ indicates corrected coefficients and $_{\text{u}_{\text{ref}}}$ indicates the experimentally measured coefficients in the channel. TACA estimated an approximate 10% reduction in the maximum power coefficient, and a shift of the performance characteristic toward lower TSR.

[17] Work is required to establish the accuracy of both types of blockage corrections for cross-flow turbines as appropriate experimental data become available. Until such detailed validation is possible, it must be assumed that well established methods for axial flow turbines are also valid for cross-flow turbines.

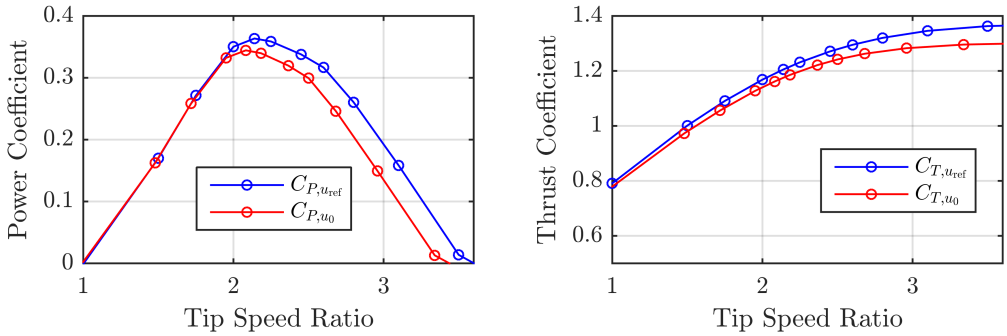

Figure 6.13: Rotor performance coefficients, corrected for blockage effect using TACA. The subscript u_0 denotes corrected performance in unbounded (i.e. *freestream*) conditions, while u_{ref} denotes un-corrected performance. (plots show $C_{\mathrm{P,u_{ref}}}(\mathrm{TSR_{u_{ref}}})$, and $C_{\mathrm{P,u_0}}(\mathrm{TSR_{u_0}})$)

6.4.3 Phase 3: Sensitizing the TACA Model to Inflow Turbulence

The fact that TACA uses the rotor-local flow to calculate power introduces additional sensitivity to its thrust and power predictions, because turbulence alters wake recovery and consequently also the rotor-local velocity (even for a single rotor). For a given freestream the rotor-local velocity is higher in a more turbulent flow[18], so left uncorrected TACA would over predict power.

The sensitivity of the physical rotor to turbulence is a separate and important consideration which is beginning to receive attention in literature. Hypothetically rotors do convert some of the turbulent energy into useful power depending on the length-scale of turbulent eddies relative to the rotor and on the timescale of eddies relative to the rotor inertia and control time-constants. Indeed, in flume tank tests of a model axial-flow rotor [116] found that power was reduced 10% when turbulence intensity changed from 7% to 14%, and that power increased with increasing length-scale.

In the present study the rotor was only tested experimentally in one channel with similar turbulence in all tests. Thus, it was assumed that the physical rotor performance was insensitive to differing turbulence.

This left the issue of addressing TACA's inherent sensitivity to the ambient turbulence, which was addressed by running a set of tuning simulations in the *open* domain. The inflow velocity was held constant at u_0=1.87 ms^{-1}, and the simulations specified:

$$T_{\text{spec}} = \frac{1}{2}\rho u_0^2 C_{Tu_0}(\text{TSR}_{\text{u}_0})A, \quad P_{\text{spec}} = \frac{1}{2}\rho u_0^3 C_{Pu_0}(\text{TSR}_{\text{u}_0})A \tag{6.30}$$

based on the blockage-corrected $C_{\{T,P\}u_0}$ in figure 6.13.

A total of 165 simulations were run covering over a wide range of turbulence conditions and rotor operating points. The intensity varied from 1% to 40% while the lengthscale (normalized by D) varied from 0.5 to 5. The rotor speed varied from TSR*= 1.2 to 5.2.

$C_{\text{T}}^\star$ and $C_{\text{P}}^\star$ were then found for each operating point and turbulence condition. The turbulence within the AC region was characterized in terms of the turbulent

[18]The wake begins mixing immediately, and in a more turbulent flow, the velocity deficit is less at the rotor, for a given thrust force.

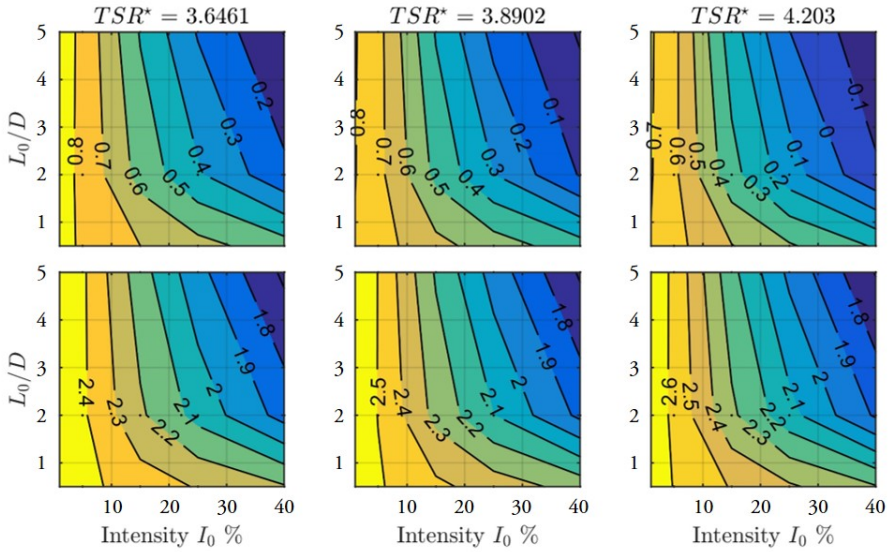

Figure 6.14: Sample rotor coefficients $C_{\mathrm{P}}^\star$ (top) and $C_{\mathrm{T}}^\star$ (bottom) sensitized to varying turbulence for three TSR* operating points. In this paper, TACA used equations 6.32 and 6.33 to define the sensitivity to turbulence, and linear interpolation between TSR* operating points.

Reynolds number $\mathrm{Re}_t^\star$ and the length-scale ratio $L^\star$.

$$Re_t^\star = \left\langle \frac{u_h D\omega}{k} \right\rangle, \quad L^\star = \left\langle \frac{\sqrt{k}}{C_\mu \omega} \right\rangle \frac{1}{D}. \tag{6.31}$$

The modelling approach was to create a regression model for $C_{\mathrm{T}}^\star$ and $C_{\mathrm{P}}^\star$ at each TSR* operating point, to capture the sensitivity to turbulence. The following form was used for the regression model.

$$C_{\mathrm{T}}^\star = A_{T1} + A_{T2} Re_t^{\star -1} + A_{T3} Re_t^{\star -2} + A_{T3} L^\star + A_{T4} L^{\star 2} \tag{6.32}$$

$$C_{\mathrm{P}}^\star = A_{P1} + A_{P2} Re_t^{\star -1} + A_{P3} Re_t^{\star -2} + A_{P3} L^\star + A_{P4} L^{\star 2} \tag{6.33}$$

Linear interpolation was then used for TSR* values between the calibration points. The final tuned model is depicted graphically in figure 6.14. Note the significant variation within the ranges of turbulent intensity and lengthscale, which highlights the need to sensitize the model to changing turbulence.

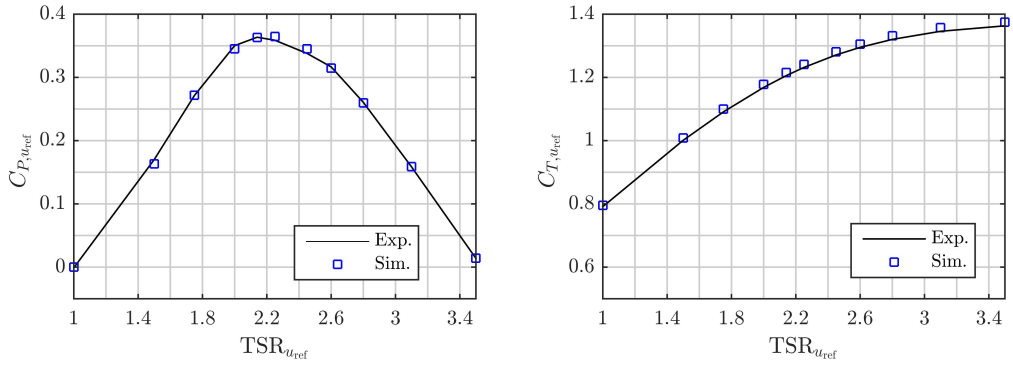

Figure 6.15: Simulation results from testing the TACA regression fits for $C_{\mathrm{T}}^{\star}$ and $C_{\mathrm{P}}^{\star}$. The black line is the best-fit from the experimental data, while the squares are from TACA.

6.5 Validation Results and Discussion

Once the regression model was finalized, TACA was validated for its intended application of predicting wakes and power output of turbine arrays. The validation simulations set the rotor speed Ω to match experiments and used the regression models for $C_{\{\mathrm{T,P}\}}^{\star}$ (equations 6.32-6.33) to define the rotor performance, leading to thrust and power predictions as part of the final converged flow solution.

6.5.1 Preliminary Validation for a Single Rotor

Prior to running simulations with multiple rotors the regression models were verified by running the SU simulations from §6.4.1, but this time setting the momentum sources using the equations 6.32-6.33. The predicted thrust and power coefficients (normalized by u_{ref}) are shown in figure 6.15, and as hoped matched the experiments almost identically.

6.5.2 Validation for the Longitudinal Arrays

The LON experiments were used to perform a quantitative assessment of TACA's ability to predict rotor wakes, and their influence on output power.

The rotor speed Ω was 28.6 rpm for the upstream rotor and 23.2 rpm for the downstream one. The *channel* domain extended from the ADP transect from the SU tests (X=17.91 m, 3.84 m (1.13D) upstream of the first rotor) to 10D downstream of the second rotor.

No ADP transects were taken upstream of both operating rotors for the LON tests. Transects were taken without the upstream rotor present, but with the downstream rotor operating at the P1, P2, and P4 locations. Thus, inflow conditions were generated using the procedure defined in Appendix B. Somewhat different inflow conditions were therefore used for each of the P1, P2 and P4 locations to account for the small temporal variation in channel flow between tests. No transect was taken at P3 without the upstream rotor operating, so the inflow created from the P2 transect was used for P3.

During the ADP transects, notes were taken of the time at which the ADP crossed upstream of each pontoon of the downstream platform. This allowed locating the downstream rotor relative to the transect data. The downstream rotor was not perfectly centred in the wake of the upstream rotor. It is impossible to be certain of the reason for the slight misalignment of the downstream rotor relative to the upstream rotor's wake. Possible factors include wake meandering, transverse flow, and/or imperfect positioning.

The steady-state simulations would not reproduce wake meandering, and did not incorporate transverse inflow components[19] (i.e. secondary flow patterns), so the simulated wake propagated directly downstream from the first rotor. Therefore in the simulations, the downstream rotor was positioned off-centre to locate it at the same lateral position relative to the wake as in the experiments.[20]

The resulting wake downstream of the first rotor is qualitatively compared to ADP transects in figure 6.16. TACA produced reasonable qualitative agreement to the measured wake, including the strong deficit at 2.1D, and the recovery progressing downstream to 8.1D. The ADP data show turbulent flow structures, which are not present in the (time-averaged) TACA simulations.

The wakes were compared quantitatively by extracting velocity along the thin

[19]This would have required time-averaged transects to differentiate between passing eddies vs. mean transverse velocities.

[20]Therefore, the present study validates TACA's ability to predict the performance of rotors located fully/partially in wakes, and how well it predicts wake mixing, but does not validate its ability to predict lateral wake shifting which may arise from meandering, curved channel sidewalls, bottom bathymetry, or other factors. Thus, further validation is needed to fully vet TACA for such flow environments.

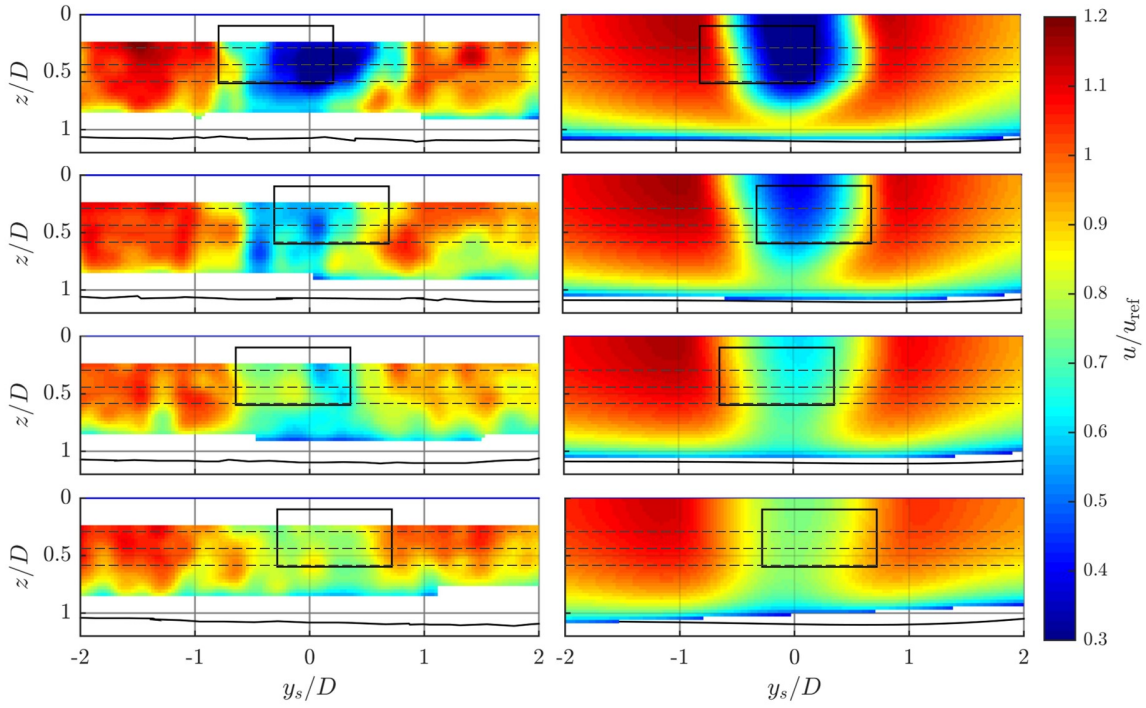

Figure 6.16: Simulated wake downstream of rotor (right panels), compared to ADP transect data (left panels). Transects taken at $x/D = \{2.1, 3.3, 5.3, 8.1\}$ downstream of the first rotor shaft. The transverse coordinate y_s is centred on the velocity deficit, while the black rectangles show the location of the downstream rotor. Velocity was extracted along the thin dashed lines for quantitative comparison.

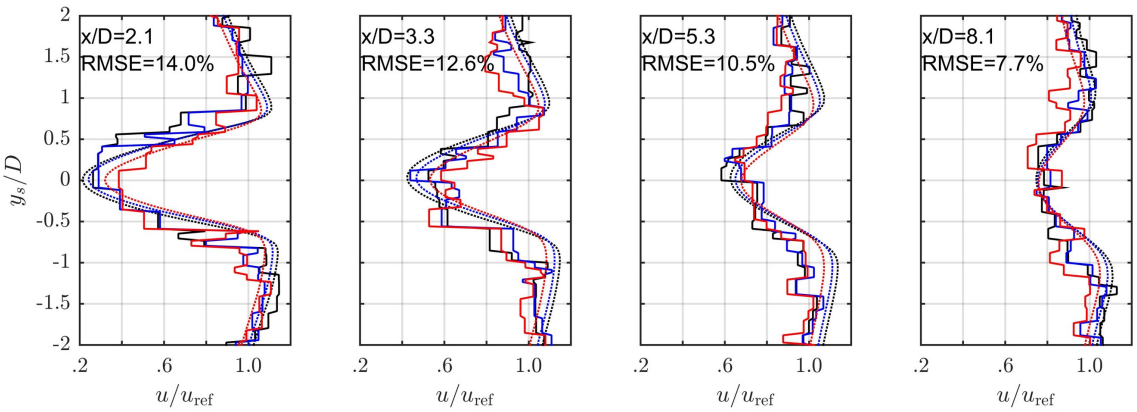

Figure 6.17: Simulated wake (dotted lines) compared to ADP transects, along lines at $z/D = \{0.3, 0.45, 0.6\}$ (black, blue, red).

dashed lines shown in figure 6.16 ($z/D = \{0.3, 0.45, 0.6\}$) and calculating:

$$\mathrm{RMSE} = \sqrt{\mathrm{mean}\left[\left(\frac{u_{\mathrm{sim}} - u_{\mathrm{adp}}}{u_{\mathrm{ref}}}\right)^2\right]} \tag{6.34}$$

which is shown in figure 6.17. RMSE trended from 14% at P1 to 7.7% at P4. The simulations predicted the minimum velocity quite well for all transects. At P1 and P2, the ADP data suggest a somewhat wider wake than the simulation results. At P3, the velocity outside the wake was somewhat lower than predicted by the simulations. Note that the ADP data represent a temporal snapshot, while the simulations represent a temporal average, which would contribute partially to the calculated RMSE even if the simulations predicted the time-averaged flow perfectly. The higher RMSE close to the rotor may be partially due to higher turbulence in the near-wake, which decays gradually progressing downstream. The ambient turbulence intensity in the channel flow was approximately 6% to 7%, quite close to the RMSE in the wake prediction at x/D=8.1.

The measured thrust was somewhat uncertain so it was prudent to evaluate the sensitivity of the simulated wake to changes in thrust. Figure 6.18 shows the sensitivity of the wake velocity (normalized by u_{ref}) to $\pm 10\%$ changes to the thrust and assumed generator/gearbox efficiency. The wake velocity was reduced slightly for increased thrust, and vice versa. The maximum changes in the wake due to changing thrust were on the order of $\pm 5\%$ at $x/D = 2.1$, reducing to about 1% at $x/D = 8.1$.

Furthermore, the generator/gearbox efficiency may not have been constant (as

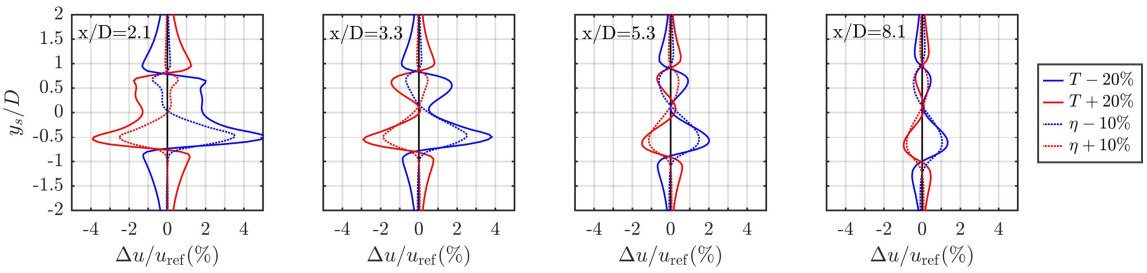

Figure 6.18: Sensitivity of the simulated wake (lateral transects located vertically on the rotor centre) to ±10% changes to the thrust and combined generator/gearbox efficiency.

assumed) over the range of tested TSR. Reducing the combined generator/gearbox efficiency from the assumed 72% to 62% shifted the wake laterally, giving higher velocities on the -y side, but lower on the +y side. Note that the decreased efficiency required a higher shaft power coefficient. Increasing the assumed efficiency had a similar but opposite effect on the wake. While altering the thrust had a direct impact on the wake velocity deficit, altering the efficiency caused a slight widening/narrowing of the wake, accompanied by a lateral shift. These changes were subtle, and did not have a major impact on the output power of the downstream rotor.

The power of the downstream rotor is compared to measurements in figure 6.19. For the cases without the upstream rotor present, the differences between the experiments and TACA were {1%, -7%, -8%, -8%} for the four test positions. TACA predicted that the upstream rotor's wake reduced the downstream power to {22%, 24%, 38%, 56%} of the output without the upstream rotor operating. The experiments showed a reduction to {14%, 31%, 45%, 65%}. These values are in reasonable agreement, particularly considering that power is proportional to the cube of local velocity, therefore requiring high accuracy in the predicted velocity.

The sensitivity to altering rotor thrust by ±10% is also depicted in figure 6.19. For the closest separation distance, the downstream rotor power changed by approximately ±2% (normalized by the upstream rotor power). Altering the assumed efficiency by ±10% changed the downstream rotor power (generator output) by ±3% for the closest spacing, reducing to ±0.2% for the largest.

It is notable that the downstream rotor was operated at a constant rotor speed for all locations, and therefore the reduced power is due to both reduced local velocity and shifting to a less-optimal TSR.

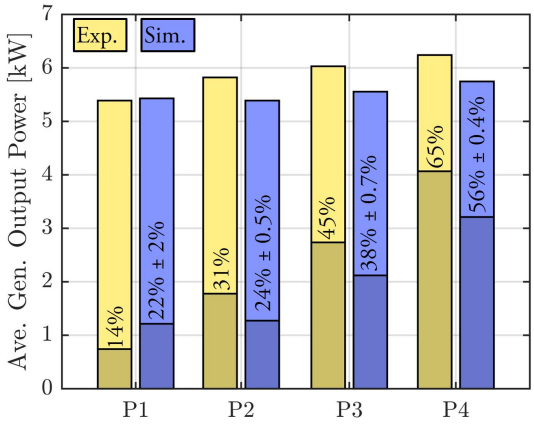

Figure 6.19: Power of downstream rotor for LON cases. The tall (short) bars represent the power without (with) the upstream rotor operating. The uncertainty ranges represent the change in power associated with changing the upstream rotor thrust by $\pm$ 10%.

6.5.3 Validation for Lateral Arrays

Simulations were also run for the LAT cases depicted in figure 6.4. The inflow conditions were generated as described in Appendix B. The inflow was tuned to provide the best match possible, simultaneously to the measured u_{ref} (from stationary ADP deployments) and to the measured lateral variation (from transect data). For case A (shown in Appendix B), the time-averaged stationary ADP agreed very well with the transect data. Therefore, the velocity in the simulations matched the ADP transect very well. For case B, the time-averaged u_{ref} from the stationary ADP was about 4% higher than u_{ref} calculated from the temporal snapshot ADP transect. This discrepancy is attributed to the somewhat non-steady nature of the channel flow. The inflow to the TACA simulation is compared to ADP transect data for case B in figure 6.20.

The experiments measured and reported the power output only from the central rotor. During the experiments, power generated by the outer turbines was dissipated in a static load bank. The experimental test report stated that the load on rotor 3 was set to give an average generator speed of 600 rpm, and the load on rotor 1 was adjusted to give the same output power as rotor 3. These conditions were matched as closely as possible in the simulations. For case B the power of rotors 1 and 3 were set equal (5.2 kW) by manually tuning the speed of rotor 1, however for case A the inflow to rotor 1 was insufficient to match the power of rotor 3 (5.0 kW), so rotor 1 was set at its maximum power speed (giving 4.0 kW).[21] Matching the exact operating point of the outer rotors, however, was not critical for comparing the output power of the central rotor since the thrust (which is less sensitive to Ω than power) of the outer rotors was the dominant factor in altering flow into the central rotor.

The generator power output from the central rotor is compared to experiments in figure 6.21. For case A without the outer rotors operating, TACA predicted the central rotor power as 4.10kW compared to 4.12kW from experiments. TACA predicted a 5.0% performance increase associated with running the outer rotors, compared to 5.9% from experiments. Thus, the agreement between TACA and the experiments was very good for case A.

[21] Given that TACA provided fair agreement to the experimental power for other tested cases, it seems unlikely that it would give a 20% error for this particular case. The discrepancy may be due to the instantaneous ADP transect giving a too low velocity upstream of rotor 1, compared to the true time-average. This brings into question the employed method of scaling the ADP transect data with a time-averaged stationary measurement. Ideally, this could have been avoided if the experiments had measured the spatio-temporal flow variation simultaneously, which would have required multiple ADP units, perhaps with one oriented horizontally instead of vertically. However, it is also unclear whether rotor 1 actually achieved 5.0 kW in the experiments.

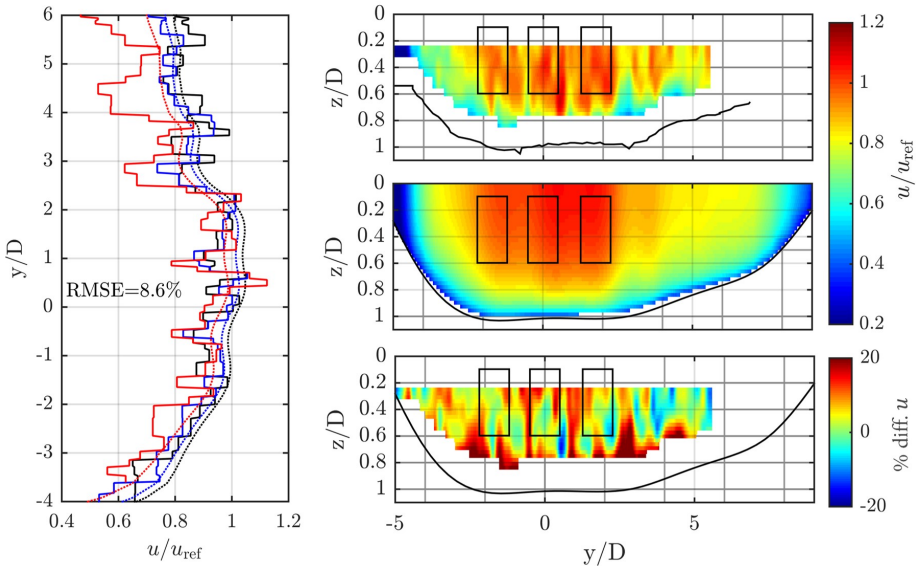

Figure 6.20: Velocity transect 8.5m upstream of the lateral array case B. The left panel compares sim. (dotted) and ADP (solid) at three horizontal lines at depths of $\{0.3, 0.45, 0.6\}$D (black, blue, red). The right panels show the transect velocity from ADP (top) and sim. (middle) and the percent difference between the two (bottom).

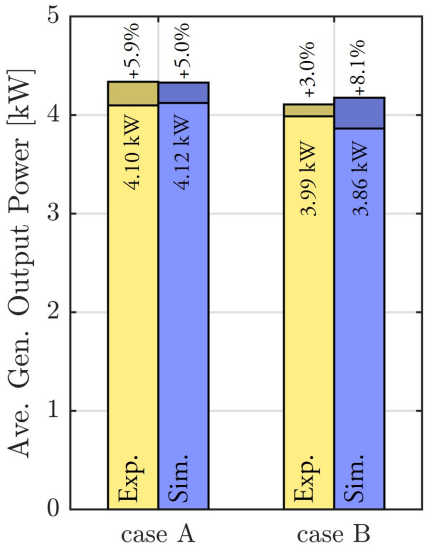

Figure 6.21: Power of central rotor for LAT cases. The tall (short) bars represent the power without (with) the outer rotors operating.

For case B, TACA under-predicted the power (by 3%) for just the central rotor operating, but over-predicted the power with all three rotors operating (by 2%). While these discrepancies are small, TACA predicted an 8% power increase for the central rotor when the outer rotors were switched on, whereas the experiments predicted an increase of only 3%. Intuitively one would expect the performance boost from lateral proximity to increase as the separation distance decreases. As rotors are brought closer together, they are exposed to a larger portion of the fast flowing water bypassing the other rotors. However, turbulent mixing reduces the bypass flow velocity, and the array diverts flow around the entire rotor group; both of which reduce the potential performance gain associated with close lateral spacing. The current experimental dataset is insufficient to tease-out such nuanced details regarding the interaction between rotors.[22] Indeed, it is possible that the mean channel flow was slightly slower during the test with all three rotors operating, compared to the test with only the central rotor, which could account for the smaller than expected performance gain seen in the experiments.

[22]With the present dataset, it is impossible to validate the details of TACA's prediction of the bypass flow or the diversion around the entire array. Qualitatively it does represent those processes, as clearly visible in figure 6.22.

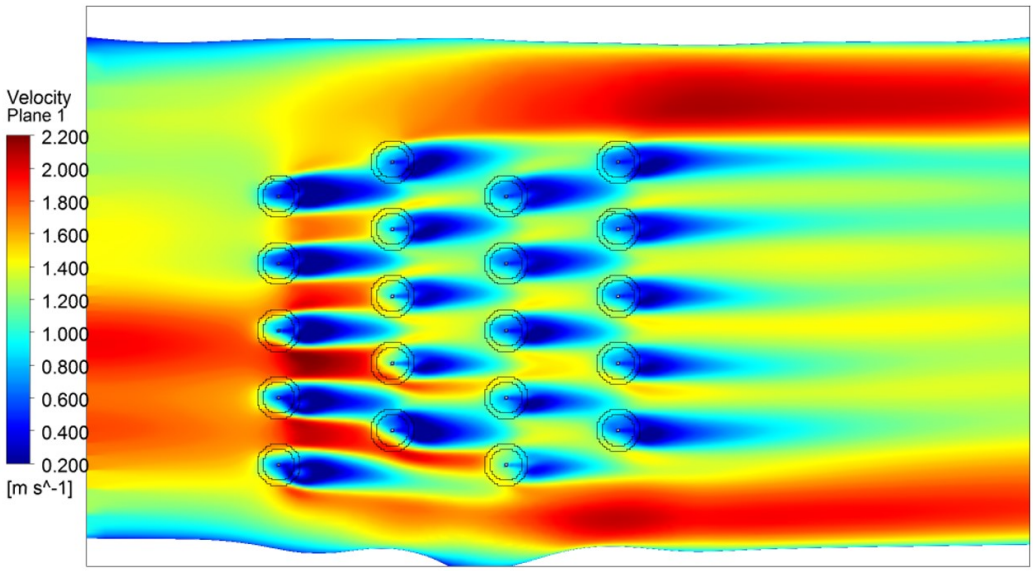

Figure 6.22: Flow velocity through a staggered 4-row array of turbines in the Duncan Dam channel.

6.6 Computational Efficiency

Since TACA is intended for modelling large turbine arrays, it was prudent to investigate how its computational cost scales with the number of rotors. As an initial study, one simulation was run in the Duncan dam outflow with 20 rotors, using the same domain and inflow conditions as case LAT-A.

The resulting flow is depicted in figure 6.22. This simulation used 1.8M elements, required 98s for mesh generation, 5 minutes for pre-processing, and approximately 30 minutes to run on a personal laptop (CPU: Intel® Core™ i7-6700HQ @ 2.60GHz).

The computational time required to complete the calibration and validation simulations presented throughout this study are presented in table 6.1. The most significant expense was sensitizing regression models to the inflow turbulence, because of the number of simulations used. Even that expense was relatively low, requiring less than 10 hours. The setup time increased with the number of rotors because of increasing mesh size and increasing number of expressions that need to be pre-processed by CFX-pre. The last column summarizes the runtime normalized by number of simulations and number of rotors, which was significantly lower for the 20 rotor array. Certainly it is tractable to run TACA simulations of numerous array layouts to perform comparative studies.

type / section	#sim	#rotor	setup	run	runtime /sim/rotor
Tune 1 (§ 6.4.1)	12	1	0.8	36.6	3.0
Tune 2 (§ 6.4.2)	12	1	0.5	36.6	3.0
Tune 3 (§ 6.4.3)	165	1	0.6	583.3	3.5
Valid. SU (§ 6.5.1)	12	1	0.7	27.5	2.3
Valid. LON (§ 6.5.2)	4	1	2.2	9.6	2.4
Valid. LON (§ 6.5.2)	4	2	3.4	19.5	2.4
Valid. LAT (§ 6.5.3)	2	1	1.0	4.9	2.4
Valid. LAT (§ 6.5.3)	2	3	3.6	15.4	2.6
Array (§ 6.6)	1	20	6.6	30.5	1.5

Table 6.1: Time required (minutes) to setup, run and post process for TACA simulations. The setup category includes mesh generation and pre-processing but excludes creating a digital elevation model from raw data points. The run category includes partitioning the domain and solving the RANS equations. All simulations done using 4 partitions on a personal laptop (CPU: Intel® Core™ i7-6700HQ @ 2.60GHz). The time required to develop inflow profiles (Appendix B) was significant but is not included.

6.7 Conclusions

This paper has introduced and validated the tuned actuator cylinder approach (TACA) for simulating cross-flow/vertical-axis rotors with wake interaction and channel blockage effects.

TACA is an adaptation of a similar methodology also developed by the authors, for horizontal-axis turbines called TADA [12], and is a natural progression from the *global* model approach of Dominguez et al. [113].

Key aspects of TACA are: 1) to normalize rotor thrust and power with respect to the rotor-local velocity, rather than the freestream, which is not available in realistic turbine farm simulations; 2) to generate regression models for rotor thrust and power coefficients, analogous to airfoil table lookups; and 3) to use the SST turbulence model, or another eddy-viscosity limiter to improve simulation predictions of near wakes.

This paper demonstrated that TACA is suitable for modelling cross flow turbines in real-world flow environments. The model was tuned using single-rotor test data and validated using test data from rotor arrays, collected at the Duncan Dam discharge channel. The validation confirmed the model's predictive ability for two rotors in a longitudinal layout (LON), and for three rotors oriented laterally (LAT). In both cases, TACA gave reasonable power predictions. TACA was able to correctly predict the upstream rotor's wake for the LON layout, as well as the downstream rotor's power output when located in the wake. It correctly predicted increasing power resulting from the LAT array configuration.

This paper also demonstrated that TACA predicted channel blockage effect consistently with an industry-standard analytical method, but is also more versatile because it can account for the influence of exact channel geometry, non-uniform inflow velocity, and turbulent mixing.

Additional contributions are an innovative technique for generating inflow conditions for RANS simulations (Appendix B), and a method to maintaining high levels of turbulence in RANS simulations (equation 8.4).

The validation presented herein is admittedly somewhat preliminary as a full error analysis has not been carried out for the experimental data. In particular, the temporal variation of the flow was only characterized at single point vertical profiles upstream of rotors, whereas the ADP transects where only available for temporal snapshots. This made it necessary to develop a complicated procedure (Appendix

B) for developing appropriate inflow conditions to the CFD simulations. Future lab and field studies should devise methods to measure the spatio-temporal variation of flow simultaneously, which would alleviate much uncertainty for subsequent validation work.

Despite many uncertainties, the close agreement between the experiments and predictions demonstrates that TACA is a promising methodology for analyzing the influence of array layout in potential tidal/river energy sites. The ability to quickly and accurately model the impact of wake interaction and channel blockage effects on turbine performance is important for predicting yield. In turn, yield estimates are required for predicting project revenue, which is critical for attracting potential investors to tidal/river energy projects.

Acknowledgments

This research was conducted in collaboration with Instream Energy Systems (IES), based out of Vancouver B.C. IES provided the experimental data used for validating the TACA methodology. David Leboe, Ronan Conron, and Shane Grovue from IES provided crucial technical and data support. Dr. Caterina Valeo from the University of Victoria provided technical support and much assistance in securing funding in the form of Engage Grant (138968) provided by the National Sciences and Engineering Research Council of Canada.

Appendix A: Considerations for calculating turbulent kinetic energy

The collected ADP data were not ideal for calculating turbulent kinetic energy. Each ADP ping was subject to a high degree of uncertainty termed Doppler noise. In practise, this uncertainty is reduced by sampling multiple pings for each data sample. The used ADP ping rate was 9 pings/s, and the averaging period was 5 s, giving 45 pings per data sample. The averaging filters out high-frequency components of the original signal, therefore reducing its total variance. In this appendix, it is shown that the reduction in variance from filtering was nearly equal to the increase in variance from noise, which justifies using the uncorrected velocity time-series to find the turbulent kinetic energy.

Turbulent kinetic energy is calculated from the sum of variances from the three (true) velocity components, i.e.:

$$k = \frac{1}{2}\left(\sigma_u^2 + \sigma_v^2 + \sigma_w^2\right) \tag{6.35}$$

However the variance of each measured velocity component is increased by Doppler noise ($\sigma_{Nu_i}^2$), but also decreased by the averaging filter ($\sigma_{Fu_i}^2$).

Therefore, the turbulent kinetic energy can be calculated using the sum of variance rule:

$$k = \frac{1}{2}\sum_{i=1}^{3}\sigma_{Mu_i}^2 - \frac{1}{2}\sum_{i=1}^{3}\sigma_{Nu_i}^2 + \frac{1}{2}\sum_{i=1}^{3}\sigma_{Fu_i}^2 \tag{6.36}$$

where the first term is the measured signal, the second is a correction for Doppler noise, and the third is a correction for the averaging filter.

The magnitude of the Doppler noise for horizontal velocity components was given by Sontek as:

$$\sigma_{N\{u,v\}} = \frac{235000}{F\Delta z\sqrt{N}}, \quad \sigma_{N_w} = \frac{78000}{F\Delta z\sqrt{N}} \tag{6.37}$$

where F is the operating frequency of the unit (1.5 MHz), Δz is the distance bin size (0.25 m) and N is the number of pings used for each sample (45). Those numbers give $\sigma_{N\{u,v\}}^2 = 8.7 \times 10^{-3}\,\mathrm{m^2 s^{-2}}$ and $\sigma_{Nw}^2 = 9.6 \times 10^{-4}\,\mathrm{m^2 s^{-2}}$. Therefore, based on manufacturer specifications the second term in equation 6.36 is $0.0092\,\mathrm{m^2 s^{-2}}$.

Determining the impact of the averaging filter (2nd term) was not trivial. An estimate was made using data from a separate experimental campaign [114]. That study simultaneously collected 2 Hz single-ping ADP data, and 16 Hz Acoustic Doppler Velocimeter (ADV) data to assess the ability of ADP for measuring turbulence quantities.

Thomson et al. [114] calculated an empirical Doppler noise value by comparing the measured variance of of the ADV and ADP signals, and found that the noise level increased with velocity, and was often higher than the manufacturer's specification. Herein, we have used the same methodology to find the Doppler noise associated with the 2 Hz ADP dataset:

$$\sigma_{Nu_i}^2 = \sigma_{\mathrm{ADP}u_i}^2 - \sigma_{\mathrm{ADV}u_i}^2 \tag{6.38}$$

Note that there was no filtering effect on the 2 Hz data because each sample was a single ping, and that 2 Hz was sufficient to resolve the main energy contribution section of the velocity spectrum.

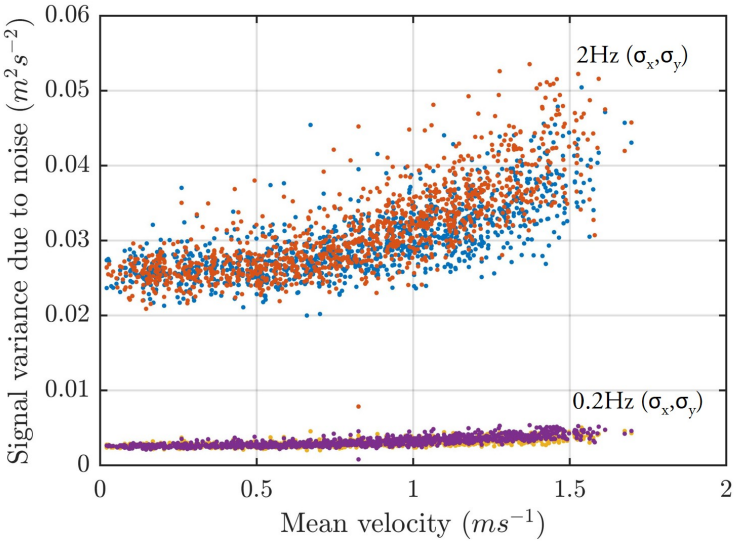

Figure 6.23: Calculated variance due to Doppler noise for the raw 2 Hz ADP data of [114], and for the same data re-sampled to 0.2 Hz using an averaging filter.

The entire time-series was segmented into 5-minute intervals, and the above equation was evaluated on each segment to determine the Doppler noise, which is depicted in figure 6.23.

The data were used to estimate the impact of a 5 s averaging filter on the measured variance. This was assessed by treating the ADP data as ground truth ($k = \frac{1}{2}\sum_{i=1}^{3}\sigma^2_{\mathrm{ADV}u_i}$) and rearranging equation 6.36 as follows:

$$\sigma^2_{Fu_i} = \sigma^2_{\mathrm{ADV}u_i} - \sigma^2_{\mathrm{ADP}u_i} + \sigma^2_{Nu_i} \tag{6.39}$$

A 5 s averaging filter was applied to the raw 2 Hz ADP data to match the sample rate used in the Duncan Dam experiments. The averaging reduced the Doppler noise variance by a factor of 10 (10 samples in each average) which is depicted in figure 6.23. Evaluating equation 6.39 gave the variance reduction from applying a 5 s averaging filter, and allowed calculating the third term in equation 6.36, which is depicted in figure 6.24.

The impact of the 5 s filter is greatest for faster flows which have a broader turbulent spectrum with more energy at high frequencies. The intersection of the filter effect trend with the Doppler noise occurs at $U = 1.77\,\mathrm{ms}^{-1}$. The flows in the Duncan Dam experiments ranged in velocity from 1.5 to $2.0\,\mathrm{ms}^{-1}$, where the lost variance due to filtering is nearly equal to the added variance from Doppler noise. Therefore it was

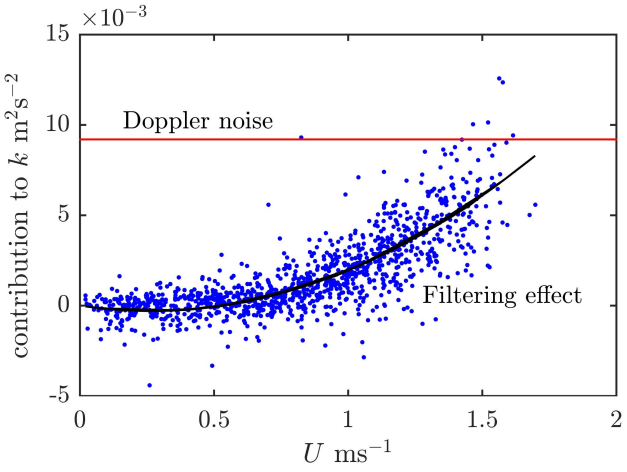

Figure 6.24: Contributions of Doppler noise and 5 s filter to the calculated turbulent kinetic energy. The filter effect is fit by a quadratic to the mean velocity ($\Delta k = 4.20 \times 10^{-3} U^2 - 2.24 \times 10^{-3} U$)

concluded that estimating k from the data was appropriate and valid.

Appendix B: Precursor Simulations to Develop Inflow Profiles

Inflow conditions were developed for each individual simulation using a precursor simulation. This was done to ensure that the vertical profile of velocity was consistent with the governing equations of the CFD simulation. Without this step (i.e. using ADP transect data directly as an inflow condition to the main simulation) there was a problematic transfer of momentum from the upper layers toward the bottom of the domain, which reduced the hub-height velocity, giving reduced power output. This happened because the ADP data suggested a vertical profile with lower velocity near the bottom, compared to the fully-developed boundary layer profiles predicted by the simulations.

The precursor simulation domain was an extrusion of the main simulation inflow plane, and was five elements long in the x-direction. The top, side and bottom boundaries used the same conditions as the main simulation, while the inlet and outlet were linked by a translational periodicity condition. This effectively created an infinitely long channel of constant cross section.

The flow was driven by a horizontal pressure gradient, which was specified to give the desired hub-height velocity u_{ref}. This was imposed on the entire flow domain using:

$$\overline{S_{\mathrm{M}x}} = \frac{dp}{dx} = C(u_{\mathrm{ref}} - u_{\mathrm{prb}}) + \frac{1}{\mathcal{V}} \int_{\mathcal{S}} \tau_w dS \tag{6.40}$$

where u_{prb} is the evolving simulation velocity at hub-height, $\mathcal{V}$ is the periodic domain volume, and the surface integral represents the total shear force acting on the bottom boundary. The control coefficient C=10 $\mathrm{Pa\,s\,m^{-2}}$ was selected to provide robust convergence.

Profiles $u(y,z)$, $k(y,z)$, and $\omega(y,z)$, were then extracted from the converged precursor simulation, and used as the inflow to the main simulation. This is depicted graphically in figure 6.25. A scaling factor $F(y)$ was applied to the velocity profile, to account for the lateral variation as measured by ADP and to ensure that u_{ref} was consistent with the available ADP data (which was from either a transect or a stationary deployment).

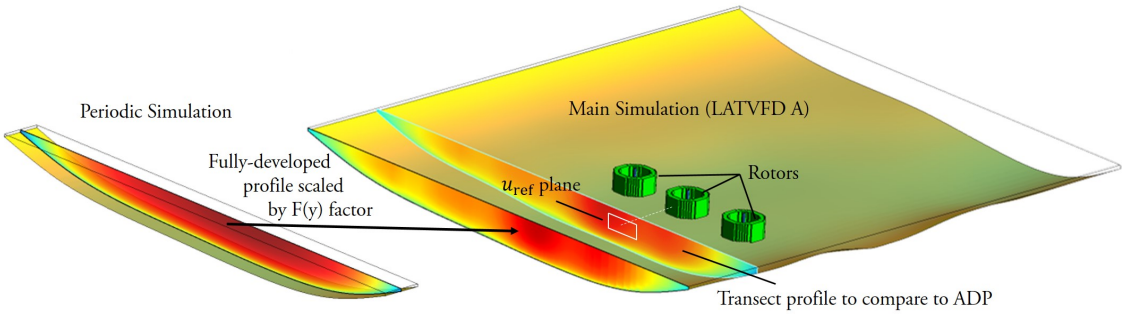

Figure 6.25: Summary of the process used for developing inflow conditions. The periodic simulation gave fully developed vertical velocity profiles consistent with the simulation turbulence and wall models. The scaling factor F(y) modified the velocity to improve agreement with available ADP data.

A sample plot showing the resulting inflow for case LAT-A is shown in figure 6.26. The figure also compares the simulated transect to the available ADP velocity.

A sample plot showing a vertical profile of velocity is shown in figure 6.27. The tuned inflow was faster near the bottom compared to the ADP data, but matched the velocity averaged over the rotor swept area. The vertical profile of turbulence intensity matched the ADP-derived profile reasonably, with the tuned value of sand-grain-roughness (0.15 m).

The ADP data suggest a nearly linear velocity profile within the first meter of the bottom, and a maximum at approximately 2 m depth. The periodic simulations did not reproduce this variation exactly. The discrepancies between fully-developed CFD profiles and ADP data may be due to a number of reasons. A better agreement may be possible by modelling a dynamic free-surface (but at great computational expense), or possibly by modelling buoyancy effects. It may be that the employed turbulence/wall function/bottom friction treatments are not perfectly suited to this particular flow. It may equally be that the real channel boundary layer was not fully developed, due to changing bottom topology, or that the ADP data quality was reduced near the bottom. The discrepancy is not due to insufficient grid resolution, as changing the wall adjacent cell size from 5 mm to 1 mm produced no change. In any event, further work is required to establish and/or validate methods for 3D RANS simulation in river/tidal channel environments. Despite the discrepancies in the vertical velocity profile, the channel flow was modelled with sufficient fidelity to demonstrate TACA's utility for simulating individual turbines and arrays.

Appendix C: Blockage Effect Study

The influence of channel walls on the flow through a turbine is to restrict the wake from expanding fully, resulting in somewhat faster flow through the rotor. This is commonly referred to as a blockage effect. Garrett and Cummins [103, 104] and Vennell [105, 106] have presented rigorous analytical studies of how blockage effect influences the optimal layout of turbines, which, for an idealized channel, is a fence of turbines spanning a single cross-sectional transect. The main factor increasing power is the blockage ratio BR, which is the total swept area of turbines in a given transect, compared to the channel cross-sectional area.

A critical capability for TACA is to predict how proximity to channel walls and to other turbines affects rotor power. TACA's ability to predict the influence of BR was

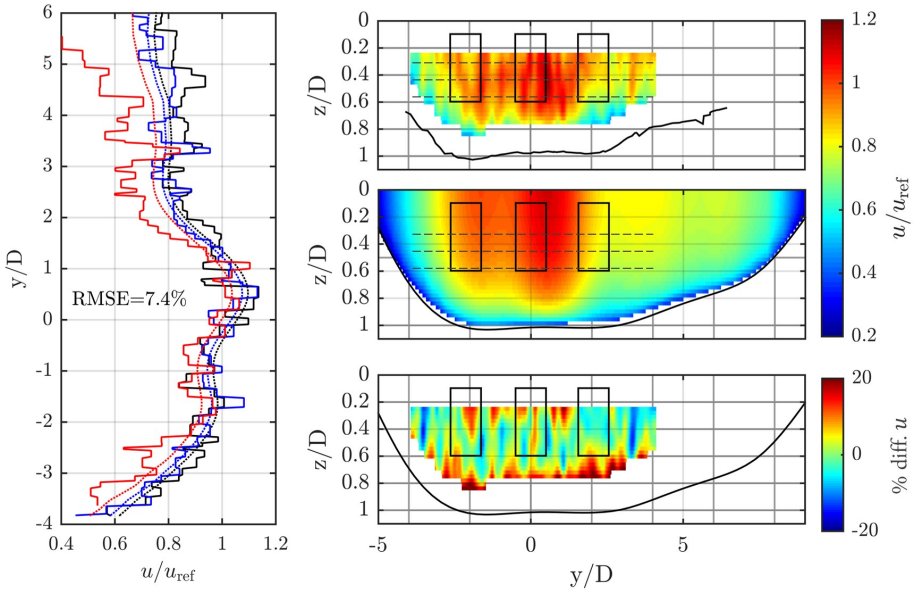

Figure 6.26: Velocity transect 8.5m upstream of the lateral array case A. The left panel compares sim. (dotted) and ADP (solid) at three horizontal lines at depths of $\{0.3, 0.45, 0.6\}$D (black, blue, red). The right panels show the transect velocity from ADP (top) and sim. (middle) and the percent difference between the two (bottom).

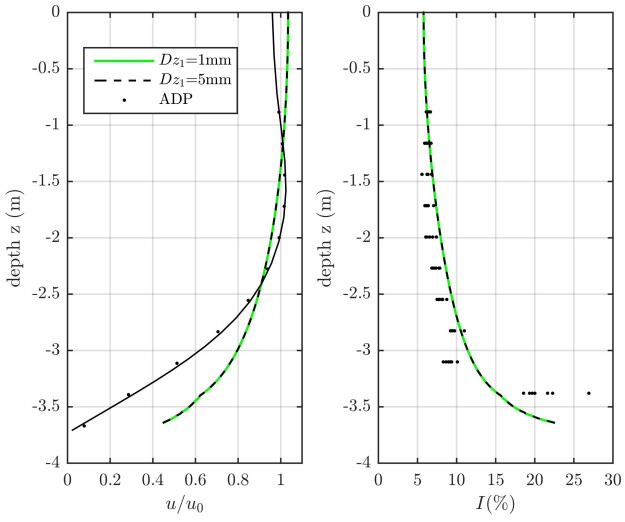

Figure 6.27: Vertical velocity profile from the simulation inflow condition, compared to a time-average profile from stationary ADP data. The vertical profile is insensitive to changing the first layer grid cell size from 5mm to 1mm.

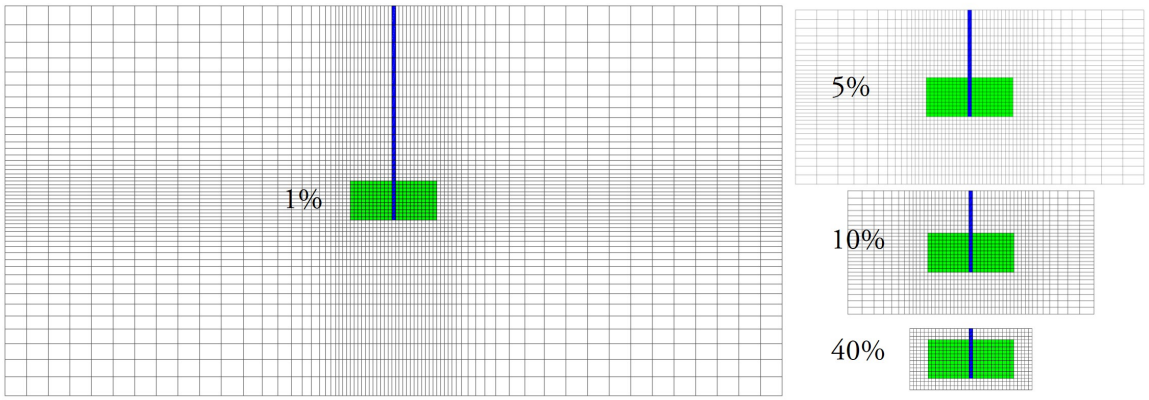

Figure 6.28: Sample mesh used for blockage ratios ranging from 1% to 40%

assessed by running simulations in artificial channels of decreasing cross sectional area. As the channel became narrower, BR increased, and TACA correctly predicted higher thrust and power. Those results were then corrected using an analytical formulation for blockage effects [107][23] to provide the rotor performance in unblocked conditions. Those corrected results were then compared to thrust and power predictions from running TACA in an unblocked *open* simulation domain.

To isolate blockage effects from variations in rotor performance, the TACA simulations used constant values $C_T^\star$=1.1 and $C_P^\star$=0.78, TSR*=3.2, rather than using table-lookups. The analytical correction becomes invalid when the rotor thrust coefficient is higher than about 0.8 as the wake transitions into so called 'turbulent wake state'. Therefore, the value of $C_T^\star$ was significantly lower than that of the test rotor. A plug flow of 2.0 ms^{-1} was specified at the inlet, and a static pressure condition at the outlet. The analytical correction was derived assuming laminar flow, so for consistency the simulations specified a very low turbulence intensity I_0=0.1% L_0=2D. The simulations used a free-slip wall condition on the sides, top and bottom, also for consistency with the analytical correction. To model the rotor in an unblocked environment (BR=0), one simulation used an 'opening for entrainment' boundary condition on the top bottom and sides, using the largest domain.

The domain used a rectangular cross section with the same aspect ratio as the rotor. Domains were created with BR ranging from 1% to 50%. Sample meshes are shown in figure 6.28, where the mesh in the actuator region remains constant for all tested BR.

The results are summarized in figure 6.29. The blue lines show the thrust and

[23] which is mathematically equivalent and was published earlier to the more often cited [103].

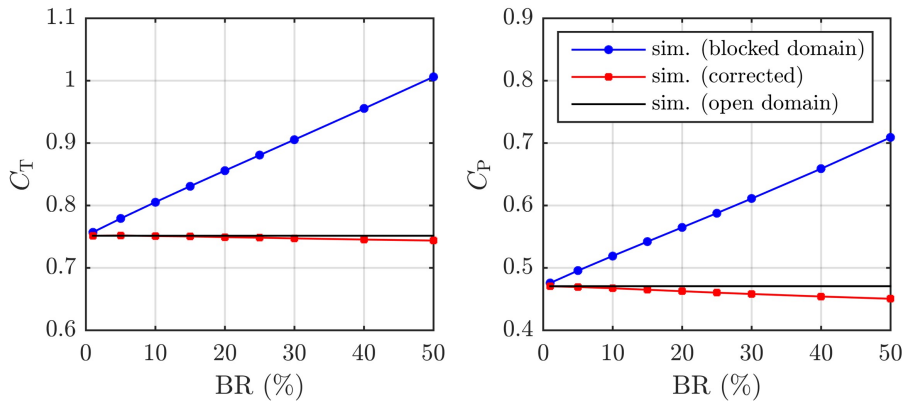

Figure 6.29: Variation of thrust and power coefficients with BR, as predicted by TACA (blue). The red line shows the result of applying the analytical correction to correct the blue line to unblocked conditions. The black line shows TACA's prediction in an open domain.

power coefficients predicted by TACA in the various domains. The red line shows the result from TACA corrected to unblocked conditions using [107]. The black line shows TACA's prediction for the unblocked model domain. The discrepancy between the black and red lines ranges from 0 at BR=0, to 1% (for C_{T}) or 4.3% (for $C_{\mathrm{P,u_0}}$) at BR=50%. These discrepancies are small compared to the impact of the blockage effect, which increased C_{P} by 49% at BR=50%. Thus, within a reasonable margin, TACA predicts blockage effects consistently with a well established analytical model, and in fact TACA should be more accurate.

Note that the analytical method is somewhat limited because it makes a number of simplifying assumptions including 1D laminar flow. TACA is more versatile because it can use exact channel geometries, and can account for the impact of turbulence on wake mixing.

Chapter 7

Computational Methods for Tidal Turbine Farm Energy Yield, Part One: Methods and Initial Validation

This chapter and the next have been submitted to the International Journal of Marine Energy as a two-part paper. These two chapters complete the thesis by presenting a hybrid 2D regional-scale / 3D farm-scale modelling approach for predicting flow fields and energy yield in large tidal farms.

Abstract

As tidal turbine development projects are nearing commercial scale there is a pressing need to establish best-practise methods to predict tidal farm energy yield and environmental impacts. Yield is critical for financial planning because it defines the project's revenue stream, while impact assessment is critical for permitting. This two-part paper presents a novel hybrid simulation method for calculating turbine output, wakes and far-field impacts of a tidal farm. The approach runs 2D coastal simulations to predict flow time-series over minute to monthly scales for basin-channel systems, and then categorizes that time-series using a method of bins. High resolution 3D simulations are run for each bin to predict vertical velocity profiles and wake interaction effects between turbines.

Part one of the paper introduces the hybrid approach and case-study field data used for validation and focuses on simulations without rotors present to confirm fundamentals of the hybrid approach. It introduces a power-conserving bin averaging procedure, and describes converting the 2D bin-averaged flow states from the coastal model to 3D boundary conditions for the high-resolution simulations. The method-of bins approach is confirmed to gives yield consistent with a full time-series within $\approx$ 1%. The boundary conditions and ability of the high-resolution simulations to predict vertical profiles are also confirmed by comparing to measured field-data. Part two adds turbines to the simulations, discusses wake predictions, and demonstrates the hybrid method for farms including up to 42 turbines.

7.1 Introduction

Tidal turbine technologies are approaching commercial-scale deployment in large-scale tidal farms. Several individual full-scale turbines have been deployed in actual working environments with grid connected systems, yet progress toward large scale tidal farms remains slow. For the tidal power industry to move forward in the near-term, project developers will need to secure funding for farms consisting of several rotors. In the longer term, the goal of tidal farm projects will be to maximize energy production by installing many turbines within limited deployment regions. Presently, uncertainty in predicting energy yield presents a significant barrier to investment. Yield, along with the energy price, defines the project's revenue, so robust estimates for yield are critical for attracting potential investors.

A second barrier is regulatory approval which requires study of potential impacts on local ecosystems and may be informed by hydrological modelling of sediment/pollutant transport, and alteration of tidal amplitudes. Such studies are critical for weighing the benefit of zero green house gas energy production against changes to the local environment and require better than 'rough estimates' to adequately weigh the pros and cons.

Standard procedures for yield analysis and impact assessment are not fully established. The International Electrotechnical Commission (IEC) standard on Tidal Energy Resource Assessment and Characterization [2] was released in 2015 and provides general guidelines for yield assessment but certainly contain no definitive procedures. Meanwhile, research consortia [3] and consultancies [4] continue to develop their own assessment methodologies. This paper contributes toward developing such procedures, by proposing specific methodologies for performing yield assessment, which have been validated and are computationally tractable for a developer to employ.

There are two key ingredients to predicting tidal farm yield. The first is a robust characterization to relate turbine performance to the rotor-local velocity, and the second is to predict the velocity field which varies in time and space and is altered by rotors.

Turbines alter tidal flows from their natural state, and the impacts can be categorized into far-field, and near-field effects. Examples of far-field effects are a bulk reduction of flow through the entire farm and/or re-directing flow around the turbine farm, or through less-resistive channels. Tidal farms may alter the amplitude and phase of tidal flows [8], and alter the natural frequency of entire basin-channel systems

if sufficient energy is extracted. Depth-averaged (2D) shallow water equation (SWE) solvers have often been used to predict far-field effects (e.g.[8, 118, 91, 119, 120, 121]) of idealized tidal farms. To date, however, such studies have not validated their turbine modelling methods for their ability to predict output power for real-world turbines affected by each other's wakes, which is critical for estimating yield. The magnitude of far-field effects depends on the ratio of the additional resistance created by turbines, relative to the natural channel bottom friction. [122] Since tidal flows vary significantly on diurnal and monthly time-scales, such SWE simulations must be run for long durations spanning e.g. several months to obtain statistics valid for inter-annual yield prediction [5].

Near-field effects include the reduction of velocity in turbine wakes, and the associated acceleration of the flow surrounding each wake. Wakes may alter yield significantly; for example, a turbine directly in the wake of another may have 80% reduced power output, even 10 diameters further downstream [76], as well as ingesting flow with altered turbulence characteristics. Conversely, it is also possible for turbines to have mutually beneficial interaction effects, when located within the accelerated flow regions surrounding each other's wakes (e.g. [123, 124]). Near field effects are most appropriately modelled using 3D flow simulations because wakes are inherently a 3D phenomenon, and methods [12] have been shown to accurately predict turbine power when affected by wakes. The issue with 3D models capable of resolving rotor wakes is that they are computationally too expensive [125] to also be used for modelling far-field effects over sufficient duration to characterize the temporal flow variation.

Yield prediction may require accounting for both far-field and/or near-field effects, depending on the scale of energy extraction, and the proximity of rotors to each other. Therefore a range of methods are required for turbine farms ranging from a single unit, to a densely packed array.

This two-part paper begins by discussing four levels of turbine farm scenarios, starting with the simple case of a single turbine deployed exactly where real-world velocity data have been collected in the field. In this case, yield can be predicted directly from field data using well-established techniques e.g.[2]. The final scenario is a farm with many turbines, extracting a significant portion of the energy available at a given site, and no a priori field-data at the deployment sites; the other two scenarios are intermediaries. In the last case, near and far field effects are important and predicting yield requires extensive flow modelling. This paper proposes and validates an integrated methodology for predicting yield, with a spectrum of sub-modelling

strategies suitable for each of the four scenarios.

The methodology uses a hybrid modelling approach, whereby 2D shallow-water-equation (SWE) simulations predict basin-scale flow phenomena (including far-field effects), while steady 3D Reynolds-averaged-Navier-Stokes (RANS) simulations predict vertical velocity profiles and turbine wake interaction (i.e. near-field effects). The total computational expense is kept tractable by running the 3D simulations only for a set of representative (bin-averaged) flows, rather than running long-duration (e.g. several months) unsteady simulations.

This hybrid approach is unprecedented. Previous yield/impact assessments have used solely 2D SWE simulation [118, 8, 126, 127, 91, 128, 129, 121, 119, 120], or 3D SWE simulation [130, 131, 132, 133, 134, 57]. Other farm layout and small-array studies have used 3D RANS [90, 135, 123, 124, 136, 113] or even large-eddy simulation [92, 137], but have focused on a single flow condition rather than considering the entire temporal regime of flows. The methods described herein are complete, in that they account for all of the major factors influencing energy yield, including the temporal flow variability (ranging from minutes to months), 3D spatial flow variability including vertical profiles arising from bathymetry and turbine wakes, and real turbine performance over the full operational range, rather than arbitrary assumed coefficients.

A closely related field to yield prediction is the optimization of farm layout [125]. To be clear, the methods presented within this paper would require modification to be computationally tractable in the context of farm optimization. The present state-of-the art in array layout optimization [138] uses the adjoint method combined with 2D SWE models[1] run for a stationary flow condition, or over a single tidal cycle.

A case-study has been used to validate critical aspects of the proposed methods, using field-data collected by acoustic Doppler profilers (ADP) in 2012 and 2014 at Digby-Gut, Nova Scotia [91]. The ADP data provided baseline yield estimates, used for validating the proposed simulation-based methods. There is not yet any real-world operational data from tidal farms yet available, thus the individual sub-models of the methodology are validated as possible against data.

The paper is presented in two parts; Part One discusses the yield assessment methods, the case-study and validation of methods appropriate for small farms with no wake interaction effects, such that the impact of rotors on the flow can be neglected.

[1] which, by necessity compromises fidelity in resolving rotor wakes for computational efficiency due to the large number of model runs required for optimization

Part Two discusses methods to incorporate rotor forcing terms into simulations, validates those methods for single-rotor cases using the ADP data, and applies them to modelling test cases of large turbine farms containing up to 42 rotors, to demonstrate their utility in delivering energy yield estimates to developers to aid in large scale tidal turbine deployment.

7.2 Turbine Farm Scenarios and Yield Prediction Methods

This section identifies four tidal farm scenarios of increasing complexity, and proposes yield prediction methods for each. All of the proposed methods require field-data of velocity and water elevation at some point(s) not necessarily at the turbine deployments, which will most likely be collected using Acoustic Doppler Profilers (ADP). This paper uses the term ADP to describe such field data, even though other measurement devices may be used.

7.2.1 Turbine Performance Characteristics

The methods all require as input, turbine performance curves, as defined by IEC guidelines [139]. The curves define thrust and power coefficients (C_T, C_P), as functions of the free-stream velocity u_0.[2] Although not specifically noted within IEC guidelines, a third coefficient C_D can be used to define drag from structural components:

$$C_T(u_0) = \frac{T}{\frac{1}{2}\rho u_0^2 A}, \quad C_P(u_0) = \frac{P}{\frac{1}{2}\rho u_0^3 A}, \quad C_D = \frac{D_s}{\frac{1}{2}\rho u_0^2 A} \tag{7.1}$$

7.2.2 Scenario 1: Single turbine at ADP

The first scenario is a single turbine deployed in a large channel, far from any solid boundaries, (i.e. mid-depth in deep water) and at the exact location of a long-term ADP deployment. In this case, the measured velocity-profile time series $u_{0t}(h)$ can

[2]The free-stream velocity u_0 refers to a flow condition where the rotor is located in uniform inflow with no lateral boundaries. When rotor performance data are collected in a confined channel, they need to be corrected for blockage effects [103] and possibly free-surface deformation effects as well [140].

be used to compute a time series of turbine power;

$$P_{et} = \frac{1}{2}\rho\tilde{u}_{0t}^3\eta_e C_P(\tilde{u}_{0t})A \tag{7.2}$$

where $\tilde{u}_{0t}$ is the instantaneous measured velocity component normal to the rotor, averaged over the rotor swept area. Averaging the measured vertical power density profile over the circular swept area can be done using;

$$\tilde{u}_{0t}^3 = \frac{\int_{-R}^{R} u_{0t}^3(h')dA}{\int_{-R}^{R} dA}, \quad dA = 2\sqrt{(R^2 - h'^2)}dh' \tag{7.3}$$

with h'=0 corresponding to the rotor hub-height. The energy yield for the ADP deployment duration is then:

$$Y = \delta t \sum_{t=1}^{N_t} P_{et} \tag{7.4}$$

where δt is the sampling period of the measured field data, and N_t is the number of recorded samples.

Of course, ADP data give a back-prediction of past yield. Forecasting future yield requires understanding how tide-forced velocities vary in time. Tidal flows can be thought of as a superposition of harmonic and aharmonic components [5]. The harmonic components are due to gravitational forcing of the tides and can be predicted well using established software such as T-Tide. The aharmonic (i.e. stochastic) components arise from meteorological events and eddy-shedding from bathymetry. One would expect the relative magnitudes of the deterministic and stochastic components to be site dependent.

This paper argues that since aharmonic components are often significant, it is conceptually simpler to treat the tidal signal purely as a stochastic process. This is supported by Kutney et al. [5], who found that a purely stochastic analysis improved AEP accuracy compared to a purely harmonic analysis, using a year-long ADP velocity time-series in Admiralty Inlet. Treating the temporal variation as a stochastic process, it is reasonable to use the available field data to determine the mean power generation over the measurement duration, and to use that value to extrapolate forward in time, either for a year (AEP) or for the project's financial lifetime (T_{life}).

$$Y_{\text{year}} = \frac{Y}{\delta t N_t} 1\,\text{yr}, \quad Y_{\text{life}} = \frac{Y}{\delta t N_t} T_{\text{life}} \tag{7.5}$$

Kutney et al. [5] found that such an approach was more accurate and had less uncertainty than a purely harmonic analysis. They also found that inter-annual variability (which cannot be predicted stochastically) was on the order of only 1% at their particular site.

Of course, stochastic analysis requires field data of sufficient duration to obtain representative statistics. The required duration ($\delta t N_t$) would need to cover at least a full spring-neap cycle, but may be site-dependent. Kutney et al. [5] recommend collecting year-long ADP records at several tidal energy sites to better understand the sensitivity of yield prediction to measurement duration, to inform more specific guidelines.

7.2.3 Scenario 2: Few sparsely-packed turbines

This scenario has one turbine or a few turbines separated by large distances so that wake interaction is negligible, and the farm is small enough that far-field effects are also negligible. The turbine(s) is/are installed away from ADP deployments, so that field data must be extrapolated spatially to the turbine locations, in addition to extrapolating forward in time.

Both spatial and temporal extrapolation can be done using numerical simulation, which is commonly done with a 2D shallow-water-equation (SWE) solver code, such as FVCOM [8], RiCOM [141], Mike21 [142], TELEMAC [143] or the vertically integrated mode of Delft3D FLOW [121]. Such models most often use a harmonic open-ocean tidal elevation time-series as a boundary condition to drive the flow through the simulation domain. SWE models can resolve aharmonic components arising from eddy-shedding from bathymetry (down to grid-resolution) despite using a harmonic boundary condition. They can also include stochastic forcing terms for wind and waves. Thus, a high quality SWE model can predict both the harmonic and aharmonic components of the tidal velocity, as previously validated by other authors [8, 141, 142, 143, 121].

For yield prediction, the relevant outputs from a 2D SWE model are a time series of the spatial field of depth-averaged ambient[3] velocity $\vec{U}_{0t}(\vec{x}_{2\mathrm{D}})$, and water elevation $\zeta_{0t}(\vec{x}_{2\mathrm{D}})$.

Computing rotor power requires the mean velocity over the rotor swept area, which differs from the depth-average. The depth variation can be estimated using

[3] i.e. with the channel in its natural state, prior to the installation of rotors.

a standard log-law profile (Appendix B) to produce a time-series of the 3D ambient velocity $\vec{u}_{0t}$, which can be used in equations 7.2, 7.3 and 7.4 to find the yield for the SWE simulation time-period, and then extrapolated in time using equation 7.5. This paper refers to this method as SLP (SWE - Log-Profile). Standard profiles inherently assume that the bottom boundary layer is fully developed, which requires a long region of relatively constant depth and flat bathymetry upstream of the rotor location. Profiles may deviate from the log-law in regions of variable bathymetry.

This paper proposes an alternative approach, described in figure 7.1. The SWE model predicts the depth-averaged velocity time-series for a long-duration, and for an entire basin-channel system. The time-series is extracted from a smaller spatial domain covering only the region where turbines are to be deployed, and is categorized into discrete flow-state bins. Then a RANS simulation is run for each discrete bin to give the 3D flow field, which can then be used to calculate yield. This approach is called SBR (SWE - Binning - RANS). Theoretically, SBR is advantageous over using standard log profiles because RANS simulations can predict boundary layer development over variable bathymetry.

In principle, a 3D SWE model (e.g. [144]) may also be able to predict the influence of bathymetry, however for a similar spatial resolution, SBR would have lower computational cost since the 3D simulations are done on a subset of N_b representative flow states, rather than a transient simulation covering the full duration of the SWE simulation.[4]

SBR and SLP are validated for their ability to predict depth-wise velocity profiles and yield in section 7.5.2. SBR is a building block toward methods presented in § 7.2.4 and § 7.2.5 for more complex farms.

7.2.4 Scenario 3: Few densely packed turbines

This scenario has a few turbines closely spaced so that wake interaction affects power output, yet the farm is small enough that far-field effects remain negligible. ADP data are available for at least one location, but not co-located with turbine deployments.

2D SWE simulations cannot accurately predict 3D wake effects,[5] so 3D simulation

[4]The RANS simulations herein required on average 80 iterations to converge, for approximately 50 flow-states for a total of 4000 computational iterations. That number of iterations would only give one hour of simulated time in a transient SWE simulation with a time-step of 1 second.

[5]A 2D model inherently assumes that the turbine occupies the entire water column, which will grossly grossly mis-represent turbine wakes and wake recovery.

1. Tune SWE bottom friction to match field data
2. Run SWE to predict N_t depth averaged flow fields ($\vec{U}_{0t}$)
3. Classify those fields into N_b bins
4. Define a bin-averaged 2D field ($\vec{U}_{0b}$) for each of the N_b bins
5. Use ($\vec{U}_{0b}$) to create boundary conditions for the next step
6. Run 3D RANS for each bin, to obtain N_b 3D flow fields ($\vec{u}_{0b}$)
7. Average $\vec{u}_{0b}$ over the swept area to obtain $\tilde{u}_{0b}$
8. Calculate:

$$P_{eb} = \frac{1}{2}\rho\tilde{u}_{0b}^3\eta_e C_P(\tilde{u}_{0b})A \tag{7.6}$$

$$Y_b = \delta t P_{eb} N_{bn}, \quad Y = \sum_{b=1}^{N_b} Y_b \tag{7.7}$$

Figure 7.1: Procedure for the SBR (SWE-Binning-RANS) method. Steps 1-2 are explained in §7.4, steps 3-4 are described in §7.5.1 and Appendix A, and steps 5-6 are described in §7.5.2.

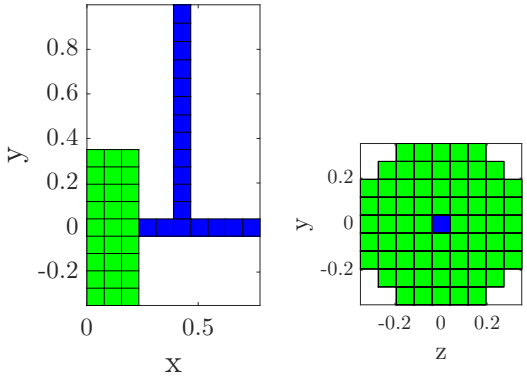

Figure 7.2: Example mesh for the actuator-disk region (green) and coarsely represented structures (blue) used by TADA. Previous work [12] found that 9 elements spanning the diameter is sufficient for modelling performance and wake interaction when using TADA.

is required.[6] This paper proposes a procedure similar to SBR except that the 3D simulations are done using TADA [12], which was specifically developed to efficiently model turbine wake interaction effects. This procedure is denoted SBT (SWE - Binning - TADA) and is described in figure 7.3. As with SBR, SBT is much more efficient compared to modelling wakes in a 3D SWE model because high-resolution 3D simulations are only done for a small set of N_b representative flow states, and over a smaller spatial domain.[7]

TADA uses 3D RANS simulations to predict turbine performance and wakes, and is described in detail in [12]. To summarize, TADA represents each turbine by adding momentum-source terms to the RANS equations, in an actuator-disk (AD) region in the computational mesh, as depicted in figure 7.2.

A challenge to modelling wake interaction is that the velocity incident to each turbine is altered by itself and by other turbines. Thus, it becomes difficult to define an appropriate free-stream velocity for each rotor [12, 98, 145]. TADA solves this by re-defining the power and thrust coefficients to depend on the rotor-local velocity,

[6]Empirical wake models could potentially be used, an option we do not explore.

[7]Hypothetically, a 3D SWE could be suitable for modeling wake interaction effects, however such models have yet to prove their ability to predict turbine power production with wake interaction. Additionally, SWE codes typically must maintain a CFL number below 1 to maintain solver stability, which would require a very small time-step when the spatial resolution is sufficient to resolve individual turbine wakes. The combined requirements of a large 3D grid, small time-step and long runtime make it very computationally intensive to use a 3D SWE to simulate wake interaction.

1. Do steps 1-5 of SBR (figure 7.1).
2. Do 3D TADA simulation for each bin, to obtain thrust and power for each bin (T_b, P_{eb})
3. Calculate Y using equation 8.1

Figure 7.3: Procedure for SBT. Compared to SBR, SBT incorporates rotors into the RANS simulations to predict wake-interaction effects. SBT is investigated in Part 2 of this paper.

rather than the free-stream:

$$C_T^\star = \frac{T}{\frac{1}{2}\rho \langle u^2 \rangle A}, \quad C_P^\star = \frac{P}{\frac{1}{2}\rho \langle u^3 \rangle A} \tag{7.8}$$

where the braces indicate volume-averaging over the actuator disk region. TADA involves a tuning procedure which uses calibration cases of a single rotor far from solid boundaries, to develop regression models defining $C_T^\star$ and $C_P^\star$ as functions of velocity $\langle u \rangle$, turbulence intensity $\langle I \rangle$ and turbulence length-scale $\langle L \rangle$, which can subsequently be applied to predict rotor performance in turbine arrays and confined channels.[12][8]

SBT is a one-way coupling between the SWE and TADA simulations, and therefore requires that the boundary conditions supplied to TADA are unaffected by the presence of the rotors. Thus, it is important to locate the boundaries sufficiently far from rotors, and to take care that the bulk flow is mainly unaffected by the presence of the rotors.[9]

7.2.5 Scenario 4: Many turbines, densely spaced

This final scenario is a large tidal farm with many densely packed turbines. Large-scale tidal farms will need to optimize the position of each turbine to maximize usage of the development area, while minimizing energy losses from wake interaction. In

[8]Other authors e.g. [145] have suggested using 1-D momentum theory to define $C^\star_{\{T,P\}}$, however that fails to account for the influence of turbulent mixing on the rotor-local flow, and would produce significant errors when applied to practical CFD grids with turbulent flow.

[9]The analytical formulation of [104] could perhaps be used to estimate the bulk impacts

large farms, far-field effects can not be neglected.

Thus, energy extraction by rotors must be included in the SWE simulations, which presents a significant challenge compared to the previous scenarios. To maintain computational efficiency, the SWE simulations are done at a resolution suitable for resolving the tidal flow dynamics, but too coarse to resolve individual turbine wakes.

Thus, turbines are represented as depth-averaged, sub-grid features. As discussed by [10, 145, 141], using standard thrust and power coefficients to define turbine performance in a SWE solver can lead to significant error in the applied force, which arises due to slowing of the flow in the grid cell containing turbines. Thus, the rotor performance needs to be expressed in terms of the grid-cell velocity $\vec{U}_j$. In an analogous manner to TADA, the turbine forcing terms can be re-expressed as:

$$K_{Tj} = \frac{T_j}{\frac{1}{2}\rho|\vec{U}_j|^2 A_j}, \quad K_{Pj} = \frac{P}{\frac{1}{2}\rho|\vec{U}_j|^3 A_j} \tag{7.9}$$

where T_j is the resistive force (rotor thrust plus structure drag) and P_j is the shaft power from turbines in the j^{th} grid cell, which may be from multiple turbines, or from portions of turbines. Appendix A of Part 2 describes an analytical method[10] for defining K_{Tj} and K_{Pj} for SWE simulations, which is herein denoted as SWET (SWE + turbine).

To compute yield for a densely-packed large turbine farm, the proposed procedure is to incorporate SWET into the SBT procedure. This way, the high-resolution TADA results can be used to evaluate errors in the rotor forces applied by SWET. That error may be significant, because 2D SWET will inherently mis-represent individual wakes and their impact on turbine thrust. Therefore, if needed, the rotor parameterization for SWET can be re-tuned and the entire procedure can be iterated. This final procedure is denoted STBT (SWET + Binning + TADA), and is defined explicitly in figure 7.4.

7.2.6 Methodology Summary

To summarize, yield assessment can use a variety of techniques depending on the need to resolve near-field and far-field effects.

Scenario 1 is a single turbine co-located with an ADP deployment, such that

[10] which is similar to those presented by [145] and [141] but can also account for turbines spanning multiple computational elements, and multiple turbines within an individual element.

1. Tune SWE bottom friction to match field data
2. Run 2D SWET to predict N_t depth-averaged flow fields ($\vec{U}_t$)
3. Classify those fields into N_b bins
4. Define a bin-averaged 2D field ($\vec{U}_b$) for each of the N_b bins
5. Use ($\vec{U}_b$) to define boundary conditions for the next step
6. Do 3D TADA simulation for each bin, to obtain thrust and power for each bin (T_b, P_{eb})
7. Assess the difference in turbine force between SWET and TADA
8. If the error is large recalibrate SWET and repeat steps 2-7
9. Calculate Y using eq 8.1

Figure 7.4: Procedure for STBT for large densely-packed turbine farms, which incorporates turbines into the SWE simulations to predict far-field effects. It may be required to iterates between SWET and TADA to recalibrate the applied forcing terms in the SWE model.

yield analysis can be done by directly applying the rotor performance coefficients to the ADP data. Temporal extrapolation of the yield can be done using stochastic or harmonic methods, however it is thought that a stochastic approach is more universal since aharmonic components of the velocity signal may be significant.

Scenario 2 is a few turbines with no wake interaction effects. The turbines are not co-located with ADP deployments, so simulation is needed to predict the inflow to each turbine. This can be done using: (a) SWE simulation and applying a standard log. profile (SLP) or (b) the proposed SBR procedure. Of these, (a) is simple and fast, while (b) can account for the impact of real bottom topology.

Scenario 3 is a few turbines with wake interaction effects, therefore requiring 3D flow modelling. 3D SWE simulation would be very computationally expensive, and SBT is proposed as a viable alternative. SBT incorporates rotor forces into the high-resolution simulations of the binned flow states, but not into the SWE simulations since far-field effects are assumed negligible.

Scenario 4 is a large farm with many turbines and wake interactions. Since far-field effects are non-negligible, a turbine model is included in the SWE simulations. It is proposed to model turbines as a sub-grid objects in 2D SWE simulations, accepting that wake interaction will be somewhat mis-represented, but that far-field effects should be predicted adequately. Wake interaction effects are predicted by the TADA simulations, which are used to predict yield.

We propose STBT as a general methodology appropriate for yield prediction and for assessing far-field effects for impact assessment studies. The SBT and SBR methods are less complex to implement than STBT, and should predict yield well when far-field effects are negligible.

The remainder of Part One focuses on validating SLP and SBR using measured field data. Part Two validates SBT, and demonstrates STBT for large turbine farms.

7.3 Case-Study Site and Field Data

The case-study was conducted for a site located in Digby Gut, the narrow passage connecting Annapolis Basin to the Bay of Fundy, depicted in figure 7.5. Field data were collected by researchers from Dalhousie University using RDI workhorse ADP[91]. The deployment locations are depicted in figure 7.6, and summarized in table 7.1. Data were provided to the authors as 10-minute averages, including horizontal velocity components and pressure, which was used to find water elevation via. the hydro-

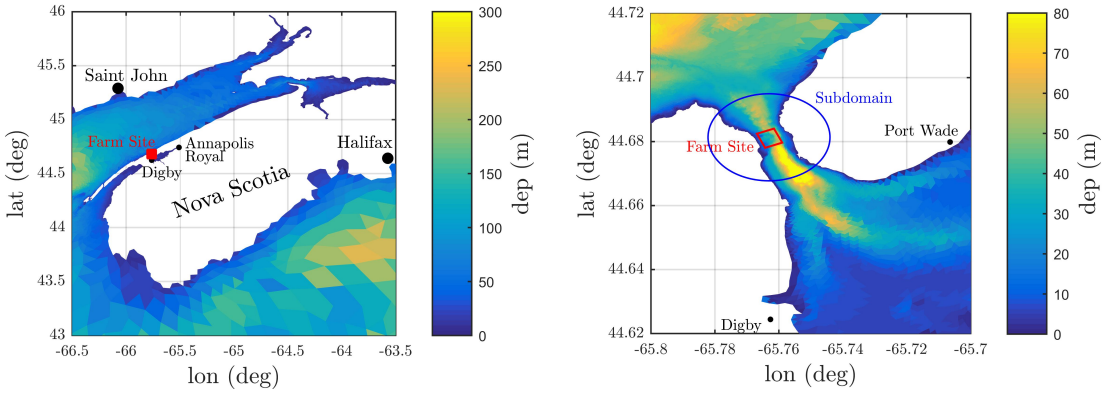

Figure 7.5: The location of the proposed tidal turbine farm. The blank areas are land, while the colours represent the depth below sea level.

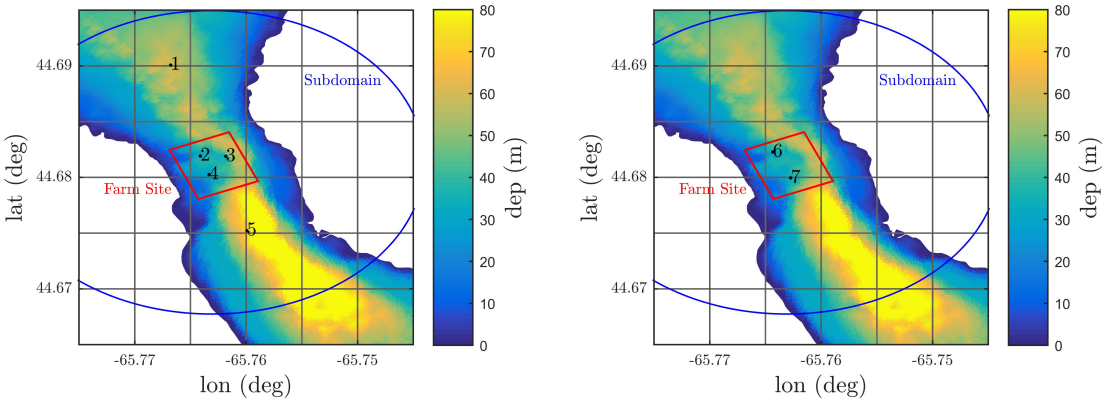

Figure 7.6: Locations of the ADP deployments. The blank areas are land, while the colours represent the depth below sea level.

static assumption. The collected vertical profiles of velocity were depth-averaged by numerical integration as described in Appendix C.

The case-study involved predicting yield for an individual, isolated turbine deployed at each of the ADP 2, 3, 4, 6, and 7 deployment locations (i.e. a level 1 turbine farm). The study considered hypothetical turbines (see figure 7.7 and table 7.2) mounted 10 m below the water surface, on floating platforms which were assumed to be fixed horizontally, but able move up and down with the rise and fall of the water surface.[11] The time series profile ADP data allowed calculating a baseline prediction for turbine yield for each deployment location, using equations 7.2 and 7.4.

[11] Of course this is an approximation, since compliant moorings will allow horizontal motion. The employed modelling framework is not yet setup for horizontal motion.

#	lon.(deg)	lat.(deg)	dep.(m)	start date	end date
1	-65.766780	44.690070	55.3	30-Jan-2012 22:00	15-Feb-2012 23:40
2	-65.764100	44.681920	33.9	30-Jan-2012 17:00	05-Mar-2012 11:40
3	-65.761820	44.681880	36.1	30-Jan-2012 17:00	16-Mar-2012 02:10
4	-65.763330	44.680250	31.4	30-Jan-2012 15:30	06-Mar-2012 15:30
5	-65.759930	44.675220	67.1	30-Jan-2012 17:00	29-Feb-2012 07:00
6	-65.764338	44.682280	30.2	15-Jan-2014 21:40	21-Feb-2014 11:49
7	-65.762733	44.679940	32.1	15-Jan-2014 21:42	02-Feb-2014 03:22

Table 7.1: ADP deployment locations and times

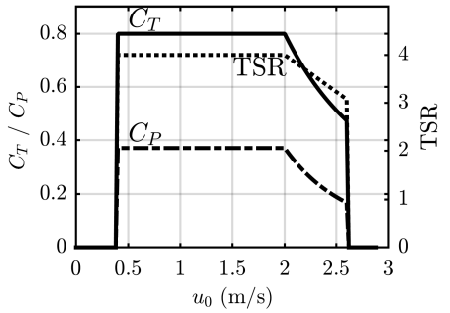

Figure 7.7: Performance curves for the hypothetical turbine used in this study.

Rotor Dia. (m)	9.00
Hub Height* (m)	-10
Cut-in Spd (m/s)	0.40
Rated Spd (m/s)	2.00
Cut-out Spd (m/s)	2.60
Rated Power (kW)	96.4
Drag coefficient C_D	0.2

Table 7.2: Characteristics of the hypothetical turbine used in this study. The turbine is to be installed on a floating platform with the hub submerged below the water surface.

This paper considered a hypothetical turbine described in table 7.2, with performance characteristics shown in figure 8.4.

For comparative analysis, the yield was also predicted by the methods proposed for scenario 2 turbine farms, namely the SLP and SBR methods.

#	year	start date	end date	duration (h)
1	2012	Jan 30 22:00	Feb 15 23:30	385.7
2	2012	Jan 30 17:00	Mar 05 11:30	834.7
3	2012	Jan 30 17:00	Mar 16 02:00	1089.0
4	2012	Jan 30 15:40	Mar 06 15:20	863.7
5	2012	Jan 30 17:00	Feb 29 06:50	710.0
6	2014	Jan 15 21:40	Jan 31 03:20	365.7
7	2014	Jan 15 21:42	Jan 31 03:12	365.5

Table 7.3: Summary of time periods used for evaluating yield for each ADP. These time-periods are where the SWE simulation and ADP records overlap in time.

7.4 SWE simulations

All of the proposed methods rely on 2D SWE simulations. This study used the FVCOM model developed by Dr. Richard Karsten's research group at Acadia University, [146, 91][12] to predict the tidally-forced flow through the farm. This section describes how the bottom friction coefficient was used to tune the SWE model for Digby Gut, and how the yield was calculated from the final tuned SWE simulations.

7.4.1 Bottom-friction

The bottom friction coefficient was tuned to optimize agreement with ADP velocity data. This was assessed by comparing velocity time-series from the model to depth-averaged (see Appendix B) ADP velocity time-series. The tuning was done manually, with the goal of minimizing the function:

$$E = \sum_{i=1}^{N_{\mathrm{ADP}}} w_i E_i \tag{7.10}$$

$$E_i = \frac{\sum_{t=1}^{N_t} (|\vec{U}_{0it}^{\mathrm{SWE}}|^3 - |\vec{U}_{0it}^{\mathrm{ADP}}|^3)}{N_t} \tag{7.11}$$

which represents the sum (from available ADP) of the time-averaged difference between the measured and simulated values for the cube of the velocity magnitude. This error metric differs from that used by [146] and [91]. Here, the cube is used because it represents the kinetic power density available to turbines. The term w_i is a weighting factor to account for proximity to the energy development site, or for data quality. This study used w_i=1 for ADP 2, 3 and 4, which were within the proposed farm site, and w_i=0 for ADP 1 and 5, which were in deeper waters outside of the farm site, where the velocity was too low to consider deploying turbines. The final tuned bottom friction coefficient was 0.002085, compared to a value of 0.0025 used in [146].[13]

Figure 7.8 compares the SWE velocity to the ADP 1-5 deployments, which were

[12]The model bathymetry has been updated since [146, 91] were published, which has improved predictions of tidal elevation and velocity in Digby Gut.

[13]The lower bottom friction used herein improved the under-predicted velocity in Digby Gut presented by [146] and [91]. In their work, the value 0.0025 gave the best model performance covering all of Digby Gut, Petit Passage and Grand Passage. Tuning the model specifically for Digby Gut as done in this work degraded its performance somewhat in the other channels.

used in tuning the model. The figure shows the signed-speed, which is the velocity magnitude, assigned a positive value for northward flow, and negative for southward flow. Simulations were run for the time period Jan. 15 to 31, 2014 to compare to ADP 6 and 7 (not used for tuning the bottom friction). A sample comparison is shown in figure 7.9, where the close match validates that the tuned bottom friction coefficient remained valid in 2014, and at (slightly) different locations.

7.4.2 SWE output

The SWE model was run with a time-step of 0.5s and contained 75k mesh nodes.[14] To save flow data over the entire mesh, and for every time-step would have produced excessively large files. The high-resolution 3D RANS/TADA simulations only cover a small region within the SWE model. Therefore, SWE model results were saved within a sub-domain, which is shown in figures 7.5 and 7.6. Additionally, the SWE model calculated running averages for 10-minute intervals, rather than saving output at every time-step.

Thus, the tuned SWE simulations provided two separate time-series of 10-minute average, depth-averaged fields ($\vec{U}_{0t}(x_{2\mathrm{D}})$, one for Jan-Mar 2012 (for ADP 1-5), and the other for Jan 2014 (for ADP 6-7). Those output time series correspond to step 2 for SLP, SBR, SBT and STBT.

7.4.3 Time-series SLP yield

A standard log profile (Appendix D) was used to determine the area weighted average velocity over the rotor-swept area (equation 7.3). This was then used to calculate a time series of the rotor power, using equation 7.2. Sample power time-series are provided in figure 7.10; recall that the turbine has a cut-out velocity, which limits the power to 96.4 kW. The figure also shows power found using the ADP profile data directly (baseline), and from assuming that the velocity is uniform with depth (i.e. using the SWE output without applying a log profile). These power-time series were then used to calculate yield via. equation 7.4.

The yield predictions are summarized in table 7.4. The table shows yield found using depth-averaged velocity (ADP and SWE) in the leftmost block. The depth-averaged SWE velocity typically over-predicted the yield compared to the depth-

[14]The employed time-step and mesh size are thought to be typical for such studies.

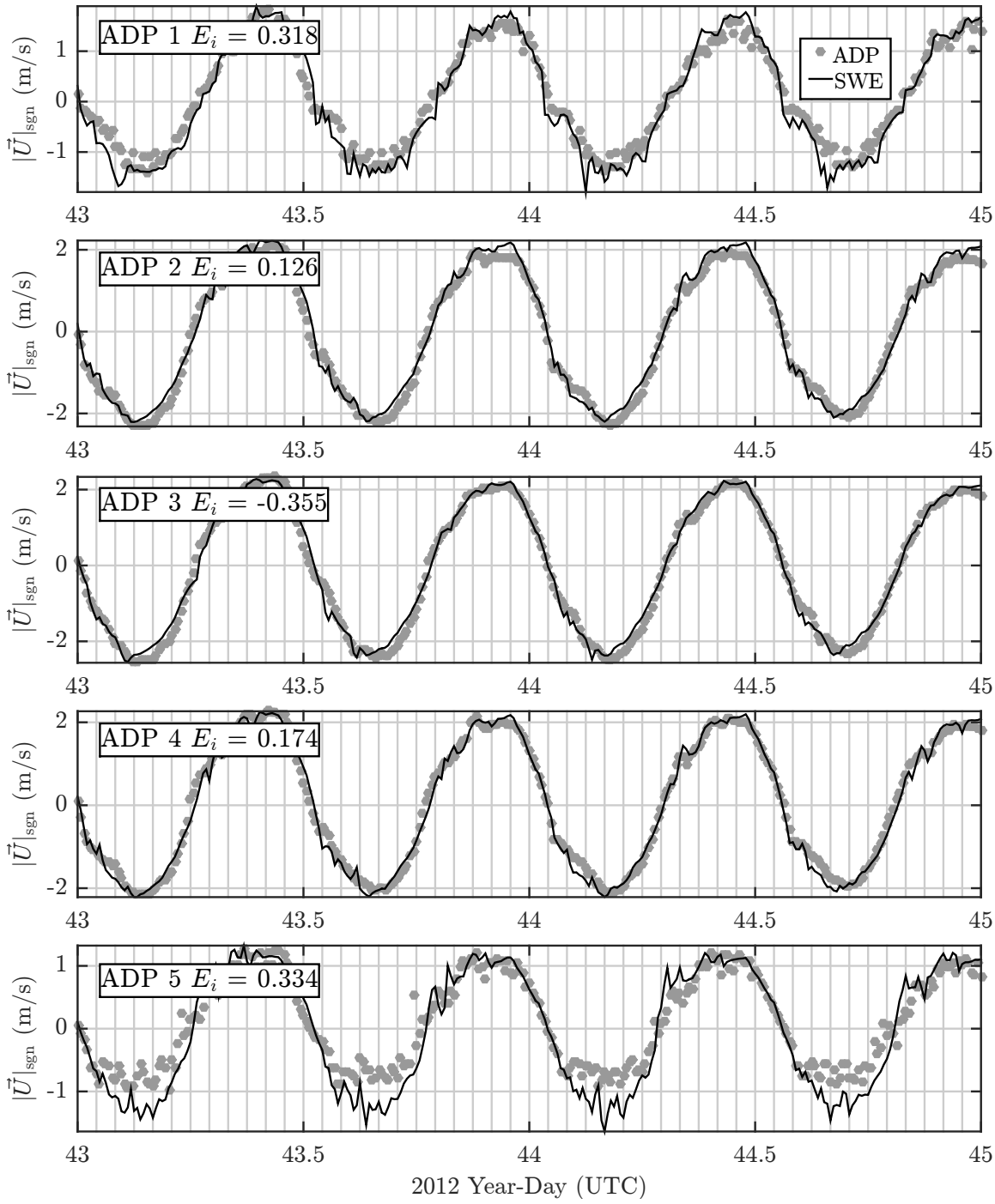

Figure 7.8: Time-series comparing the signed speed from the tuned SWE model to ADP 1-5.

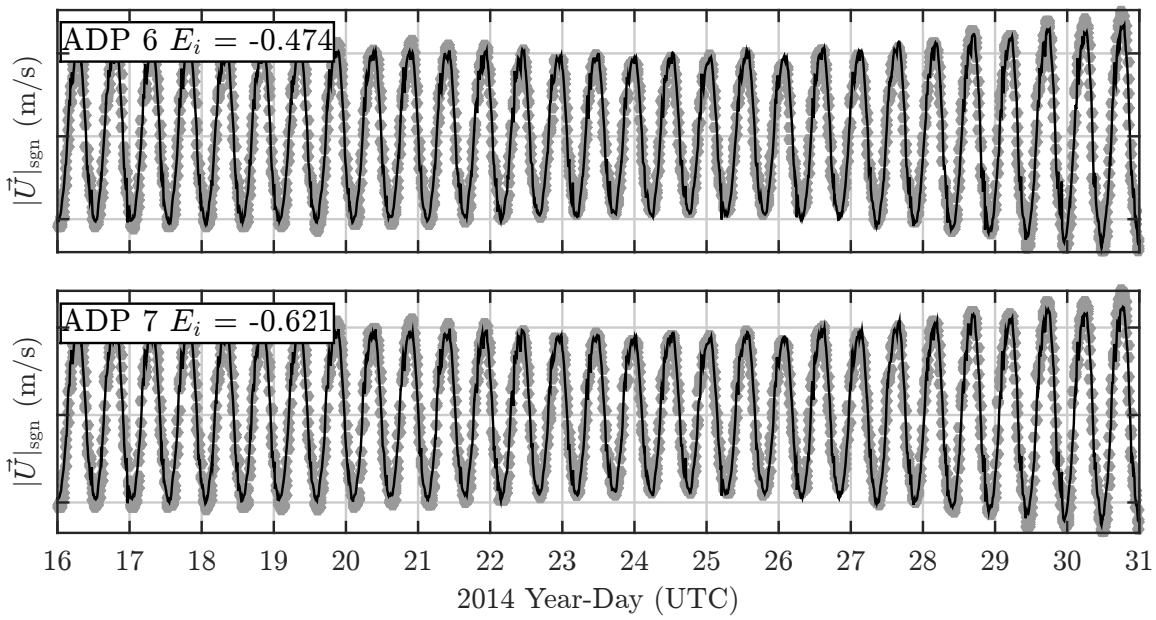

Figure 7.9: Time-series comparing the signed speed from the tuned SWE model to ADP 6-7, which were not used for tuning the bottom friction. The y-axis scale has been removed to avoid disclosing confidential data.

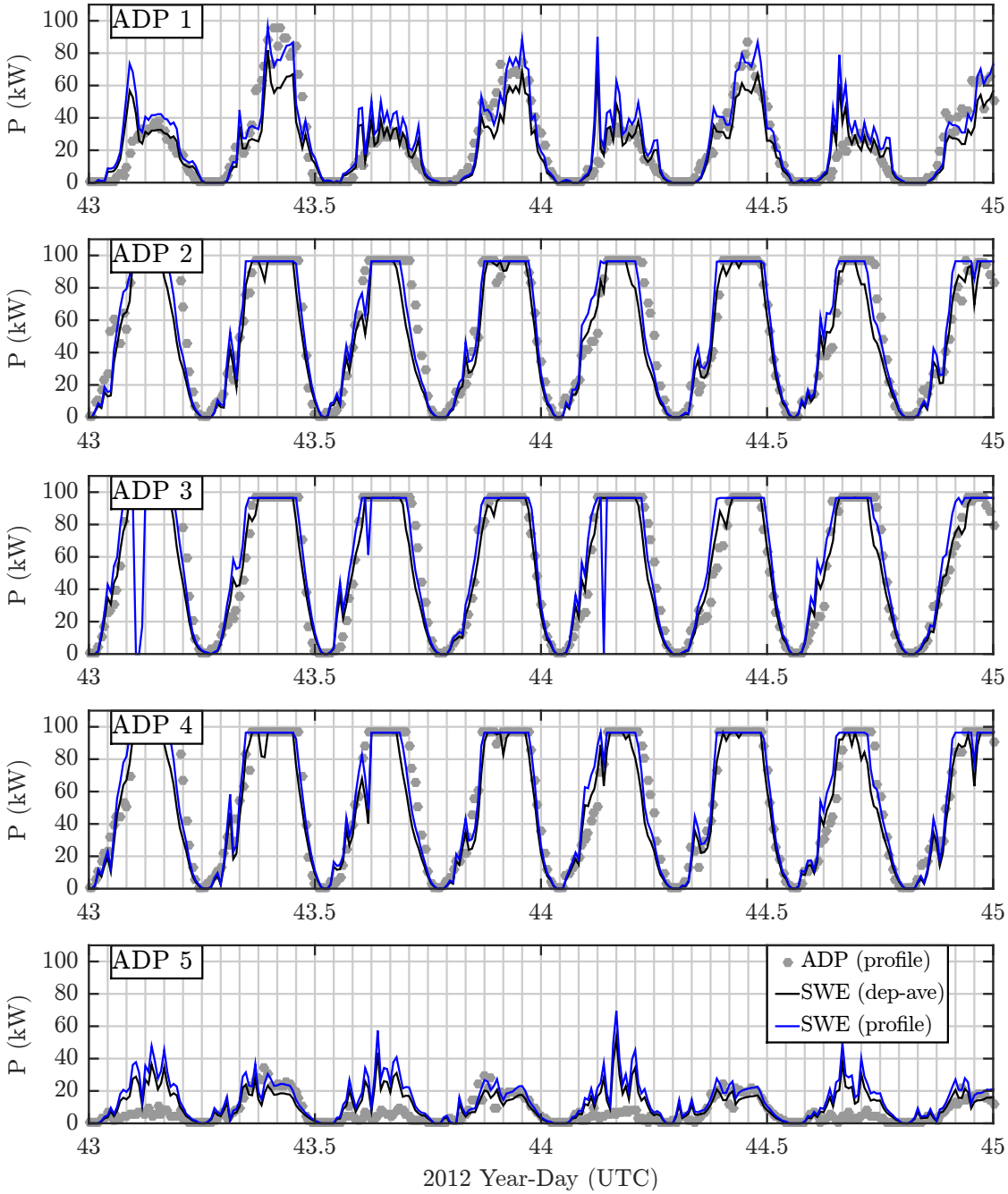

Figure 7.10: Sample time-series of rotor power for ADP 1-5, predicted from the ADP profile data, SWE depth-averaged velocity and from SWE velocity with an assumed standard log. profile. Note the spikes toward zero power at ADP3 are at times when the velocity was above the rotor cut out speed.

averaged ADP. At the sites of interest (2,3,4,6,7) the % difference between the SWE and ADP model predictions was less than 10%.

The predictions were quite poor at ADP 1 and 5. Those sites are of lesser interest because of their much lower yield compared to the higher velocity locations, however such large discrepancies are concerning, and highlight the potential for gross under/over prediction of yield, even while using state-of-the-art modelling practises.

The central block of table 7.4 shows yield estimated from the ADP profile data, and from SLP. The SLP predictions are typically somewhat higher than the ADP, and very poor for ADP 5, but within 11% for the other sites. Since ADP 6-7 were not used in tuning the SWE model, the yield predictions for those sites can be considered as validation data. The yield estimates from the SWE model agree within 10% with the ADP data for those sites, which is quite encouraging.

The last two columns of the table show the % difference in yield estimates using depth-average vs. profiled velocity. These values are positive because the turbines are located in the upper part of the water column where the velocity is higher than the depth average. While these values are in reasonable agreement between the ADP and SLP approach, there are some notable discrepancies. For locations 1, 2 and 4, the % differences are greater for the ADP data than for SLP, which implies that the measured velocity profiles typically have higher velocities at the rotor, compared to the depth average. At locations 3, 5, 6 and 7 the % differences are smaller for the ADP, implying that the measured profiles had lower velocities compared to the depth average (i.e. closer to a uniform profile). Clearly, a standard log profile does not represent the velocity profile perfectly, a topic which is further explored in section 7.5.2.

7.4.4 Yield-Based Scaling Factor

The SWE model was run for a time-period which was longer than the ADP 2, 3 and 4 records. SBR predicted yield based on the entire SWE time-period, so to compare to yield predicted by the ADP, it was necessary to define a scaling factor to account for the difference in duration. At a glance, the obvious choice would be to scale the yield by a simple ratio of time, however this can lead to significant error if for example the ADP deployment was during a more-energetic-than-average time in the tides natural variation.

To compare apples to apples, the portion of the SWE simulation duration which overlapped in time with the corresponding ADP deployment was isolated, and used to

	Predicted Yield [MWh]						Dep-Ave. vs.	
ADP	Depth-Ave.		%	Profile		%	Profile (% diff.)	
#	ADP	SWE	diff.	ADP	SLP	diff.	ADP-ADP	SWE-SLP
1	4.4	5.9	34	7.0	7.6	10	58	30
2	26.9	28.7	7	32.4	33.2	2	21	16
3	45.1	45.9	2	45.9	51.0	11	2	11
4	27.8	29.8	7	33.8	34.4	2	21	16
5	3.0	5.9	95	3.8	7.8	105	25	31
6	16.4	16.9	3	16.7	18.4	10	1	9
7	15.7	14.5	-7	16.3	17.1	5	4	17

Table 7.4: Summary of yield predictions using time-series analysis of the ADP field data, and time-series-analysis from the 2D SWE simulations. SLP refers to applying a log profile to the SWE velocity before calculating yield. The final two columns show the percent difference between yield found from the profile vs. depth average i.e. ADP-profile vs ADP depth-ave and SWE vs. SLP

	time (h)			Yield MWh		
ADP	Full	Overlap	Time SF	Full	Overlap	Yield SF
1	1090.8	385.7	0.354	17.52	5.89	0.336
2	1090.8	834.7	0.765	40.67	28.70	0.706
3	1090.8	1089.0	0.998	45.98	45.93	0.999
4	1090.8	863.7	0.792	40.82	29.75	0.729
5	1090.8	710.0	0.651	9.16	5.90	0.644
6	365.7	365.7	1.000	16.86	16.86	1.000
7	365.7	365.5	0.999	14.59	14.54	1.000

Table 7.5: Table summarizing the yield scaling factor. The 1^{st} and 2^{nd} columns show the SWE sim duration, the duration overlapping with ADP data. The 4^{th} column shows the time scaling factor. The 5^{th} column shows yield (MWh) predicted from time-series analysis of the SWE depth-averaged flow for the full duration, while the 6^{th} column shows the same, but for the overlapping duration. The final column shows the yield-based scaling factor.

calculate the *overlap* yield (from the depth-averaged velocity), this was then divided by yield calculated in the same manner for the entire SWE simulation duration to find the yield-based scaling factor Yield SF summarized in table 7.5.

7.5 Application and Validation of SBR

This section describes how the SBR method was applied to predicting the flow through a portion of the SWE domain, and to calculating yield for isolated devices. First, the bin classification process, and RANS simulations are described in detail. Then, velocity profiles obtained from RANS simulations are compared to ADP and SLP profiles. Finally, the yield computed by SBR is compared to the time-series predictions by ADP and SLP previously summarized in table 7.4.

Thus, in this section, two critical components of the proposed SBR, SBT and STBT methods are validated; namely, 1) treating the temporal variation of the flow statistically using a method of bins, and 2) using RANS to obtain 3D bin-averaged flow fields.

7.5.1 Bin-Classification

Prior to running the RANS simulations, it was necessary to categorize the depth-averaged SWE flow fields using a method of bins. This categorization consists of collecting similar flow-states into discrete bins based on the flow speed, direction, and

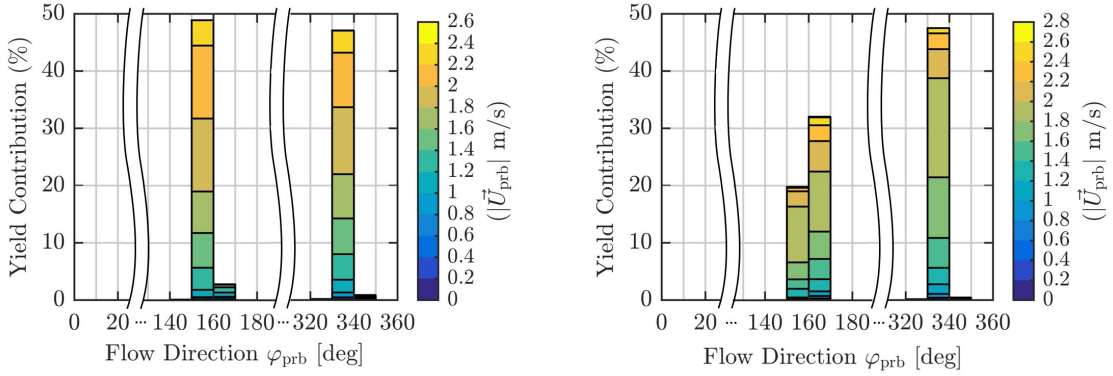

Figure 7.11: Variation of yield contribution with flow direction and speed. The left panel is for the 2012 SWE results for a turbine farm with three rotors located at ADP 2, 3 and 4. The right panel is for the 2014 SWE results considering turbines at ADP 6 and 7. In Digby Gut there are two dominant flow directions corresponding to ebb and flood.

water elevation. Then the flow power density is averaged for each bin to define a bin-average flow state. Finally, the bins are sorted according to their contribution to the total energy yield. These steps are explained in detail in Appendix A.

For this study the classification ranges were 10° for flow direction, $0.2\,\text{ms}^{-1}$ for speed and 2 m for surface elevation.[15] This section summarizes the results of bin classification, bin-averaging and bin-sorting for the two SWE simulations.

For the 2012 simulations, the yield contribution analysis (see Appendix A) considered a turbine-farm with three rotors located at the ADP 2, 3 and 4 locations. For the 2014 simulation, it considered a farm with rotors at ADP 6 and 7.

Figure 7.11 depicts the variation of yield contribution with flow direction and flow speed. Nearly all of the energy is produced for flows from 158° or from 335°, and speeds between 1.2 and $2.2\,\text{ms}^{-1}$. The directionality of the flow is an important consideration for designing a turbine farm. Flows that are bidirectional lend themselves well to a fence configuration, while flows with more variable direction may be optimal with other layouts.

Figure 7.12 shows sample results of the bin-averaged 2D velocity field for the top yield contribution bins for the 2012 SWE results. The bin averaging was done on the entire spatial field. Note that an underwater ridge just northwest of ADP 2 created the distinct high-velocity region in the plots. The left plot is an average of

[15]Evaluating sensitivities to the classification ranges is a high priority for future research, but has not been carried out yet due to time constraints.

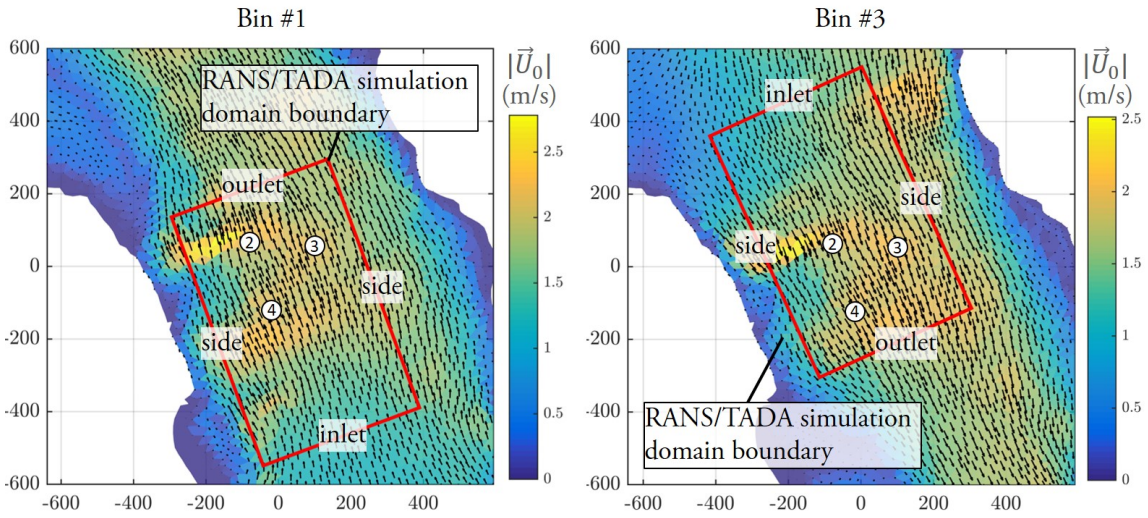

Figure 7.12: Sample bin-averaged flow fields for the highest yield bins for ebb and flood directions. The ADP 2, 3 and 4 locations are shown, as are the domain boundaries for RANS/TADA simulations.

N_{bn}=188 time instances, and the right plot is an average of N_{bn}=179 instances. The bin averaged flow fields were used to define flow conditions at the outer boundaries of the RANS simulations.

To mitigate some computational expense, only the flow bins which cumulatively added up to 95% of the total energy yield were used for detailed CFD simulations in the SBR (and later SBT/STBT studies presented in Part Two to this paper). A 5% correction factor was post applied to the total yield predicted by those methods to compensate. For the 2012 SWE simulation this required N_b=51 bins, and for the 2014 SWE simulation N_b=54 bins were used.

7.5.2 RANS Simulations

The domain was rectangular in (x,y) and conformed vertically to the depth using supplied bathymetry data, and water elevation from the bin-averaged SWE field. A new mesh was created for each binned flow state, using an automated in-house tool. Each mesh used hexadedral elements and was aligned with the spatially-averaged flow direction to minimize numerical diffusion error. High resolution (0.5 m) bathymetry point-data[16] (with limited spatial coverage) were integrated into the existing SWE depth model, which was then spatially smoothed and interpolated onto the RANS grid

[16]Provided by the Offshore Energy Research Association (OERA) of Nova Scotia.

#	YC	CYC	Pr	φ_{prb}	$\lvert\vec{U}_{\text{prb}}\rvert$	ζ_{prb}	Power [kW]		
							Rotor 1	Rotor 2	Rotor 3
1	7.09	7.09	2.87	159	2.10	-1.1	96.4	96.4	96.4
2	6.10	13.18	2.84	158	1.91	1.0	84.1	81.6	86.7
3	5.82	19.01	2.74	335	1.91	1.0	76.0	96.4	78.2
4	5.48	24.49	2.26	335	2.11	-1.0	96.4	96.4	96.4
...									
48	0.34	94.23	0.76	156	1.12	2.8	18.5	16.2	16.8
49	0.33	94.56	0.17	336	1.85	2.2	67.8	92.9	71.2
50	0.33	94.89	1.36	336	0.92	-3.1	8.5	10.8	8.9
51	0.32	95.21	0.67	335	1.15	-1.6	16.4	23.8	16.0

Table 7.6: Sample statistics from the binning analysis for the 2012 case with rotors at ADP 2, 3 and 4. CYC is the % cumulative yield contribution, YC is the % yield contribution of the particular bin, Pr is the occurrence probability, φ is the flow direction, $|\vec{U}|$ is the velocity magnitude and ζ is the water elevation. The subscript prb refers to the 'probe' as explained in Appendix A. The power shown here is an initial estimate as described in Appendix A.

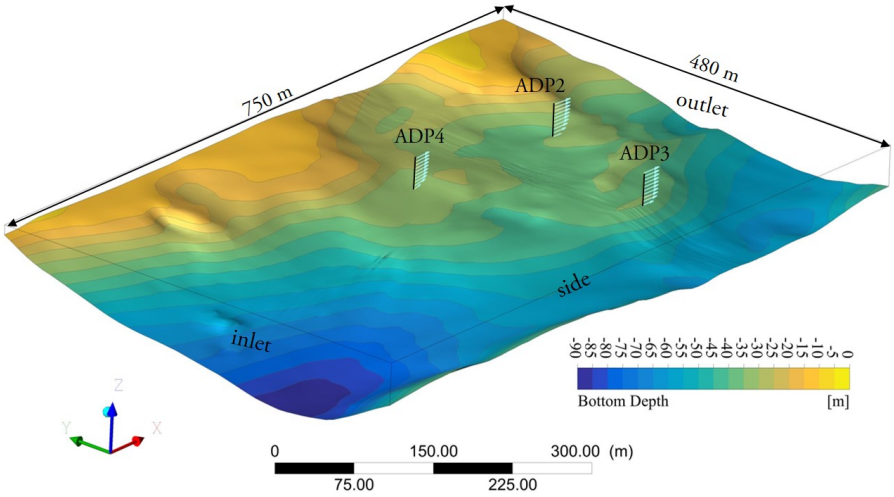

Figure 7.13: Sample SBR domain for the top yield contribution bin for the 2012 simulations. Velocity profiles were extracted from the SBR simulations at the ADP locations (as depicted) for comparing to ADP data.

by the meshing tool. A sample domain corresponding to the top yield contribution bin ($\varphi_b = 159°$) for the 2012 simulation is depicted in figure 7.13.

The domain was centred laterally on the centroid of the ADP locations, and used hexahedral mesh elements with a side length of 10 m. The vertical mesh spacing was 0.2 m at the domain bottom, and increased upward with a geometric growth law (ratio 1.15). The number of depth layers was chosen such that the maximum element size at the domain top was less than 10 m. Note that a finer mesh is used when turbines are present in the simulations, as discussed in part two of this paper. The inlet was located 500 m upstream of the domain centre to allow the velocity profiles to develop over sufficient upstream terrain. The outlet and domain sides were located 230 m away from the domain centre.[17]

Boundary conditions were created from bin-averaged 2D SWE fields (as depicted in figure 7.12). At the inlet and side boundaries, an *opening* [80] condition was used, which set the velocity ($\vec{u}$), turbulent kinetic energy (k) and dissipation rate (ε). Along these boundaries, the depth-averaged SWE velocity field was used to create

[17]Reducing the horizontal mesh scale to 5 m, gave profiles that were barely distinguishable from those from the 10 m mesh, and changed the average RMS errors shown in table 7.7 by less than 0.009. Reducing the first-layer vertical scale to 0.005 m had no visible impact on the profiles, and changed the RMS error by less than 0.006. Increasing the inlet location to 750m upstream of the domain centre had a somewhat more pronounced effect at ADP 3, increasing the average RMS error by 0.02, but much smaller impact at the other sites.

vertical profiles of $\vec{u}$, k and ε using the log profile in Appendix C. The log profile was used to set k and ϵ because the SWE simulations did not calculate turbulence parameters which could be related to the RANS simulations.[18] The velocity field was free to develop over the channel bathymetry moving downstream from the supplied boundary conditions.

At the downstream boundary, the *opening for entrainment* [80] option was used to allow the velocity to evolve as part of the simulation, while fixing the pressure by a hydrostatic assumption, $p = \rho g \zeta_b$.

Along the bottom, a rough wall function [80] was used, which required specifying the equivalent sand-grain-roughness (sgr). Ideally, sgr would be set using field data, and would vary spatially, however such data are unlikely to be available covering a large spatial region. This study evaluated values of 10 cm and 50 cm for sgr and found a notable impact on the predicted velocity profiles, so future studies ought to assess sensitivity to bottom roughness in more detail.[19]

The RANS simulations employed the k-ω SST turbulence model [32], because it has been validated to perform well in wake interaction studies [12], and because it has well established performance for mildly separated flows, which may be important in tidal channel scenarios with variable bathymetry.

Velocity Profile Prediction

Validating the velocity profiles predicted by SBR required classifying and bin-averaging the ADP time-series, using the same method as for the SWE results (Appendix A). Profiles were also predicted by applying a log profile (Appendix C) to the bin-averaged 2D SWE velocity (denoted 'SLP').

Figure 7.14 gives sample results showing the comparison for ADP 2, 3 and 4 locations for the top yield-contribution bins for ebb and flood directions. Notable in the figures is the that each boundary layer has a unique shape, some having higher gradients near the bottom (e.g. ADP3 ebb) and others with lower gradients (e.g ADP2 ebb), and also some with reducing velocity approaching the water surface.

[18] The time-resolved SWE simulations on the other hand used a Smagorinski turbulence model which separates grid-resolved and sub-gird turbulent scales using a spatial filter. The sub grid scales are modelled using the eddy viscosity concept set by element-local parameters, while the resolved scales are directly simulated. In contrast, the steady RANS simulations do not resolve any turbulent fluctuations and use eddy viscosity calculated via solved transport equations for turbulent kinetic energy and dissipation rate.

[19] The sand grain roughness will also have an impact on the turbulence intensity, and therefore could be set based on measurements of turbulence (which were not available for the present study).

Physically, the boundary layer shape is influenced by turbulence levels, bottom slope and roughness, sharp batrymetric features, wave-induced drift velocities and wind loading, however it is not possible to tease-out such influences in the present study.

The top left panel shows the profile for ADP2 with northward flow, and is of particular interest because of the distinct linear region of the profile below 10 m. It is thought that this shape was created by a region of slowed flow downstream of the small hill close to ADP4 (see figure 7.13) which altered the boundary layer from its fully-developed state. The linear region was well-predicted by SBR when sgr was set to 50 cm (denoted SBR_{50}). Neither, SBR_{10} (sgr set to 10 cm) nor SLP predicted the linear region.

The bottom left panel shows the profile for ADP2 for southward flow. When the flow was southward, SBR_{10} gave a better prediction than SBR_{50}, but SLP gave the best prediction of the profile. It is interesting that the best value of sgr for ADP2 varied with flow direction, implying a spatially-varying bottom-roughness could improve the SBR results somewhat compared to a constant value.

The centre panels of figure 7.14 shows profiles for ADP3. In both ebb and flood directions SBR_{10} gave the best prediction, while SLP misrepresented the bottom part of the profile. The rightmost panels show profiles for ADP4, which like ADP2, had significant ebb-flood asymmetry, which was better captured by SBR than SLP. For northward flow (bottom panels), both ADP3 and ADP4 showed distinctly lower speeds at the surface than at mid-depth, which was not predicted by SBR nor by SLP. This slowing of the flow approaching the top surface is not well understood at present and would be an interesting area of future study.

Figure 7.15, gives sample results comparing SBR (only with sgr=10cm) and SLP to the ADP results. In general, SLP gave a similar shaped velocity profile in all cases, however the ADP data showed notable variation in the profile shape, which was reproduced more reasonably by SBR.

SBR tended to give better profiles compared to SLP, because it predicted the evolution of the velocity field over the variable upstream bathymetry. This was most evident in the ADP 3 and 7 profiles.

Figures 7.14 and 7.15 only show results for two out of 51 (or 54) flow-state bins. To evaluate SLP and SBR for the entire flow regime, the RMS error (ms^{-1}) in velocity magnitude was evaluated over the water column for every flow bin, and then averaged over all bins, using the yield-contribution YC_b as a weighting factor. These results are summarized in table 7.7. Except at ADP 2, SBR statistically gave

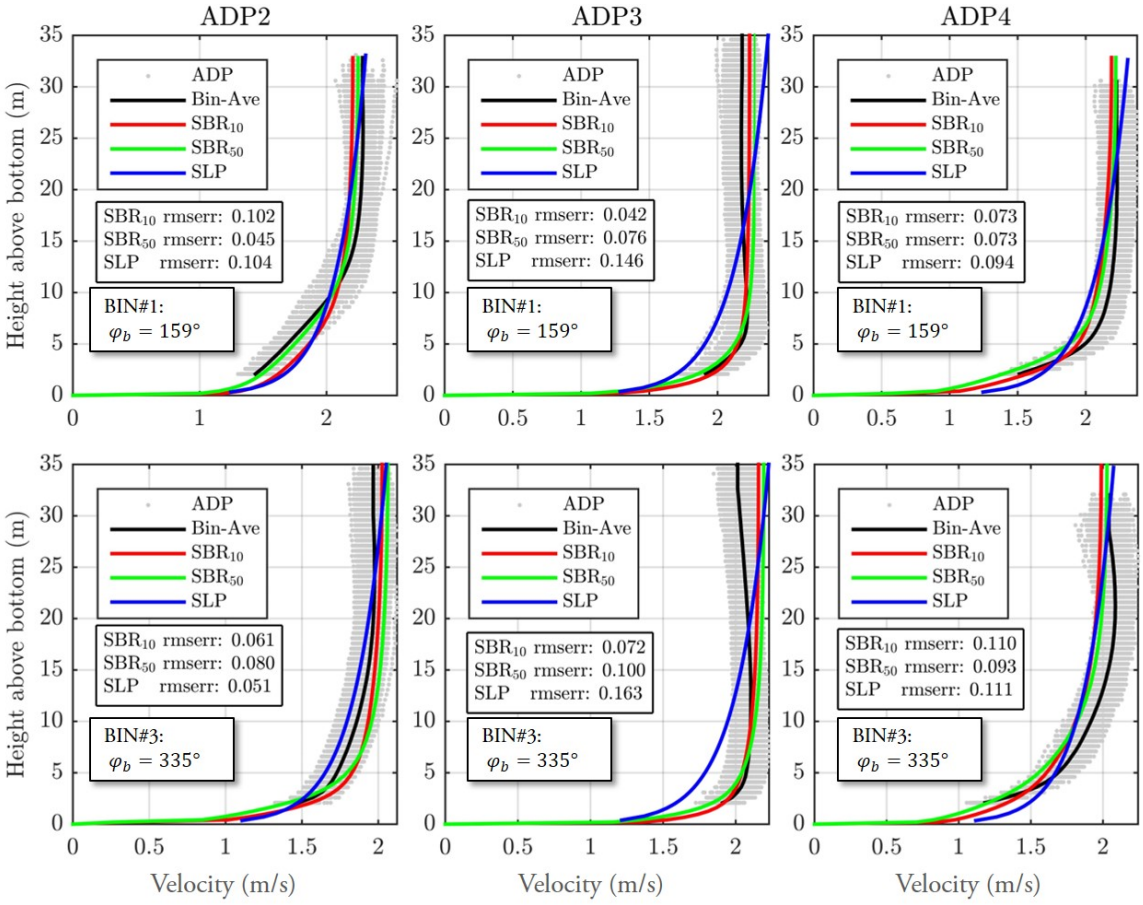

Figure 7.14: Comparison of vertical velocity profiles predicted by SBR and SLP to bin-averaged ADP data for the highest-yield bins for ebb (top) and flood (bottom), for ADP 2, 3 and 4. rmserr is given in ms^{-1}

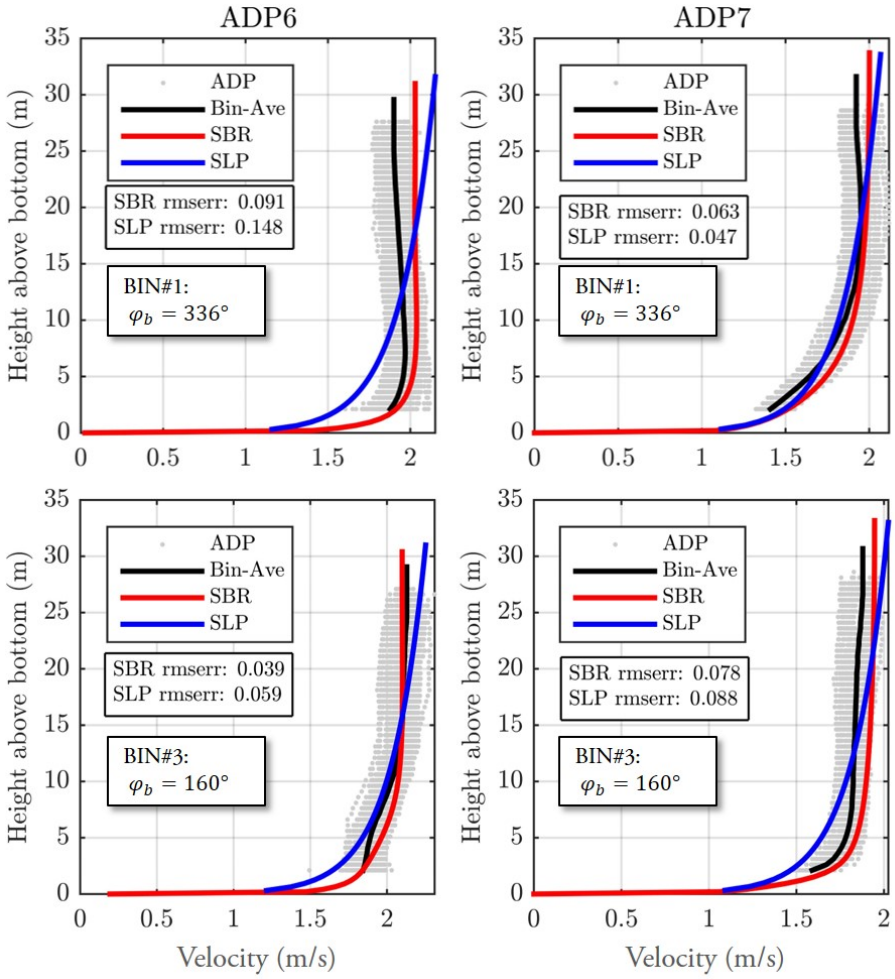

Figure 7.15: Comparison of vertical velocity profiles predicted by SBR (SGR=10cm) and SLP to bin-averaged ADP data for the highest-yield bins for ebb (top) and flood (bottom), for ADP 6 and 7. rmserr is given in ms^{-1}

ADP	SLP	SBR_{10}	SBR_{50}
2	0.0683	0.0860	0.0731
3	0.1333	0.0620	0.0901
4	0.0857	0.0668	0.0604
6	0.0958	0.0644	no data
7	0.0644	0.0629	no data

Table 7.7: RMS velocity profile error (ms^{-1}), YC-weighted average over all flow-state bins

better predictions of the velocity profile than SLP. The best sand grain roughness value for SBR varied from one ADP to the next, and also varied with flow direction for each ADP. Thus, SBR's prediction of velocity profiles could likely be improved by a spatially varying sand-grain-roughness for the bottom boundary. However without field data, specifying such variation could be challenging.

SBR Yield Predictions

The velocity profiles predicted by SBR were used to calculate the energy yield for turbines located at each ADP deployment. First, it was necessary to calculate the mean flow velocity over the rotor swept area using equation 7.3. Then, for each bin the power of each rotor was found using;

$$P_b = \frac{1}{2}\rho \left\langle |\vec{u}_b|^3 \right\rangle C_{Pi}(\langle |\vec{u}_b| \rangle) A_i \tag{7.12}$$

where $\vec{u}_b$ was taken from the CFD simulation corresponding to the b^{th} binned flow state. The yield was then calculated using equation 7.7 and is summarized in table 7.8. Yield predicted using SBR was very similar to that predicted by time-series analysis of the SWE results with an assumed log profile.

The % error in predicting yield (compared to time-series analysis using the ADP profile data) is summarized in table 7.9. The errors for SBR were very similar to using timeseries analysis on the 2D SWE method with the assumed log profile, and ranged from 0.8% to 11.7%.

The discrepancies between the time-series analysis using SLP and the bin-method analysis using SBR are partly due to the binning method, and partly due to different vertical profiles. To evaluate the binning procedure independently from the method used to predict vertical profiles, the time-series yield predicted from the depth-averaged SWE velocity (column 4), can be compared to the method-of-bins

		Y (MWh) (time-series)			Y (MWh) (binned)	
ADP #	T (h)	ADP profile	SWE DA	SWE SLP	SWE DA	SBR RANS
2	834.5	32.4	28.7	33.2	28.9	33.7
3	1089	45.9	45.9	51.0	46.2	51.3
4	863.7	33.8	29.8	34.4	29.9	34.0
6	365.7	16.7	16.9	18.4	16.9	18.2
7	365.5	16.3	14.5	17.1	14.5	17.1

Table 7.8: Summary of yield predictions using the various methods presented in this study

yield from the depth-averaged SWE velocity (column 6). The very close agreement indicates that the binning procedure introduced very little error into the analysis.

It is interesting that the improved accuracy in predicting the vertical profiles with SBR did not translate to more accurate yield prediction relative to ADP profiles. This is because at some ADP locations, the velocity at the rotor was predicted less-well by SBR than by SLP, even though the vertical profile as a whole was predicted more accurately. Figures 7.14 and 7.15 show that the SBR profiles are much closer to the ADP in the lower part of the water column, and the differences are smaller at the rotor hub 10 m below the surface.

Furthermore, the profiles at ADP 3 and 6 were actually better modelled by the 2D depth-average velocity than by any of the profile methods, and consequently, SWE DA gave the lowest error in the yield estimates for those particular locations. This unexpected result can be partially explained by the ADP data showing almost uniform profiles at those locations (see figures 7.14 and 7.15) for certain flow directions. Indeed, the profile at ADP 3 in flood had reducing velocity approaching the water surface, which could be thought of as an inverse velocity profile. Developing a better understanding of such abnormally uniform and even inverse profiles, and how to model them accurately in simulations presents an opportunity for future research.

For the particular locations assessed, the increased complexity of the SBR methodology was not warranted over SLP, because it did not improve yield predictions significantly. However, densely packed turbine farms will require RANS simulations (TADA) to predict the wake interaction effects. So, validating the ability of RANS to predict vertical velocity profiles lends confidence to applying it to more complex farm scenarios.

		(time-series)			(binned)	
ADP #	T (h)	ADP profile	SWE DA	SWE SLP	SWE DA	SBR RANS
2	834.5	0	-11.4	2.4	-11.0	4.1
3	1089	0	0.1	11.2	0.6	11.7
4	863.7	0	-11.9	1.9	-11.5	0.8
6	365.7	0	1.1	10.3	1.2	9.0
7	365.5	0	-10.9	4.6	-11.0	4.7

Table 7.9: Summary of the percent error in yield predictions using the various methods presented in this study

7.6 Conclusions

This paper has introduced tidal farm yield analysis methods for a range of farm scenarios of increasing complexity. For a single rotor deployed at the same location as collected ADP field data, yield prediction consists of applying rotor performance characteristics to the measured velocity. For rotors deployed away from ADP data locations it becomes necessary to model the tide-driven flow, which can be done using a 2D SWE solver. For farms with closely spaced rotors, 3D modelling is required to predict wake interaction effects. The transition from 2D to 3D modelling increases the computational expense significantly, but can be mitigated by performing yield analysis for a discrete set of binned flow states rather than by time-series analysis.

It is important to account for the vertical position of the rotor within the water-column, as the velocity varies significantly with depth. Such variation can reasonably be modelled using a typical log-law for scenarios where the bottom boundary layer is sufficiently well-developed. In channels with highly variable bathymetry, the bottom boundary layer development is disrupted by features such as ridges. For such scenarios, 3D modelling with RANS is expected to give more accurate predictions of the vertical velocity profiles. This hypothesis has been verified in this study, since SBR predicted vertical velocity profiles with greater accuracy than the assumed logarithmic profile. Note that in its present form, SBR predicts influences from bathymetry on shaping vertical profiles however other factors such as persistent secondary flow patterns, wave-induced currents and/or surface wind loads may be important for future studies. Indeed, the profiles at ADP 3 and 6 were not modelled well by SLP or SBR, and in fact were very close to uniform, which is why the best yield predictions for those sites were from assuming the hub height velocity was equal to the depth-average. Despite this, the proposed SBR method did predict yield within less than 12% of the baseline, even at the problematic sites, and within less than 5% at the other sites.

This paper has also demonstrated that categorizing the flow into discrete binned states is an accurate alternative to time-series analysis for predicting yield. In this study, using a binning approach combined with RANS (SBR) was not worth the additional effort, compared to assuming a standard log profile to do time series yield analysis directly from SWE simulations because it did not improve the yield estimates significantly. However, in locations with more complex bathymetry, SBR may be required as log profiles become less valid, which is explored in more detail in Part

Two.

To summarize, Part One has studied single turbine scenarios to gain insight into two critical components of the methods presented in section 7.2, namely 1) that RANS simulations can predict vertical velocity profiles with reasonable accuracy, and 2) that the bin-averaging approach is valid.

Part Two explores methods suitable for multiple rotors. The combined binning+TADA (SBT) approach is expected to be advantageous for more densely packed farms, where it is necessary to run 3D simulations to predict wake interaction effects. In that case, simply applying standard log profiles cannot account for the rotor wakes. For large farms it is necessary to incorporate turbines into the SWE simulations in addition to using TADA to predict wake-interaction effects accurately (i.e. the STBT method). Part Two demonstrates the utility of STBT in simulating turbine farms with up to 42 turbines.

Acknowledgments

The authors thank the National Sciences and Engineering Research Council (NSERC) of Canada and the University of Victoria for financial support.

Appendix A: Categorizing the flow into discrete bins

Step 3 of the SBR, SBT and STBT methods, is to categorize the depth-averaged SWE output time-series $\vec{U}_{0t}(\vec{x})$ into a set of N_b discrete bins, based on the flow speed, direction and water elevation. This appendix describes the classification process in detail.

It is possible to classify the 2D depth-averaged flow based-on a single point location (x,y), or a weighted average over several points. In this study, averages from ADP 2-4 were used for the first time-series, and averages from ADP 6-7 for the second time-series. For notation, the velocity/elevation time-series used for classification is referred to as the "Probe" velocity/elevation ($\vec{U}_{\text{prb}}$).

$$\vec{U}_{\text{prb}t} = \frac{1}{N}\sum_{i=1}^{N}\vec{U}_{0it}, \quad \zeta_{\text{prb}t} = \frac{1}{N}\sum_{i=1}^{N}\zeta_{0it} \tag{7.13}$$

where $\vec{U}_{0it}$ and ζ_{0it} are the SWE model outputs at the i^{th} ADP location, and N is the number of locations used for determining the average.

Every time-record within the SWE time-series was placed into a bin. The classification identified an index of discrete times for each flow bin, denoted as t_{bn}, and containing N_{bn} time-records. The subscript b refers to the b^{th} bin, and the subscript n refers to the n^{th} entry in bin b. Thus for any general variable ($\phi(t,\vec{x})$) which varies in time and space, $\phi_{bn}(\vec{x}) = \phi(t_{bn},\vec{x})$ is the n^{th} entry contained in the b^{th} bin. The categorization process used simple logic statements to identify t_{bn} for each bin.

7.6.1 Bin-averaging

Once t_{bn} was identified for each bin, it was possible to calculate a bin-averaged flow-state at any spatial location. The goal of bin-averaging was to ensure that the bin-averaged flow-state would provide an equivalent yield prediction as a time-series analysis of all time-instances within that particular bin.

The bin-averaged value of a general variable was denoted ϕ_b. Bin-averaging was

performed on the velocity magnitude and direction separately. For the magnitude:

$$|\vec{U}_b|(\vec{x}) = \left(\frac{1}{N_{bn}} \sum_{n=1}^{N_{bn}} |\vec{U}_{bn}(\vec{x})|^3 \right)^{\frac{1}{3}} \tag{7.14}$$

which maintains the average power since turbine power scales with velocity magnitude cubed.

To obtain the bin-averaged vector velocity, a weighted, normalized velocity vector was used:

$$\hat{U}_b(\vec{x}) = \frac{\sum_{n=1}^{N_{bn}} w_{bn} \vec{U}_{bn}(\vec{x})}{|\sum_{n=1}^{N_{bn}} w_{bn} \vec{U}_{bn}(\vec{x})|} \tag{7.15}$$

The bin-averaged vector velocity was then:

$$\vec{U}_b(\vec{x}) = |\vec{U}_b|(\vec{x}) \hat{U}_b(\vec{x}) \tag{7.16}$$

This formulation ensured that the flow energy calculated using the bin-averaged velocity ($E_{b\text{ave}}$) is consistent with the energy calculated by summing the individual bin entries ($E_{b\text{sum}}$). Namely;

$$E_{b\text{ave}} = E_{b\text{sum}} \tag{7.17}$$

$$\rho |\vec{U}_b(\vec{x})|^3 \delta t N_{bn} = \sum_{n=1}^{N_{bn}} \rho |\vec{U}_{bn}(\vec{x})|^3 \delta t \tag{7.18}$$

The bin-averaged water elevation was found using;

$$\zeta_b(\vec{x}) = \sum_{n=1}^{N_b} w_{bn} \zeta_{bn}(\vec{x}) \tag{7.19}$$

The normalized weights w_{bn} were calculated using a spatial average of the cubed velocity magnitude;

$$w_{bn} = \frac{\frac{1}{N_j} \sum_{j=1}^{N_j} |\vec{U}_{bnj}|^3}{\sum_{n=1}^{N_{bn}} \left(\frac{1}{N_j} \sum_{n=1}^{N_j} |\vec{U}_{bnj}|^3 \right)} \tag{7.20}$$

where N_j was the number of SWE nodes over-which the spatial average was done. Summation over the index j was used for spatial-averaging while summing over index n was used for bin-averaging. The above weighting scheme ensures that more-energetic flow states contribute more heavily to the bin-averaged velocity direction, and water elevation. The bin averaging process was applied to all SWE nodes contained within

the sub-domain region depicted in figure 7.6.

7.6.2 Bin Sorting

The flow-state bins were sorted in descending order of their contribution to energy yield. This was done to prioritize the high-resolution 3D simulations, and to exclude flow-states with zero or negligible contribution to the energy yield.

At the bin-sorting stage, the yield associated with each binned flow state is still unknown, and a preliminary estimate is therefore required. This study estimated the yield from a farm of rotors located at the ADP 2, 3 and 4 deployments for the 2012 simulations, and for a farm of turbines located at ADP 6 and 7 for the 2014 simulations.

For this preliminary assessment, the total yield (over the SWE simulation duration) for the i^{th} turbine (Y_i) was found from the SWE output time-series using equations 7.2 and 7.4 assuming that ($\tilde{u}_{0it}$) was equal to the SWE model output $|\vec{U}_{0it}|$. (I.e. assuming that the velocity was constant with depth.)

The yield associated with the b^{th} flow-state, for the i^{th} turbine (Y_{ib}), was estimated using a similar approach, where the summation was only carried out for the N_{bn} discrete time intervals contained in the b^{th} bin, namely:

$$P_{ebn} = \frac{1}{2}\rho|\vec{U}_{0ibn}|^3\eta_e C_P(|\vec{U}_{0ibn}|)A \tag{7.21}$$

$$Y_{ib} = \delta_t \sum_{n=1}^{N_{bn}} P_{ebn} \tag{7.22}$$

Then the percent yield contribution of each binned flow-state (YC_b) was found using;

$$\mathrm{YC}_b = \sum_{i=1}^{N_i} Y_{ib}/Y_i \tag{7.23}$$

The yield contribution is an interesting way to interpret the tidal resource similar to a velocity rose. Sorting the binned flow states by descending order of their yield contribution also reduces the total number of high resolution simulations required for the SBR, SBT or STBT methods, by eliminating flow bins that make a negligible contribution to the energy yield.

Appendix B: Depth-Averaging of ADP data

The range of valid ADP measurements was limited by the blanking distance at close proximity to the device, and by side-lobe-interference near the water surface. The ADP data were collected by bottom-mounted units, with the lowest measurement at h_1 , highest measurement at $h_{\max}$, and a vertical resolution of δ_h. The reported measurements $\vec{u}_i$ represent spatial averages for vertical bins with height δ_h centred on h_i. Figure 7.16 shows sample data.

Since the lowest and uppermost parts of the water column were not measured, depth-averaging was done by integrating in three parts. The lowest part assumed a logarithmic profile, the middle part used measured data, and the top part assumed the velocity remained constant above $h_{\max}$. For the lowest part, a neutrally stratified logarithmic profile was used;

$$\vec{u}(h) = \frac{u^\star}{\kappa} \ln\left(\frac{h}{h_0}\right) \frac{\vec{u}_1}{|\vec{u}_1|} \tag{7.24}$$

where $u^\star$ is the friction velocity, κ=0.41 is the von Karman constant, h_0 is the bottom roughness scale, and $\vec{u}_1/|\vec{u}_1|$ defined the flow direction. Fitting equation 7.24 to the lowest two measurements gave:

$$u^\star = \frac{\kappa\left(|\vec{u}_2| - |\vec{u}_1|\right)}{\ln\left(\frac{h_2}{h_1}\right)}, \qquad h_0 = \frac{h_1}{\exp\left(\frac{\kappa|\vec{u}_1|}{u^\star}\right)} \tag{7.25}$$

Integrating equation 7.24 from h_0 to $h_1 - \delta_h/2$ then gave:

$$\vec{I_1} = \frac{u^\star}{\kappa}\left\{\left(h_1 - \frac{\delta_h}{2}\right)\left[\ln\left(\frac{h_1 - \frac{\delta_h}{2}}{h_0}\right) - 1\right] + h_0\right\}\frac{\vec{u}_1}{|\vec{u}_1|} \tag{7.26}$$

The measurements were integrated numerically from $h_1 - \delta_h/2$ to $h_{\max} + \delta_h/2$, giving:

$$\vec{I_2} = \sum_{i=1}^{N} \vec{u}_i \delta_h \tag{7.27}$$

For the uppermost segment, from $h_{\max} + \delta_h/2$ to the water surface (H):

$$\vec{I_3} = H - (h_{\max} + \delta_h/2)\,\vec{u}(h_{\max}) \tag{7.28}$$

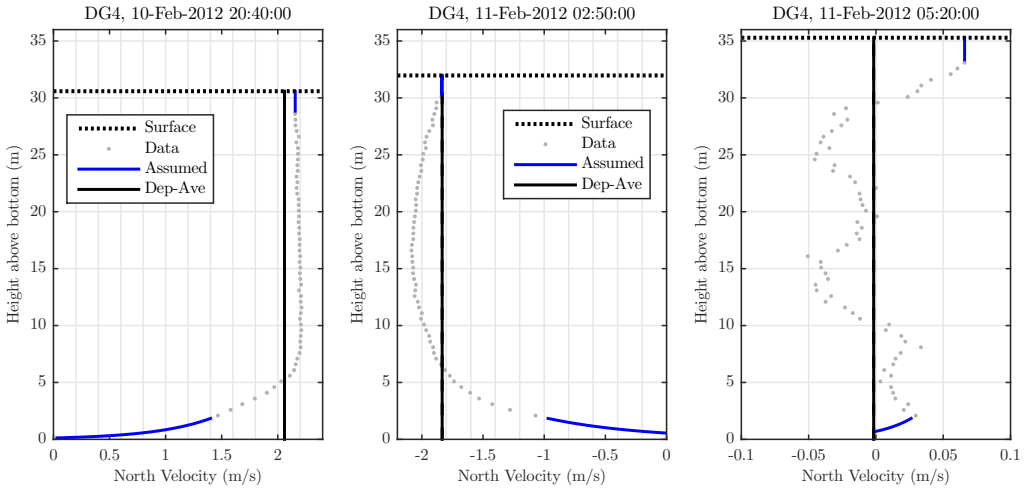

Figure 7.16: Sample ADCP profile data and depth-average at DG4, max ebb (left), max flood (center) and slack tide (right).

The depth-averaged velocity was then found as:

$$\vec{U} = \frac{\vec{I}_1 + \vec{I}_2 + \vec{I}_3}{H} \tag{7.29}$$

Figure 7.16 shows sample ADP data and the calculated depth-averages for the northward velocity component at DG4 in max ebb, max flood and slack tide conditions.

Appendix C: Converting depth-averaged velocity to profiles

Without specific knowledge of of the vertical profiles of velocity, a neutrally stratified logarithmic profile may be assumed to estimate the relationship between the depth-averaged flow field and the 3D flow field. The following equations have been derived considering the vertical integration of equation 7.24, to relate a log profile to depth-averaged velocity. They can be used to define vertical profiles for velocity and turbulence parameters, using the depth-averaged velocity $\vec{U}$, bottom friction coefficient C_{BF} used by the SWE model, and the assumed logarithmic profile. Note that the profile assumes a fully developed boundary layer which has evolved over a long upstream fetch.

$$U_\star = \sqrt{\mathrm{C_{BF}}}|\vec{U}|, \quad H_0 = \frac{H}{\exp\left(\kappa\frac{|\vec{U}|}{U_*}+1\right)} \tag{7.30}$$

$$\vec{u} = \vec{U}\frac{\ln\left(\frac{h}{H_0}\right)}{\ln\left(\frac{H}{H_0}\right)-1}, \quad k = \frac{U_*^2}{\sqrt{C_\mu}}, \quad \varepsilon = \frac{U_*^3}{\kappa h} \tag{7.31}$$

where $U_\star$ is the friction velocity based on the depth-averaged velocity, $\mathrm{C_{BF}}$ is the bottom friction coefficient, H is the water depth, k is the turbulent kinetic energy, ε is the dissipation rate, and h is the height above the bottom surface. C_μ =0.09 is a turbulence model coefficient.

Chapter 8

Computational Methods for Tidal Farm Energy Yield Part Two: Rotor Models and Large Farms

This chapter and the preceding have been submitted to the International Journal of Marine Energy as a two-part paper. These two chapters complete the thesis by presenting a hybrid 2D regional-scale / 3D farm-scale modelling approach for predicting flow fields and energy yield in large tidal farms.

Abstract

As tidal turbine development projects are nearing commercial scale there is a pressing need to establish best-practise methods to predict tidal farm energy yield and environmental impacts. Yield is critical for financial planning because it defines the project's revenue stream, while impact assessment is critical for permitting. This two-part paper presents a novel hybrid simulation method for calculating turbine output, wakes and far-field impacts of a tidal farm. The approach runs 2D coastal simulations to predict flow time-series over minute to monthly scales for basin-channel systems, and then categorizes that time-series using a method of bins. High resolution 3D simulations are run for each bin to predict vertical velocity profiles and wake interaction effects between turbines.

Part one verified the method-of-bins approach and vertical velocity profiles predicted by the 3D simulations. Part two provides robust methods to incorporate turbines into the coastal simulations as sub-grid objects, and into the high resolution 3D simulations using a specialized actuator disk method appropriate for densely packed turbine farms. In both simulation types, the turbine models respond to changing inflow according to known performance operational profiles, including the correct behaviour at cut-in, rated, and limit speeds. The 3D simulations predict wake profiles in detail, which is important for obtaining accurate yield. On the other hand, the 2D simulations can be run for very long durations at lower computational cost, and predict the added resistance from turbines within about 20% compared to the 3D simulations, which is likely sufficient for determining back-effects of the farm altering the flow through the tidal channel. The combined method leverages the strengths of each simulation type. The study culminates by simulating three different turbine farms in Petit Passage, Nova Scotia with up to 42 turbines, with a comparative analysis of yield and capacity factor. The method is computationally tractable with modest resources and is therefore of practical value to tidal power developers for assessing turbine layout.

8.1 Introduction

As tidal turbine technologies are approaching commercial-scale deployment there is a pressing need to fully establish best practises for predicting energy yield and impact assessment. IEC standards [2] provide general guidelines, but require more precise requirements for the numerical models employed. Research consortia [3] and consultancies [4] are making headway toward establishing more definitive guidelines. This two-part paper contributes to such efforts by introducing specific methods to model tidal farms which have been validated and are computationally tractable.

Part One summarized major physical phenomena which influence tidal flow dynamics through proposed farms. To calculate energy yield, it is necessary to predict the long-term flow variability through the farm region, while simultaneously accounting for the farm's far-field impact (e.g. bulk reduction of flow, redirecting of flow around the farm or into less-resistive channels, altered amplitude and/or phase of tidal flows) and near-field effects (turbine wakes, channel blockage effects). At any given time, the thrust force/power of each turbine depends on the square/cube of local flow velocity, which depends on the vertical velocity profile, in addition to both far-field and near-field effects. The yield is the integral of power over a given duration, which can be calculated by time-series analysis, or using a method of bins.

For a single rotor, both far-field and near-field effects are often negligible, allowing yield to be back-predicted directly from field measurements, or forward-predicted from 2D coastal (SWE) simulations assuming a vertical profile to obtain the hub-height velocity.[1] As discussed in Part One, standard profiles may not be suitable in channels with sharp bathymetric features, and in such cases 3D simulations using RANS may provide better accuracy. To alleviate the computational cost increase from switching from 2D, the 3D simulations can be performed on a set of bin-averaged flow states, rather than for a long duration transient simulation. This method of bins is applied over the entire spatial region of the farm, and was validated to provide similar yield as a full time-series analysis in Part One.

For large turbine farms, far-field and near-field effects will influence energy yield. It is proposed to predict far-field effects by introducing sub-grid turbine forcing terms into the time-domain 2D coastal simulations, and then in turn to predict near-field effects by introducing grid-resolved forcing terms into the binned 3D RANS simulations around the tidal farm domain.

[1] More precisely, the area-averaged velocity over the rotor swept area.

Part Two describes the employed forcing terms in detail. The sub-grid terms (for the time-domain coastal SWE simulations) introduced herein use an analytical formulation based on actuator-disk theory, which is similar to previous works [57, 147, 148, 145], but importantly, also allows for multiple rotors and/or portions of rotors in each grid cell. The 2D coastal SWE model including the sub-grid turbine forcing is referred to as SWET. For the binned steady 3D RANS simulations, the grid-resolved forcing terms are set using a robust method called the tuned-actuator-disk-approach (TADA) [12] which uses known performance operational profiles to tune the forcing terms.

This paper validates bin-domain TADA simulations (i.e. the SBT procedure defined in Part One) to predict yield by comparing to the baseline predictions obtained by direct use of ADP data. It then provides a comparative analysis of force, power and wakes predicted by TADA and SWET for single rotors.

Finally, the paper demonstrates yield/impact assessment studies for three turbine farms, using the full STBT procedure (i.e. with rotor forces included in both the coastal 2D and the 3D RANS simulations). The cases included a staggered row of 21 turbines, two-staggered rows with 42 turbines total, and a non-staggered row of 21 rotors. Those studies allowed for further comparative analysis, observing differences between rotor thrust, power, yield and wakes, between the 2D SWET and 3D TADA simulations. On their own, the 2D simulations inherently under-predict the influence of inter-turbine wake interactions, demonstrating the need to model rotors and their wakes in 3D, hence justifying the hybrid time-domain SWET / bin-domain TADA methodology.

The hybrid modelling approach is a novel contribution to tidal energy simulation for yield and impact assessment, which can provide critical information to inform project economics and regulatory decisions, while at the same time remaining computationally tractable for developers to employ in practise.

8.2 Yield Methodologies

For completeness, this section reiterates the yield assessment methods for level 3 and 4 scenarios identified in Part One. Please refer to Part One for more discussion on the rationale behind the methodologies.

The level three scenario has a few turbines closely spaced so that wake interaction affects power output, yet the farm is small enough that far-field effects remain negli-

1. Tune SWE bottom friction to match field data
2. Run SWE to predict N_t depth averaged flow fields ($\vec{U}_{0t}$)
3. Classify those fields into N_b bins
4. Define a bin-averaged 2D field ($\vec{U}_{0b}$) for each of the N_b bins
5. Use ($\vec{U}_{0b}$) to create boundary conditions for the next step
6. Run 3D TADA for each bin, to obtain thrust and power (T_b, P_{eb})
7. Calculate Y using:

$$Y_b = \delta t P_{eb} N_{bn}, \quad Y = \sum_{b=1}^{N_b} Y_b \tag{8.1}$$

Figure 8.1: Procedure for SBT. The first 5 steps are the same as SBR, however SBT incorporates rotors into the RANS simulations to predict wake-interaction effects.

gible. The proposed method suitable for a level 3 farm is called SBT (SWE - binning - TADA), and incorporates TADA rotor models into the high resolution simulations performed for each binned flow state. The SBT procedure is summarized in figure 8.1.

The level four scenario is a large farm with many densely packed turbines. Far-field effects can not be neglected, and wake interaction affects yield. The appropriate procedure is called STBT (SWET - binning - TADA), and incorporates a turbine model into the SWE simulation to include far-field effects. The STBT procedure is summarized in figure 8.2.

8.3 Single-Rotor TADA Simulations to Validate SBT

SBT incorporates TADA [12] rotor models, which were designed to account for wake interaction effects, into the 3D simulations. In this study, TADA has been validated in the context of SBT for single isolated rotors.[2]

[2]A full validation of SBT yield prediction for farms with wake interaction is not currently possible because there is no baseline data for yield in a densely-packed turbine farm. However TADA's ability to predict rotor performance in direct wake-shadow has been validated using flume tank data in [12],

1. Tune SWE bottom friction to match field data
2. Run 2D SWET to predict N_t depth-averaged flow fields ($\vec{U}_t$)
3. Classify those fields into N_b bins
4. Define a bin-averaged 2D field ($\vec{U}_b$) for each of the N_b bins
5. Use ($\vec{U}_b$) to define boundary conditions for the next step
6. Do 3D TADA simulation for each bin, to obtain thrust and power for each bin (T_b, P_{eb})
7. Assess the difference in turbine force between SWET and TADA
8. If the error is large recalibrate SWET and repeat steps 2-6
9. Calculate Y using eq 8.1

Figure 8.2: Procedure for STBT for large densely-packed turbine farms, which incorporates turbines into the SWE simulations to predict far-field effects. It may be required to iterate between SWET and TADA to recalibrate the applied forcing terms in the SWE model.

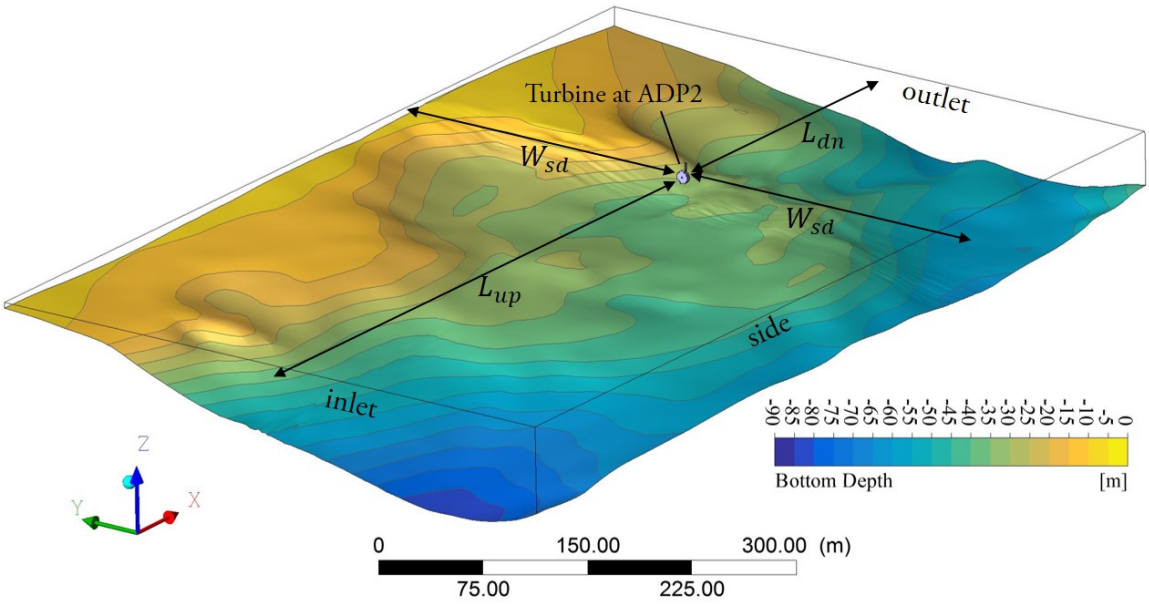

Figure 8.3: Sample domain used in TADA farm simulations with a single rotor present. The domain lengths are L_{up}=500 m, L_{dn} = 230 m, W_{sd}=230 m.

The TADA simulations were similar to the RANS simulations used for SBR described in Part One, except that they also included a turbine, and placed boundaries at somewhat different locations as depicted in figure 8.3. Also, the mesh was more refined in the vicinity of the rotor to ensure that the rotor diameter was resolved by 9 elements, a resolution which provided accurate predictions of rotor performance and wakes in [12].

8.3.1 TADA Turbine Model

In the context of a turbine farms in real bathymetry, the free-stream velocity is difficult to define ([98, 10, 141]) which confuses the matter of predicting turbine performance using standard performance parameters ($C_{\{\mathrm{T,P}\}}$ and TSR). TADA [12] is an innovative method which re-maps these parameters from being dependent on the free-stream u_0 to being dependent on the local area-averaged velocity at the rotor $\langle u \rangle$. The re-mapped performance parameters are denoted $C^{\star}_{\{\mathrm{T,P}\}}$, and TSR*, and are used within simulations to define momentum source terms to emulate rotors.

There are several differences to how TADA was implemented in the present study

which also demonstrated that TADA predicts the influence of channel blockage effects consistently with well-established analytical solutions.

compared to [12]. The first is that while [12] used raw performance data collected from a flume tank, the present study uses hypothetical data (figure 8.4 and table 8.1), corresponding to an unconstrained flow without any influence of channel walls. Therefore, whereas the tuning stage simulations in [12] used a domain mimicking the flume tank, the present study uses a so-called *open* domain (as described in [13]). The open domain has no wall boundary conditions, and therefore eliminates the influence of channel blockage effects on rotor performance, which is consistent with traditionally defined performance characteristics (or performance characteristics from flume tanks or confined channels which have been corrected for blockage effects).

The second difference is that in [12], the physical rotor's performance was sensitive to the turbulence intensity (with data collected at I_0=3%, I_0=15%), while herein, the physical rotor's performance is assumed to be insensitive to turbulence (i.e. the curves shown in figure 8.4 were used for all turbulence conditions.) However, even though this study assumes the physical rotor is insensitive to turbulence, the simulated disk-average velocity is sensitive to the turbulence intensity and length-scale because of their impact on mixing in simulations. Higher turbulence simulations predict faster wake recovery, and therefore higher rotor-local velocity. Therefore, the TADA model was sensitized to the disk-averaged turbulence intensity $\langle I \rangle$ and length-scale $\langle L \rangle$. So, the present study added the turbulent length scale as an independent variable during the tuning stage, compared to [12], which only used the intensity.[3]

The third difference is that while [12] considered the rotor performance as a function of TSR, the present study considers performance curves as a function of inflow velocity, to better represent practical turbine operation. While [12] remapped $C_{\{\mathrm{T,P}\}}\left(\mathrm{TSR}, I_0\right)$ to $C^{\star}_{\{\mathrm{T,P}\}}\left(\mathrm{TSR}^{\star}, \langle I \rangle\right)$ the current study remaps $C_{\{\mathrm{T,P}\}}\left(u_0\right)$ to $C^{\star}_{\{\mathrm{T,P}\}}\left(\langle u \rangle, \langle I \rangle, \langle L \rangle\right)$ and also remaps $\mathrm{TSR}(u_0)$ to $\mathrm{TSR}(\langle u \rangle, \langle I \rangle, \langle L \rangle)$. Because of the discontinuities in the performance curves, it was also necessary to also re-map the cut-in, rated and cut-out speeds to their disk-averaged equivalents.

Finally, the fourth difference is that the present study defines the re-mapped parameters as regression based models, rather than by the three-part linear-interpolation scheme used in [12].

The calibration points used for tuning the TADA model were u_0={0.4, 2.0, 2.15, 2.3, 2.45, 2.6} ms^{-1}, I_0={1, 3, 5, 10, 20} % and length scale L_0={5, 10, 50, 100, 200} m. The lowest velocity was the cut-in speed and the second velocity was the rated

[3]Recent experimental work [116] has identified that physical rotor performance can be sensitive to the turbulent length scale, in addition to the intensity.

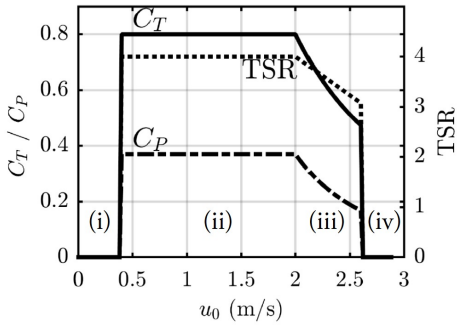

Figure 8.4: Performance curves (referenced to the free-stream velocity u_0) for the hypothetical turbine used in this study. The operating zones are: (i) below cut-in, (ii) cut-in to rated, (iii) rated to cut-out, (iv) above cut-out.

Rotor Dia. (m)	9.00
Hub Height* (m)	-10
Cut-in Spd (m/s)	0.40
Rated Spd (m/s)	2.00
Cut-out Spd (m/s)	2.60
Rated Power (kW)	96.4
Drag coefficient C_D	0.2

Table 8.1: Characteristics of the hypothetical turbine used in this study. *The turbine is to be installed on a floating platform with the hub submerged below the water surface. The drag coefficient refers to the drag of the supporting structures.

speed. Points were not needed between cut-in and rated because within that range the performance coefficients are constant. The final velocity calibration point was the cut-out speed, so the tuning covered the entire operational range of the turbines. The ranges of intensity and length scale were chosen to cover the ranges expected within Digby Gut; at more turbulent sites, a wider range may be necessary. For each calibration point, a tuning simulation was run, using $\{u_0,\ I_0,\ L_0,\ C_\mathrm{T},\ C_\mathrm{P},\ \mathrm{TSR}\}$ as inputs to calculate $\{\langle u\rangle,\ \langle I\rangle,\ \langle L\rangle,\ C^\star_\mathrm{T},\ C^\star_\mathrm{P},\ \mathrm{TSR}^\star\}$.

The tuning simulations used a open model domain depicted in figure 8.5. The simulations used the k-ω SST turbulence model. The top, bottom and sides used an opening for entrainment boundary condition, while the outlet used a pressure condition. The inlet specified a plug flow condition with $u{=}U_0$, which was used to specify the applied momentum source terms according to:

$$\overline{S_{\mathrm{M}x}} = -T_\mathrm{spec}\left[\frac{u^2 c_x}{\int_\mathcal{V} u^2 c_x d\mathcal{V}}\right], \quad \overline{S_{\mathrm{M}\theta}} = -\frac{1}{r\Omega}P_\mathrm{spec}\left[\frac{u^2 c_\theta r}{\int_\mathcal{V} u^2 c_\theta r d\mathcal{V}}\right] \tag{8.2}$$

$$T_\mathrm{spec} = \frac{1}{2}\rho U_0^2 C_T(U_0)A, \quad P_\mathrm{spec} = \frac{1}{2}\rho U_0^3 C_P(U_0)A \tag{8.3}$$

which were applied in the actuator disk region. In the tuning simulations, the ambient (no-rotor case) turbulence was maintained by adding turbulence source terms in the entire domain, as done in [13]. This approach ensured that the turbulence did not decay from the inlet, to allow control over the ambient turbulence at the rotor:

$$S_k = C_\mu \rho k_\mathrm{in}\omega_\mathrm{in}, \quad S_\omega = \beta\rho\omega_\mathrm{in}^2 \tag{8.4}$$

After running the calibration simulations, regression models were fit to the calibration points using least-squares multi-variable linear regression, for regions (ii) between cut-in and rated and (iii) between rated and cut-out, as depicted in figure 8.4. For region (ii) the performance coefficients ($C^\star_{\{\mathrm{T,P}\}}$ and $\mathrm{TSR}^\star$) were constant with flow speed but did vary with $\langle I\rangle$ and $\langle L\rangle$. The regression model for thrust in region (ii) was:

$$C^{\star ir}_\mathrm{T} = c^{ir}_{1t} + c^{ir}_{2t}\langle I\rangle + c^{ir}_{3t}\langle I\rangle^2 + c^{ir}_{4t}\langle L\rangle + c^{ir}_{5t}\langle L\rangle^2 \tag{8.5}$$

The same form was used for $C^\star_\mathrm{P}$ and $\mathrm{TSR}^\star$. The variation of $C^{\star ir}_{\{\mathrm{T,P}\}}$ and $\mathrm{TSR}^{\star ir}$ with ambient turbulence is shown in the left panels of figure 8.6, while the regression model and its estimated % error is shown in the centre and right panels.[4]

[4]The regression model is only valid for $\langle I\rangle$ and $\langle L\rangle$ within the ranges used for tuning the model,

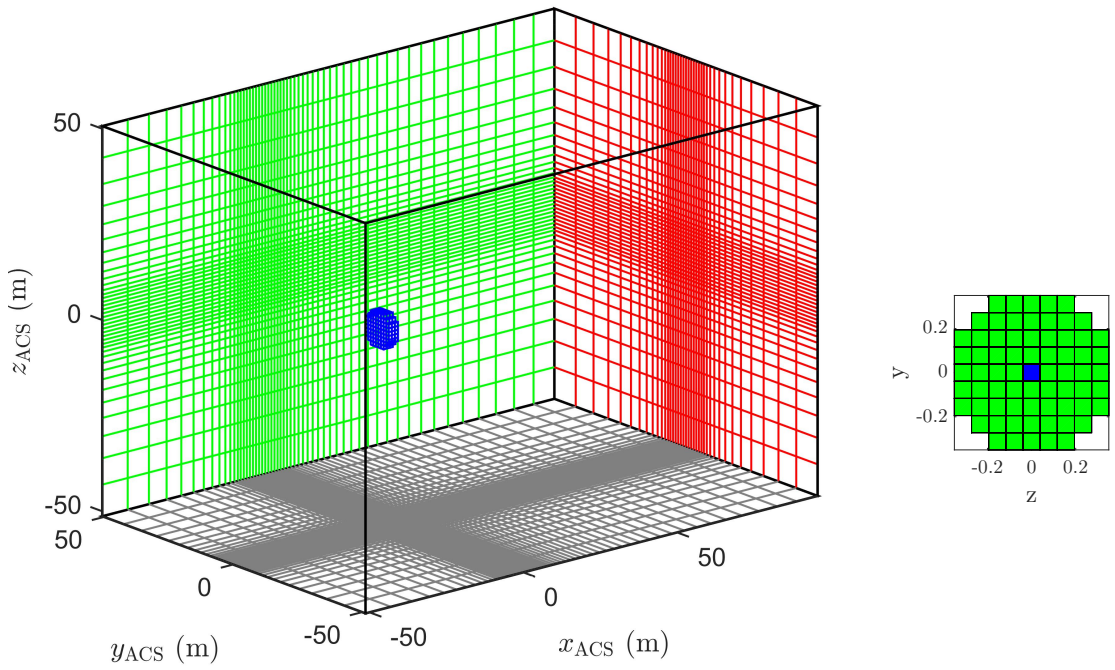

Figure 8.5: Open model domain used for the TADA tuning simulations (left). The rotor (depicted in blue) is located 5D from the inlet, sides, top and bottom, and 10D from the outlet. The right plot shows the mesh on the actuator-disk, which is resolved using 9 elements spanning the diameter.

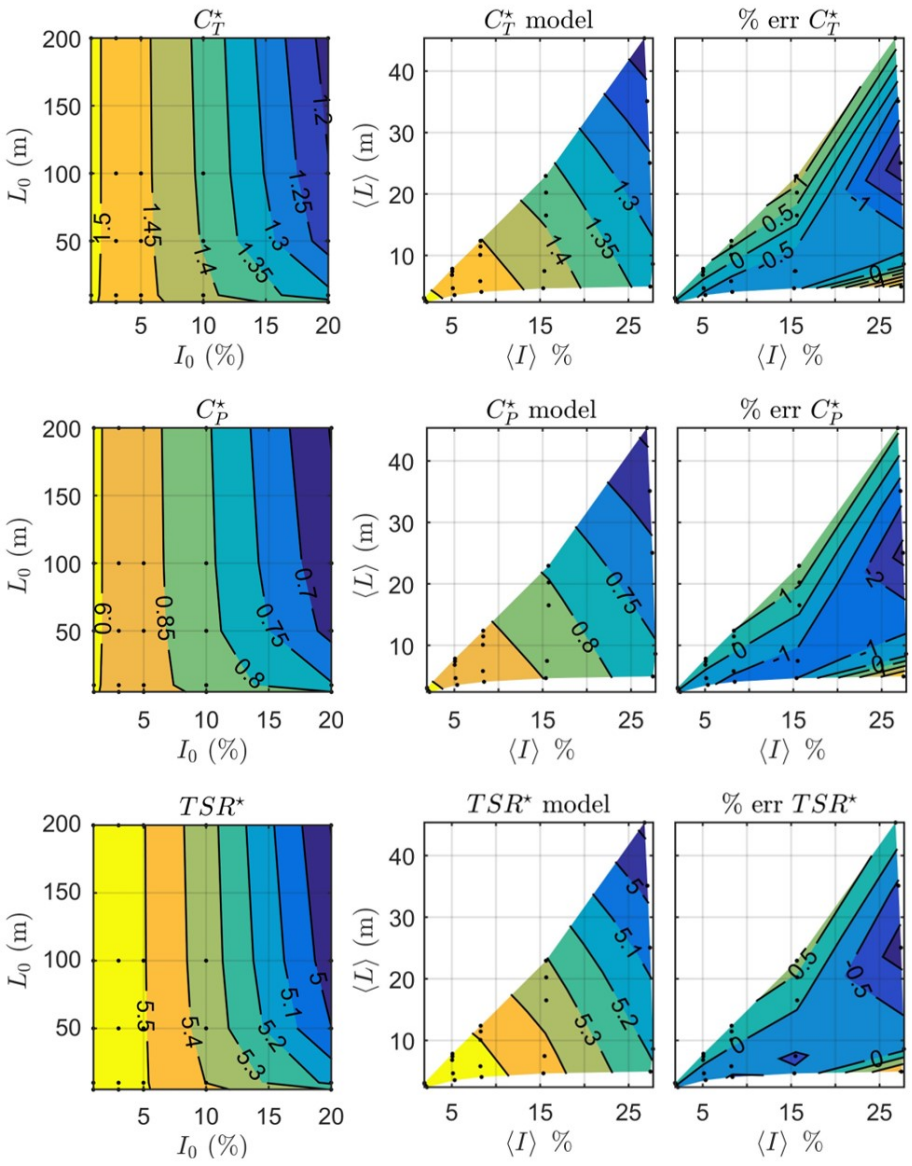

Figure 8.6: Re-mapped performance between cut-in and rated speeds. The left panels show the variation with ambient conditions I_0 and L_0. The centre panels show the regression model variation with disk-averaged $\langle I \rangle$ and $\langle L \rangle$. The right panel shows the % error of the curve-fit compared to the calibration points, which are depicted as black dots.

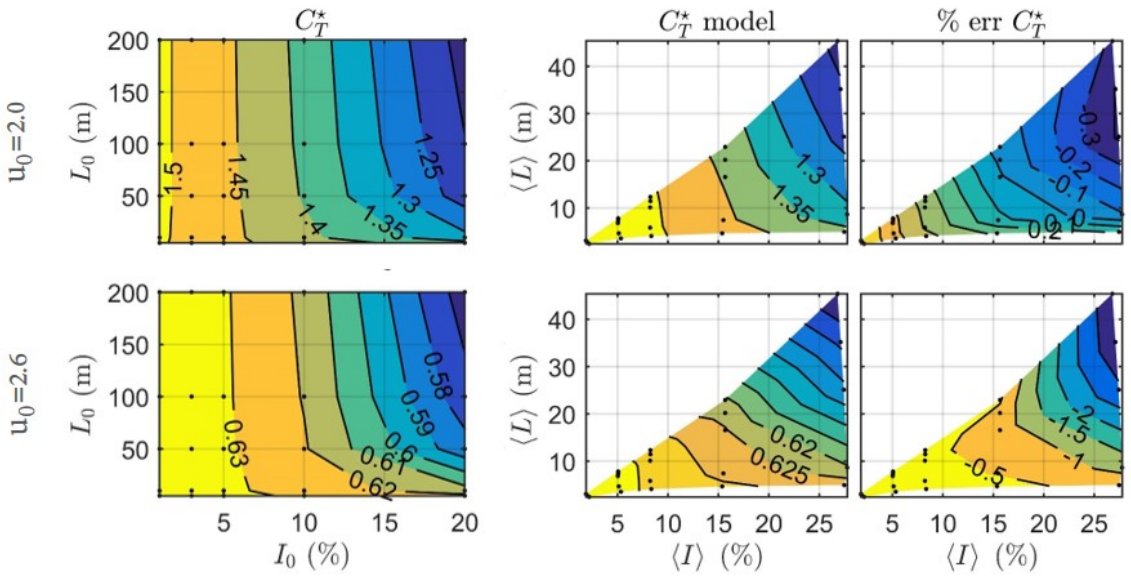

Figure 8.7: Re-mapped $C_{\mathrm{T}}^{\star ro}$ at the rated and cut-out speeds. The left panels show the variation with ambient conditions I_0 and L_0. The centre panels show the regression model variation with disk-averaged $\langle I \rangle$ and $\langle L \rangle$. The right panel shows the % error of the curve-fit compared to the calibration points, which are depicted as black dots.

For region (iii) $C_{\mathrm{T}}^\star$ varied with velocity and turbulence as:

$$C_{\mathrm{T}}^{\star ro} = c_{1t}^{ro} + c_{2t}^{ro} \langle I \rangle + c_{3t}^{ro} \langle I \rangle^2 + c_{4t}^{ro} \langle L \rangle + c_{5t}^{ro} \langle L \rangle^2 + c_{6t}^{ro} \langle u \rangle + c_{5t}^{ro} \langle u \rangle^2 \tag{8.6}$$

which is depicted graphically in figure 8.7. A similar regression model was defined for TSR*. In region 3, power was constant at the rated power, which was used to define $C_{\mathrm{P}}^\star$:

$$C_{\mathrm{P}}^{\star ro} = \frac{P_{\mathrm{rated}}}{\frac{1}{2}\rho \langle u^3 \rangle A} \tag{8.7}$$

Because the disk-averaged velocity was sensitive to turbulence, it was also necessary to define regression models for the cut-in, rated, and cut-out speeds. For the cut-in:

$$\langle u_i \rangle = c_{1i} + c_{2i} \langle I \rangle + c_{3i} \langle I \rangle^2 + c_{4i} \langle L \rangle + c_{5i} \langle L \rangle^2 \tag{8.8}$$

Similar regression fits were defined for the rated ($\langle u_r \rangle$) and cut-out ($\langle u_o \rangle$) speeds. The variation of the re-mapped cut-in, rated and cut-out speeds with turbulent conditions

i.e. the model *envelope*. The regression model may produce incorrect or even non-physical values outside of its envelope, so care must be taken at the tuning stage to cover a wide enough range of I_0 and L_0.

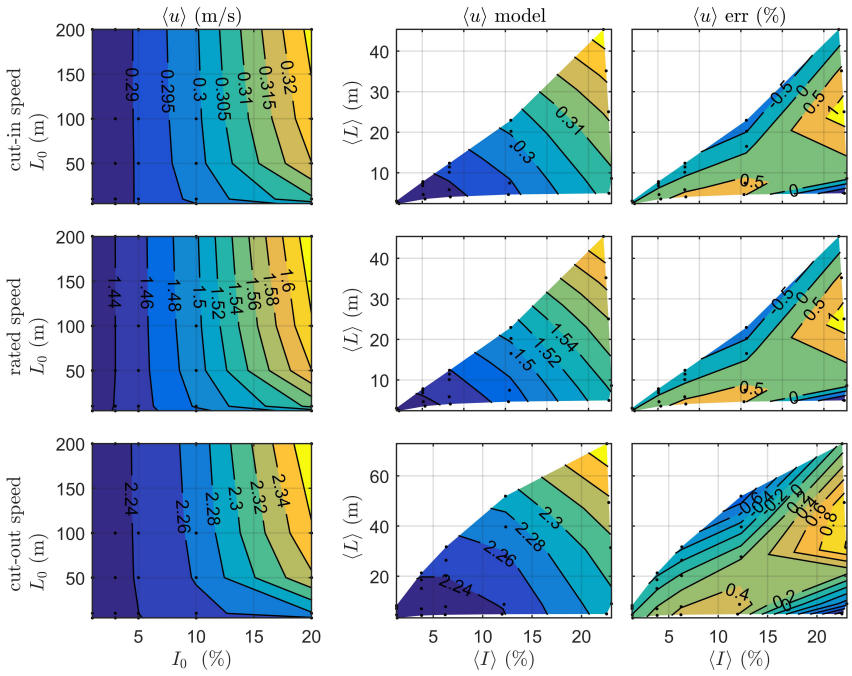

Figure 8.8: Re-mapped speeds for cut-in $\langle u_i \rangle$, rated power $\langle u_r \rangle$ and cut-out $\langle u_o \rangle$. The left panels show the variation with ambient conditions I_0 and L_0. The centre panels show the regression model variation with $\langle I \rangle$ and $\langle L \rangle$. The right panel shows the % error. The black dots show the calibration points.

is depicted in figure 8.8.

Special care needed to be taken to treat the rotor's cut-in and cut-out behaviour. When the rotor is off (either below cut-in or above cut-out), the disk-averaged velocity $\langle u \rangle$ corresponds to the free-stream, because there is no thrust force acting on a parked rotor. So, if the speed is below cut in and the rotor is off, it should only start operating if $\langle u \rangle$ increases beyond u_{0i} (free stream cut-in speed). When it is already operating but the flow speed decreases, it should only stop if $\langle u \rangle$ decreases below $\langle u_i \rangle$ (re-mapped cut in speed). Similar logic had to be applied for the cut-out behaviour. So with the rotor operating and the flow speed increasing, the rotor should stop when $\langle u \rangle$ increases beyond $\langle u_o \rangle$ (re-mapped cut out speed). Finally, when the rotor is stopped with the speed above cut-out, it should start when $\langle u \rangle$ decreases past u_{0o} (free-stream cut-out speed). To avoid numerical instabilities (cycles of on-off oscillation) the following

logic worked well for stable flows:

$$C^{\star \mathrm{on}}_{\{\mathrm{T,P}\}} = \begin{cases} C^{\star ir}_{\{\mathrm{T,P}\}}, & \text{for } \ 0.9\,\langle u_i \rangle < \langle u \rangle < \langle u_r \rangle \\ C^{\star ro}_{\{\mathrm{T,P}\}}, & \text{for } \ \langle u_r \rangle \leq \langle u \rangle < 1.05\,\langle u_o \rangle \\ 0 & \text{otherwise} \end{cases} \tag{8.9}$$

$$C^{\star}_{\mathrm{T}} = \begin{cases} C^{\star on}_{\mathrm{T}}, & \text{if ON} \\ 0, & \text{if OFF } \& \ [\langle u \rangle < 0.98 u_{0i}] \\ 0.8 \min C^{\star ir}_{\mathrm{T}}, & \text{if OFF } \& \ \left[0.98 u_{0i} \leq \langle u \rangle < \tfrac{1}{2}\,(u_{0i} + u_{0o})\right] \\ 1.5 \max C^{\star ir}_{\mathrm{T}}, & \text{if OFF } \& \ \left[\tfrac{1}{2}\,(u_{0i} + u_{0o}) \leq \langle u \rangle < u_{0o}\right] \\ 0, & \text{if OFF } \& \ [\langle u \rangle > u_{0o}] \end{cases} \tag{8.10}$$

$$C^{\star}_{\mathrm{P}} = \begin{cases} C^{\star on}_{\mathrm{P}}, & \text{if ON} \\ 0, & \text{if OFF} \end{cases} \tag{8.11}$$

The logical parameter ON/OFF is ON if $C^{\star}_{T}$ was non-zero at the previous iteration of the solver algorithm.[5]

8.3.2 Yield and Power using TADA

The TADA simulations predicted power for each binned flow state, P_{eb}, allowing the yield to be predicted using equation 8.1.

The yield from each of the top 30 bins is summarized in figures 8.9 and 8.10. Predictions are shown from three methods. The first (SDA) was from assuming $\tilde{u}_{0b}$ equal to the depth-averaged SWE velocity and using equation 8.1; the second is from SBR and the third is from SBT. The very good agreement between SBR and SBT indicates that the TADA rotor parameterization produced reliable power predictions,

[5] In certain unstable flow regimes, e.g. with the rotor located on the edge of a region of separated flow, the above logic still resulted in cyclic on-off behaviour. In reality, rotors may switch on and off in such flows, but the oscillation was very problematic for obtaining converged steady-state simulations. In those select cases, the parameter 0.98 was increased to 1.2, to keep the rotor off once it had shut down once in the simulation. For such cases, steady-state simulations likely do not represent the true flow behaviour well, however from an operational perspective it would be undesirable to locate turbines in separated-flow regions, so in practise, such turbines would likely be re-located to steadier flows.

		Y (MWh) (time-series)			Y (MWh) (binned)		
ADP	T	ADP	SWE	SWE	SWE	SBR	SBT
#	(h)	profile	DA	SLP	DA	RANS	TADA
2	834.5	32.4	28.7	33.2	28.9	33.7	33.6
3	1089	45.9	45.9	51.0	46.2	51.3	48.4
4	863.7	33.8	29.8	34.4	29.9	34.0	34.7
6	365.7	16.7	16.9	18.4	16.9	18.2	18.6
7	365.5	16.3	14.5	17.1	14.5	17.1	17.2

Table 8.2: Summary of yield predictions using the various methods presented in this study. This table is the same as Part One, table 7.8, but with the addition of the SBT method.

in the context of a single rotor.[6] Note that the total yield shown in figures 8.9 and 8.10 was calculated for the entire SWE simulation time duration of 1090.8 h for ADP 2-4 and 365.7 h for ADP 6 and 7.

Summing the power over all bins gave the total yield for the entire simulation duration, which was then scaled by the yield scaling factor (discussed in Part One §7.4.4) to allow comparing to the ADP baseline yield. The yield predictions are summarized in table 8.2, and the percent error compared to the baseline is shown in table 8.3. SBT predicted very similar yield to SBR, which verifies the TADA rotor model in the context of SBT. The discrepancies in yield between SBT and the baseline were less than 12% for all considered locations, and typically less than 6%. As discussed in Part One §7.5.2, the nearly uniform (even inverse) ADP velocity profiles at ADP 3 and 6 were not well-predicted by any of the velocity profile methods, which explains why the SWE DA method gave the lowest errors for those particular sites; future numerical models may be able to improve the modelling of such vertical profiles. SBT uses the same governing equations and models as SBT, but also incorporated the TADA rotor model. Thus, SBT was not expected to give improved yield predictions compared to SBR for single isolated rotors, and ideally the two methods would have given equivalent results.

[6]Since the rotor was in the upper portion of the water column, the resolved velocity profile from the SBR and SBT simulations gave higher yield estimates compared to using the depth-averaged velocity (SDA). Note that for flow bins where the depth-average velocity was above the turbine's rated speed (and below the cut-out), all three methods predicted the rated power. Interestingly, while reducing the turbine's rated speed would decrease yield, it would also reduce uncertainty in yield.

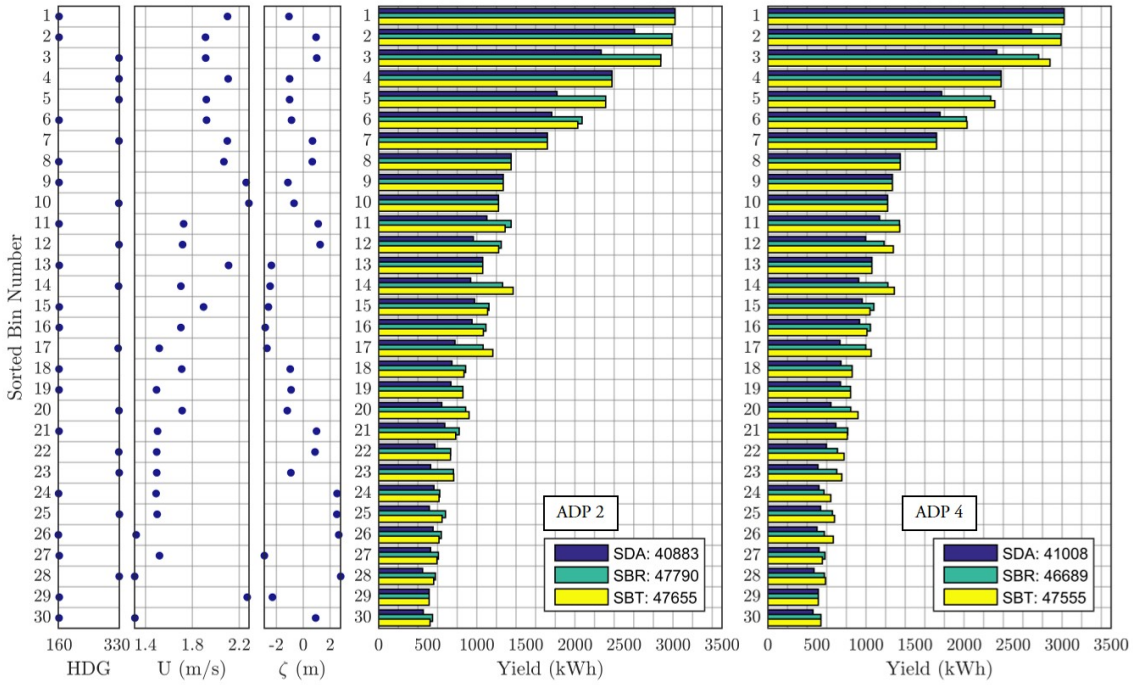

Figure 8.9: Summary of yield predictions for ADP 2 and 4 from the top 30 binned flow-states (a total of 54 states were simulated). The left panels show the *probe* heading (HDG (deg)), velocity and elevation used to classify the bins (see Part One Appendix A) . Note that SDA refers to using the SWE-Depth Average velocity to predict power for each bin. The inset panels at the bottom right show the total yield (sum of all bins) for each method.

		% error (time-series)			% error (binned)		
ADP #	T (h)	ADP profile	SWE DA	SWE SLP	SWE DA	SBR RANS	SBT TADA
2	834.5	0	-11.4	2.4	-11.0	4.1	3.8
3	1089	0	0.1	11.2	0.6	11.7	5.6
4	863.7	0	-11.9	1.9	-11.5	0.8	2.7
6	365.7	0	1.1	10.3	1.2	9.0	11.3
7	365.5	0	-10.9	4.6	-11.0	4.7	5.2

Table 8.3: Summary of the percent error in yield predictions using the various methods presented in this study. This table is the same as Part One, table 7.9, but with the addition of the SBT method.

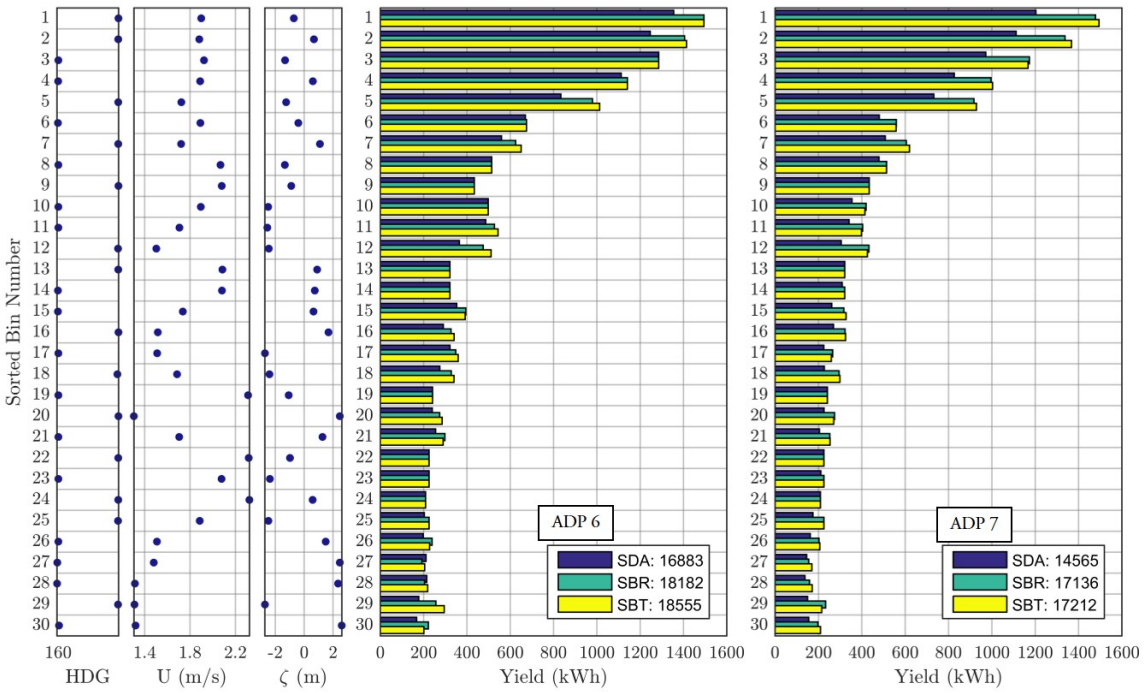

Figure 8.10: Summary of yield predictions for ADP 6 and 7 from the top 30 binned flow-states (a total of 54 states were simulated). The left panels show the probe heading (HDG (deg)), velocity and elevation used to classify the bins. Note that SDA refers to using the SWE-Depth Average velocity to predict power for each bin. The inset panels at the bottom right show the total yield (sum of all bins) for each method.

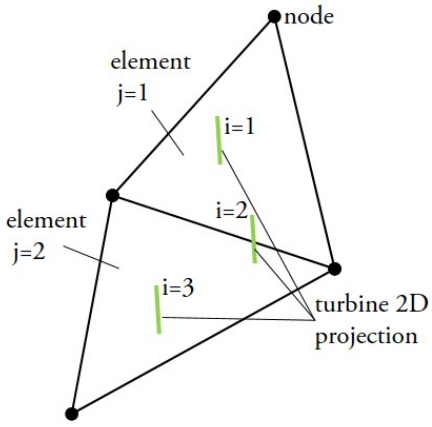

Figure 8.11: Depiction of turbines contained within grid cells in the regional-scale model. Turbine i=1 is entirely contained within element j=1, while turbine i=2 is split between elements j=1 and 2. The thrust force allocated to each element j is the sum from the portion of each turbine contained within that element.

8.4 SWET Sub-Grid Turbine Model

For large tidal farms, rotor forces must be included in SWE simulations to predict far-field effects for impact assessment and to predict the farm's influence on boundary conditions passed to the 3D TADA simulations. Thus, it is important that the added drag is consistent with actual turbines, within a reasonable degree of accuracy.

This section presents an analytical formulation to specify the sub-grid-scale turbines in SWE simulations. As depicted in figure 8.11, any SWE grid cell may contain multiple turbines, or portions of turbines. The term γ_{ij} represents the percentage of the swept area of the i^{th} turbine contained within the j^{th} grid cell.

Analogous to TADA using the local disk-averaged velocity $\langle u \rangle$ to set rotor forces, the SWET model uses the grid cell velocity $\vec{u}_j$. Doing so requires remapping performance coefficients similarly to TADA (§8.3.1), however with additional complications because each grid cell may contain multiple rotors or portions thereof. Thus, while TADA can ensure that a consistent grid spacing can be used for all rotors, SWET cannot. The simulation-based tuning strategy for TADA involves simulations over ranges of velocity and two turbulence quantities. To apply a similar strategy for the SWE simulations would introduce at least one more parameter relating the ratio of grid-cell frontal area, compared to total swept area, and perhaps additional parameters relating to the proximity/layout of multiple rotors within each cell.

Therefore, SWET uses actuator disk theory to relate the grid cell velocity to

the free-stream in a similar manner as [57, 147, 148, 145]. This paper expands on those previous studies by allowing turbines to span multiple computational elements, and allowing for multiple rotors within each element. A resistance coefficient K_{Tj} is defined in each turbine-containing grid cell;

$$T_j = -\frac{1}{2}\rho_j K_{Tj} |\vec{U}_j| \vec{U}_j A_{fj} \tag{8.12}$$

where A_{fj} is the frontal area of the grid cell, calculated as the nominal depth (at mean sea level), multiplied by the cell's equivalent diameter ($2\sqrt{A_{tri}/\pi}$).

Considering a hypothetical free-stream velocity u_0[7], and neglecting wake interaction and channel blockage effects, it is possible to define a second equation for T_j using standard thrust and drag coefficients:

$$T_j = \sum_{i=1}^{N_j} -\frac{1}{2}\rho u_0^2 (C_{Ti} + C_{Di}) \pi R_i^2 \gamma_{ij} \tag{8.13}$$

It is possible to relate $|\vec{u}_j|$ to K_{Tj} by analogy to well established actuator-disk theory:[8]

$$K_{Tj} = \frac{4a}{(1-a)}, \quad |\vec{U}_j| = u_0(1-a). \tag{8.14}$$

where a is an axial induction factor for the SWE grid cell. These relationships allow the velocity at the rotor grid cell as a function of the applied forcing term K_T:

$$|\vec{U}_j|^2 = u_0^2 \left(\frac{4}{4 + K_{Tj}} \right)^2 \tag{8.15}$$

Combining equations 8.12, 8.13 and 8.15, it is possible to write:

$$\frac{4}{4 + K_{Tj}} K_{Tj} A_{fj} = \sum_{i=1}^{N_j} (C_{Ti} + C_{Di}) \pi R_i^2 \gamma_{ij} \tag{8.16}$$

which can be solved for K_{Tj} as:

$$K_{Tj} = -4 + \frac{8A_{fj}}{C_1} \left(1 - \sqrt{1 - \frac{C_1}{A_{fj}}} \right) \tag{8.17}$$

[7] In the context of a spatially varying flow, the free-stream velocity may be thought of as the velocity at the rotor hub, if the rotor were not present[98].

[8] as described in many texts on wind power, for example [82]

where C_1 is the right-hand-side of equation 8.15. For a single rotor fully contained in a single grid cell, this is equivalent to the correction developed by [145].

This analytical solution is strictly valid only for unbounded flows (i.e. no lateral boundaries and no interaction with adjacent turbines) and assumes that the flow through each turbine rotor is uniform and non-turbulent. It is also limited to $K_T<2$, due to the well known turbulent wake state. Furthermore, it does not account for the boundary-layer profile. These assumptions are somewhat limiting, but are likely acceptable for predicting far-field effects, and boundary conditions for higher-resolution TADA simulations, which are the main functions of the SWET simulations within the STBT method.

The power can similarly be defined as:

$$P_j = \frac{1}{2}\rho_j K_{Pj} |\vec{U}_j|^3 A_{fj} \tag{8.18}$$

or as:

$$P_j = \sum_{i=1}^{N_j} \frac{1}{2}\rho u_0^3 C_{Pi} \pi R_i^2 \gamma_{ij} \tag{8.19}$$

which, combined with equation 8.15 allows defining K_{Pj} as:

$$K_{Pj} = \frac{(4 + K_{Tj})^3}{64 A_{fj}} \sum_{i=1}^{N_j} C_{Pi} \pi R_i^2 \gamma_{ij} \tag{8.20}$$

Thus, equations 8.17, 8.20 and 8.15 allow using the rotor operational profiles (figure 8.4) to create lookup tables for K_{Tj} and K_{Pj} as functions of $|U_j|$. This process was automated to create a unique lookup table for each grid-cell that contained turbines.

The STBT procedure uses the above analytical solutions as an initial guess for the first iteration and, if required, can create regression-based models informed by TADA simulation results (which then would account for wake-interaction, channel blockage and velocity profiles effects) for subsequent iterations.

8.4.1 Verifying SWET Force and Power

The SWET rotor parameterization was verified by comparing its predictions of rotor thrust and power to analogous predictions by TADA, which has been validated to provide accurate wakes and power in [12], justifying its use as a reasonable benchmark.

Six simulations were run, using the same parameters as the SWE simulations in

Part One, but also including a single rotor located at one of the ADP locations. The forcing terms were set using equations 8.17 and 8.20, within the grid cells depicted in figure 8.12. The rotor was in a single cell for ADP 6, split between two cells for ADP 2, 3 and 7, and split between three cells for ADP 4. Note that the depicted rotors (red lines) were set perpendicular to the average of the maximum-yield ebb and flood directions (identified in Part One §7.5.1) to choose which grid-cells would have added forces applied to them. This process was done prior to running simulations, so the selected cells were fixed for the simulation duration. In practise, the rotors may yaw (either passively or actively) to realign with the flow in real-time, yet the present methods assume the rotors are fixed.

The rotor force and power predicted by SWET were bin-averaged to compare to analogous predictions by TADA, depicted in figures 8.13 and 8.14.[9]

Note that the apparent scatter in the force and power predictions by TADA is due to the chosen x-axis, which is the bin-averaged velocity from the corresponding SWET element ($|U_{bj}|$). For a given ($|U_{bj}|$) TADA predicted different speeds at the rotor depending on the bathymetry as the flow approached the rotor from different flow directions.

Observing figures 8.13 and 8.14, it is apparent that SWET correctly split the force and power of each rotor between grid cells according to the percentage of the turbine rotor in each element. Furthermore, the cut-in and cut-out were modelled correctly in both TADA and SWET.

Compared to TADA, SWET tended to under-predict the force and power, mainly from assuming the hub-height velocity equal to the depth average. An obvious future improvement to SWET would be to estimate the hub-height velocity using a typical log profile. Yet, as-is, SWET provided reasonable estimates of rotor force. Thus, equations 8.17 and 8.20 provided reasonable thrust and power predictions in 2D SWET simulations, and predicted the transitions in rotor performance at cut-in and cut-out.

8.4.2 Verifying SWET wake predictions for an isolated rotor

The wake from SWET is compared to that of TADA, (validated in [12]) for the highest yield bin at DG2 in figure 8.15. The figure displays the depth-averaged

[9]Inherently, this comparison assumed that the inclusion of the single rotor in SWET had negligible impact on the boundary conditions supplied to TADA simulations. This assumption was verified by comparing the yield predicted for ADP 2 by SBT vs. STBT, which gave only a 0.6% change.

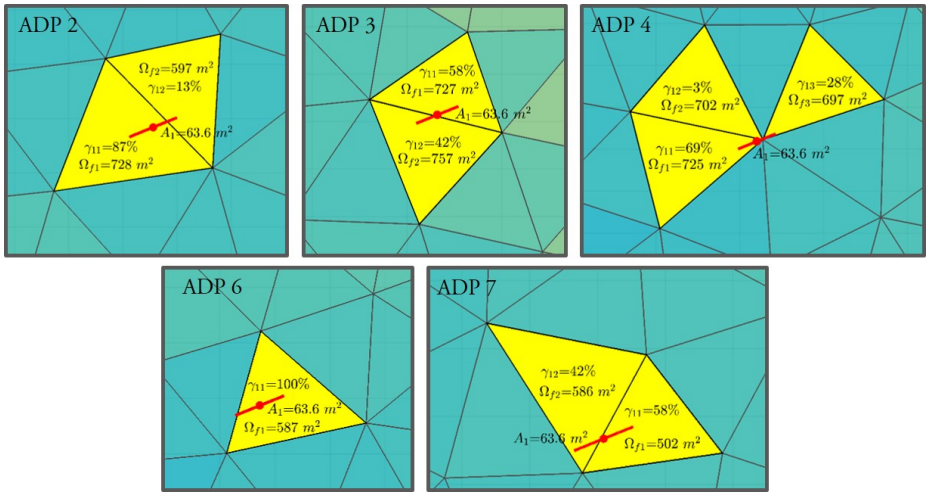

Figure 8.12: Elements allocated to turbines in the SWET simulations. The rotor is depicted by the red line, and SWE elements allocated to rotors are high lighted in yellow.

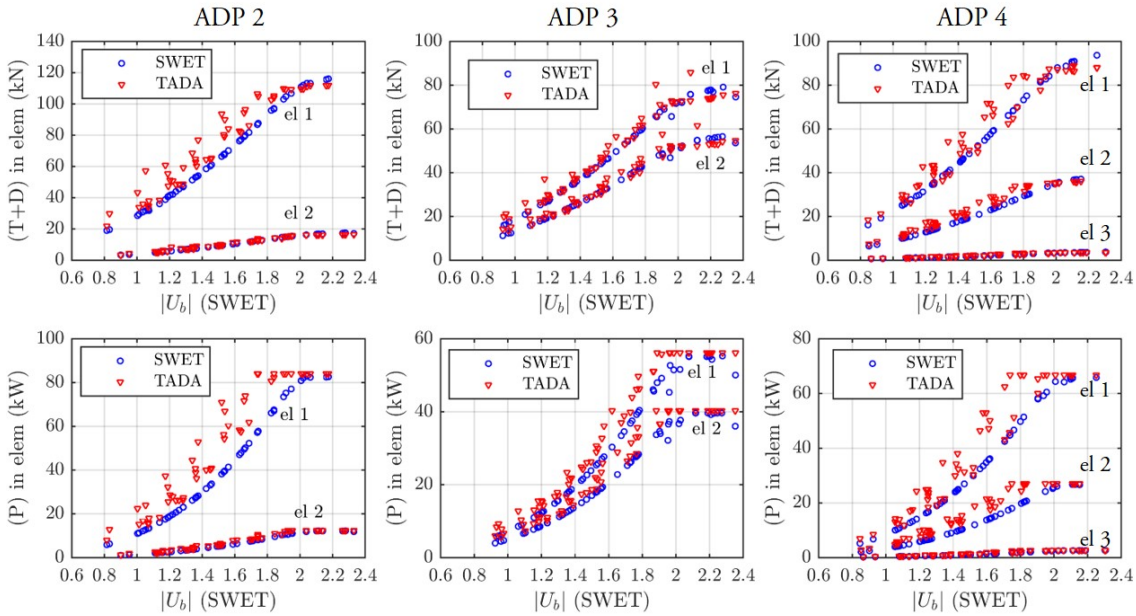

Figure 8.13: Bin-averaged SWET predictions for rotor force and power compared to corresponding results using TADA, for ADP 2, 3 and 4 locations.

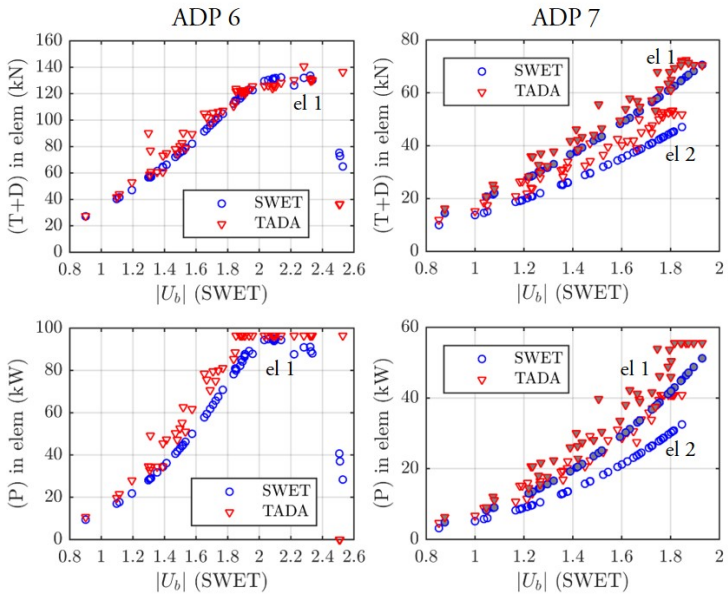

Figure 8.14: Bin-averaged SWET predictions for rotor force and power compared to corresponding results using TADA, for ADP 6 and 7 locations.

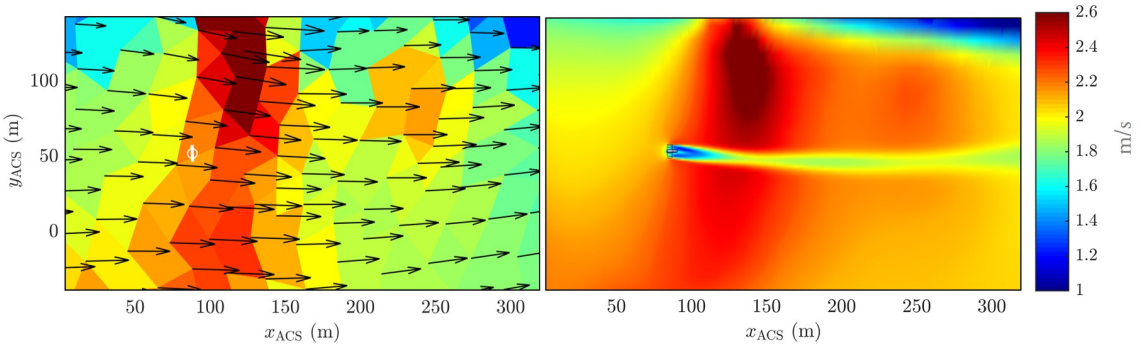

Figure 8.15: Bin-averaged 2D SWET velocity (left) compared to 3D TADA (right), for the highest yield bin at ADP 2. The colour represents the depth-averaged velocity for SWET (left) and the velocity on a horizontal plane cutting through the centre of the rotor for TADA (right). The rotor is depicted as a white line in the left plot, where the tessellations of solid colour depict the grid resolution.

velocity for SWET, whereas it depicts a horizontal slice at hub-height through the 3D velocity field for TADA. The wake was not evident in the SWET simulation, because the rotor force was distributed over a much larger spatial region compared to the actual rotor diameter. Similar trends were found at all ADP locations. Even if the SWET simulations had used a more refined horizontal resolution, the wake would still have been much less pronounced compared to TADA, since the force still would have been applied over elements spanning the entire water column. Observing this effect it is apparent that a 2D model can not be expected to resolve turbine wakes in detail, despite being able to predict isolated individual turbine forces with reasonable accuracy.

8.5 Large Turbine Farms (STBT method)

The analysis to this point has focused on validating various aspects of the SBR, SBT and STBT procedures. Part One of this paper demonstrated that RANS simulations can predict velocity profiles reasonably, and that yield can be calculated accurately using bin-averaged flow states. Part Two has verified that the TADA rotor model provides reasonable yield predictions in the context of SBT for a single rotor. Previous work [12] has also demonstrated that TADA can accurately predict turbine wakes and their impact on other rotors performance. Furthermore, Part Two has shown that SWET (using equation 8.17) provides reasonable turbine forces, which is necessary for predicting far-field effects and boundary conditions passed to TADA. However

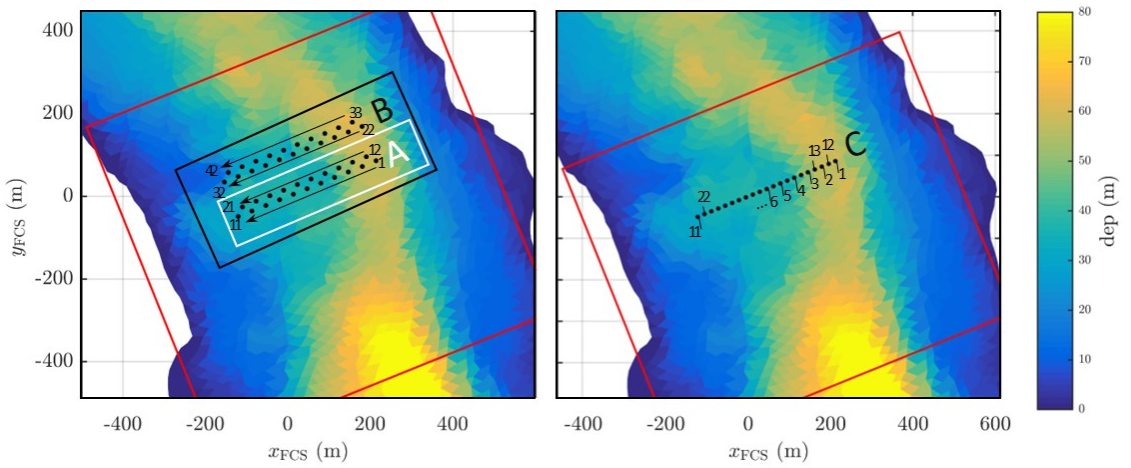

Figure 8.16: Layout of rotors for the farm cases A, B and C. The rotors were numbered 1 through 42 as depicted. Case C has rotors 1-11 in the same positions as case A, but with rotors 12-22 brought in line with rotors 1-11.

SWET does not resolve wakes accurately, which is why 3D TADA simulations are required when wake-interactions may occur, e.g. within a farm. Thus, the proposed yield prediction methods have been validated to the extent possible with the available laboratory and field-data. The component parts of STBT have been validated and/or verified, and therefore the method as a whole can be applied with some confidence.

The next phase of the study was to apply STBT to large-scale turbine farms. Three farms (depicted in figure 8.16) were analysed; case A with a staggered row of 21 rotors, case B with two staggered rows (42 rotors), and case C with a linear row (non-staggered) of 21 rotors.[10] Within each row, the rotors were spaced laterally at 2D intervals (hub-to-hub). For staggered rows, the longitudinal separation was 2D, and for case B, the second staggered row was 10D away from the first. The rows were oriented perpendicular to the heading 158°, which was identified as the flow direction associated with the highest contribution to yield in Part One. The farm layouts were not optimized in any manner, but were selected to be similar to previous studies e.g.[95, 136] suggesting appropriate array layouts.

[10]Due to time constraints, only one iteration of STBT was run, i.e. the SWE rotor forcing terms were specified using equation 8.17, and not updated after the CFD run to capture primary inter-model interaction effects.

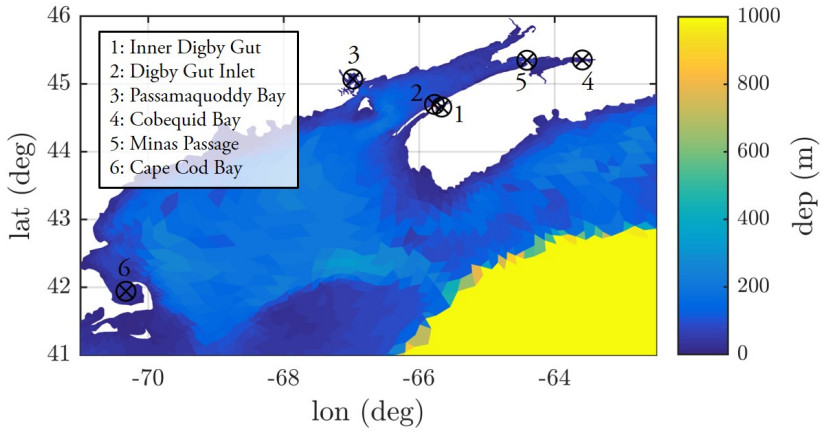

Figure 8.17: Locations used for assessing far-field effects.

Location	case A		case B	
#	Δa (%)	$\Delta\theta$ (deg)	Δa (%)	$\Delta\theta$ (deg)
1	-0.059	0.127	-0.088	0.261
2	0.003	-0.015	-0.007	-0.023
3	-0.005	-0.003	-0.002	0.002
4	-0.001	-0.005	0.003	-0.000
5	-0.004	-0.003	0.001	0.003
6	0.004	-0.004	0.004	0.001

Table 8.4: Impact on tidal amplitude and phase for farm cases A and B. Δa (%) is the percent change to the average tidal amplitude while $\Delta\theta$ (deg) is the change to phase (when modelled using only the dominant M2 component). Results for case C (not shown) were similar to case A.

8.5.1 Far-Field Impact

To assess far-field impacts, the SWET simulations output time-series data at selected locations depicted in figure 8.17. Changes to tidal amplitude and phase were assessed by fitting an M2 component to the elevation time-series, and comparing to the no-rotor case. The results are summarized in table 8.4. The change to the tidal amplitude was only notable within inner Digby Gut, and even with 42 turbines present, the amplitude was only altered by one-tenth of a percent from its natural state (reduced by 3 mm from 3.411 m), while the maximum phase change was 0.267° (32 s time lag). These far-field effects seem unlikely to affect local habitats.

8.5.2 Near-Field Effects

The turbines had more pronounced local effects in proximity to the turbine arrays. Figures 8.18, and 8.19, show the velocity alteration for the highest-yield ebb and flood flow states. The left panels show the velocity field with rotors present, while the right panels show the change compared to the no-rotor case. SWET predicted farm-scale wake behaviour in a depth-averaged sense, namely, the wake of the entire farm, and the increased velocity around its sides. For case A, the change in velocity was on the order of $0.1\,\mathrm{ms}^{-1}$ for case A and $0.2\,\mathrm{ms}^{-1}$ for case B, which were non-negligible compared to typical velocities of about $2\,\mathrm{ms}^{-1}$ in the channel. Case C (not shown) produced similar results to Case A.

Figures 8.18 and 8.19 demonstrate that SWET predicted farm-scale impacts on the flow, at least qualitatively. However, due to its 2D assumption and coarse mesh, it did not predict the wakes of individual turbines well. On the other hand, the 3D

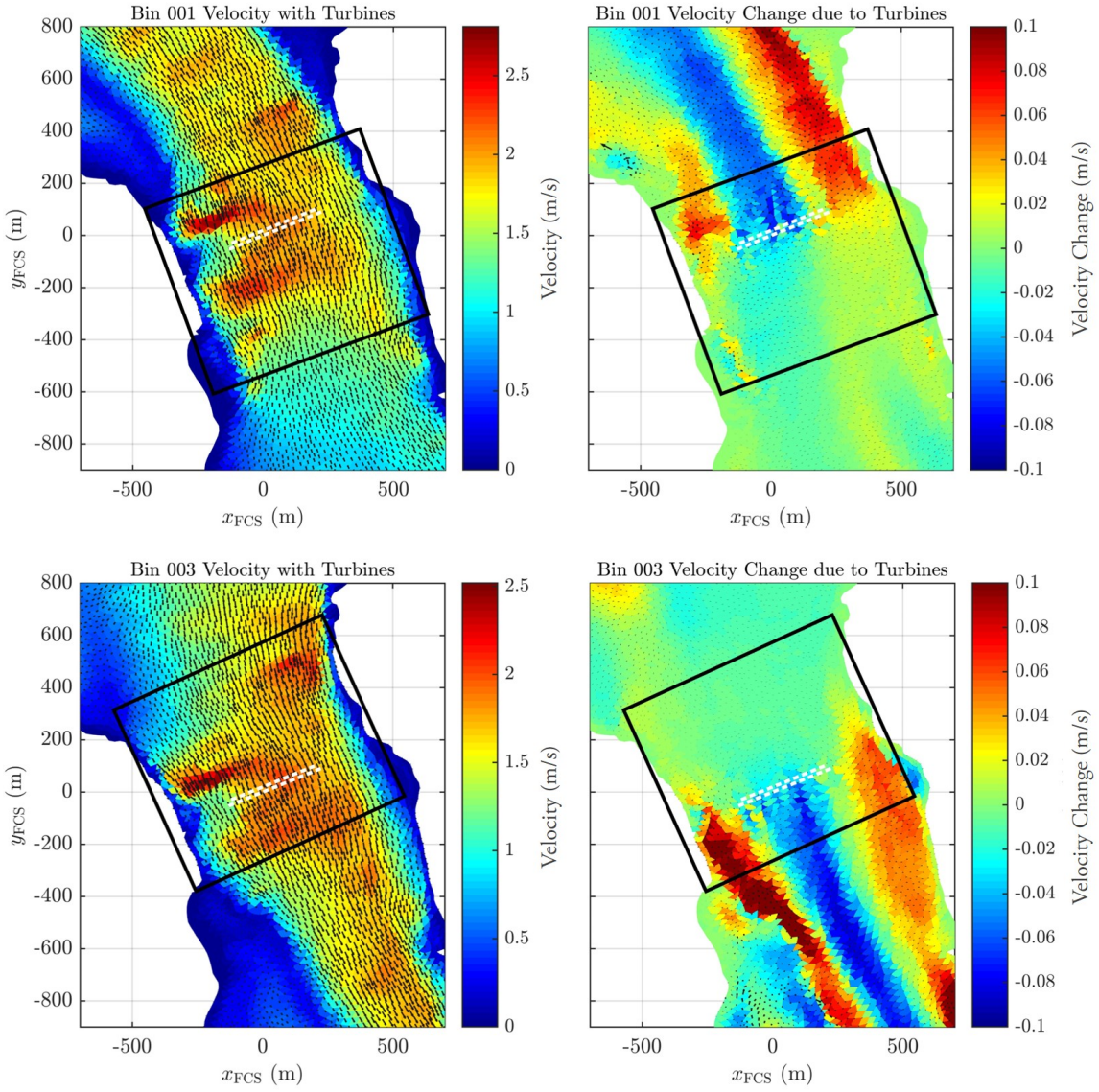

Figure 8.18: Impact of the turbines on the bin-averaged flow for the case A turbine farm. The left image shows the 2D SWET (with turbines) flow through the turbine farm, while the right image shows the change in velocity compared to an SWE simulation with no rotors present. The top images are for a representative ebb-tide state and the bottom are for flood. Turbines are depicted as white lines.

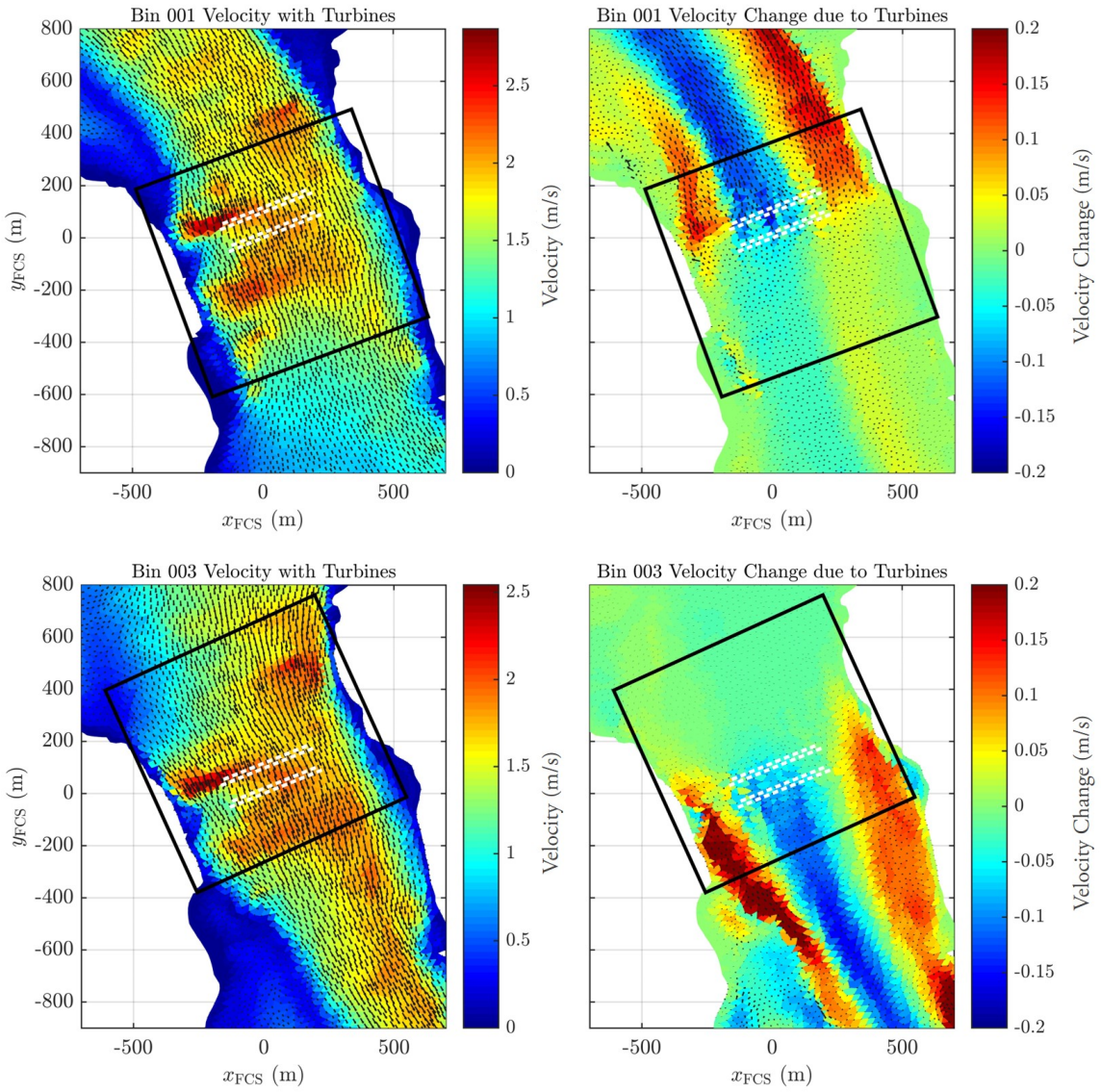

Figure 8.19: Impact of the turbines on the bin-averaged flow for the case B turbine farm. The left image shows the 2D SWET (with turbines) flow through the turbine farm, while the right image shows the change in velocity compared to an SWE simulation with no rotors present. The top images are for a representative ebb-tide state and the bottom are for flood. Turbines are depicted as white lines. Note the different scale compared figure 8.18

TADA simulations resolved each turbine's individual wake. Figures 8.20 and 8.21 highlight the differences in wake prediction between SWET and TADA. Since in SWET velocities are depth-averaged, its wakes have a weaker velocity deficit and less pronounced flow acceleration between wakes.

Further, TADA predicted velocity profiles generated by bathymetry, while of course SWET did not. For case B, this was most important for turbine 32, which was located just south of a ridge. The flow approaching rotor 32 is depicted in figure 8.22. On the flood tide, the flow separated from the seabed downstream of the ridge, creating a sheltered region of low velocity just below the rotor, which was in the faster flow above the separated region.

It is notable that both SWET and TADA resolved the distinctive flow acceleration over the underwater hill located in the upper right corner of figure 8.18 (lower left corner of figure 8.19. Thus both models were able to predict the first-order influence bathymetry on flow velocity, but only the 3D TADA simulations could predict the influence on the vertical profile.

8.5.3 Power and Force

Since SWET could not resolve individual rotor wakes (or velocity profiles) accurately, it also did not predict the rotor power/force as accurately as TADA in the earlier isolated rotor validation exercises. The implications of poorly predicted rotor forces in SWET are a) under/overestimated far field effects and/or b) under/overestimated impact of rotors on the boundary conditions supplied to TADA. Thus, it was important to assess discrepancies between SWET and TADA in the context of the large array cases.

For example, in the staggered configuration, turbines in the downstream row had a slight performance enhancement compared to those upstream. This was caused by flow acceleration between upstream rotors as shown in figures 8.20 and 8.21, which was correctly resolved by TADA but not by SWET. Figure 8.23 demonstrates the impact of this effect on rotor power, for both ebb and flood tides using results from farm A. On the ebb tide, the downstream (higher-numbered) rotors had higher power than their upstream neighbours due to local flow concentration by the upstream rotors in the same manner as a duct. Similarly, with the flow in the opposite direction on the flood tide, the lower-numbered rotors had a higher power due to the same flow concentrating effect. In both cases, TADA showed a distinctive stair step pattern in

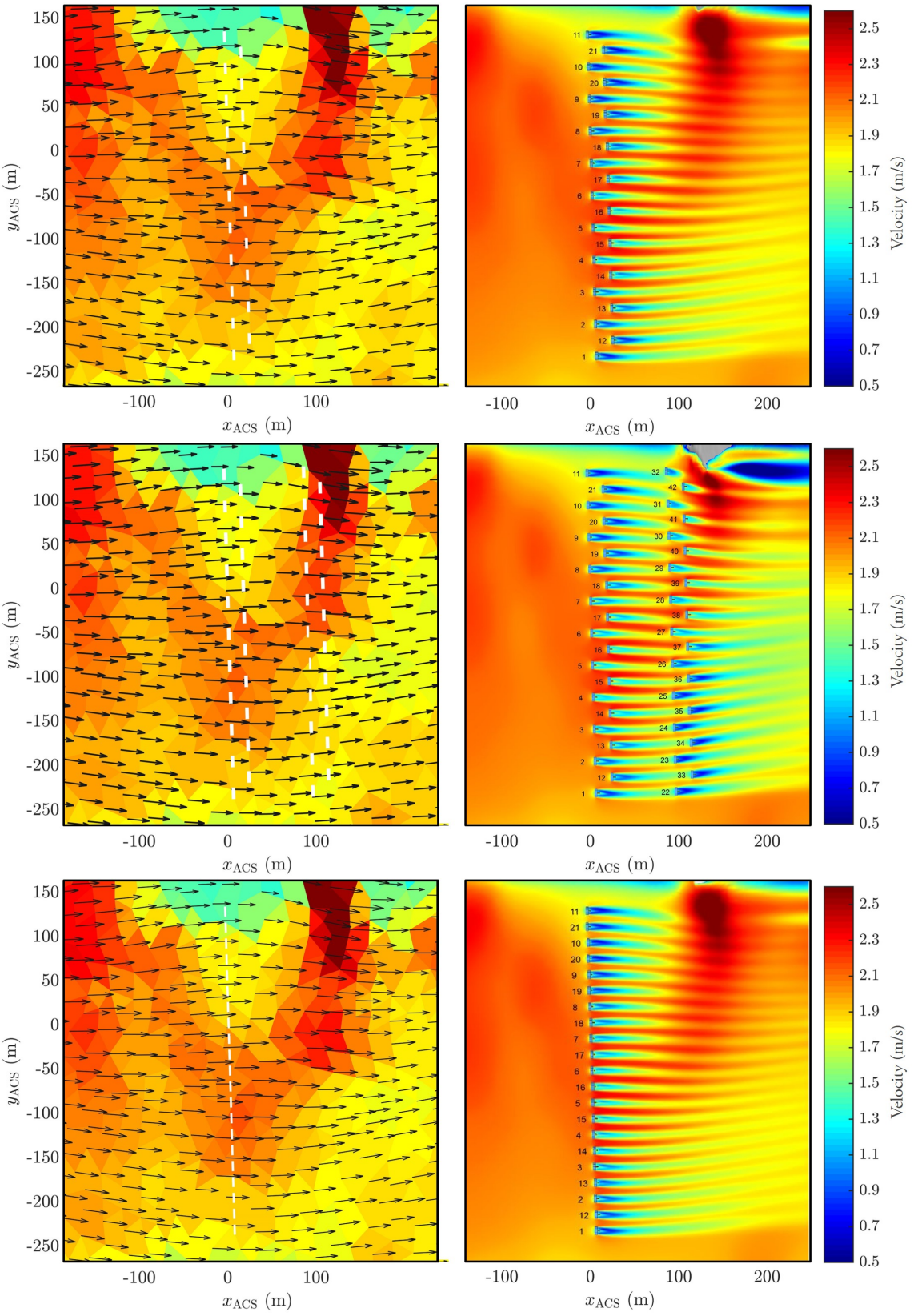

Figure 8.20: Flow fields for turbine farms A (top), B (mid), and C (bottom) corresponding to the highest yield contribution flow bin (an ebb tide). The left images shows the depth-averaged flow predicted by SWET, while the right images show a horizontal slice through the 3D flow field predicted by TADA.

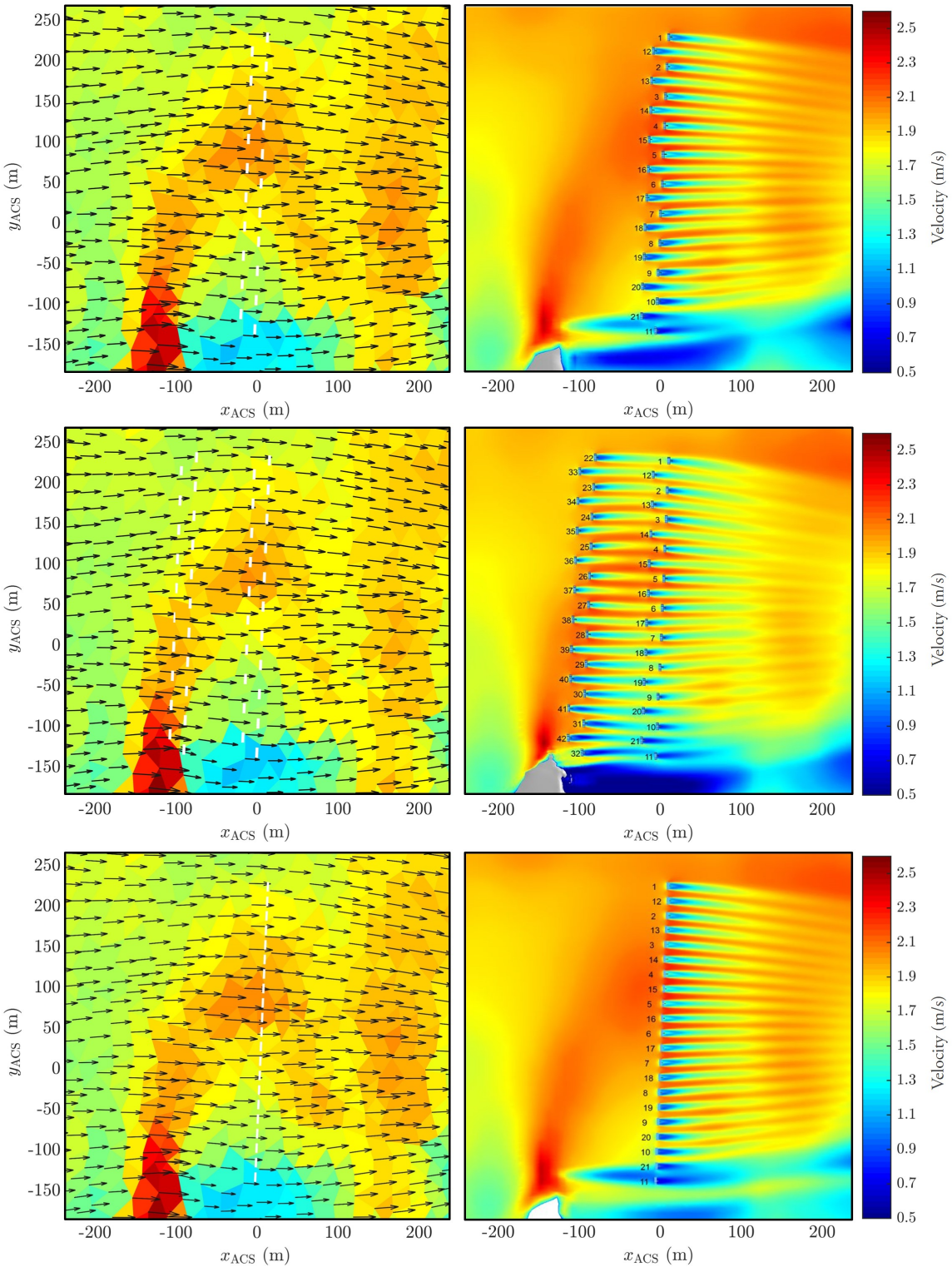

Figure 8.21: Flow fields for turbine farms A (top), B (mid), and C (bottom) corresponding to the third highest yield contribution flow bin (a flood tide). The left image shows the depth-averaged flow predicted by SWET, while the right image shows a horizontal slice through the 3D flow field predicted by TADA.

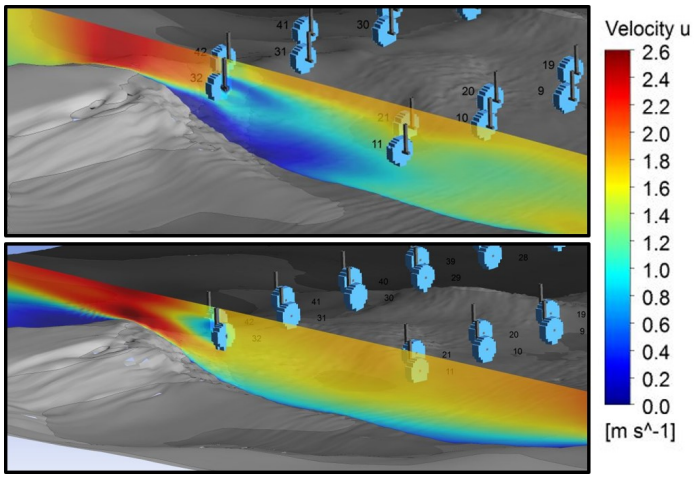

Figure 8.22: Vertical slice of the flow field for the case B turbine farm, with 42 rotors. On the flood tide, the flow approaching rotor 32 is accelerated over a ridge, while on the ebb (bottom) the flow approaching rotor 32 passes over a relatively flat region.

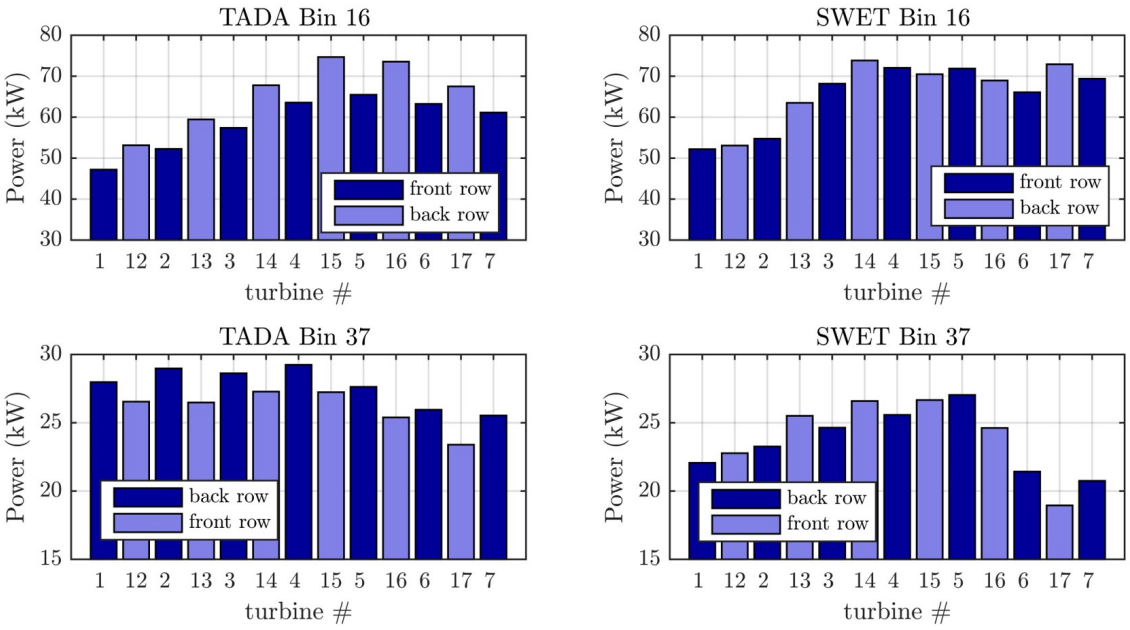

Figure 8.23: Sample rotor power for farm A, from TADA and SWET. The upper plots are for an ebb tide, while the lower plots are for a flood tide. In both cases, the downstream row of turbines have enhanced performance compared to the upstream ones, which is correctly captured by TADA, but not by the 2D SWET model.

rotor power, due to its ability to resolve individual wakes. SWET did not show the distinct stair step, because its wakes were not as pronounced or distinct.

Predictions of thrust and power by SWET and TADA are compared in figure 8.24. In these plots, the x-axis is the bin-averaged velocity predicted by SWET. The data points for SWET represent the bin-averaged force/power. The TADA data points show the force/power predicted by the single steady-state TADA simulation for the corresponding bin-averaged flow state. Therefore, there are 51 data points total, one for each binned flow-state.

For rotor 32 (left plot) TADA predicted much higher power than SWET on the flood tide, when the rotor was in the fast flowing jet downstream of the ridge (see figure 8.22). This was because the 2D SWET simulation could not predict the fast flowing jet. For rotor 24 (middle plot), TADA predicted higher force and power on the flood tides, and lower on the ebb, compared to SWET. Rotor 24 had a small performance enhancement on the flood because it was in the accelerated flow between rotors 34 and 35. On the ebb, rotor 24 was in the wake of rotor 3, so its performance was reduced. Similarly, for rotor 19 (right plot), TADA predicted more thrust/power compared to SWET on the ebb tide when its inflow was accelerated between rotors

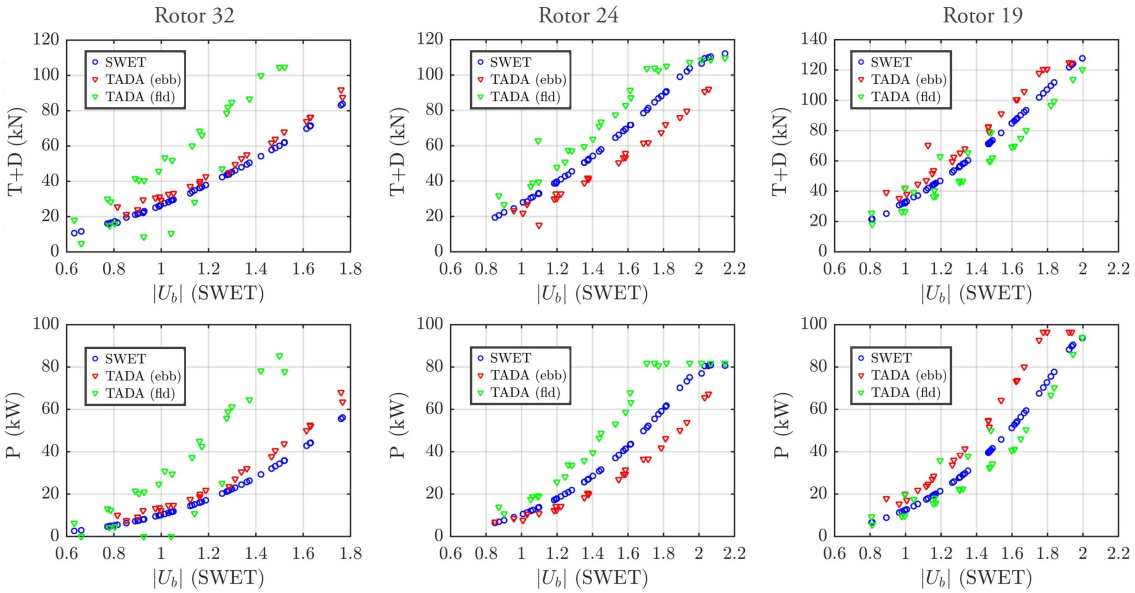

Figure 8.24: Force and power predictions by TADA and SWET, for the case B farm, highlighting ebb-flood asymmetry in wake interaction effects, which are predicted by TADA, but not SWET.

8 and 9, and less thrust/power on the flood, when it was in the wake of rotor 30.

The discrepancies highlight the inherently weaker wake interaction effects predicted by the 2D SWET model, and are likely indicative of coarse-resolution depth-averaged simulations in general.[11]

Despite the glaring discrepancies in select rotors shown in figure 8.24, the total force applied by the farm was predicted reasonably by SWET. The total resistive force is compared to TADA's prediction in figure 8.25. This figure shows that SWET typically underestimated the total farm force by about 10%, which is mainly attributable to using the depth-average velocity without correcting to hub-height. This is an encouraging result since far-field effects would scale with the total resistance of the farm, rather than the exact distribution of forces among individual rotors.

8.5.4 Yield

The yield for each farm was predicted for the entire SWE simulation duration of 1090.7h, by time-series analysis of the SWET power predictions, and by the method of bins for TADA. The results are summarized in table 8.5.

[11]However the SWET model could be re-defined by regression analysis of the TADA simulations to improve its force/power predictions according to the procedures outlined for STBT.

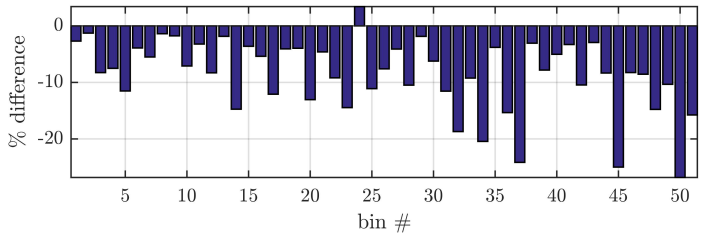

Figure 8.25: Percent difference in total resistive force predicted by SWET vs. TADA for each flow bin.

Case	Total Yield (GWh) time-series bin-analysis		Time-average power per-rotor (kW)		Average capacity factor	
	SWET	TADA	SWET	TADA	SWET	TADA
A	0.749	0.935	32.71	40.83	33.9	42.4
B	1.491	1.720	32.50	37.60	33.7	39.0
C	0.753	0.940	32.71	41.05	33.9	42.6

Table 8.5: Yield predictions for farm cases A, B and C using time-series analysis on the SWET simulation, or the entire STBT method (labelled TADA).

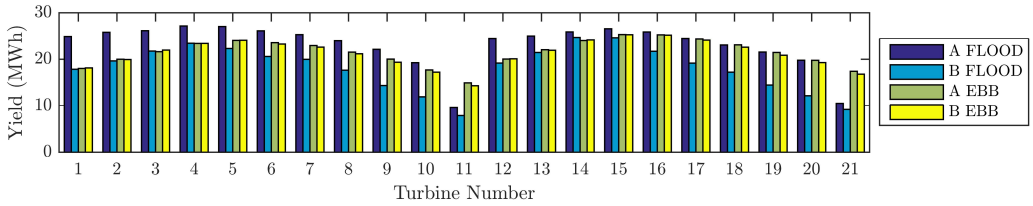

Figure 8.26: Yield (STBT) for turbines 1-21 for cases A and B, categorized by flood and ebb flow directions.

The impact of doubling the number of rotors in the farm (adding rotors 22-42 in case B) was to increase energy production by a factor of 1.99 (SWET) or 1.84 (TADA). TADA predicted a diminishing return, which was expected because of wake interaction effects between the two staggered rows, while SWET did not predict a diminishing return. The wake interaction effect on yield is depicted in figure 8.26, where rotors 1-21 produced significantly less energy on the flood tide for case B than for case A. This was simply because they were in the wakes of rotors 22-42 on the flood. The difference was much smaller for rotors 1-21 on the ebb tide, since they were upstream of rotors 22-42, but there was still a small difference, due to more flow being re-directed around the entire farm for case B.

The impact of aligning the rotors in a non-staggered row (case C) was to increase yield by about 0.5% compared to case A (similar prediction by TADA and SWET). This trend agrees with analytical models (e.g. [106, 149]) showing that the optimal layout for hydrodynamic performance is a single line of closely-spaced rotors. It also agrees with Hunter et al. [136] who showed that non-staggered arrays have better performance than staggered arrays, using idealized actuator disk turbine models in 3D RANS simulations. Physically, this effect can be seen in figures 8.20-8.21 where the rotor-local speed-up is higher for the non-staggered array.

8.5.5 Computational Expense

The bulk of the computational expense for the large farm simulations was associated with the 3D TADA simulations. The computational expense was benchmarked using 4 cores on a Intel®i7-6700HQ CPU (2.60GHz) on a personal laptop, running simulations for 300 iterations to ensure convergence. (Although many of the simulations were run on the SHARCNET HPC cluster. SHARCNET (`www.sharcnet.ca`) is a consortium of 18 colleges, universities and research institutes operating a network of high-performance computer clusters across south western, central and northern

Ontario

For case A, the TADA mesh contained 2.9M elements, and the average time required per iteration was 57 seconds. For the 51 bins, the total run-time was approximately 970 cpu-hours. For case B, the TADA mesh contained 4.2M elements, and the total run-time was about 1600 cpu-hours. For case C, the TADA mesh contained 2.6M elements, and the total run-time was about 900 cpu-hours. These compute times are tractable even on 4-core PC, yet for practical applications, a small cluster would provide reasonable computing times. For example, a 32-core cluster could compute all of the TADA simulations for case B within 2-days.

While computing yield required running TADA for all 51 binned flow states, farm layout optimization could likely use a smaller subset of bins, perhaps only two corresponding to the highest-yield ebb and flood flow states. Optimization could then be tractable either for manual modifications and parametric studies or numerical procedures.

There are many measures possible to reduce the total computational cost. For example, in the present study the bin-domain was truncated at 95% yield contribution, requiring 51 flow states to be simulated. At the end of the analysis a 5% correction factor was applied to account for flow states not included in the bin-domain. Reducing the threshold to 90% would have required only 39 flow states, providing a 23% computation reduction. Another measure would be to reduce the resolution in the binning procedure, which used 10° for flow direction, $0.2\,\mathrm{ms}^{-1}$ for speed and 2 m for surface elevation. Future studies assessing the sensitivity to different binning resolution can find an optimal balance between accuracy and computational cost for particular design study and practical farm design applications.

8.6 Discussion and Conclusions

This two part paper has proposed comprehensive methods for yield/impact assessment using a novel hybrid time-domain SWE / bin-domain RANS based modelling approach. The methods incorporate a novel forcing terms to emulate turbines. For the 2D SWE simulations, rotors are treated as sub-grid-scale objects using a formulation that reflects their operational profiles from cut-in to cut-out, and allows for multiple rotors and or partial rotors in each grid cell. For the 3D simulations, rotors are treated using TADA, which resolves rotors by a grid resolution of 9 elements per diameter, and has been validated [12] to provide accurate turbine wakes and power.

Four levels of turbine farm scenarios were defined, ranging from a single turbine deployed at the same location as measured ADP field data, to large turbine farms with many interacting wakes which alter basin-scale dynamics. Procedures were defined for each scenario, and have been validated to the extent possible with available field data. Each method was a logical progression from the previous one, allowing for a progressive validation of the key modelling techniques.

Part One of this paper demonstrated that RANS simulations predict reasonable velocity profiles, and that the flow-state binning approach provided accurate yield predictions.

Part Two verified TADA's ability to predict yield for a single rotor (SBT), and verified that the sub-grid SWET formulation (using equation 8.17), provided reasonable estimates of forces applied by entire turbine farms ($\approx\pm 25\%$), as required for predicting the far-field effects and boundary conditions passed to TADA. This could be improved simply by incorporating a log law profile to estimate hub-height velocity from the depth-average.

As expected, SWET gave imperfect predictions of individual turbine wakes and its predictions of power and forces applied by individual turbines were not completely reliable. Thus, the high resolution 3D TADA simulations are required to obtain reliable yield predictions when wake effects are important. For example, SWET predicted twice as much yield for case B compared to case A whereas TADA predicted an increase of only 1.84, with the difference being due to TADA's ability to resolve rotor wakes.

The methods proposed herein are a logical progression from past work in the field of numerical modelling of turbine farms. While previous studies have focused on using either 2D coastal simulations for impact assessment, or on 3D RANS simulations for assessing farm layout with wake interaction, the present hybrid approach leverages the advantages of each simulation type in a unified framework. Thus, the proposed methods allow for high-fidelity yield and impact assessment, which are critical to inform economic and regulatory decision-making for proposed tidal farms.

Acknowledgments

The authors thank the National Sciences and Engineering Research Council (NSERC) of Canada and the University of Victoria for financial support. We are grateful for the collaborative efforts of Dr. Richard Karsten and his research group at Acadia

University; particularly Mitchell OFlaherty-Sproul who did extensive work improving the FVCOM model grid. We also thank the Offshore Energy Research Association (OERA) of Nova Scotia, and Dr. Alex Hay and Justine McMillan from Dalhousie University for sharing crucial bathymetry and ADP data. Finally we also thank Compute Canada for providing access to the ACENET and SHARCNET HPC clusters used for the SWE and TADA simulations, respectively.

Chapter 9

Conclusions and Future Work

This chapter completes the dissertation by summarizing major conclusions, evaluating whether the thesis goals were achieved and discussing avenues for future work.

9.1 Conclusions

The principal objective of this work was to develop a simulation-based methodology for modelling flows through tidal turbine farms, including turbine wakes, and to be able to predict each rotor's performance and yield. The intended applications are predicting yield, performing turbine layout case-studies, and assessing the impact of turbine farms on tidal flows. The methods could also potentially be incorporated into an automated tidal farm layout optimization routine.

The methods are presented in this thesis in three sub-categories; 3D RANS methods (chapters 2, 4, 5 and 6); 2D SWE methods (chapters: 3, 7 and 8) and coupling methods (3, 7 and 8). The thesis is presented as a collection of seven papers which have been published in conference proceedings, peer-reviewed journals, or have been submitted to peer-reviewed journals. The major accomplishments and contributions are summarized in figure 9.1 and the remainder of this section summarizes the conclusions.

9.1.1 3D RANS methods

3D RANS simulations were used to model individual turbine wakes and performance. The simulations did not resolve turbine blades explicitly, rather emulating them by applying forcing terms to the governing flow equations. Initially, actuator line type

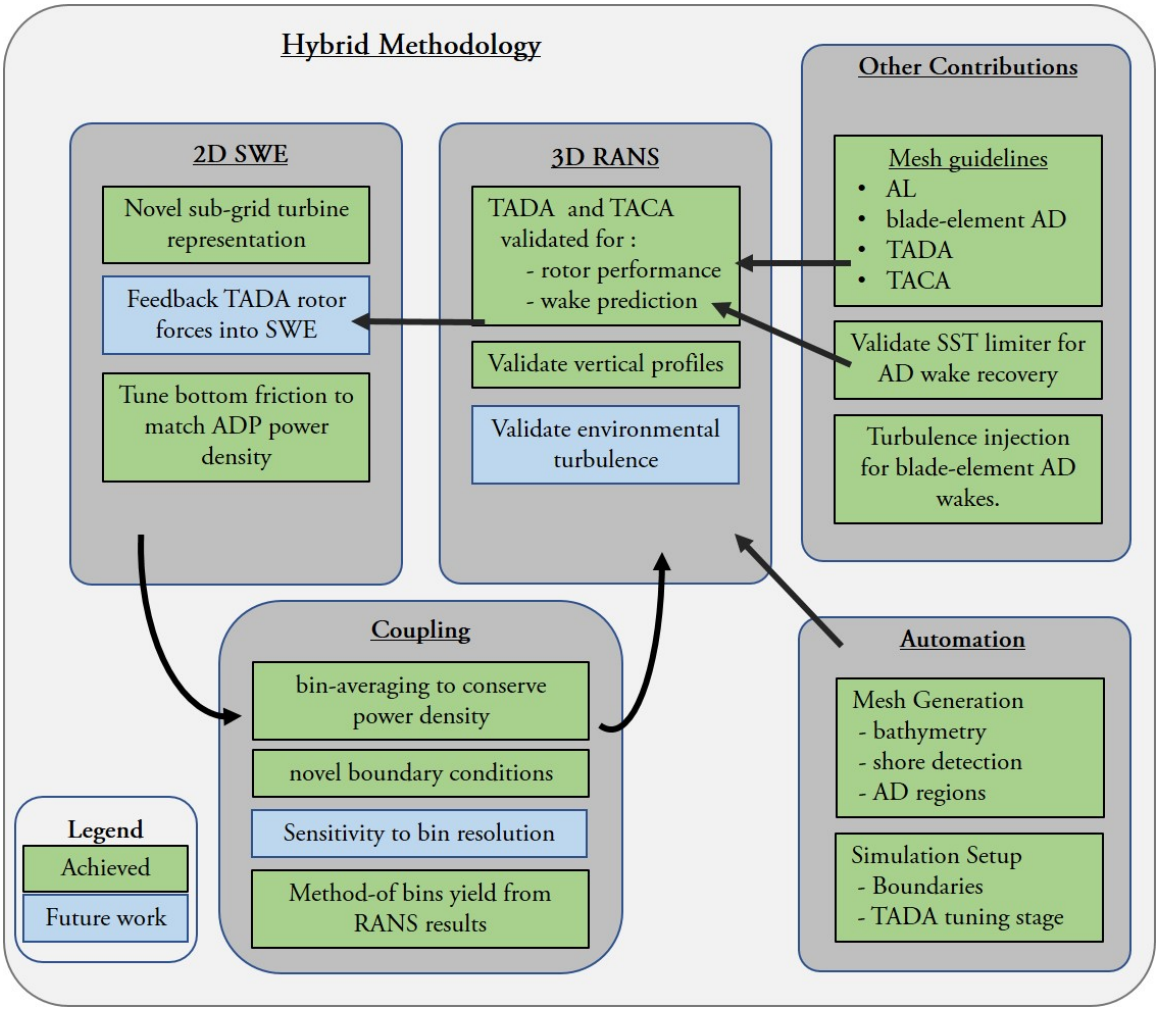

Figure 9.1: Summary of contributions, accomplishments and future work, within the hybrid methodology framework.

were considered, but were found to be too computationally costly for simulations with many rotors (Chapter 2). We also studied blade-element based actuator-disk simulations, which time-average the blade forces and apply them over the entire rotor swept area (Chapter 4). We found that wake prediction was significantly improved by using the SST eddy viscosity limiter (compared to standard k-ε or k-ω models) in chapter 4.

Finally, we established a novel actuator-disk method which uses tabulated rotor performance (called TADA), rather than blade section coefficients, to set the turbine loads (chapter 5). This alleviated mesh requirements significantly compared to blade-element based approaches, and allowed fast simulations of turbine farms with many rotors. TADA can be tuned to either experimental or higher-resolution CFD data, so that overall fidelity is maintained with significant computational cost reduction. In chapter 6, the TADA method was adapted to cross-flow type turbines. We found that using the rotor-local velocity to calculate performance, rather than the traditionally used free-stream velocity, allowed simulations to react correctly to power changes due to: reduced inflow velocity in turbine wakes, and funnelling effects in narrow channels, or between upstream turbines, as verified in chapters 5 and 6. Finally, in chapter 7) we also verified that 3D RANS simulations were able to predict vertical velocity profiles in a tidal channel with reasonable accuracy.

9.1.2 2D SWE

Depth-averaged 2D simulations were enhanced by deriving a novel sub-grid-scale turbine treatment, which correctly models turbine performance over its operational range. The treatment allows for multiple rotors and/or portions of rotors within each grid cell, and is not specific to the element shape. We have verified the sub-grid treatment by comparing to higher resolution TADA simulations in chapter 8.

It is standard practise to modify the bottom-friction in SWE simulations to reduce the RMS error in velocity compared to measured ADP data. In chapter 7, we introduced using the flow power density (u^3) rather than the velocity, which gave better agreement in predicting yield.

9.1.3 Coupling Method

A direct coupling of 3D RANS simulations with coastal SWE simulations would not be computationally tractable for long durations. Thus, we introduced a novel coupling

method that bin-averages (conserving flow power density) the spatial flow fields predicted by the time-domain SWE simulations, then runs high-resolution 3D TADA (or TACA) simulations for each bin (chapters 7 and 8). This allows SWE simulations to predict the temporal flow variation for sufficient duration to obtain converged future-predictions, while also allowing wake interaction effects to be predicted with sufficient resolution by the 3D simulations. This coupling required mapping the bin-averaged 2D flow field onto the 3D TADA domain boundaries, which was done assuming a neutrally-stratified log profile (chapter 7).

9.2 Yield Methodology Goals

The hybrid methodology combining: a) 2D SWE simulations including the sub-grid turbine model, b) the novel power-conserving bin-averaging method, and c) TADA/TACA simulations, is a novel approach to tidal farm yield prediction. The overall methodology meets the requirements set out in the introduction, as summarized below:

Far-Field Effects are captured by the SWE model, which applies accurate sub-grid forcing terms to the flow, increasing the resistance to flow. The forcing terms match actual turbine performance, an improvement over previous methods applying, for example, constant thrust coefficients.

Bathymetry is accounted for by the SWE model, where the depth-averaged flow reacts to changing bathymetry according to conservation of mass. Bathymetry is accounted for in more detail in TADA/TACA simulations which predict the influence of variable bathymetry on vertical velocity profiles, allowing a more accurate prediction of rotor-performance at a certain height in the water-column.

Water Depth is predicted by the SWE simulations, and then used to set the water surface height in the TADA/TACA simulations. This treatment alters the total flow cross-sectional area in TADA/TACA simulations, which modifies the blockage ratio which affects the rotor performance. SWE simulations are known to provide accurate water elevations, and chapters 5 and 6 demonstrated that TADA/TACA simulations respond correctly to blockage ratio.

Turbine Interactions include reduced power in wake-shadow, increased power in funnelled flow between upstream rotors, and altering the blockage ratio. These effects are modelled correctly by the TADA/TACA simulations, as verified in chapters 5, 6 and demonstrated for large arrays in chapter 8.

Turbulence affects the rate of wake mixing and thus directly impacts turbine performance when in wake shadow. TADA was verified to predict this influence in flows with turbulence intensity of 3% and 15% in chapter 5. Turbulence also interacts directly with blade boundary layers and affects rotor performance even without wake interaction effects. Such sensitivities were included in the TADA simulations in chapter 5.

Sheared inflow influences rotor power but as shown by [116] normalizing power by the area-average of the cubed velocity over the rotor's swept area collapses power curves from differing shear profiles. Since TADA and TACA calculate the rotor performance based-on the area-average cubed velocity, they should inherently account for sheared inflow. However this assertion remains to be validated in detail.

Temporal variation in tidal flows presented a significant challenge to developing a robust yield-prediction methodology. Many of the above requirements pushed the methodology toward high-resolution RANS simulations, yet accurate characterization of tidal flow temporal variation requires time-series on the order of 3 months. Simulations of such long duration would not be feasible on numerical grids appropriate for modelling wake interaction effects, which led to the presented hybrid approach which uses the method of bins to separate the spatial and temporal aspects of the problem. Thus, temporal variation is explicitly modelled by the SWET simulations, and treated by the method of bins when running TADA/TACA simulations to predict yield.

9.3 Future Work

This section identifies several avenues for future research and further development.

9.3.1 Sensitivity Analysis

There are several model sensitivities that while pertinent could not be addressed in the thesis work due to time limitations. Flows were binned according to water direction (10° increments), speed (0.2 m/s increments), and water elevation (2 m increments). Widening the bins may provide significant computational savings, which can be assessed based on the sensitivity of yield to the employed bin ranges. Also, the sensitivity of AEP (annual yield) to the SWE simulation duration should also be established in greater detail.

If the TADA simulations are to be used to optimize the layout of a certain number of turbines using e.g. an adjoint method (like that of [138]), it would be advantageous to employ a reduced set of flow bins rather than the entire set. A reasonable approach would be to perform an initial optimization using only the highest-yield flood and ebb bins, and observe how the optimal farm layout changes with the addition of further flow bins in a multi-stage optimization process.

9.3.2 Turbulence

The SWE simulations employ a Smagorinski turbulence model for horizontal motions, which applies a spatial filter to directly resolve scales larger than the grid, and to model sub-grid scales. It is unclear how to pass this turbulence through the bin-averaging process to create boundary conditions for turbulence to the TADA/TACA simulations, or indeed whether the SWE-predicted turbulence is even realistic compared to field data. In this thesis, the TADA turbine farm simulations in chapter 8 set turbulence conditions on the model boundaries based on a neutrally-stratified log profile, which likely under-predicted actual turbulence, because it would not include large-scale horizontal eddy motions. Modelling turbulence accurately in the TADA simulations is important because of its strong influence on wake recovery. More work is needed to obtain accurate measurements of turbulence at potential tidal energy sites, and to improve methods to specify turbulence in RANS simulations.

Furthermore, specifying high turbulence at the RANS simulation boundaries may not be sufficient in itself, as the turbulence may decay too quickly. This may occur because the RANS simulations inherently neglect certain turbulence-producing terms, such as buoyancy effects and free-surface waves. While such physics could be included in simulations, there is an associated trade-off in computational expense. A pragmatic compromise may be to set turbulence source terms such as those mentioned in 6.3.3 to raise the turbulence in the simulations to as-measured levels from field data. The practical value of such an approach is that the simulations could easily be tuned to match field data which presumably would be available for any tidal energy site under serious consideration, without the need to use more advanced turbulence models, to resolve free surface waves and/or to transition to much more costly LES simulation.

9.3.3 Vertical Profiles

While the RANS simulations in chapter 7 predicted velocity profiles more accurately compared to a standard log profile, there were significant differences compared to the ADP measured velocity profiles. In particular, the measured trend of reducing velocity approaching the water surface was not modelled by the RANS simulations. Future work should focus on refining numerical simulation methods to reproduce 3D velocity fields in tidal channels with good fidelity. This is a relatively new field of research, due to high quality ADP data from tidal channels becoming available only recently.

9.3.4 Turbine Motion

The present implementation fixes both the position and orientation of turbines, a significant limitation for farms consisting of moored buoyant turbines. It would be interesting to incorporate a method to predict the equilibrium position of each turbine in the array, for each of the bin-averaged TADA simulations. Transient platform motion due to waves and/or changing tides would be a further challenge to incorporate into the simulations as an unsteady effect.

9.3.5 Sub-grid turbine force updates

Presently, the STBT method in chapter 8 has only been implemented to run the first iteration in the STBT procedure. That is, the sub-grid turbine model is implemented to apply the analytical-based methodology, but does not update the forcing based on the TADA simulation results. In chapter 8, the update was not done because the total applied force in the SWE simulations was in reasonable agreement with the TADA simulations. For farms with stronger wake interaction effects, the update step may be more important. Future work should establish precise guidelines for updating the sub-grid terms.

9.3.6 Open Source

The automation code has all been written using Matlab and the 3D TADA/TACA methods use the commercial code ANSYS CFX. For future research, it may be beneficial to translate the code into open source languages, such as Python and OpenFoam, so that a wider user community can adopt and extend the methods.

Bibliography

[1] IPCC, "Climate change 2014: Synthesis report," tech. rep., International Panel on Climate Change, 2014.

[2] IEC, "Marine energy - wave, tidal and other water current converters - part 201: Tidal energy resource assessment and characterization," Tech. Rep. IEC TS 62600-201, International Electrotechnical Commission, 2015.

[3] R. Murray, R. Maclver, N. Reddy, V. Venugopal, S. Baston, S. Waldman, J. Side, I. Fairley, H. Karunarathna, A. Sabatino, R. Clement, M. Heath, D. McKee, and N. Serpetti, "A toolbox of methods to better understand and asses the effects of tidal and wave energy arrays on the marine environment," tech. rep., TeraWatt Consortium, 2015.

[4] S. Livermore, "Wave and tidal energy yield uncertainty," Reference Document PN000083-SRT-005, Frazer-Nash Consultancy, April 2015.

[5] T. Kutney, R. Karsten, and B. Polagye, "Priorities for reducing tidal energy resource uncertainty," in *European Wave and Tidal Energy Conference Series*, 2013.

[6] N. Adams, D. Ranford, and D. Livingston, "Modelling and optimisation of tidal arrays," in *European Wave and Tidal Energy Conference Series*, 2011.

[7] M. Thomson, J. Whelan, and L. Gill, "The development of a tool for the design and optimization of tidal stream turbine arrays," in *European Wave and Tidal Energy Conference Series*, 2011.

[8] R. H. Karsten, J. M. McMillan, M. J. Lickley, and R. D. Haynes, "Assessment of tidal current energy in the minas passage, bay of fundy," *Proc. IMechE Vol. 222 Part A: J. Power and Energy*, vol. 222, pp. 493–507, 2008.

[9] M. Shives and C. Crawford, "Mesh and load distribution requirements for actuator line cfd simulations," *Wind Energy*, vol. 16, pp. 1183–1196, 2013.

[10] M. Shives, C. Crawford, C. Hiles, and R. Walters, "Combining numerical methods for basin and turbine scales for improved modelling of in-situ turbine arrays," in *Proceedings of the 10th European Wave and Tidal Energy Conference*, (Aalborg, Denmark), September 2013.

[11] M. Shives and C. Crawford, "Adapted two-equation turbulence closures for actuator disk RANS simulations of wind & tidal turbine wakes," *Renewable Energy*, vol. 92, pp. 273–292, 2016.

[12] M. Shives and C. Crawford, "Tuned actuator disk approach for predicting tidal turbine performance with wake interaction," *International Journal of Marine Energy*, vol. 17, pp. 1–20, April 2017.

[13] M. Shives, C. Crawford, and S. Grovue, "A tuned actuator cylinder approach for predicting cross-flow turbine performance with wake interaction and channel blockage effects," *International Journal of Marine Energy*, 2017.

[14] M. Shives, "Actuator cylinder model for instream g3 rotor: Model development, validation, and array studies," tech. rep., Instream Energy Systems Ltd., 2016.

[15] M. Shives and C. Crawford, "Computational methods for tidal turbine farm energy yield, part one: Methods and initial validation," *Submitted for review to the International Journal of Marine Energy*, 2017.

[16] M. Shives and C. Crawford, "Computational methods for tidal farm energy yield part two: Rotor models and large farms," *Submitted for review to the International Journal of Marine Energy*, 2017.

[17] L. A. Martínez-Tossas, M. J. Churchfield, and C. Meneveau, "Optimal smoothing length scale for actuator line models of wind turbine blades based on Gaussian body force distribution," *Wind Energy*, pp. n/a–n/a, Jan. 2017. `http://onlinelibrary.wiley.com/doi/10.1002/we.2081/abstract`.

[18] J. N. Sørensen and W. Z. Shen, "Numerical modeling of wind turbine wakes," *Journal of Fluids Engineering*, vol. 124, pp. 393–399, 2002.

[19] R. Mikkelsen, *Actuator Disc Methods Applied to Wind Turbines*. PhD thesis, University of Denmark, 2003.

[20] S. Ivanell, J. N. Sørensen, R. Mikkelsen, and D. Henningson, "Analysis of numerically generated wake structures," *Wind Energy*, vol. 12, pp. 63–80, 2009.

[21] W. Z. Shen, J. H. Zhang, and J. N. Sørensen, "The actuator surface model: A new navierstokes based model for rotor computations," *Journal of Solar Energy Engineering*, vol. 131, pp. 011002–1 to 011002–9, 2009.

[22] C. Sibuet Watters, S. Breton, and C. Masson, "Application of the actuator surface concept to wind turbine rotor aerodynamics," *Wind Energy*, vol. 13, pp. 433–447, 2010.

[23] N. Troldborg, J. N. Sørensen, and R. Mikkelsen, "Numerical simulations of wake characteristics of a wind turbine in uniform inflow," *Wind Energy*, vol. 13, pp. 86–99, 2009.

[24] N. Troldborg, G. C. Larsen, H. A. Madsen, K. S. Hansen, J. N. Sørensen, and R. Mikkelsen, "Numerical simulations of wake interaction between two wind turbines at various inflow conditions," *Wind Energy*, vol. 14, pp. 859–876, 2011.

[25] ANSYS, "Ansys cfd, release 12.0," tech. rep., 2009. CFX software documentation.

[26] G. Corten, "Heat generation by a wind turbine," in *IEA symposium on the aerodynamics of wind turbines*, vol. 14, NREL, Dec 4-5 2000.

[27] H. Versteeg and W. Malalasekera, *An Introduction to Computational Fluid Dynamics: The Finite Vloume Method*. Pearson Education Limited, 2 ed., 2007. ISBN: 978-0-13-127498-3.

[28] F. R. Menter, "Two-equation eddy-viscosity turbulence models for engineering applications," *AIAA Journal*, vol. 32, pp. 1598–1605, 1994.

[29] F. Menter, "A comparison of some recent eddy viscosity turbulence models," *Journal of Fluids Engineering*, vol. 118, pp. 514–519, 1996.

[30] J. Bardina, P. Huang, and T. Coakley, "Turbulence modeling validation testing and development," Technical Memorandun 110446, NASA, April 1997.

[31] M. I. Yaras and A. D. Grosvenor, "Evaluation of one- and two-equation low-re turbulence models. part iaxisymmetric separating and swirling flows," *International Journal For Numerical Methods In Fluids*, vol. 42, pp. 1293–1319, 2003.

[32] F. R. Menter, "Review of the shear-stress transport turbulence model experience from an industrial perspective," *International Journal of Computational Fluid Dynamics*, vol. 23, no. 4, pp. 305–316, 2009.

[33] J.-J. Chattot, "Helicoidal vortex model for steady and unsteady flows," *Computers & Fluids*, vol. 35, pp. 733–741, 2006.

[34] W. Johnson, *Helicopter Theory*. Dover Publications Inc., 1994. ISBN 1-486-68230-7.

[35] J. D. Anderson, *Fundamentals of Aerodynamics*. McGraw Hill, 2 ed., 1991.

[36] J. G. Leishman, *Principles of Helicopter Aerodynamics*. Cambridge Aerospace Series, 2 ed., 2006. ISBN-10 0-521-85860-7.

[37] R. Walters and V. Casulli, "A robust, finite element model for hydrostatic surface water flows," *Communications in Numerical Methods in Engineering*, vol. 14, pp. 931–940, 1998.

[38] R. Walters, "Design considerations for a finite element coastal ocean model," *Ocean Modelling*, vol. 15, pp. 90–100, 2006.

[39] R. Walters and D. Plew, "Numerical modeling of environmental flows using dam: Some preliminary results," *Acta Geophysica*, vol. 56, pp. 918–934, 2008.

[40] R. Walters, E. Hanert, J. Pietrzak, and D. Le Roux, "Comparison of unstructured, staggered grid methods for the shallow water equations," *Ocean Modelling*, vol. 28, pp. 106–117, 2009.

[41] M. Shives, "Hydrodynamic modeling, optimization and performance assessment for ducted and non-ducted tidal turbines," Master's thesis, University of Victoria, 2011.

[42] I. Celik, U. Ghia, P. Roache, C. Freitas, H. Coleman, and P. Raad, "Procedure for estimation and reporting of uncertainty due to discretization in cfd applications," *Journal of Fluids Engineering*, vol. 130, 2008.

[43] T. Xing and F. Stern, "Closure to discussion of factors of safety for richardson extrapolation (2011, asme j. fluids eng., 133, p. 115501)," *Journal of Fluids Engineering*, vol. 133, pp. 1–6, 2011.

[44] P. V. Sucsy, B. R. Pearce, and V. G. Panchang, "Comparison of two- and three-dimensional model simulation of the effect of a tidal barrier on the gulf of maine tides," *Journal of Physical Oceanography*, vol. 130, pp. 114–118, 1993.

[45] D. R. Parrott, B. J. Todd, J. Shaw, J. E. H. Clarke, J. Griffin, B. MacGowan, M. Lamplugh, and T. Webster, "Integration of multibeam bathymetry and lidar surveys of the bay of fundy, canada," in *Proceedings of the Canadian Hydrographic Conference and National Surveyors Conference*, 2008.

[46] M. O. L. Hansen, J. N. Sørensen, S. Voutsinas, N. Sørensen, and H. A. Madsen, "State of the art in wind turbine aerodynamics and aeroelasticity," *Progress in Aerospace Sciences*, vol. 42, pp. 285–330, 2006.

[47] B. Sanderse, S. P. van der Pijl, and B. Koren, "Review of computational fluid dynamics for wind turbine wake aerodynamics," *Wind Energy*, vol. 14, pp. 799–819, 2011.

[48] P.-E. Réthoré, P. van der Laan, N. Troldborg, F. Zahle, and N. N. Sørensen, "Verification and validation of an actuator disc model," *Wind Energy*, vol. 17, pp. 919–937, 2013.

[49] I. Masters, A. Williams, T. N. Croft, M. Togneri, M. Edmunds, E. Zangiabadi, I. Fairley, and H. Karunarathna, "A comparison of numerical modelling techniques for tidal stream turbine analysis," *Energies*, vol. 8, pp. 7833–7853, 2015.

[50] A. Crespo, F. Manuel, D. Moreno, E. Fraga, and J. Hernandez, "Numerical analysis of wind turbine wakes," in *Proceedings of Delphi Workshop on Wind Energy Applications, Delphi, Greece, pp. 15-25*, 1985.

[51] A. El Kasmi and C. Masson, "An extended k-ϵ model for turbulent flow through horizontal-axis wind turbines," *Journal of Wind Engineering and Industrial Aerodynamics*, vol. 96, pp. 103–122, 2008.

[52] D. Cabezón, J. Sanz, I. Marti, and A. Crespo, "Cfd modelling of the interaction between the surface boundary layer and rotor wake: Comparison of results

obtained with different turbulence models and mesh strategies," in *Proceedings of the European Wind Energy Conference*, (Marseille, France), March 2009.

[53] K. Rados, J. Prospathopoulos, N. Stefanatos, E. Politis, P. Chaviaropoulos, and A. Zervos, "Cfd modeling issues of wind turbine wakes under stable atmospheric conditions," in *Proceedings of the European Wind Energy Conference*, (Marseille, France), March 2009.

[54] P. E. Réthoré, N. N. Sørensen, A. Bechmann, and F. Zhale, "Study of the atmospheric wake turbulence of a cfd actuator disc model," in *Proceedings of the European Wind Energy Conference*, (Marseille, France), March 2009.

[55] P. E. Réthoré, *Wind Turbine Wake in Atmospheric Turbulence*. PhD thesis, Aalborg University, 2009.

[56] J. M. Prospathopoulos, E. S. Politis, K. G. Rados, and P. K. Chaviaropoulos, "Evaluation of the effects of turbulence model enhancements on wind turbine wake predictions," *Wind Energy*, vol. 14, pp. 285–300, 2011.

[57] T. Roc, D. C. Conley, and D. Greaves, "Methodology for tidal turbine representation in ocean circulation model," *Renewable Energy*, vol. 51, pp. 448–464, 2013.

[58] A. M. AbdelSalam and V. Ramalingam, "Wake prediction of horizontal-axis wind turbine using full-rotor modeling," *Journal of Wind Engineering and Industrial Aerodynamics*, vol. 124, pp. 7–19, 2014.

[59] M. P. van der Laan, N. N. Sørensen, P.-E. Réthoré, J. Mann, M. C. Kelly, N. Troldborg, J. G. Schepers, and E. Machefaux, "An improved k-ϵ model applied to a wind turbine wake in atmospheric turbulence," *Wind Energy*, vol. 18, pp. 889–907, 2014.

[60] B. E. Launder and D. Spalding, *Mathematical Models of Turbulence*. London: Academic Press, 1972.

[61] D. C. Wilcox, *Turbulence Modeling for CFD*. La Cañada, California: DCW Industries, 1994.

[62] J. Doran and K. Packard, "Comparison of model and observations of the wake of a mod-0a wind turbine," Tech. Rep. PNL-4433, Pacific Northwest Laboratory, Richland, WA, 1982.

[63] B. Pederson and P. Nielson, "Description of the two danish 630kw wind turbines, nibe-a and nibe-b, and some preliminary test results," in *Third International Symposium on Wind Energy Systems, August 26-29, pp. 223-238*, 1980.

[64] G. Taylor, D. Milborrow, D. McIntosh, and D. Swift-Hook, "Wake measurements on the nibe windmills," in *Proceedings of the Seventh BWEA Wind Energy Conference, Oxford, pp. 67-73*, 1985.

[65] M. Magnusson, K. Rados, and S. Voutsinas, "A study of the flow downstream of wind turbine using measurements and simulations," *Wind Eng.*, vol. 20, pp. 389–403, 1996.

[66] J. W. Cleijne, "Results of the sexbierum wind farm; single wake measurements," Tech. Rep. TNO Report 93-082, TNO Institute of Environmental and Energy Technology, The Netherlands, 1993.

[67] L. A. H. Machielse, P. J. Eecen, H. Korterink, S. P. van der Pijl, and J. G. Schepers, "Ecn test farm measurements for validation of wake models," in *Proceedings of the European Wind Energy Conference*, (Milan, Italy), May 2007.

[68] P. Durbin, "On the k-ϵ stagnation point anomaly.," *International Journal of Heat and Fluid Flow*, vol. 17, pp. 89–90, 1996.

[69] M. P. van der Laan, N. N. Sørensen, P.-E. Réthoré, J. Mann, M. C. Kelly, and G. Schepers, "Nonlinear eddy viscosity models applied to wind turbine wakes," in *Proceedings of International Conference on Aerodynamics of Offshore Wind Energy Systems and Wakes*, (Copenhagen, Denmark), 2013. 514-525.

[70] N. Troldborg, F. Zahle, P.-E. Réthoré, and N. N. Sørensen, "Comparison of wind turbine wake properties in non-sheared inflow predicted by different computational fluid dynamics rotor models," *Wind Energy*, vol. 18, pp. 1239–1250, 2015.

[71] J. I. Whelan and T. Stallard, "Arguments for modifying the geometry of a scale model rotor," in *European Wave and Tidal Energy Conference Series*, 2011.

[72] T. Stallard, R. Collings, T. Feng, and J. Whelan, "Interactions between tidal turbine wakes: Experimental study of a group of 3-bladed rotors," in *European Wave and Tidal Energy Conference Series*, 2011.

[73] T. Stallard, R. Collings, T. Feng, and J. Whelan, "Interactions between tidal turbine wakes: experimental study of a group of three-bladed rotors," *Phil Trans R Soc A*, vol. 371, pp. 1–13, 2013.

[74] T. Stallard, T. Feng, and P. Stansby, "Experimental study of the mean wake of a tidal stream rotor in a shallow turbulent flow," *Journal of Fluids and Structures*, vol. 54, pp. 235–246, 2015.

[75] L. P. Chamorro, R. E. A. Arndt, and F. Sotiropoulos, "Reynolds number dependence of turbulence statistics in the wake of wind turbines," *Wind Energy*, vol. 15, pp. 733–742, 2012.

[76] P. Mycek, B. Gaurier, G. Germain, G. Pinon, and E. Rivoalen, "Experimental study of the turbulence intensity effects on marine current turbines behaviour. part i: One single turbine," *Renewable Energy*, vol. 66, pp. 729–746, 2014.

[77] P. Mycek, B. Gaurier, G. Germain, G. Pinon, and E. Rivoalen, "Experimental study of the turbulence intensity effects on marine current turbines behaviour. part ii: Two interacting turbines," *Renewable Energy*, vol. 68, pp. 876–892, 2014.

[78] S. B. Pope, *Turbulent Flows*. Cambridge University Press, 9^{th} printing ed., 2011.

[79] F. Menter, "Influence of freestream values on k-ω turbulence model predictions," *AIAA Journal*, vol. 30, pp. 1651–1659, 1992.

[80] ANSYS, "Ansys CFX-solver theory guide: Release 15.0," Tech. Rep. Release 15.0, ANSYS, Inc., 275 Technology Drive, Canonsburg, PA 15317, November 2013. http://www.ansys.com.

[81] L. Myers and A. Bahaj, "Experimental analysis of the flow field around horizontal axis tidal turbines by use of scale mesh disk rotor simulators," *Ocean Engineering*, vol. 37, pp. 218–227, 2010.

[82] T. Burton, D. Sharpe, N. Jenkins, and E. Bossanyi, *Wind Energy Handbook*. John Wiley & Sons Ltd., 2001.

[83] W. Zhang, C. D. Markfort, and F. Porte-Agel, "Near-wake flow structure downwind of a wind turbine in a turbulent boundary layer," *Exp. Fluids*, vol. 52, pp. 1219–1235, 2012.

[84] N. Zhou, J. Chen, D. E. Adams, , and S. Fleeter, "Influence of inflow conditions on turbine loading and wake structures predicted by large eddy simulations using exact geometry," *Wind Energy*, 2015.

[85] U. Hassan, "A wind tunnel investigation of the wake structure within small wind turbine farms," Tech. Rep. WN 5113, ETSU, 1993.

[86] L. A. Viterna and R. D. Corrigan, "Fixed pitch performance of large horizontal axis wind turbines," in *DOE/NASA workshop on large horizontal axis wind turbines, Cleveland, Ohio*, 1981.

[87] I. Ammara, C. Leclerc, and C. Masson, "A viscous three-dimensional differential/actuator-disk method for the aerodynamic analysis of wind farms," *Journal of Solar Energy Engineering*, vol. 124, pp. 343–356, 2002.

[88] S. Miley, "A catalog of low reynolds number airfoil data for wind turbine applications," Tech. Rep. DE82-021712, NTIS, 1982.

[89] I. H. Abbott, A. E. von Doenhoff, and L. S. Stivers Jr, "Summary of airfoil data," Tech. Rep. Report No 824, NACA, 1945.

[90] M. Harrison, *The Accuracy of the Actuator Disc-RANS Approach for Modelling Performance and Wake Characteristics of a Horizontal Axis Tidal Stream Turbine*. PhD thesis, University of Southampton, 2011.

[91] J. M. McMillan, A. E. Hay, R. H. Karsten, G. Trowse, D. Schillinger, and M. O'Flaherty-Sproul, "Comprehensive tidal energy resource assessment in the lower Bay of Fundy, Canada," in *European Wave and Tidal Energy Conference Series*, 2013.

[92] M. J. Churchfield, Y. Li, and P. J. Moriarty, "A large-eddy simulation study of wake propagation and power production in an array of tidal-current turbines," *Phil Trans R Soc A*, vol. 371, 2013.

[93] M. Shives and C. Crawford, "Validation of a practical cfd method for predicting hydrokinetic turbine performance in wake shadow," in *Proceedings of the European Wave and Tidal Energy Conference*, (Nantes, France), 2015.

[94] M. P. van der Laan, N. N. Sørensen, P.-E. Réthoré, J. Mann, M. C. Kelly, and N. Troldborg, "The k-ϵ-f_p model applied to double wind turbine wakes using different actuator disk force methods," *Wind Energy*, vol. 18, no. 12, pp. 2223–2240, 2015.

[95] R. Malki, I. Masters, A. J. Williams, and T. N. Croft, "Planning tidal stream turbine array layouts using a coupled blade element momentum – computational fluid dynamics model," *Renewable Energy*, vol. 63, pp. 46–54, 2014.

[96] H. G. Kim and V. C. Patel, "Test of turbulence models for wind flow over terrain with separation and recirculation," *Boundary-Layer Meteorology*, vol. 94, pp. 5–21, 2000.

[97] G. A. A. Moreira, André, A. C. dos Santos, C. A. M. do Nascimento, and R. M. Valle, "Numerical study of the neutral atmospheric boundary layer over complex terrain," *Boundary-Layer Meteorology*, vol. 143, pp. 393–407, 2012.

[98] E. S. Politis, J. Prospathopoulos, D. Cabezon, K. S. Hansen, P. K. Chaviaropoulos, and R. J. Barthelmie, "Modeling wake effects in large wind farms in complex terrain: the problem, the methods and the issues," *Wind Energy*, vol. 15, pp. 161–182, 2012.

[99] M. Shives and C. Crawford, "Turbulence modelling for accurate wake prediction in tidal turbine arrays," in *5th International Conference on Ocean Energy, 4 November, Halifax*, 2014.

[100] ANSYS, "Automatic near-wall treatment for omega-based models, ansys cfx release 12 documentation," tech. rep., ANSYS, 2009.

[101] T. Burton, N. Jenkins, D. Sharpe, and E. Bossanyi, *Wind Energy Handbook*. John Wiley & Sons, Ltd., second ed., 2011. ISBN: 978-0-470-69975-1.

[102] R. Malki, A. Williams, T. Croft, M. Togneri, and I. Masters, "A coupled blade element momentum computational fluid dynamics model for evaluating tidal stream turbine performance," *Applied Mathematical Modelling*, vol. 37, pp. 3006–3020, 2013.

[103] C. Garrett and P. Cummins, "The efficiency of a turbine in a tidal channel," *Journal of Fluid Mechanics*, vol. 588, pp. 243–251, 2007.

[104] C. Garrett and P. Cummins, "Limits to tidal current power," *Renewable Energy*, vol. 33, pp. 2485–2490, 2008.

[105] R. Vennell, "Tuning turbines in a tidal channel," *J. Fluid Mech.*, vol. 663, pp. 253–267, 2010.

[106] R. Vennell, "Tuning tidal turbines in-concert to maximise farm efficiency," *J. Fluid Mech.*, vol. 671, pp. 587–604, 2011.

[107] J. N. Sørensen, W. Z. Shen, and R. Mikkelsen, "Wall correction model for wind tunnels with open test section," *AIAA Journal*, vol. 44, pp. 1890–1894, 2006.

[108] M. O. L. Hansen, N. N. Sørensen, and R. G. J. Flay, "Effect of placing a diffuser around a wind turbine," *Wind Energy*, vol. 3, pp. 207–213, 2000.

[109] H. A. Madsen, *The Actuator Cylinder - A Flow Model for Vertical Axis Wind Turbines*. PhD thesis, Aalborg University, 1982.

[110] R. G. Rajagopalan, D. E. Berg, and P. C. Klimas, "Development of a three dimensional model for the darrius rotor and its wake," *Journal of Propulsion and Power*, vol. 11, pp. 185–195, March 1995.

[111] A. H. Madsen, T. J. Larsen, P. U. Schmidt, and L. Vita, "Implementation of the actuator cylinder flow model in the HAWC2 code for aeroelastic simulations on vertical axis wind turbines," in *Proceedings of 51st AIAA Aerospace Sciences Meeting including the New Horizons Forum and Aerospace Exposition*, no. 2013-0913, 2013.

[112] S. Shamsoddin and F. Porté-Agel, "Large eddy simulation of vertical axis wind turbine wakes," *Energies*, vol. 7, pp. 890–912, 2014.

[113] F. Dominguez, J.-L. Achard, J. Zanette, and C. Corre, "Fast power output prediction for a single row of ducted cross-flow water turbines using a BEM-RANS approach," *Renewable Energy*, vol. 89, pp. 658–670, 2016.

[114] J. Thomson, B. Polagye, V. Durgesh, and M. C. Richmond, "Measurements of turbulence at two tidal energy sites in Puget Sound, WA.," *IEEE Journal of Oceanic Engineering*, vol. 37, pp. 363–374, 2012.

[115] E. A. Nystrom, C. R. Rehmann, and K. A. Oberg, "Evaluation of mean velocity and turbulence measurements with ADCPs," *Journal of Hydraulic Engineering*, vol. 133-12, pp. 1310–1318, 2007.

[116] T. Blackmore, L. E. Myers, and A. S. Bahaj, "Effects of turbulence on tidal turbines: Implications to performance, blade loads, and condition monitoring," *International Journal of Marine Energy*, vol. 14, pp. 1–26, 2016.

[117] J. Schluntz and R. Willden, "The effect of blockage on tidal turbine rotor design and performance," *Renewable Energy*, vol. 81, pp. 423–441, 2015.

[118] G. Sutherland, M. Foreman, and C. Garrett, "Tidal current energy assessment for johnstone strait, vancouver island," *Proc. IMechE Vol. 221 Part A: J. Power and Energy*, vol. 221, pp. 147–157, 2007.

[119] S. Nash, N. O'Brien, A. Olbert, and M. Hartnett, "Modelling the far field hydro-environmental impacts of tidal farms a focus on tidal regime, inter-tidal zones and flushing," *Computers & Geosciences*, vol. 71, pp. 20–27, 2014.

[120] D. Fallon, M. Hartnett, A. Olbert, and S. Nash, "The effects of array configuration on the hydro-environmental impacts of tidal turbines," *Renewable Energy*, vol. 64, pp. 10–25, 2014.

[121] V. Ramos, R. Carballo, M. S. M. Álvarez a, and G. Iglesias, "Assessment of the impacts of tidal stream energy through high-resolution numerical modeling," *Energy*, vol. 61, pp. 541–554, 2013.

[122] C. Garrett and P. Cummins, "Generating power from tidal currents," *Journal of waterway, port, coastal and ocean engineering*, vol. 130-3, pp. 114–118, 2004.

[123] S. R. Turnock, A. B. Phillips, J. Banks, and R. Nicholls-Lee, "Modelling tidal current turbine wakes using a coupled rans-bemt approach as a tool for analysing power capture of arrays of turbines," *Ocean Engineering*, vol. 38, pp. 1300–1307, 2011.

[124] R. Malki, I. Masters, A. Williams, and T. Croft, "The influence of tidal stream turbine spacing on performance," in *European Wave and Tidal Energy Conference Series*, 2011.

[125] R. Vennell, S. W.Funke, S. Draper, C. Stevens, and T. Divett, "Designing large arrays of tidal turbines: A synthesis and review," *Renewable and Sustainable Energy Reviews*, vol. 41, pp. 454–472, 2015.

[126] I. Walkington and R. Burrows, "Modelling tidal stream power potential," *Applied Ocean Research*, vol. 31, 2009.

[127] R. Ahmadian and R. A. Falconer, "Assessment of array shape of tidal stream turbines on hydro-environmental impacts and power output," *Renewable Energy*, vol. 44, pp. 318–327, 2012.

[128] T. A. A. Adcock, S. Draper, G. T. Houlsby, A. G. L. Borthwick, and S. Serhadlıoğlu, "The available power from tidal stream turbines in the pentland firth," *Proc R Soc A*, vol. 496, 2013.

[129] S. Draper, T. A. Adcock, A. G. Borthwick, and G. T. Houlsby, "Estimate of the tidal stream power resource of the pentland firth," *Renewable Energy*, vol. 63, pp. 650–657, 2013.

[130] D. Hasegawa, J. Sheng, D. A. Greenberg, and K. R. Thompson, "Far-field effects of tidal energy extraction in the minas passage on tidal circulation in the bay of fundy and gulf of maine using a nested-grid coastal circulation model," *Ocean Dynamics*, vol. 61, pp. 1845–1868, 2011.

[131] G. I. Shapiro, "Effect of tidal stream power generation on the region-wide circulation in a shallow sea," *Ocean Science*, vol. 7, pp. 165–174, 2011.

[132] S. P. Neill, J. R. Jordan, and S. J. Couch, "Impact of tidal energy converter (tec) arrays on the dynamics of headland sand banks," *Renewable Energy*, vol. 37, pp. 387–397, 2012.

[133] P. A. Work, K. A. Haas, Z. Defne, and T. Gay, "Tidal stream energy site assessment via three-dimensional model and measurements," *Applied Energy*, vol. 102, pp. 510–519, 2013.

[134] Z. Yang, T. Wang, and A. E. Copping, "Modeling tidal stream energy extraction and its effects on transport processes in a tidal channel and bay system using a three-dimensional coastal ocean model," *Renewable Energy*, vol. 50, pp. 605–613, 2013.

[135] S. H. Lee, S. H. Lee, K. Jang, J. Lee, and N. Hur, "A numerical study for the optimal arrangement of ocean current turbine generators in the ocean current power parks," *Current Applied Physics*, vol. Supplement: The Proceeding of the International Renewable Energy Conference and Exhibition 2008 (RE2008), pp. S137–S141, 2010.

[136] W. Hunter, T. Nishino, and R. H. Willden, "Investigation of tidal turbine array tuning using 3D Reynolds-Averaged NavierStokes simulations," *International Journal of Marine Energy*, vol. 10, pp. 39–51, 2015.

[137] T. Divett, R. Vennell, and C. Stevens, "Channel-scale optimisation and tuning of large tidal turbine arrays using les with adaptive mesh," *Renewable Energy*, vol. 86, pp. 1394–1405, 2016.

[138] S. Funke, P. Farrell, and M. Piggott, "Tidal turbine array optimisation using the adjoint approach," *Renewable Energy*, vol. 63, pp. 658–673, 2014.

[139] IEC, "Marine energy wave, tidal and other water current converters part 200: Electricity producing tidal energy converters - power performance assessment," Technical Specification 62600-200, International Electrrotechnical Commission, 2013.

[140] J. I. Whelan, J. M. R. Graham, and J. Peir, "A free-surface and blockage correction for tidal turbines," *J. Fluid Mech*, vol. 624, pp. 281–291, 2009.

[141] R. A. Walters, "A coastal ocean model with subgrid approximation," *Ocean Modelling*, vol. 102, pp. 45–54, 2016.

[142] J. Lawrence, H. Kofoed-Hansen, and C. Chevalier, "High-resolution metocean modelling at emecs (uk) marine energy test sites," in *Proceedings of the 8th European Wave and Tidal Energy*, (Uppsala, Sweden), 2009.

[143] L. Blunden and A. Bahaj, "Initial evaluation of tidal stream energy resources at portland bill, uk," *Renewable Energy*, vol. 31, pp. 121–132, 2006.

[144] R. Karsten, "An assessment of the potential of tidal power from minas passage, bay of fundy, using three dimensional models," in *Proceedings of the ASME 2011 30th International Conference on Ocean, Offshore and Arctic Engineering OMAE, Rotterdam, Netherlands*, June 1924 2011.

[145] S. Waldman, G. Genet, S. Bastón, and J. Side, "Correcting for mesh size dependency in a regional models representation of tidal turbines," in *Proceedings of the 11th European Wave and Tidal Energy Conference 6-11th Sept 2015, Nantes, France*, 2015.

[146] M. OFlaherty-Sproul, "New high and low resolution numerical models of the tidal currents through the digby neck passages," Master's thesis, Acadia University, 2013.

[147] S. Crammond, R. Caljouw, I. Jones, A. Wells, I. Hamill, and O. Petersen, "Meygen tidal energy project: Numerical modelling of tidal turbine wake interactions," in *European Wave and Tidal Energy Conference Series*, 2013.

[148] F. Castellani and A. Vignaroli, "An application of the actuator disc model for wind turbine wakes calculations," *Applied Energy*, vol. 101, pp. 432–440, 2013.

[149] S. Draper and T. Nishino, "Centred and staggered arrangements of tidal turbines," *Journal of Fluid Mechanics*, vol. 739, pp. 72–93, 2014.